THE CANARIAS INFRARED CAMERA EXPERIMENT (CIRCE) AND THE SEARCH FOR AND STUDY OF MASSIVE STARS

By

MICHELLE L. EDWARDS

A DISSERTATION PRESENTED TO THE GRADUATE SCHOOL
OF THE UNIVERSITY OF FLORIDA IN PARTIAL FULFILLMENT
OF THE REQUIREMENTS FOR THE DEGREE OF
DOCTOR OF PHILOSOPHY

UNIVERSITY OF FLORIDA

2008

To my husband, David.

Now I feel no rain, no cold, no loneliness – for you are my shelter, my warmth, and my companion. We are two people but there is one life before us. May beauty surround us in the journey ahead and through all the years to come.

ACKNOWLEDGMENTS

This dissertation is the result of the help, talent, and encouragement of many people whom I would like to thank. First, I acknowledge my advisers, Drs. Stephen Eikenberry and Reba Bandyopadhyay. Over the last 2 years, Reba has offered impeccable advice about my science, writing, and career as a scientist and I look to her as a role model and mentor. I feel secure in saying that this work would not exist in its current state if she had not agreed to be my co-adviser.

While there is little I can say or do to repay Steve for his friendship, advice, and constant cheerleading during my early graduate career, what he gave me in these last years was the most valuable gift an adviser can give a senior student - a push out of the nest and the freedom to make and follow my own path. I am certain I would not have developed the self-confidence and poise necessary to write this dissertation and defend it without that experience.

I thank my committee, Dr. Charlie Telesco, Dr. Ata Sarajedini, Dr. Guido Mueller, and Dr. Rafael Guzman for useful input and discussions. I also acknowledge Dr. Fred Hamann for many chats and a great introduction to stellar winds.

I thank P.E.O. International for awarding me a P.E.O. Scholar Award, which helped support me financially during the last two years of my graduate career. I am especially grateful to Anne Seymour and Chapter H in Baltimore, MD for nominating me.

I acknowledge many close friends whose help and camaraderie made the last seven years of graduate school navigable. These include Rachel and Marcus Chen, Dan and Jodi Bell, Veronica Donoso, Joe Carson, Andrew Gosling, Mike Barker, Ashley Espy, Valerie Mikles, Ana Matkovic, Suvrath Mahadevan, Maren Hempel, Ileana Vass, Veera Boonyasait, Joanna Levine, Eric McKenzie, Dan Capellupo, Ineta Jonusas, Deborah Herbstman, Dimitri Veras and especially, my classmate, constant companion, and dearest friend, David Clark.

I also acknowledge my CIRCE teammates, Miguel Charcos-Llorens, Nestor Lasso, and Dr. Antonio Marin-Franch, as well as the UF instrumentation group, particularly, Dr. S. Nicholas Raines, Dr. Chris Packham, and Jeff Julian, with whom it was a pleasure and privilege to work. I thank Dr. Craig Warner whose tireless efforts on the FATBOY data reduction pipeline made Chapters 5 and 6 possible.

Throughout my life, I have been lucky to have excellent teachers who inspired and encouraged me. To a few, I owe many, many thanks: Dr. John Oliver, Dr. Robert Boyle, Drs. Ken and Priscilla Laws, Mr. Joe Coleman, Mrs. Karen Fishman, Mr. Neil Wood, and especially Dr. Tony Morgan, my close friend and adviser, who took me to Flagstaff, pointed me in the direction of a telescope, and changed my life forever.

I acknowledge the many gifted choirs and choir directors in Gainesville who welcomed me into their folds, especially Dr. William Kesling and the UF University Choir; it was a great honor to sing with such consummate professionals.

I would like to acknowledge my loving family including my mother, Linda, who pursued her own college degree while raising two small children and inspired me to be a fighter and never give up on my dreams, my father Walter, a constant source of support and encouragement whose passion for history showed me what it was to really love to study something, and my hilarious, musically-talented brother Matthew and his smart, beautiful wife Jackie who have brought incredible joy and many laughs into my life. I also thank the entire Carney and Edwards families for cheering me on through years and years (and years) of school.

I thank my parents-in-law, Marie and Paul Edmeades, kindred spirits, whose support and love throughout the years (and especially in the last few months) has been a source of constant joy in our lives. I thank their many friends and extended family members who have also supported me.

Last but not least, I acknowledge my husband and love for 9 years, David Edmeades, to whom I dedicate this work. Wherever you are, dear, I call home.

TABLE OF CONTENTS

LIST OF TABLES

LIST OF FIGURES

Abstract of Dissertation Presented to the Graduate School
of the University of Florida in Partial Fulfillment of the
Requirements for the Degree of Doctor of Philosophy

THE CANARIAS INFRARED CAMERA EXPERIMENT (CIRCE) AND THE SEARCH FOR AND STUDY OF MASSIVE STARS

By

Michelle L. Edwards

August 2008

Chair: Stephen Eikenberry
CoChair: Reba Bandyopadhyay
Major: Astronomy

I report on the design status of the Canarias InfraRed Camera Experiment (CIRCE), an all-reflective near-infrared visitor instrument for the 10.4 meter Gran Telescopio Canarias (GTC). In addition to functioning as a 1-2.5 micron imager, CIRCE will have the capacity for narrow-band imaging, low- and moderate- resolution grism spectroscopy, and imaging- and spectro- polarimetry. I present my contributions to the optical, opto- and cryo- mechanical design.

I then detail my search for and study of massive stars around magnetars using the current generation of near-infrared instruments. I survey the environments of Soft Gamma Repeaters using near-infrared narrow-band imaging to probe for Brγ and HeI features indicative of massive stars. Using this technique, I successfully detect previously known massive stars in Cl 1806-20, the established natal cluster of SGR 1806-20. I also identify new candidate massive stars in this cluster and around two other SGRs, which may represent the bulk of the heretofore undiscovered massive star populations associated with these objects.

Finally, I discuss a serendipitous discovery that developed from my study of massive stars in clusters. Analyses of the five Luminous Blue Variables (LBVs) and LBV candidates in massive cluster environments reveal that four of these rare, massive objects lie on the outskirts of their host clusters. I demonstrate that the chance probability of

a cluster star lying consistently at or beyond the radii of these LBVs is 0.02%. Mass segregation theories suggest that these stars, the most massive objects in their respective clusters should fall inward over dynamical time-scales. Thus, while one would expect to find a significant bias toward centrally located LBVs, my analyses show that these massive stars are instead located on the periphery of their host clusters.

CHAPTER 1
INTRODUCTION

In 1800, the famed astronomer William Herschel performed an experiment to measure the temperatures of different colors of light. Using a prism, he dispersed sunlight into a spectrum and placed a thermometer at the position of every color. As a control, he also placed a thermometer slightly redward of the visible light. What he discovered upon analyzing the results surprised him; the control thermometer was hotter than the others. He postulated that it was warmed by invisible light from the sun, which he called "calorific rays" (Herschel 1801). Today, we term the region of the electromagnetic spectrum discovered by Herschel "infrared radiation" (Glass 1999).

Divided into three regimes, defined here as near- (1 - 5 μm), mid- (5 - 25 μm), and far- (25 - 350 μm), infrared radiation is crucial to understanding a wide variety of processes in our universe (Glass 1999). For example, near-infrared (NIR) observations of the Galactic Plane have revealed millions of previously undetected stars, each whose visible light is blocked by the dust and gas in the disk of our Galaxy (Skrutskie et al. 2006). Mid-infrared (MIR) studies of young stars have uncovered protoplanetary disks, the precursors to exosolar planets and asteroid belts (Lagage & Pantin 1994; Telesco 2000). Meanwhile, cold dust clouds in the earliest phases of star formation (Mezger 1986; Wszolek et al. 1989), are visible in the the far-infrared (FIR).

These discoveries and many others have only become possible in the last 40 years; compared to the $>$ 4000 year tradition of visible light observations (Chaisson & McMillan 1996), IR astronomy is a very young field. Successes in the early 1950s and 1960s with lead-sulphide and gallium-doped germanium bolometers led to the first infrared sky surveys, the Air Force Infrared Survey (Kleinmann et al. 1981) and the Two Micron Sky Survey (Neugebauer & Leighton 1969). The 1970s gave rise to FIR balloon experiments and the flight of the Kuiper Airborne Observatory, an infrared telescope housed in a jet (Gillespie 1981; Low et al. 2007). Then in the 1980s, IR astronomy took a giant

leap forward with the development of IR arrays and the launch of IRAS, the InfraRed Astronomical Satellite. The former heralded the coming of age of infrared instrumentation and prepared the way for hundreds of modern infrared astronomical cameras (Rieke 2007). The latter guaranteed continued interest in infrared science, unveiling $>$ 350,000 infrared sources.

Today, a variety of current and planned space-based infrared telescopes, including the Spitzer Space Telescope, Herschel Space Observatory, and James Webb Space Telescope (Werner et al. 2004; Pilbratt 2004; Sabelhaus et al. 2005), promise deep, high resolution infrared images and spectra. Further, the location of large observatories above the water vapor that absorbs infrared radiation, has made ground-based near- and mid- infrared observing a reality. Every 8 - 10 meter class telescope now has a variety of infrared instruments; most equipped with mercury cadmium telluride (HgCdTe) or indium antimonide (InSb) detectors many times larger and more sensitive than the first arrays (Rieke 2007). Additionally, a number of telescopes, like the 8-meter Gemini North and South telescopes are themselves optimized for infrared science, utilizing special designs and mirror coatings to limit emissivity, as well as undersized, lightweight secondary mirrors capable of quick movements for MIR observing (Mountain et al. 1997; Roche 2004)

Following in the footsteps of great international observatories like Keck and Gemini is the Gran Telescopio Canarias (GTC), the world's largest optical/infrared telescope (Alvarez et al. 2000; Rodriguez Espinosa & Alvarez Martin 2006). Also optimized for IR observing, the GTC promises to be yet another positive step in the relatively new, but clearly important field of IR astronomy. In the following sections, I will offer an overview of the GTC and its collection of cutting-edge instruments. I will particularly focus on one NIR instrument, the Canarias InfraRed Camera Experiment (CIRCE), the design of which comprised a major part of my thesis work.

1.1 The Gran Telescopio Canarias

Located on the island of La Palma in the Canary Islands, the Gran Telescopio Canarias (GTC) is a joint venture between Spain, Mexico, and the University of Florida (UF). Currently in the final stages of construction, first science light is expected in late 2008. Upon its completion it will be the largest optical/infrared telescope in the world.

The GTC is a Ritchey-Chretien telescope, built with hyperbolic primary and secondary mirrors to eliminate coma and spherical aberration. The primary is segmented and composed of 36 hexagonal pieces each made of a specialized zero-expansion glass ceramic manufactured by Schott Inc. The secondary is honeycomb-shaped and composed of light-weight beryllium coated with nickel. The reduced mass of this mirror allows for quick motions, or chopping, crucial for MIR observing (Rodríguez Espinosa & Alvarez 2003; Rodriguez Espinosa & Alvarez Martin 2006). As of May 2008 the telescope structure and dome are complete and in place at the Roque de los Muchachos Observatory. The secondary mirror is mounted in its structure at the prime focus and 24 of the 36 primary mirror segments are in place (Rodriguez-Espinosa, *private communication*). Once fully assembled, the collecting surface of the primary mirror will be equivalent to a 10.4 meter telescope.

Figure 1-1 shows the GTC's mirrors and foci. The primary mirror is designated M1, the secondary M2, and the movable tertiary M3. Light from the sky falling on the primary is reflected to the secondary. When the tertiary is not in the optical path, light from the secondary is reflected back down through a hole in the primary to the Cassegrain Focus. When the tertiary is inserted into the GTC's optical path it directs light from the secondary perpendicular to the telescope's native optical axis to one of four Bent or Folded Cassegrain Foci (FCF) or one of two Nasymth Foci (NF). In all, the telescope can accommodate 7 instruments, although astronomers can only observe with one at a time. (Rodríguez Espinosa & Alvarez 2003).

As with most modern large observatories, the GTC will have a suite of instruments that cover the full range of optical and infrared wavelengths. While built by the GTC partners, these cameras, often called facility instruments, belong to the observatory and will be available to the entire community. Given the complexity and cost of building cutting-edge facility instruments, the GTC has spread this process over several generations. First generation instruments include CanariCam, a MIR imager, spectrograph, polarimeter, and coronograph intended for the Cassegrain focus (Telesco et al. 2003) and OSIRIS an optical spectrograph and imager that will mount at a Nasmyth focus (Cepa et al. 2003). The GTC will commission both these instruments on the telescope during the year after first scientific light. The observatory will commission the second generation instruments EMIR, a NIR camera and high-resolution spectrograph and FRIDA, a NIR integral field unit (IFU), upon their completion several years into the telescope's operation (Garzón et al. 2003).

1.2 A NIR Visitor Instrument

While the final suite of GTC instruments will sample all crucial optical and infrared regimes, the first-generation of facility instruments do not include a NIR camera. Professor Stephen Eikenberry designed the Canarias InfraRed Camera Experiment, CIRCE, to fill the crucial gap between the telescope's inception and the commissioning of the second-generation NIR facility instrument EMIR and serves as principal investigator (PI) for this project. While CIRCE is officially a "visitor" instrument, built solely with funds from the University of Florida and the National Science Foundation, the instrument is specialized for the GTC and is not intended to travel to other observatories. Further, as opposed to traditional "visitor" instruments only used by the build team or with specific permission from the instrument PI, the entire GTC community will be welcome to use CIRCE. In return the CIRCE team receives "pay-back" time – guaranteed nights on the telescope.

Besides functioning as a 1-2.5 μm broad-band imager, CIRCE will have the capacity for narrow- band imaging, low- and moderate- resolution grism spectroscopy, and imaging polarimetry. Other design features include fully cryogenic filter, slit, and grism wheels, high-speed photometry modes, and broad-band imaging in J, H, and Ks filters (Edwards et al. 2004, 2006). CIRCE's $0.10''$ per pixel plate scale provides seeing limited images even in the most excellent atmospheric conditions at the GTC site, estimated at $\sim 0.2''$ (Munoz-Tunon et al. 1997). Also, the planned $3.4' \times 3.4'$ field is 25 times larger than NIRC on the KECK Telescope (Matthews & Soifer 1994) and 3 times larger than NIRI on the Gemini North Telescope (Hodapp et al. 2003).

In the first three chapters of this thesis, I describe the optical, opto- and cryo-mechanical design of CIRCE. In Chapter 2, I show how CIRCE's scientific goals and role as a "workhorse" instrument influenced crucial features and specifications. I also present the completed optical layout and our in-depth analyses of the optical design, concentrating on characteristics such as enclosed energy and field-of-view. In Chapter 3, I discuss the opto-mechanical design, starting with how I used the optical design to constrain all major opto-mechanical components. I then review the mechanical design of brackets and the optical bench. Finally in Chapter 4 , I detail my work on the cryo-mechanical design, specifically the filter wheel or "pupil" box.

1.3 Science with CIRCE

While new instruments like CIRCE, EMIR, OSIRIS, and CanariCam explore the "bleeding edge" of technology, it is important to remember that they are fundamentally driven by science; observatories fund instruments that meet the needs of their users. Occasionally, this requires commissioning a specialized instrument that will solve one or two very specific scientific problems. More often scientists have an array of projects in mind that drive the instrument. An observatory may organize an advisory committee to discuss these broad goal and help define the instrument's purpose.

CIRCE has such a committee, with membership spanning all of the GTC partners. The CIRCE Advisory Committee members are: Drs. Stephen Eikenberry (principal investigator) and Ata Sarajedini from the University of Florida, Dr Evenico Mediavilla from the Instituto de Astrofisica de Canarias, Dr. Alberto Castro-Tirado from the Instituto de Astrofisica de Andalucia, Mauricio Tapia from the Universidad Nacional Autonoma de Mexico, and Dr. Peter Hammersley from the Gran Telecopio Canarias Observatory.

Our team, with input from this advisory committee, designed CIRCE with a broad range of scientific objectives in mind. Examples of projects outlined in the original NSF grant proposal written by Dr. Stephen Eikenberry with contributions from the advisory committee include: a campaign to observe microquasar GRS 1915+105 with high-speed photometry and low-resolution spectroscopy, a polarimetric study of the relativistic jets of microquasars, and JHK photometry of Galactic Globular clusters. These are only a few of the myriad of projects one is capable of completing with CIRCE's combination of modes and features.

In this dissertation, I focus on another project that could hypothetically utilize CIRCE's capabilities; an emission-line search for massive star clusters around Soft Gamma Repeaters (SGRs). While CIRCE's FOV and narrow-band filter selection makes it well-equipped for this survey, I did not use CIRCE to collect the observations presented in this work. Given CIRCE's anticipated completion in 2009, this was a strategic decision made early in the project. By choosing to use the previous generation of NIR imagers to obtain my observations, I was able to both participate in the early design work of CIRCE and complete a viable science project within the timescale typical of a thesis. However, I discuss how I plan to use CIRCE to continue the research presented in Chapters 5 and 6 in the future work portion of my conclusions (Chapter 8).

1.4 The Search for and Study of Massive Stars

Massive stars are defined as any star with an initial mass $> 8\ M_{\odot}$ (Phillips 1999; Heger et al. 2003a). During their life on the main sequence, they produce energy by fusing hydrogen into helium via the carbon-nitrogen-oxygen (CNO) cycle. Unlike their less massive counterparts, massive stars have convective cores; the bulk motion of gas particles is responsible for heat transfer within their interiors. Massive stars are also supported, in large part, by radiation pressure, making them less stable than stars like the sun (Phillips 1999).

While far outnumbered by low and intermediate mass stars, massive stars dominate power output, CNO enrichment and ultraviolet (UV) radiation in the Milky Way (Morris & Serabyn 1996). However, a large portion of the massive star population remains undiscovered; their location in areas subject to high extinction and overcrowding, such as the Galactic Plane, has barred optical surveys from detecting 95% of very massive star clusters (Hanson 2003).

Despite lacking observations of significant portions of the Galactic massive star population, intriguing discoveries of individual objects continue to surface, often posing more questions than they answer. For instance, observations of the Pistol Star (Figer et al. 1998), and LBV 1806-20 (Eikenberry et al. 2004b), with potential masses > 150 $M_{\odot}$, indicate that the maximum stellar mass may exceed the canonical theoretical limit of 100 $M_{\odot}$ (Phillips 1999). Until we locate and study the majority of the massive star population, the potential for discovering more "Very Massive Stars" that challenge our current understanding of stellar physics is a reasonable possibility.

Furthermore, studies by Heger et al. (2003a) suggest that the deaths and resulting progeny of massive stars may also defy our canonical picture of stellar evolution. Initially, it was believed that stars with initial masses $<$ 22-25 $M_{\odot}$ formed neutron stars while stars with initial masses $> 25\ M_{\odot}$ became black holes. New research indicates that this picture may be too simplistic (Fryer 1999; Fryer & Kalogera 2001; Heger et al. 2003b).

During the late stages of their evolution, massive stars often have strong stellar winds that result in significant mass loss. Thus, objects originally destined to end their lives as black holes may lose enough mass during pre-supernovae Wolf-Rayet (WR) or Luminous Blue Variable (LBV) phases to instead evolve into neutron stars (Heger et al. 2003a,b).

With these interesting problems in mind, we proposed a survey to search for massive stars. In particular, we chose a "targeted" approach, probing for massive stars around interesting objects potentially associated with young clusters; in this case Soft Gamma Repeaters (SGRs). SGRs are magnetars – a rare type of neutron star (Duncan & Thompson 1992). Besides the potential to increase the size of the known massive star population, we hoped our investigation of SGR environments might shed light on the astrophysical problem of the origins of magnetars and the fates of windy massive stars.

In the following sections, I review magnetars, previous observations of their environment and the mechanics of our search for massive stars in the following sections.

1.5 Observations of Magnetars

On March 5, 1979, a giant gamma-ray burst, peaking at 10^{45} ergs s^{-1}, flooded every gamma-ray detector in orbit around Earth. The hard spike was followed by a tail of soft-gamma ray bursts that varied with an 8s period (Mazets et al. 1979; Golenetskii et al. 1984) and lasted three minutes. In the following years, the same source, located in the Large Magellanic Cloud, emitted a number of lower energy soft-gamma bursts lasting from 50 ms to 3.5s (Golenetskii et al. 1984). The repetitive nature, absence of high-energy gamma-rays, and duration of these bursts was similar to bursts seen subsequently in two other anomalous Galactic sources (Laros et al. 1987). Notably different from classic gamma-ray bursts (GRBs) which do not repeat, the objects earned their own classification: Soft Gamma Repeaters (SGRs). The LMC source was designated SGR 0526-66; the other two are SGR 1806-20 and SGR 1900+14.

While a variety of hypothesis to explain these objects abounded in the following two decades, the most successful theory, developed by Duncan & Thompson (1992)

is the magnetar model. In this scenario a newborn neutron star rotating very quickly creates a dynamo that strengthens the stars magnetic field. As the star cools, the dynamo action stops; however, the magnetic field, which has reached 10^{14} - 10^{16} G, is locked into the star's dense interior. Duncan & Thompson (1992) believed that instabilities in this strong magnetic field created both the large and small soft gamma-ray flares. They also predicted that the dissipation of rotational energy by magnetic waves would slow a magnetar in the first few seconds of its birth, resulting in a rotation period of $\sim$ 10s. Further observations of SGRs led to the discovery of persistent X-ray emission (Murakami et al. 1994; Rothschild et al. 1994; Vasisht et al. 1994), explained by Thompson & Duncan (1996) as decay of the magnetic field.

As relayed in Woods & Thompson (2006), significant confirmation of the magnetar model came in 1998 with the discovery of a 7.5 s period and 0.0026 s year^{-1} spin-down in the X-ray emission of SGR 1806-20. The spin-down was attributed to magnetic braking of a neutron star with a 10^{15} G magnetic field (Kouveliotou et al. 1998a), in the range of that predicted by the magnetar model (Duncan & Thompson 1992). Then, on the heels of this announcement, Hurley et al. (1999) reported observations of a giant flare from SGR 1900+14 , similar in morphology to the earlier SGR 0526-66 event (see Figure 1-2). This effectively settled any doubt that SGR 1900+14 and SGR 0526-66 were indeed the same class of object. Soon after, SGR 1627-41 was added to the roster of SGRs after Kouveliotou et al. (1998b) and Woods et al. (1999) reported 100 soft gamma-ray bursts emitted from the source. This brought the total number of SGRs to four, where it has remained since.

There is significant evidence that another flavor of neutron star, known as Anomalous X-ray Pulsars (AXPs), are also magnetars. First discovered by Fahlman & Gregory (1981), AXPs exhibit fast spin-down rates, 5-7 s periods, and 10^{35} - 10^{37} erg s^{-1} X-ray emission. Isolated objects, they were originally termed "anomalous" due to the absence of a reasonable mechanism to explain their high X-ray luminosity. However, while accounting

for similar X-ray luminosities in SGRs, Thompson & Duncan (1996) proposed magnetic decay as the source of AXPs' energy and included these objects in their consensus of magnetars. This interpretation was strengthened by Gavriil et al. (2002) and Kaspi & Gavriil (2003) with the discovery of SGR-like bursts from two AXPs, 1E 1048.1-5937 and 1E 2259+586 (see Figure 1-3). Currently, astronomers recognize 8 AXPs and candidate AXPs.

In summary, SGRs exhibit: [1] "giant" ($\sim 10^{44}$ ergs/s) gamma-ray bursts characterized by a hard spike and soft-gamma ray tail with variations on the order of 10s (Figure 1-2), [2] repetitive, bright ($\sim 10^{41}$ erg/s) soft-gamma ray bursts lasting $\sim$ 100 ms (Figure 1-3) and [3] persistent X-ray emission with a typical luminosity $\sim 10^{35}$ - 10^{37} ergs/s. Less common and not well understood are "intermediate" SGR bursts, which display characteristics of both the repetitive soft gamma-ray and the giant bursts (Woods & Thompson 2006, and references therein). AXPs exhibit [1] SGR-like soft gamma-ray bursts and [2] persistent X-ray emission similar to SGR X-ray emission. To date, no "giant" AXP flares have been observed.

Magnetars are set apart from other neutron stars on the spin period vs. period derivative (P-$\dot{P}$) diagram. Shown in Figure 1-4 (Woods & Thompson 2006), a P-$\dot{P}$ diagram groups neutron stars according to their periods (P), change in periods over time ($\dot{P}$), and magnetic fields (B). Classical neutron stars are located in the central region of the diagram. Magnetars, which spin down more quickly and have longer periods and stronger magnetic fields than classical neutron stars, populate the upper left corner.

1.6 Environments of Soft Gamma Repeaters (SGRs)

Magnetars offer a unique opportunity to investigate the exotic endpoints of stellar evolution. With only a handful of confirmed members plus a few additional candidates known, the potential to study the entire population of magnetars, establish formation scenarios, and characterize their progenitors is a tantalizing and realistic objective.

To this end, several authors have performed studies focused on magnetars and their environments. Interestingly, of the four SGRs known, three are potentially associated with massive star clusters. SGR 1806-20 is embedded in a cluster of massive stars, Cl 1806-20 (Fuchs et al. 1999; Corbel & Eikenberry 2004; McClure-Griffiths & Gaensler 2005; Bibby et al. 2008) that contains both a Wolf-Rayet star and LBV 1806- 20, potentially the most massive stellar object discovered to date (Eikenberry et al. 2004a). Vrba et al. (2000) reported the discovery of a potential massive stellar cluster with at least 13 members a few arcseconds from SGR 1900+14; recent observations by Wachter et al. (2008) suggest that the cluster and magnetar are at the same distance. Finally, Klose et al. (2004) reported the discovery of a young cluster of stars in the vicinity of SGR 0526-66.

This observational evidence, combined with recent theoretical models developed by Heger et al. (2003a) raises an interesting question: if magnetars are uniformly associated with clusters of massive stars, might we conclude that their progenitors were also very massive? Magnetars are compact objects formed from stars that have already progressed through most of their evolutionary stages. Since stellar evolution dictates that in order to have already reached the endpoint of their stellar lifespan, these progenitors must be more massive than the most massive stars currently in their natal clusters, this suggests scenarios in which exceptionally massive stars explode to form not only neutron stars, but particularly, highly-magnetized neutron stars (Eikenberry et al. 2004a; Figer et al. 2005; Muno et al. 2006).

The existence of massive stars and neutron stars in the same cluster could also be evidence of multi-epoch star formation (Eikenberry et al. 2004a). This theory proposes that shocks from the explosive death of one star might induce a wave of star formation, yielding a new generation of stars. Observational evidence for this mode of triggered star formation reaches back for decades and encompasses several well-known OB associations including Sco OB2 (Preibisch & Zinnecker 2001) and CepOB3 (Assousa et al. 1977; Pozzo et al. 2003).

While these possibilities are intriguing, one must first address a number of factors before developing either idea into a fully realized and corroborated scenario. SGR 1806-20 is currently the only SGR clearly linked by distance measurements to a surrounding cluster of massive stars, Cl 1806-20 (Corbel & Eikenberry 2004; McClure-Griffiths & Gaensler 2005; Bibby et al. 2008). Kaplan et al. (2002) raised concern over whether SGR 1900+14 was a member or former member of its nearby cluster and the cluster membership of SGR 0526-66 has yet to be established (Klose et al. 2004). I could find no effort in the literature to find a cluster associated with SGR 1627-41.

To investigate the potential association of SGRs with massive clusters I utilize near-infrared narrow-band imaging to search for emission lines indicative of stellar winds in massive stars (Figer et al. 1997; Hanson et al. 1996). Specifically, I use a narrow-band filter centered on the Brγ 2.16μm line, or a He I filter centered on the 2.058 μm line. In extremely massive stars, these emission lines are very pronounced. For instance, the equivalent width of the Brγ line in one previously identified WR in Cl 1806-20, Star 22 in LaVine et al. (2003) (also known as Star 2 in Figer et al. 2005), exceeds 40Å; the He I line in Star B is $>$ 100Å.

These prominent emission lines may be useful in crowded fields, identifying massive stars even when they are scattered amongst many field stars. As opposed to other emission lines characteristically used to identify massive stars, most notably Hα in the optical, the Brγ and HeI lines are located in the near-IR and therefore detectable even in regions highly affected by interstellar extinction (such as Cl 1806-20). This study may also yield detections of OBI cluster stars with Brγ absorption. While less marked than reported Brγ emission lines in WRs, Brγ absorption may reach EW = 5Å in some OBI stars (Hanson et al. 1996).

We present the results of our narrow-band imaging search for massive stars around SGRs in Chapter 5 and 6. In Chapter 5 we detail the observations, analysis, and photometric techniques used in this study, particularly as they apply to Cl 1806-20.

In Chapter 6, we will present results on our narrow-band imaging of the other three SGR environments.

1.7 The Locations of Luminous Blue Variables (LBVs)

While researching Westerlund 1 and Cl 1806-20, two Super Star Clusters associated with magnetars, I noted that both clusters also hosted a Luminous Blue Variable (LBVs), a rare type of evolved massive star. While examining finder charts for both clusters, I serendipitously noticed that both LBVs are on the outskirts of their respective clusters. Upon further investigation, I found that the LBVs in the Quintuplet, another SSC, are also not centrally located. In fact, four of five LBVs in young massive clusters appear to be located on the periphery of their host clusters. The exception to this observation is Eta Carina in Trumpler 16.

LBVs are also thought to be at the extreme of the mass spectrum; in fact Eta Carinae and the Pistol Star and LBV 1806-20 vie for the title of most massive star in the Galaxy each estimated at $> 120\ M_{\odot}$ (Figer et al. 1998; Eikenberry et al. 2004a). Clearly, given the extreme masses of LBVs and the dictates of mass segregation one would suppose that LBVs would be centrally located (Spitzer 1987; Binney & Tremaine 1987). Theory suggests that LBVs should not be on the outskirts of their cluster, which is where I found them upon my initial visual inspection.

In Chapter 7, we evaluate the status of LBVs as "peripheral" cluster members. We calculate the probability of finding at least one star in every cluster at or outside the radius of the resident LBV and determine the robustness of our result using a Monte Carlo simulation. Finally, we compare our finding to theoretical models that predict the locations of massive stars in clusters and contrast these with scenarios that reproduce the observed positions.

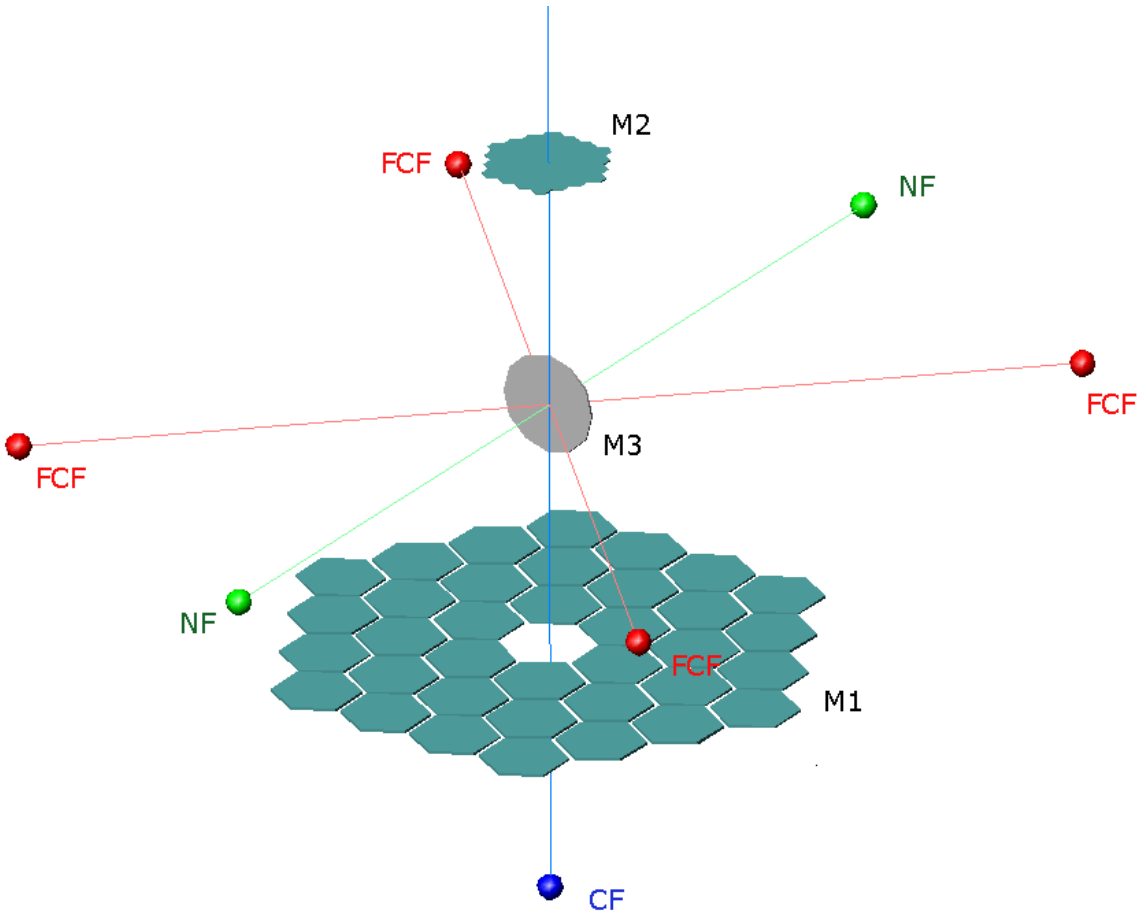

Figure 1-1. The mirrors and foci of the GTC. M1 is the 36 segment primary mirror, M2 is the lightweight beryllium secondary mirror, and M3 is a movable tertiary mirror. When the tertiary is not in the optical path, light will travel to the Cassegrain Focus (CF). When it is in the path, light can be directed to any one of the four Bent or Folded Cassegrain Foci (FCF) or one of the two Nasmyth Foci (NF)

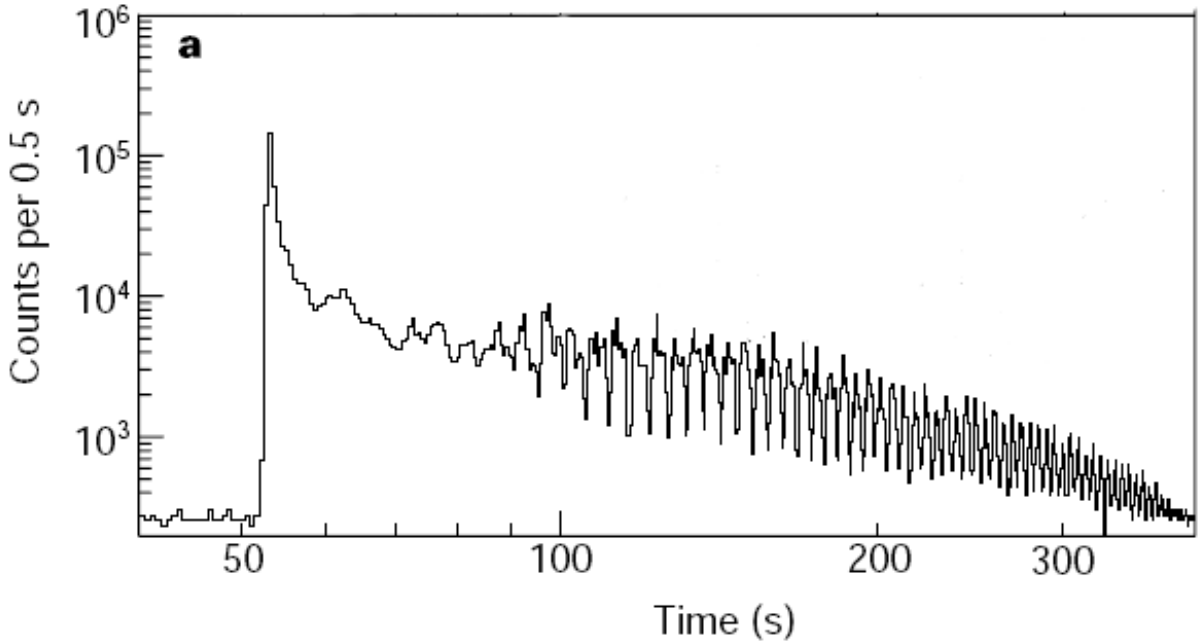

Figure 1-2. The 1998 August 27 observations of the giant gamma-ray burst from SGR 1900+14 as reported by Hurley et al. (1999, see Figure 1). Note the bright spike followed by a long tail. The period of the oscillations in the tail is $\sim$ 5s

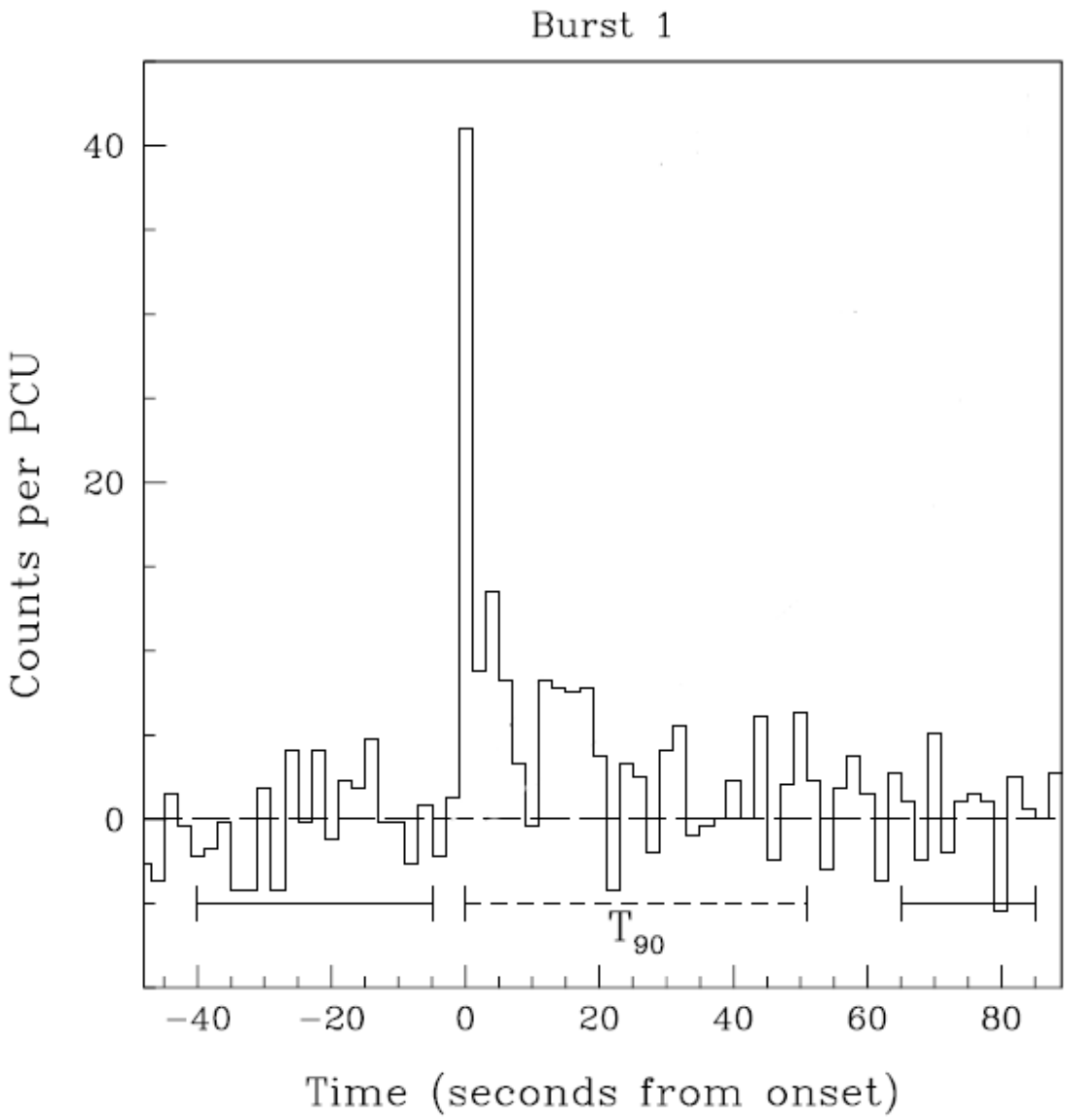

Figure 1-3. This figure, from Gavriil et al. (2002, see Figure 1) shows a typical soft-gamma ray burst from a magnetar. This burst was from 1E 1048-5937, an AXP; however, SGR bursts have almost identical morphologies.

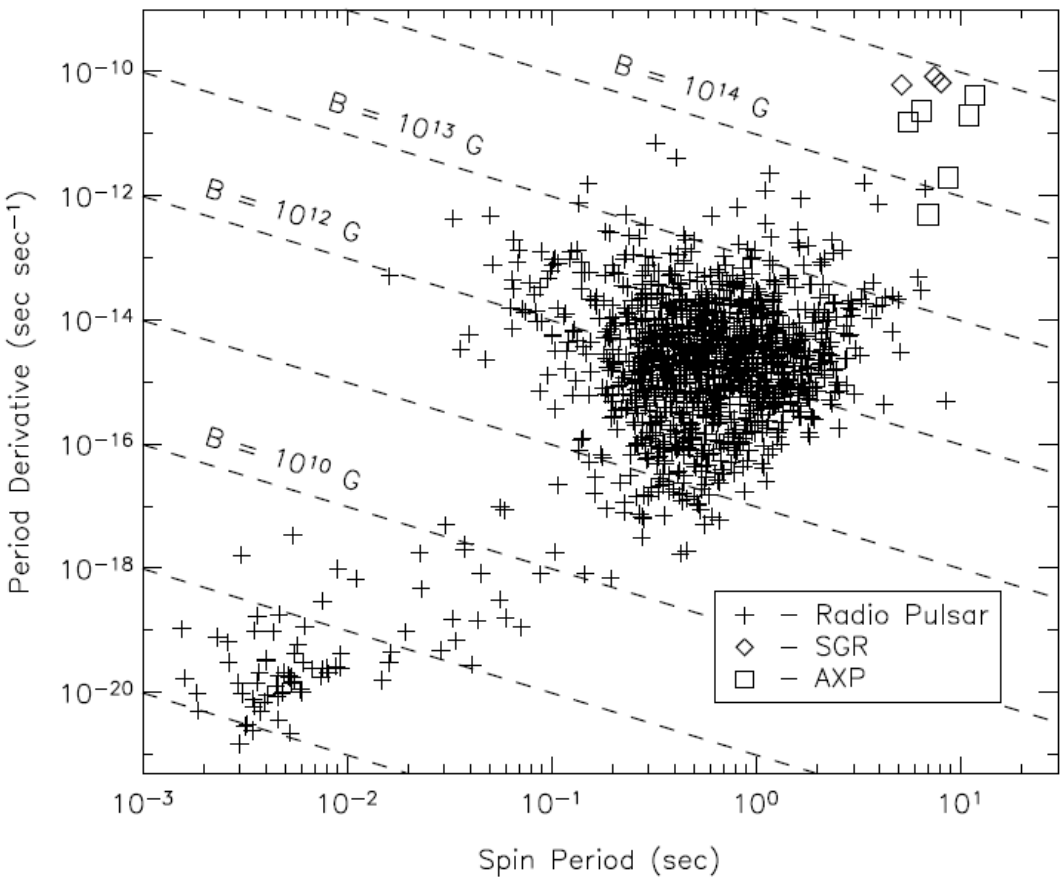

Figure 1-4. This figure from Woods & Thompson (2006) shows the class spin period vs. period derivative (P $\dot{P}$) diagram for neutron stars. Period derivative is defined as the change in the period over time. The diagram also has lines denoting magnetic field strength. Classical neutron stars are located in the central region of the diagram. Millisecond pulsars are located on the bottom left. Magnetars are located at the upper right. They spin down more quickly and have longer periods than classical neutron stars. They have magnetic fields $\sim$ 10^{14} - 10^{16} G.

CHAPTER 2
OPTICAL DESIGN AND ANALYSIS OF CIRCE

As with all astronomical instruments, the design of the Canarias InfraRed Camera Experiment (CIRCE) was heavily influenced by the science interests of its intended users – in this case the consortium of GTC astronomers. As the only near-infrared (NIR) instrument planned for the early phases of the GTC's operation, CIRCE was envisioned as a "workhorse" camera, capable of meeting the NIR needs of the entire community.

To satisfy this criterion, CIRCE was conceptualized with two basic modes, imaging and spectroscopy. A third mode, polarimetry, was added to ensure that CIRCE would remain scientifically viable after EMIR, the facility NIR imager and spectrograph, is commissioned on the GTC. CIRCE's optical design was strongly influenced by these early decisions as well as a number of specifications intended to optimize the instrument's performance. In this chapter, I review the various stages of CIRCE's optical designs. I discuss the initial specifications and their impact on the layout, changes implemented to meet GTC requirements, and our analysis of the system.

2.1 Preliminary Optical Designs

The earliest CIRCE optical layout, created before I joined the CIRCE team, was an all-refractive design. All-refractive systems use only lenses as powered optics – elements that change how the beam of light from the telescope converges or diverges. The initial CIRCE design, shown in Figure 2-1, consisted of 8 lenses made of a variety of materials including Barium Fluoride and Zinc Selenide.

Often, designers employ all-refractive systems (e.g. WIRC (Wilson et al. 2003) and Flamingos-1 (Elston et al. 2003)) because they are the simplest option, allowing light to travel from lens to lens along a single axis. However, in the case of CIRCE the all-refractive design, which called for expensive anti-reflective coatings and high-index glass, was costly, overly-complex, and less stable in cryogenic environments. Further, the

expected throughput, the amount of light propagated through the optical system, was only average since light from the telescope passed through 8 lenses before striking the detector.

When I joined the CIRCE team, the CIRCE PI was considering another option; an all-reflective system, which utilizes only mirrors as powered optics. Besides promising better throughput for less money (see §2.5), a reflective design also solved a major problem associated with cryogenic environments. As with most NIR instruments, CIRCE's components will be enclosed in a vacuum vessel, or dewar, cooled to 77 K. While some lenses and coatings are designed for these extreme conditions, damage to lenses is still possible. As temperatures drop inside the dewar, lenses, composed of a variety of materials, contract differently than their aluminum mounts. If a lens is accidentally compressed by a misaligned or poorly designed mount, it will crack or shatter.

Mirrors do not face this problem. Diamond-turned from 6061-T6 aluminum (see 3.1), the same material used to make all other opto-mechanical components (described in Chapter 3), the optics have the same coefficient of thermal expansion as the bench and optical mounts. Thus, the entire system undergoes homologous contraction. Besides preventing damage to expensive optical components, homologous contraction also means that a system aligned while warm will remain aligned when cooled; a significant advantage during integration. In light of these benefits, the CIRCE team decided to pursue mirrors instead of lenses for CIRCE's optical design.

This decision was bolstered by the successful implementation of all-reflective optics by the InfraRed Astrophysics Group (IAG) in the Department of Astronomy at the University of Florida (UF). The IAG successfully installed and aligned reflective optics in two mid-infrared instruments, T-ReCS and CanariCam (Telesco et al. 2003, 1998) and a NIR Integral Field Unit (IFU), FISICA (Eikenberry et al. 2004a). While diamond-turned aspheres have been historically difficult to align and test, advances in manufacturing resulted in a "bolt and go" technique that nullified alignment issues. Given the experience of the engineers and instrument scientists of the IAG, who acted in an advisory role

throughout the design and manufacture of CIRCE, we felt that using mirrors was not only feasible, but the best available option.

With this in mind, the CIRCE PI, Professor Stephen Eikenberry, contracted Optical Research Associates (ORA) in Pasadena, California to perform a feasibility study. The PI developed a number of design specifications that would accommodate the desired observing modes (imaging, spectroscopy, and polarimetry), minimize optical aberrations, and meet design and envelope constraints imposed by the GTC (§2.3).

Several of these specifications influenced the optical design at the most elementary level. First, we required that the system contain an accessible exit pupil, where we could place a "cold stop". A cold stop is a mask placed into the optical path that stops scattered light from propagating to the detector focal plane. We also specified a large collimated airspace to accommodate several filter and grism wheels. This avoided positioning filters near the detector focal plane, where dust and filter defects would be projected onto the detector. The easiest way to meet this requirement was with a collimator/imager system; a common configuration for IR instruments. I detail this system further in §2.4.

We limited the size of the beam at the exit pupil to 55mm in diameter to minimize filter and grism costs, which increase dramatically with physical size. We set the pixel scale at 0.1 $''$ per pixel to sample the optimal 0.2 arcsec seeing at the GTC site (Munoz-Tunon et al. 1997) and required a $3.3' \times 3.3'$ field-of-view (FOV). At the time of the design study, this FOV was considerably larger than that offered by similar NIR instruments available on 8-10 meter class telescopes. I discuss the CIRCE FOV further in §2.5

After reviewing several proposed optical layouts presented by ORA optical designer Michael Rodgers, the final result of the feasibility study was the choice of a two mirror collimator with a four-mirror camera. This design had the best performance of the

systems presented (discussed in detail in §2.5) and met the abovementioned design specifications.

Once we chose the basic layout, ORA completed an in-depth study of the system. To avoid spherical aberration, the initial design used a variety of higher-order aspheres (see Equation 2–1). Since these are difficult to manufacture, the CIRCE PI requested that ORA modify the imager to minimize the number of aspheres. ORA incorporated this consideration into the next integration. I present the completed preliminary design, a 2-dimensional layout of CIRCE in Figure 2-2.

2.2 Introduction to Optical Design Software and Terminology

Before the advent of modern computing, tracing a single ray through an optical system could take many days of careful calculation. Now, optical designers can choose from a variety of software to complete hundreds of ray traces, analysis, and optimization in a few hours (Smith 2005). Throughout this dissertation, I will discuss work completed with two such programs, CODE V and ZEMAX.

As the manufacturers of CODE V (Harris 1991), ORA chose this program to model their preliminary designs of CIRCE. Since ZEMAX was available at UF, I translated the CIRCE optical prescription from CODE V to ZEMAX. This required learning optical design principles and the intricacies of both programs. While I will not detail the latter, I will discuss the former, reviewing coordinate systems and terminology referenced throughout Chapters 2 and §3.

In standard practice, the coordinate system used in optical design is the right-handed Cartesian system shown in Figure 2-3 (Schroeder 2000). The Y-axis is vertical and increases from bottom to top. The X-axis runs into and out of the page and increases into the paper. The horizontal Z-axis increases from left to right. In layouts where all optics are coaxial (aligned on a single axis) the Z-axis aligns with the optical axis, the imaginary line along which light moves or propagates through the system. This is not the case with CIRCE, where many optics are off-axis.

Examining Figure 2-2 in terms of this coordinate system, note that we are looking at the optics as though they were suspended directly above us. Further we are only observing a two-dimensional (2-D) cross section taken at X = 0; practically speaking we see each optic's length and width, but not its height. This point-of-view will become particularly important in Chapter 3.

Next I move on to a few basic optical design concepts. Both CODE V and ZEMAX have spreadsheet-like interfaces that allow the user to enter information about each optical element. Figure 2-4 is an example of the CIRCE optical prescription displayed in the ZEMAX interface. Of particular import are the following user input variables: surface type, glass, thickness, decenter, tilt, and aperture decenter.

Surface type is a mathematical description of an optic's face. As discussed in §2.1, most of CIRCE's optics are aspheres, used specifically to eliminate spherical aberration. Aspheres are described by the following equation:

$$Z(R) = \frac{UR^2}{\sqrt{1-(1+K)C^2R^2}} + A_4Y^4 + A_6Y^6 + ...A_nY^n \tag{2–1}$$

where U is the radius of curvature, K is the conic constant, R is the height from the optical axis, Z(R) is the sag, or shape of the surface at height R, and A_n are the aspheric coefficients. Five of CIRCE's six powered optics are conic aspheres with only a conic constant, K, and no higher order terms. The fourth mirror in the imager is a sixth order even asphere, with two aspheric coefficients, A_4 and A_6.

A coordinate break is another important surface type. It is a false or dummy surface that allows for the off-axis placement of optical components. A coordinate break defines a new coordinate system in terms of the coordinate system currently in use. Decenters shift the new system in X and Y, while tilts rotate the new system in X, Y, and Z. Tilts around X are defined as α, Y as β, and Z as γ.

Thickness is the distance along the local Z-axis from one surface to the next. Practically, this may have different physical meanings depending on the type of optic.

In the case of filters, lenses, and entrance windows, the thickness between the front and back face of the optic is the width of the element. In the case of mirrors, with only one face, the thickness is the distance between one mirror and the next. The "glass" designation therefore denotes the physical meaning of the thickness associated with a surface. Reflective optics are listed as mirrors while the composition of refractive optics is explicitly stated. The optical properties of thousands of materials are stored within the optical design software.

All of CIRCE's powered mirrors are segments of larger aspheric optics called "parent" mirrors. For each optic in a complex system, an optical designer chooses the radius of curvature (RC) necessary to correct aberrations and direct light toward the next mirror in the optical path. The RC sets the size of the optic; a larger radius of curvature results in a large optic. Using a mirror approximately the size of the beam, as shown in Figure 2-5a, may yield a radius of curvature too small to correctly reflect the light to the next optic. Figure 2-5b demonstrates that although a large RC, and therefore larger mirror, is necessary, only a portion of this "parent" mirror is needed to reflect the beam of light directed at it by previous optics. The remainder of the mirror not only adds cost to the project, but might block light intended for another optic. Thus, we use the smallest segment of the parent mirror that still accommodates the entire beam of light. Finding this optimum size is discussed in Chapter 3.

The two collimating mirrors in CIRCE are off-axis sections of coaxial parent mirrors. The four imaging mirrors are smaller segments of non-coaxial parent mirrors. Figure 2-6 shows the parent mirrors used in the design of CIRCE. When using sections of parent mirrors, we define the aperture decenter as the distance between the vertex of the parent mirror and the mechanical center of the mirror segment. Aperture decenters should not be confused with coordinate break decenters.

As a complex off-axis optical system, the CIRCE layout has many coordinate breaks, aperture decenters, glasses, and thicknesses. A complete prescription for the preliminary

CIRCE optical system, which defines all optical elements and coordinate breaks, is listed in Table A-1 and A-2.

2.3 Envelope Re-design and GTC Integration

As CIRCE moved forward from the preliminary design phase, I became more involved with the project and assisted with several stages of the optical design, beginning with an analysis of the optical layout. One important consideration was the GTC envelope size. CIRCE was designed for the Bent Cassegrain port of the telescope, which has specific weight and size constraints. While CIRCE fit into the 1.0-m $\times$ 1.5-m cylindrical volume planned for the Bent Cassegrain port, further investigation of the attachment points, shown in Figure 2-7, uncovered a problem. The telescope's optical axis is centered on the 1.0-meter cylinder, allowing for only a 0.5-m clearance to the farthest optic on the Y-axis. If we aligned CIRCE's entrance window (located at the upper left of the layout in Figure 2-2) to the telescope's beam, CIRCE's farthest optic would be 1-m from the optical axis. Thus the size of the cylinder necessary to contain the optics would be 2.0-m $\times$ 1.5-m, double the diameter specified by the GTC (Figure 2-7).

I contacted ORA with this information, while simultaneously beginning to alter the CIRCE design. My initial idea was to add fold mirrors in critical places along the optical path. Fold mirrors are unpowered optics and therefore only change the direction of the light as it travels through the system. They are especially useful in situations that require fitting an existing optical design into a smaller space without radically altering the position of the powered mirrors.

In this case, I needed to compress the CIRCE design in the vertical (Y) direction. In Figure 2-8, I show my first re-design, consisting of 10 mirrors: two collimators, four imagers, and four fold mirrors. The first set of fold mirrors translated a large thickness between the entrance window and the collimating optics into an offset in the positive Y direction. I added a second set of fold mirrors aft of the collimator that reflected the light

off of the X = 0 plane into the negative X direction. In this plan, two optical benches supported the optics instead of one.

While this design met the envelope specifications detailed by the GTC it faced several other problems. Foremost, it lacked space for a large filter box. With a variety of filters and grisms planned for the instrument, we anticipated a multi-wheel filter box aft of the collimator. Concerns that the additional fold mirrors would greatly limit our access to the collimated airspace necessary for the filter box dominated discussion of this new layout.

Despite these concerns, I sent our 10-mirror CIRCE concept to ORA. After several iterations, ORA delivered a final design which I present in Figure 2-9 . While including the fold mirrors fore of the collimator, as in our design, this new layout utilized a slightly altered four-mirror imager to meet the envelope specifications. Specifically, the modified α tilt on the first imager directed the light upwards toward positive Y values. This greatly compressed the design while leaving the collimated airspace necessary for the filter box virtually unchanged. Deleting two fold mirrors from our design also decreased the cost and removed the second optical bench.

Once the final design was complete I worked with ORA to integrate the CIRCE optical design with that of the GTC. Members of the CanariCam and Elmer teams provided me with the ZEMAX spreadsheet for the GTC. Since the primary and secondary mirror of the GTC are polygons, both teams used complex user-defined surfaces contained in file types specific to ZEMAX to model the GTC optics. To share these designs with ORA (who used CODE V) I simplified the schematics of the GTC optics while maintaining the basic optical properties. This new GTC design was sent to ORA and all future work and analysis used this layout.

I then mated the CIRCE optical design to the GTC optical design using the telescope's focal plane. I modeled the telescope focal plane in the CIRCE design as a "dummy" surface, placed directly after the entrance window. While this dummy surface had no optical properties, it marked the position of future mechanical mechanisms. After

taking account slight shifts in the location of the focal plane due to the entrance window, I matched the final focal plane of the GTC to the focal plane in the CIRCE design.

2.4 Final Optical Design

I now review the final optical design presented in Figure 2-9. An F/17 beam from the telescopes enters the CIRCE entrance window [1] before passing to the GTC focal plane [2]. As discussed in §2.3 this focal plane marks the location of the first of CIRCE's cryo-mechanisms, a device to move slits and field masks in and out of the beam.

After passing through the focal plane mechanism, light will strike two unpowered fold mirrors before passing to two collimating conic mirrors; the first concave and the second convex. As with the preliminary design, both are off-axis segments of coaxial parent mirrors. These optics produce an exit pupil, the image of the aperture stop, which in this case is the GTC secondary mirror (Schroeder 2000). The $\sim$ F/5 beam is $\sim$ 55mm in diameter at the exit pupil. As previously mentioned, to stop stray light from propagating into the camera, we will place a mechanical cold stop at this position with this dimension. Aft of the collimator is $\sim$ 300mm of collimated airspace designed to accommodate the second cryo-mechanism, a large filter wheel box housing a cold stop [3], filters, grisms, and optics for polarimetry [4].

Next is the four-mirror imager. The first imaging mirror is a concave conic mirror, the second and third imaging mirrors are convex conic mirrors, and the fourth a concave 6th-order asphere. Neither the parent or segments of the imaging mirrors are co-axial. While this will make manufacturing more difficult, the extra tilt and decenter parameters increased ORA's ability to minimize aberrations when optimizing the design.

The camera focuses light onto the detector focal plane [5], where we will position a mercury cadmium telluride (HdCdTe) HAWAII 2048 $\times$ 2048 infrared detector.

2.5 Optical Analysis of Imaging Mode

With the final design complete, I began an in-depth optical analysis of the system. I used several key utilities in ZEMAX to predict how well CIRCE would perform. First, I

checked the CIRCE field-of-view (FOV). Using ZEMAX, I virtually launched rays into the telescope pupil that corresponded to a $3.4' \times 3.4'$ square on sky, the expected FOV of the system. I then set the aperture size at the final focal plane equal to 36.86mm $\times$ 36.86mm, the size of the the HAWAII 2K detector. Using the FOOTPRINT utility in ZEMAX, which shows where each propagated ray will hit any surface in the design, I examined the focal plane. In Figure 2-10, I show the results. The marks on the diagram represent rays launched from 8 locations on the pupil plane that mark the boundaries of a $3.4' \times 3.4'$ square on the "sky". This defines the CIRCE FOV.

I then analyzed the system's encircled energy. Encircled energy (EE) is the percentage of total energy enclosed as a function of distance from the center of the PSF. With this analysis we can predict how much light CIRCE will collect within a given number of pixels at the detector focal plane. Since the HAWAII 2K detector has 18μm pixels, I was interested in the encircled energy at a radius of 18μm, or two pixels in diameter, which guarantees Nyquist sampling (Schroeder 2000).

I present the results of my encircled energy analysis for the J- and K- band in Figures 2-11 and Figure 2-12, respectively. Figure 2-11 shows that at the center of the field (0, 0) the encircled energy is $> 90\%$ in two pixels. At $\sim 1.5'$ from the center (0.250, 0.250) the EE within 2 pixels is 80% and in the corner (-0.028, -0.028) decreases to 75%. This slight drop-off in EE at the corners was expected; we requested ORA to optimize the image quality over a $205''$ field diameter, sacrificing a uniform field for excellent throughput (80% EE in two pixels) over $>$ two-thirds of the detector. We note that the EE over the entire field is significantly better than the original lens design for CIRCE, which had only 60% EE over two pixels.

Figure 2-12 shows the EE diagram for the K-band. Note that the percentage of energy enclosed at each position is slightly worse than in the J-band. This was expected since diffraction, and therefore spotsize increases with wavelength, however, we still have

$> 70\%$ EE at two pixels, even in the corner, the worst part of the field. In the center (0,0) we reach $> 90\%$ EE within two pixels.

I then performed a spot size analysis shown in Figure 2-13. This shows where rays from a given field position will fall on the detector focal plane. The theoretical Airy Disk is also plotted for comparison. The spot size is a measure of how close to ideal the optical system is to the diffraction limit; generally the tighter, more uniform and circular the spot, the better the design. Spot diagrams also provide insight into the major sources of aberration in an optical system. For example, coma appears as a "comet", spherical aberration as a circle with a tight core and underdense outer region, and astigmatism as an exaggerated oval. In systems with chromatic aberration, which is the most obvious aberration, different wavelengths appear as spots with varying sizes and shapes.

Often, more complex systems like CIRCE have a combination of these effects, along with other higher-order aberrations, which make it difficult to determine what is causing the shape of the spot. However, when examining Figure 2-13 I note no obvious signs of chromatic or spherical aberration. While there may be some coma, the spot size is very small, mostly within the Airy radius.

The analysis of the CIRCE spot diagram confirms the validity of our design specifications. Since CIRCE uses mirrors instead of lenses and aspheres instead of spheres we eliminated spherical and chromatic aberration by design. Further, specifying excellent image quality (measured in terms of encircled energy) across the bulk of the field ensured a tight spot size; rays must land close together to ensure 80% energy within two or three pixels.

Finally, we examined the distortion in the system. If one imagines a grid of lines, distortion is a measure of how the lines diverge or warp as distances increases from the optical axis. In a system with no distortion, the lines remain straight. If distortion is extreme the lines curve and the field takes on a barrel or pincushion shape. Our specifications called for less than a 10 pixel distortion in a $205'$ radius from the center

of the image. Our analysis in ZEMAX showed that CIRCE exceeded this specification, experiencing 4 pixels of distortion in the 205′ radius.

2.6 Spectroscopy and Polarimetry

To this point, we have reviewed the general optical properties of the optical design and analyzed CIRCE's performance as an imager. CIRCE has two additional modes, spectroscopy and polarimetry.

CIRCE spectroscopy includes two grisms, both of which are derived from designs for the Flamingos-2 instrument for Gemini. To save time and money, the CIRCE grisms share the grating ruling masters custom-built for Flamingos-2. The first grism will cover the 1.25 - 2.4 μm bandpass at a resolution of R = 410 at 1.25 μm and R = 725 at 2.20 μm with a three pixel slit. The second grism will cover a single band at a resolution of R $\sim$ 1500 in its 3rd order (K-band), 4th order (H-band), or 5th order (J-band). The CIRCE optics will maintain seeing-limited image quality with the grism in the optical path over the entire bandpass.

CIRCE will also have a Wollaston prism polarimetric mode. In this mode, a Wollaston prism will be placed in the beam after a rotating half-wave plate (HWP) located at the focal plane. This prism will deviate the ordinary and extraordinary polarization beams at the pupil, resulting in a shift of the "o" and "e" images on the detector. Coupled with a half- size field mask also at the telescope focus, this will provide spatially-separated images, allowing polarimetric measurements. A rotating HWP, positioned at angles of 0-degrees and 45-degrees allows the measurement of the "Q" polarization component. Rotating the plate to 22.5-degrees and 67.5-degrees allows the measurement of the "U" component, and thus the complete determination of linear polarization in the source. Finally, by placing a grism in the beam after the Wollaston prism, CIRCE will also be capable of spectropolarimetry. Another member of the CIRCE team, Miguel Charcos, is leading the polarimetric design.

2.7 Tolerancing Analysis

Up to this point, the analyses that I have reviewed in §2.5 assume perfect optical elements. While the precision and accuracy used to manufacture diamond-turned optics is very high, small defects invariably occur during machining and alignment. These errors may adversely affect the final image quality and render our carefully completed analyses inaccurate. Fortunately, we can specify a maximum acceptable error, or tolerance, on every dimension used to produce the mirror. These include the X, Y, and Z location of the mechanical center and the radius of curvature. If an optic returns from the manufacturer with errors larger than those declared on the drawing, we can reject it. The manufacture is then obliged to re-make the piece.

Deciding what range of errors are acceptable is a delicate process. It is critical to find the right balance between quality and cost. If a manufacturer agrees to produce a piece with very small or "tight" tolerances, they assume a large risk. Besides guaranteeing a near-perfect optic, they are also responsible for testing the optic to prove they have met the tolerance. Obviously, the tighter the constraints, the more difficult the manufacture process, the greater the expense. However, if tolerances are too "loose" and the optics poorly manufactured, the instrument could be unusable, negating any benefit gains from reducing costs. Also, a limit in machining accuracy does exist; we are ultimately constrained by the tools and technologies available.

To add realism to our system and determine the tolerances for our CIRCE optics for the opto-mechanical design, I completed a tolerancing analysis. Using macros written by ORA, based on an analytical technique detailed in Koch (1978), I ran an iterative process to identify specific parameters that impacted image quality. By deciding which variables in our optical design had large effects on two measures of system quality, distortion and encircled energy, I determined which parameters required tight tolerances. This would ultimately help determine CIRCE's cost and manufacturing difficulty.

The basic parameters that I adjusted were tilt, decenter, curvature, aspheric irregularities, and window and fold mirror materials: 45 variables in all. Within the macro, I could specify tolerances for each parameter and a list of field positions, similar to those used for the initial EE calculation. CODE V then performed the analytical calculation and output two tables. The first measured the diameter of a circle necessary to enclose 80% of the energy. This was similar to ZEMAX's encircled energy analysis described above; however, in this case, the percentage is held constant and the diameter in microns is reported. The smaller the diameter, the smaller the spot size. The second analysis measured the distortion (in pixels) at each field position.

Each table had five values of the 80% EE or distortion for each field position. The first was the nominal value, assuming no errors in the system. The next four values were the expectation values for four confidence levels, 50%, 84.1%, 97.7%, and 99.9%.

For example, for the initial run, I stipulated a tolerance on the α and β tilt of every mirror in the system equal to 0.001 degree a typical tolerance for optical alignment. The results are shown in Table 2-1. Originally, we found that at the center of the field (0,0) the nominal value of the 80% EE was 25μm in diameter, about 1.5 pixels. However, assuming that the tilt could be as much as 1 μm larger or smaller than the nominal value, the 50% value was 35μm; 50% of the time we could guarantee an 80% EE in 2 pixels or less. The remaining 50% of the time the value would be larger, most likely in situations where multiple tilts were off by the maximum amount. On the other hand, 84.1% of the time, we guaranteed the 80% EE would be 36.30μm or less, 97.7% of the time, 41.9μm or less, and 99.9% of the time 47.50μm or less. Recalling that the center of the field often has considerably better image quality, these values are rather large in comparison to the nominal value. We determined that this tolerance was not "tight" enough; if we aligned the optics to this level of error, our image quality would most likely be poorer than originally specified.

After completing multiple runs of the program like the one detailed above, I identified the parameters that most affected the performance of the system. I also set benchmarks for acceptable image quality threshold. At all field positions, I sought an 80% EE of 32μm and a distortion of < 4.4 pixels at the 84.1% confidence level. After ~ 10 runs, I found a reasonable combination of tolerances that gave me both acceptable values for the 80% EE and distortion. Further, after consulting with the IAG, I determined these tolerances were within the ability of the UF machine shop and most major manufacturers. The table with the output from CODE V using the final tolerances is shown in Table 2-2. I present the tolerances themselves in Table 2-3.

Once the tolerancing was complete, I was ready to begin the opto-mechanical design. This process and the outcome is described in the next chapter.

Table 2-1. Values of 80% Enclosed Energy for initial tolerancing run with $\alpha = \beta = \gamma =$ 0.0001 degrees for all optics

X [a]	Y [a]	Nominal Value [b]	50% [b]	84.1% [b]	97.7% [b]	99.9% [b]
0.0000	-0.0285	26.4	29.2	35.2	41.3	47.4
0.0000	0.0000	25.0	30.7	36.3	41.9	47.5
0.0000	0.0285	22.2	35.0	41.2	47.5	53.8
0.0000	-0.0140	21.7	29.1	33.5	37.8	42.2
0.0000	0.0140	24.9	32.1	37.7	43.3	48.9
0.0140	0.0000	22.8	30.7	35.4	40.2	44.9
0.0285	0.0000	29.1	34.5	40.2	46.0	51.8
-0.0140	0.0000	22.8	30.7	35.5	40.2	45.0
-0.0285	0.0000	29.1	34.5	40.3	46.1	51.9

[a] units are degrees

[b] units are μm

Table 2-2. Values of 80% Enclosed Energy for final tolerancing run

X [a]	Y [a]	Nominal Value [b]	50% [b]	84.1% [b]	97.7% [b]	99.9% [b]
0.0000	-0.0285	26.4	26.6	29.6	32,7	35.8
0.0000	0.0000	25.0	25.7	28.4	31.1	33.8
0.0000	0.0285	22.2	25.2	26.7	28.2	29.7
0.0000	-0.0140	21.7	23.8	25.8	27.8	29.8
0.0000	0.0140	24.9	25.8	28.2	30.7	33.1
0.0140	0.0000	22.8	24.3	26.1	27.8	29.5
0.0285	0.0000	29.1	29.6	31.9	34.3	36.6
-0.0140	0.0000	22.8	24.4	26.1	27.9	29.6
-0.0285	0.0000	29.1	29.6	32.0	34.4	36.7

[a] units are degrees

[b] units are μm

Table 2-3. Final tolerances for decenters and tilts. These were the most sensitive (and therefore most important) values in my tolerancing analysis. Tolerances for the X, Y, Z decenters and α, β, γ tilts are not total errors for all three axes, but for each axis individually.

Mirror	Curvature % error	Decenter (X,Y,Z) mm	Tilt (α,β,γ) (°)
C1	0.15	0.037	0.0003
C2	0.20	0.037	0.0003
Im1	0.09	0.037	0.0003
Im2	0.50	0.037	0.0003
Im3	0.15	0.037	0.0003
Im4	0.10	0.037	0.0001

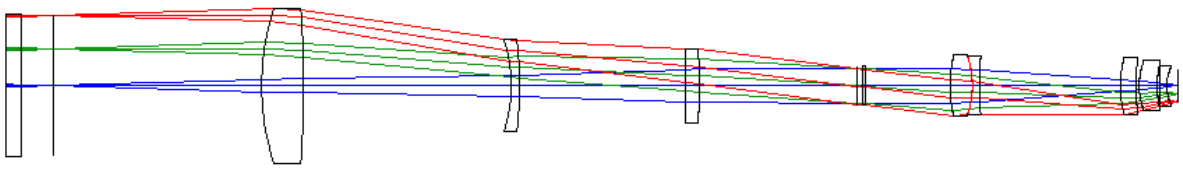

Figure 2-1. The initial 8-lens optical design of CIRCE.

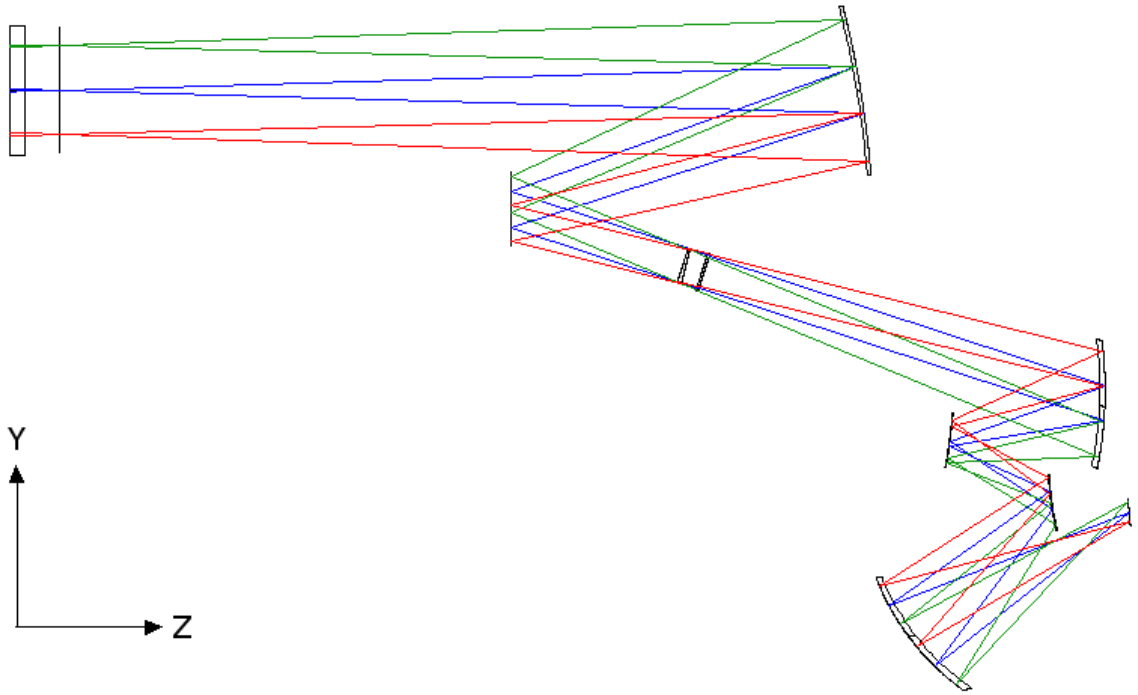

Figure 2-2. ORA's preliminary 6-mirror optical design of CIRCE.

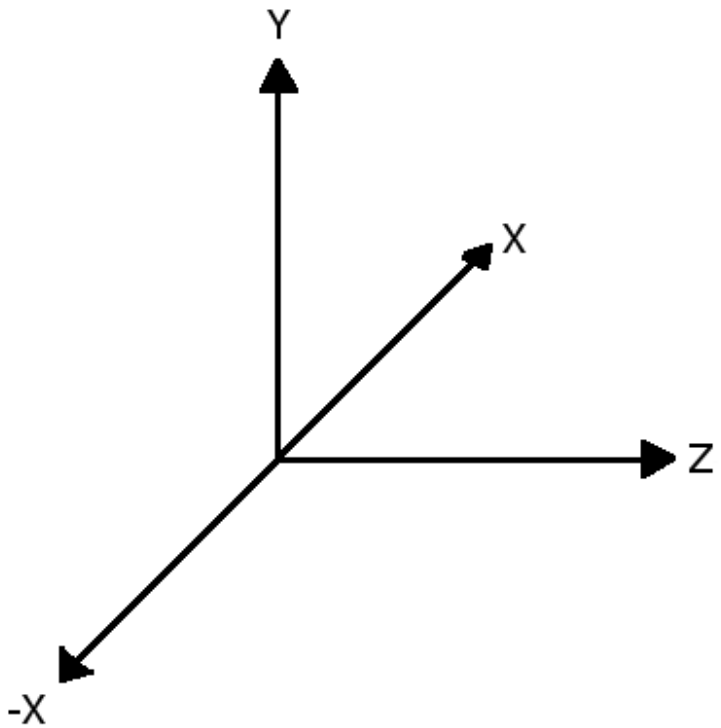

Figure 2-3. The standard right-handed Cartesian coordinate system used by ZEMAX and CODE V. Note the X-axis is positive into the page and negative out of the page.

Lens Data Editor: Config 1/3

Edit Solves Options Help

	Surf:Type	Comment	Radius	Thickness		Glass	Semi-Diameter		Conic	Par 0(unused)	Decenter X	Decenter Y
OBJ	Standard		Infinity	Infinity			Infinity		0.000000			
1	Standard		Infinity	14740.000000			5096.958586		0.000000			
2*	Standard	M1	-33000.000000	-14739.410000		MIRROR	5764.853240	U	-1.002250			
3	Standard		Infinity	0.000000			547.811635		0.000000			
STO*	Standard	M2	-3899.678000	10739.410000		MIRROR	535.000000	U	-1.504835			
5	Standard		Infinity	0.000000	P		273.087525		0.000000			
6*	Standard	TERTIARY POSS	Infinity	7334.581782			310.586874	U	0.000000			
7*	Standard		Infinity	22.000000		CAF2	95.000000	U	0.000000			
8*	Standard		Infinity	50.000000			95.000000	U	0.000000			
9	Standard	FOCAL PLANE	Infinity	1200.000000			92.391436		0.000000			
10	Coord Break			0.000000		-	0.000000				0.000000	-279.251800
11	Coord Break			0.000000		-	0.000000				0.000000	0.000000
12*	Standard	C1	-1465.459128	-534.229900		MIRROR	383.351497		-0.345400			
13*	Standard	C2	-2765.027927	252.323500		MIRROR	137.292882		-48.703000			
14	Coord Break			0.000000		-	0.000000				0.000000	13.962600
15	Coord Break			0.000000		-	0.000000				0.000000	0.000000
16	Coord Break			5.000000		-	0.000000				0.000000	-0.500000
17	Coord Break			0.000000		-	0.000000				0.000000	0.000000
18	Standard		Infinity	0.000000			26.285099		0.000000			
19	Coord Break			0.000000		-	0.000000				0.000000	0.000000
20	Coord Break			-5.000000		-	0.000000				0.000000	0.500000
21	Standard		Infinity	30.000000			26.356138		0.000000			
22	Standard	FILTER	Infinity	3.000000		SILICA	28.376660		0.000000			
23	Standard		Infinity	640.000000			28.601396		0.000000			
24	Coord Break			0.000000		-	0.000000				0.000000	-200.581300
25	Coord Break	IM1		0.000000		-	0.000000				0.000000	0.000000
26*	Standard		-492.220456	-216.452000		MIRROR	267.088017		-0.657718			
27	Coord Break			0.000000		-	0.000000				0.000000	21.085000
28	Coord Break			0.000000		-	0.000000				0.000000	0.000000
29*	Standard	IM2	-576.661361	165.097800		MIRROR	69.461173		-140.378072			
30	Coord Break			0.000000		-	0.000000				0.000000	-41.298400
31	Coord Break			0.000000		-	0.000000				0.000000	0.000000
32*	Standard	IM3	387.499273	-279.062300		MIRROR	49.541816		9.594355			
33	Coord Break			0.000000		-	0.000000				0.000000	-4.996100
34	Coord Break			0.000000		-	0.000000				0.000000	0.000000
35*	Even Asphere	IM4	372.298047	387.679300		MIRROR	223.229053		0.072891		0.000000	-1.02427E-010
36	Coord Break			0.000000		-	0.000000				0.000000	-44.138900
37	Coord Break			0.455028		-	0.000000				0.000000	0.000000
IMA	Standard		Infinity				20.129614		0.000000			

Figure 2-4. An example of the ZEMAX user interface spreadsheet.

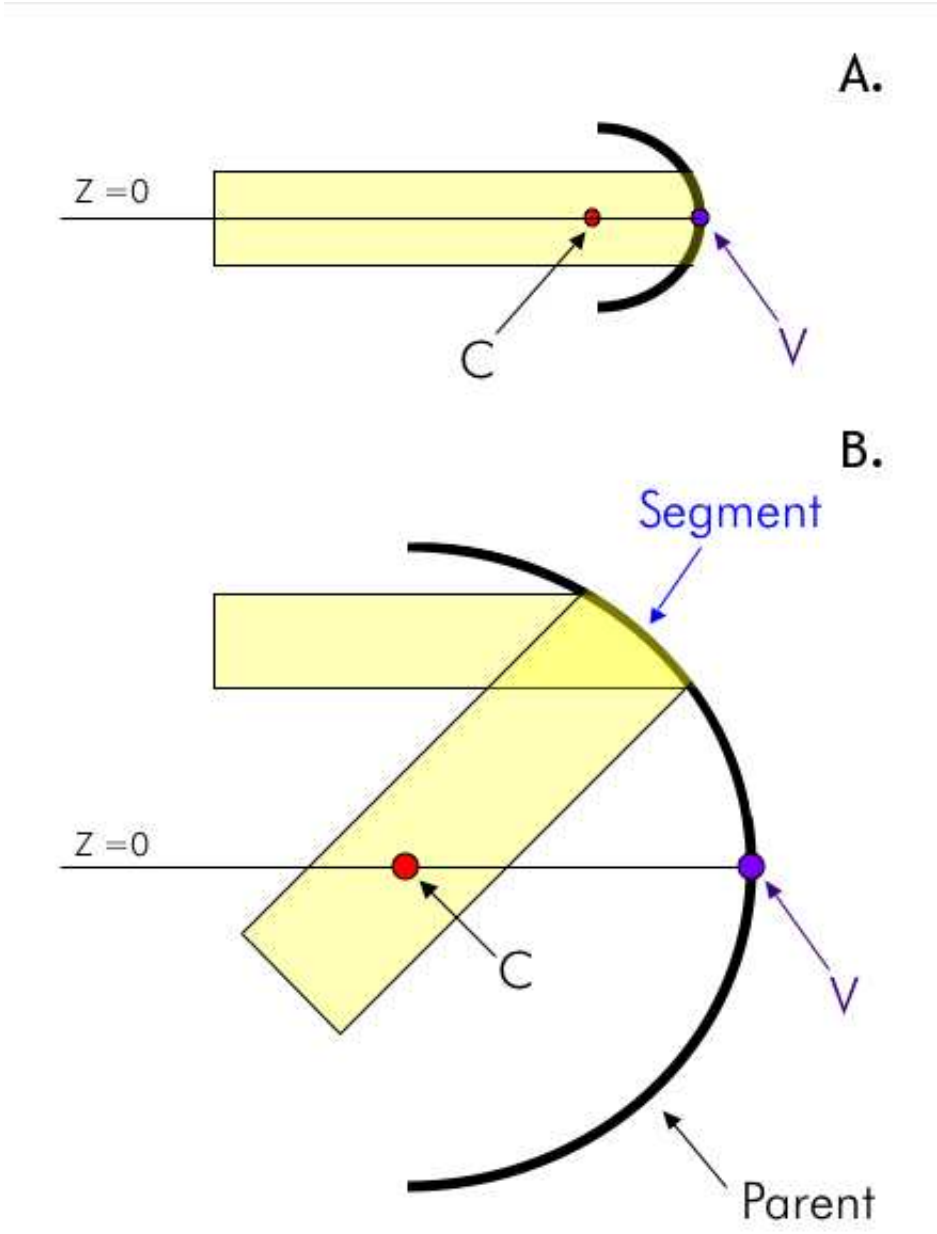

Figure 2-5. The relation between radius of curvature (RC) and mirror size. For a spherical mirror, the radius of curvature is the distance between the center of the "sphere" from which the mirror was cut (C) and the vertex (V). Thus the larger the radius, the larger the optic. A) An optic approximately the size of the the beam would have the wrong radius of curvature to direct the light to the next optic. B) A small segment of a larger parent mirrors allows the designer to choose the radius of curvature necessary to correctly direct the light.

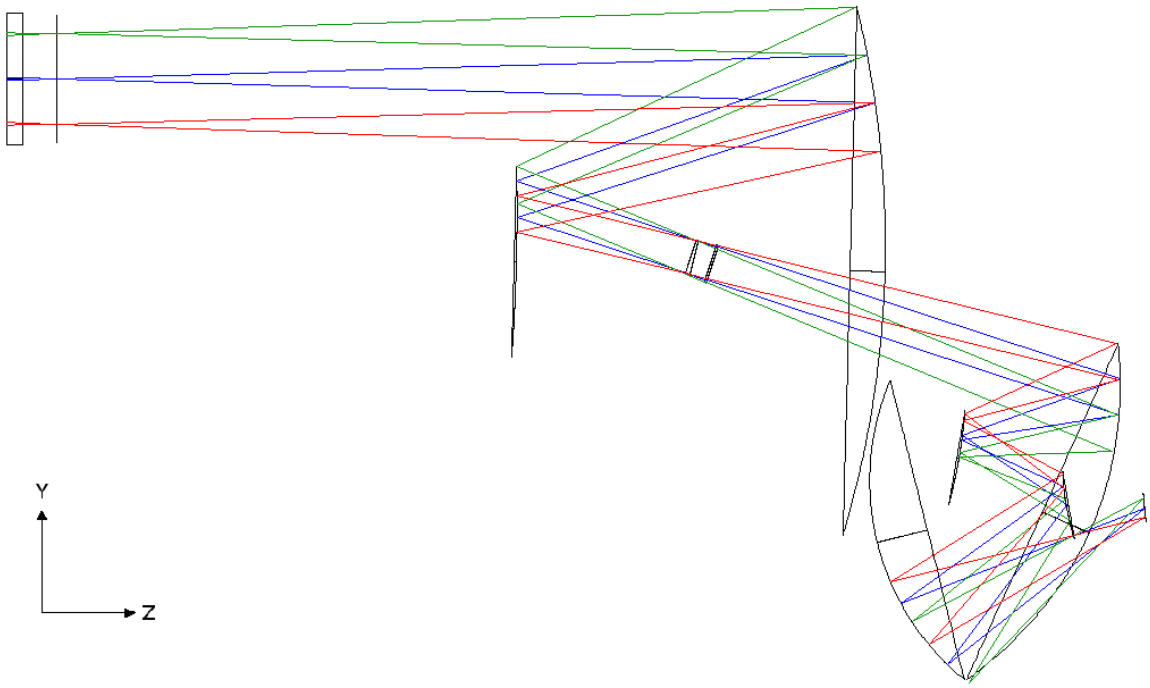

Figure 2-6. Parent mirrors used in the preliminary CIRCE design pictured in Figure 2-1. Note that the parent mirrors are much larger than the beam size and often collide with one another. Using smaller segments of these mirrors greatly reduces cost, makes manufacture more practical, and allows light to propagate through the system.

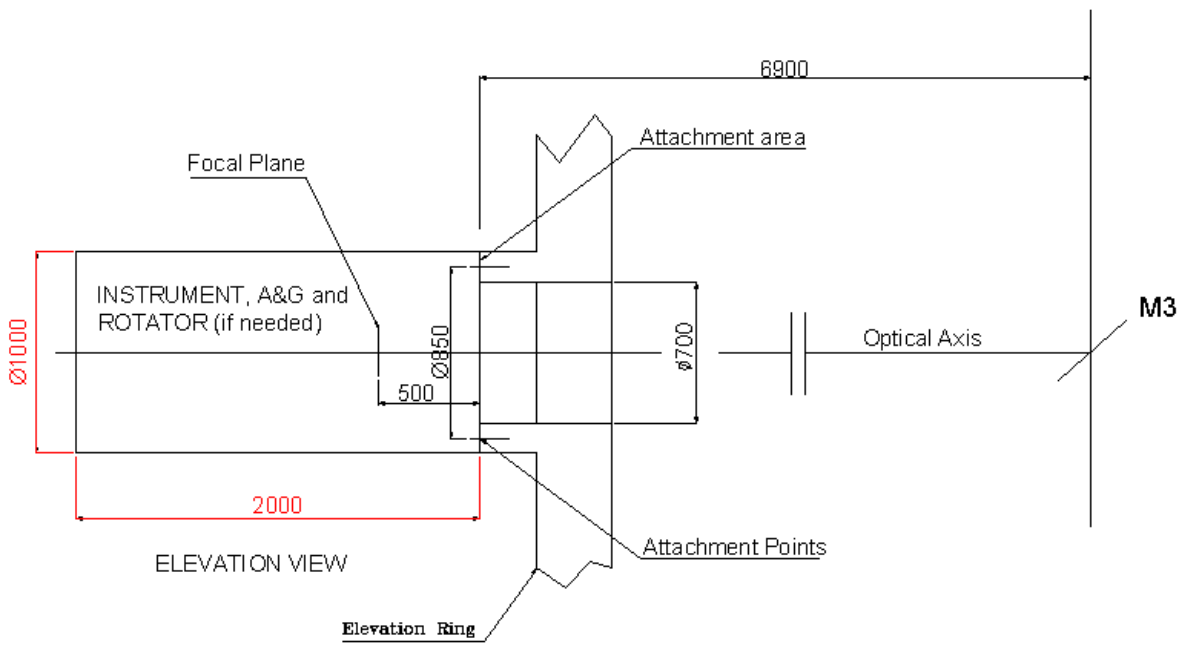

Figure 2-7. The original Folded Cassegrain focal station envelope. Note the 1000 mm diameter of the cylinder. The 2000 mm length includes acquisition and guide and rotator hardware; the length specified for CIRCE was only 1500mm.

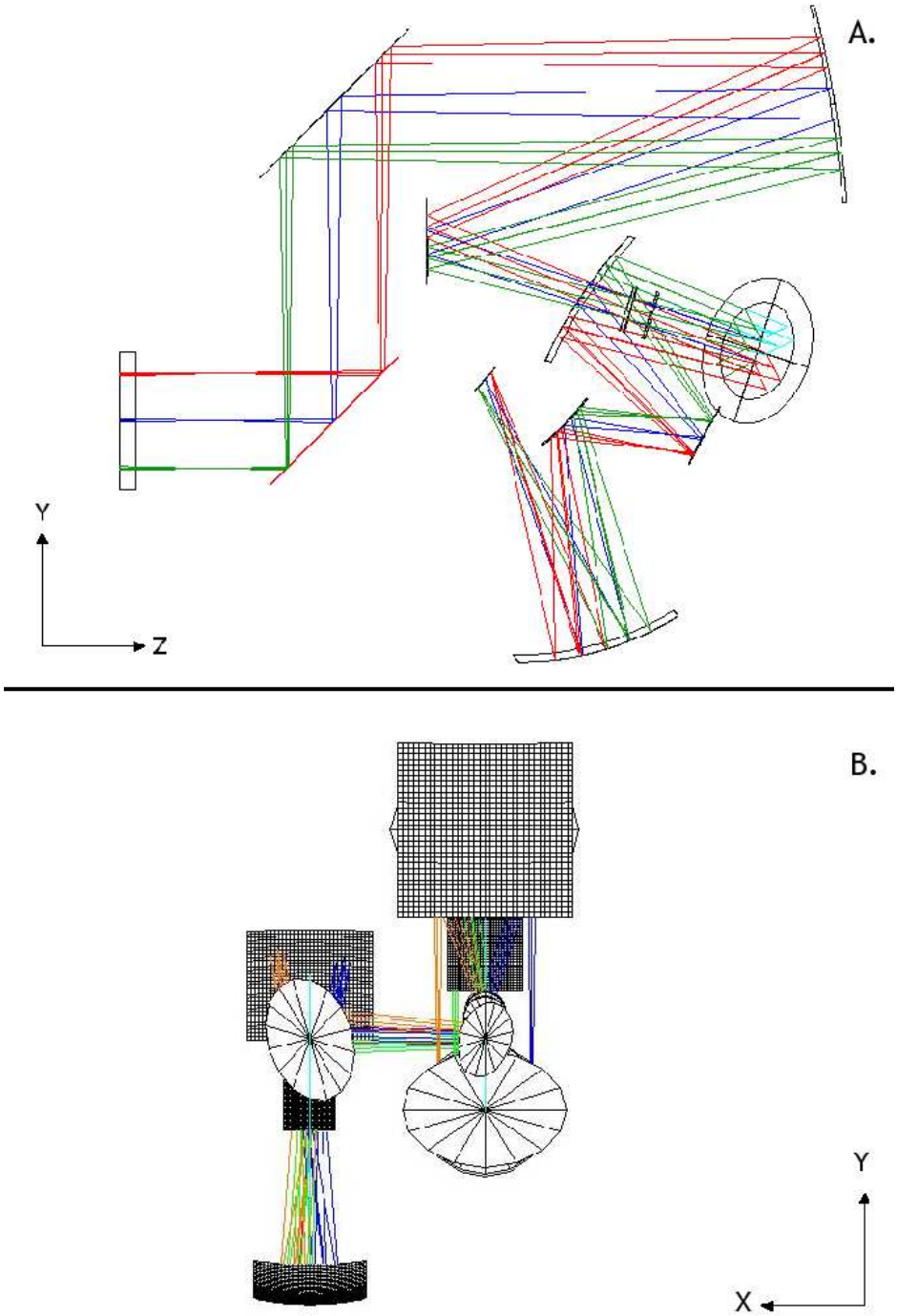

Figure 2-8. The University of Florida CIRCE redesign. The addition of the folds compressed the design along the Y-axis and allowed it to fit inside the GTC Folded Cassegrain envelope. A) A layout of CIRCE with X, Y, Z = 0. B) The layout rotated to Y = 270 degrees. Note that this configuration called for two optical benches or a single bench with optics attached to both sides.

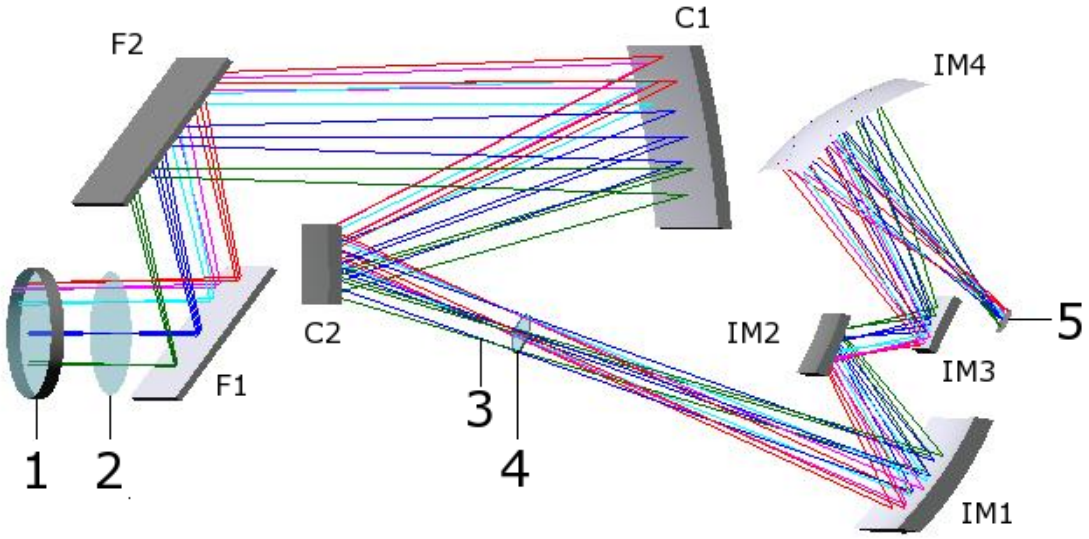

Figure 2-9. The final CIRCE optical design. To fit into the GTC envelope, ORA added two fold mirrors, F1 and F2, before the first collimator, C1, and rotated the first imaging mirror, IM1, to direct the light in a positive Y direction. In this design, light passes through the entrance window (1), to the telescope focal plane (2), before being reflected by two fold mirrors into the collimating optics (C1 and C2). The collimated light propagates to the Lyot or cold stop (3) and passes through a filter (4), before being imaged on the detector focal plane (5) by the four-mirror camera.

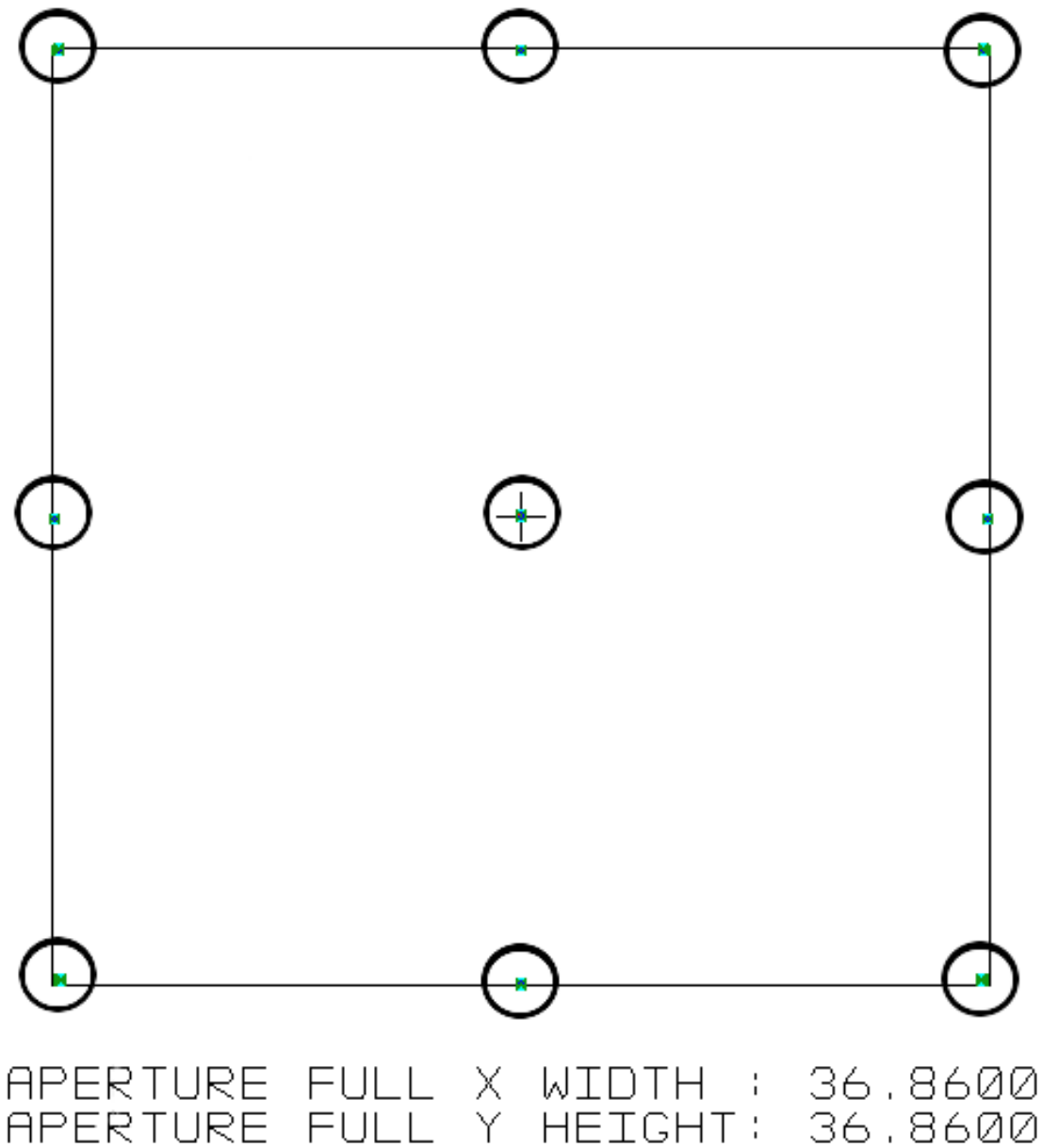

Figure 2-10. The footprint at the detector focal plane. The square aperture defines the area of the HAWAII 2K infrared detector that we will place at the focal plane. The marks (circled for easier identification) represent rays launched from 8 locations that mark the boundaries of a $3.4' \times 3.4'$ area on the "sky". This defines our FOV; any positions on the sky within this FOV will also land on the detector.

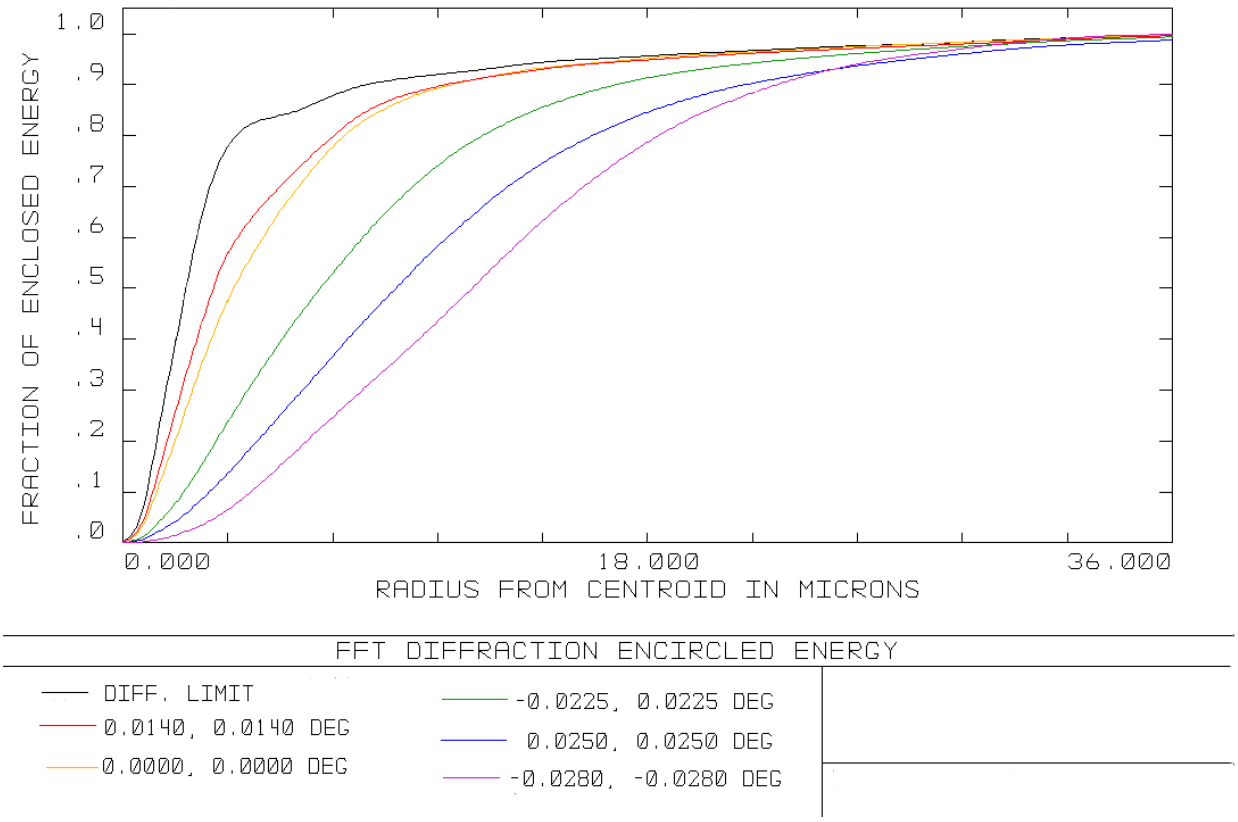

Figure 2-11. The J-band encircled energy diagram. I chose five positions on the detector to measure the amount of energy enclosed as a function of distance. These five positions are the center (0(°,0(°), the bottom left corner (-0.0280°, -0.0280°), a spot halfway (0.014°, 0.014°) and 3/4 (0.025°, 0.025°) between the center and the upper right corner, and a position 2/3 between the center and bottom right corner. Note that the EE curves for each positions are almost identical to positions in different quadrants but at similar radii from the detector. The black curve represents the diffraction limited case, the best achievable EE.

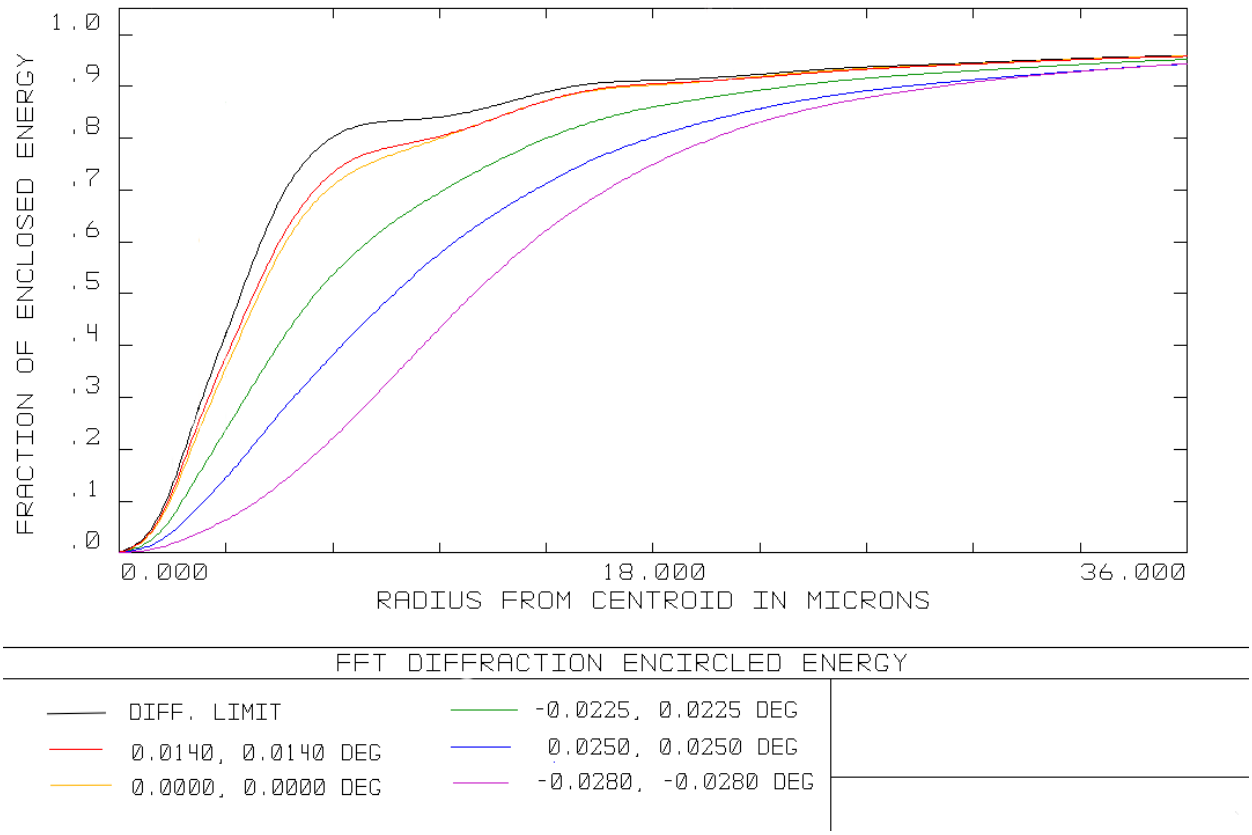

Figure 2-12. Same as Figure 2-9 but for the K-band. Note that the EE enclosed within a radius is slightly lower for every position on the detector. Still, we find excellent values; the EE in two pixels at the very corner of the detector is > 70%.

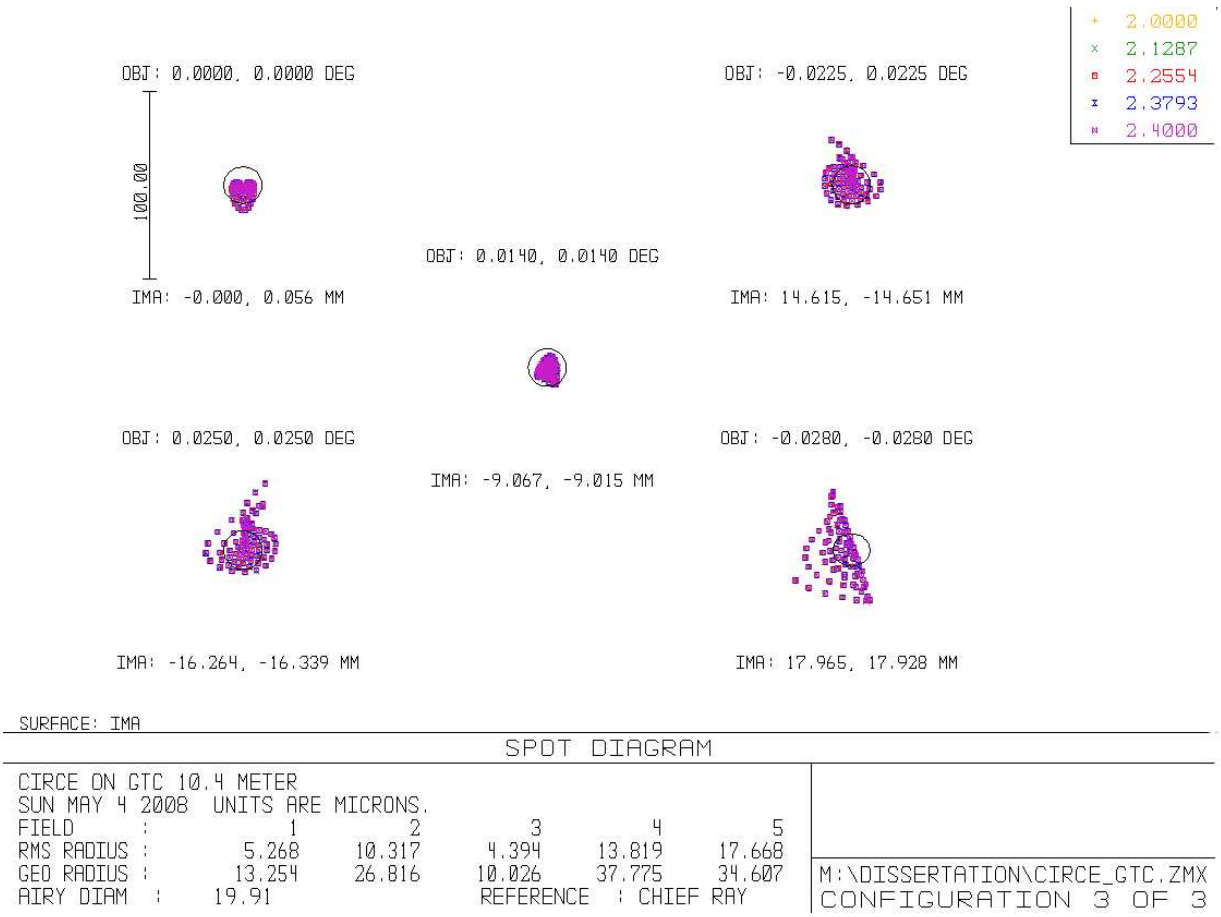

Figure 2-13. The K-band spot diagram for CIRCE. We note that for many field positions, the majority of the rays fall within one Airy Disk (shown by the black circle) and are tightly packed. The corners show the most aberration, but no one particular type dominates and the spot sizes are still small, if irregularly shaped.

CHAPTER 3
OPTO-MECHANICAL DESIGN OF CIRCE

3.1 Basics of Mechanical Design

In Chapter 2, I reviewed the optical design for CIRCE, detailing how I [1] used the instrument's science drivers to constrain broad optical characteristics, [2] helped create an optical layout that met these specifications, [3] analyzed the expected performance, and [4] evaluated the likely performance, accounting for potential errors during manufacture. The next step was to complete the CIRCE opto-mechanical design. Opto-mechanical design is the process of creating mechanical drawings of precision optics and associated hardware using details from the optical prescription.

Mechanical drawings depict objects to scale and include the precise dimensions and tolerances necessary to manufacture a desired piece. While the two- and three-dimensional layouts presented in Chapter 2 describe only the front surface, the aspheric "face", of each optic, mechanical drawings show every surface of the mirror. Furthermore, optical layouts display the mirror with a "dummy" thickness of zero. In reality, mirrors are thick blocks of 6061-T6 aluminum with a reflective surface on the front and bolt and pin holes on the back (see Figure 3-1).

The first step in manufacturing a mirror is to create a "blank", a physical block of material machined to the length, width, and height of the final optic. Next, a machinist adds bolt and pin holes to the back surface of the blank. Once this is complete the aspheric surface described by the optical prescription is diamond-turned onto the blank. In this process, a Computer Numerical Control (CNC) lathe will rotate the front face of the blank against a diamond-tipped cutting tool to produce the exact aspheric surface in the optical prescription. Diamond-turning typically produces sub-μm form accuracy and sub-nm surface accuracy. After the diamond-turning is complete, the mirror is plated with a gold coating, which is 97% reflective in the NIR.

For manufacturing purposes I needed to create a separate mechanical drawing of each optic. Besides noting the length, width, and height of every mirror, the mechanical drawings also provide a reference between the complex aspheric surface on the aluminum block and a particular pin or bolt hole on the back face of the blank. This is the basis of the "bolt-and-go" or "bolt-together" technique mentioned in §2.1; alignment and placement of optics is easier if the reference is a well-defined physical hole on the back of the mirror instead of the mechanical center of a theoretical aspheric surface.

In the following sections, I will detail my work on the opto-mechanical design of CIRCE. Specifically, I discuss [1] the steps I took to create two-dimensional mechanical drawings of each optic and its bracket for manufacturing purposes, [2] opto-mechanical layouts of the entire system in both two and three dimensions, and [3] a preliminary design of the optical bench.

3.2 Mechanical Design Software

While one can produce mechanical drawings with nothing more than a pencil, paper, and ruler, modern technology offers more advanced options; specifically Computer Assisted Design (CAD) programs that allow users to manipulate lines and shapes to produce accurate representations of objects. One of the most popular CAD programs is AutoCAD. Along with its offshoot, Mechanical Desktop, AutoCAD is an industry standard and used for both two- and three- dimensional mechanical design (Bethune 1997).

AutoCAD's native geometry is a Cartesian coordinate system with the X-axis increasing positively to the right, the Y-axis increasing positively to the top, and the Z-axis increasing positively out of the paper. When drawing in AutoCAD, users may change their viewpoint and see different faces of an object. However, the definitions of X, Y, and Z used when entering dimensions for an object do not change regardless of the object's orientation.

It is useful to point out that while most optical designers and design programs use metric units, mechanical drawings in the United States are almost always in English units. This is for practical manufacturing purposes; most lathes, drill presses, and other tools in the US use English units. Therefore all mechanical drawings discussed in this section are dimensioned in inches. This is important to be aware of as all the dimensions and decenters from ZEMAX and Code V, as well as the tolerances necessary for the designs discussed in §2.7, are in millimeters.

The easiest method for drawing complex shapes is to deconstruct the object into its basic shape, draw these shapes to the correct scale, and then use tools within AutoCAD to alter them until the result replicates the desired object exactly (Bethune 1997). For objects created from scratch, this process requires that the designer has either a very specific list of dimensions for the final object from another source, or firsthand knowledge of the object's specifications and purpose. For CIRCE, the latter situation applied (see §3.3). Either option allows the designer to create the most accurate drawing possible for the manufacturer.

While AutoCAD allows users to model objects in both two- and three- dimensions, it is easer to label and less confusing to read two-dimensional drawings. Thus, most mechanical designs sent to manufacturers are presented in two-dimensions. Two-dimensional drawings show a slice or cross-section of a three-dimensional object. Usually this is accomplished by taking a plane and slicing an object perpendicular to one axis as in Figure 3-2. For instance, an XY cross-section requires slicing perpendicular to the Z-axis; in effect, holding it constant at one value. This allows us to see the shape of an object at a particular value of Z.

To create a cross-section, designers have two options. For simple objects, where the specifications of the cross-section are well-known, they may draw the cross-section directly using two-dimensional shapes. If the object is very complex and the exact dimensions of its cross-section difficult to extrapolate, a designer might opt instead to draw the

object in three-dimensions and use AutoCAD to produce slices of the appropriate planes. Three-dimensional drawing, also called solid modeling, uses shapes like spheres, cylinders, cones, etc. to construct an exact model of an object.

I employed both two-dimensional drawing and solid modeling to produce mechanical drawings of the CIRCE optics. I then used these designs to determine the positions of the mirrors on the optical bench, – a flat, table-like surface that supports brackets, optics, cryo-mechanisms, electronics and the detector and create brackets with the correct dimensions and hole patterns to hold them in place. I will first discuss the initial two-dimensional designs of the mirrors and the process that I used to determine the correct dimensions for the blanks.

3.3 Designing and Drawing the CIRCE Mirrors

As discussed above, designers can create two-dimensional drawings in one of two ways: directly with two-dimensional shapes or indirectly from solid models. Although solid modeling is very powerful (see §3.6), it is also more time-consuming. Since my first drawings were primarily used to consult with members of the InfraRed Astrophysics Group (IAG) regarding locations and sizes of bolt and pin holes, "blank" dimensions, and mechanical drawing techniques, I initially used the faster 2-D method. This allowed me to make corrections very quickly, reducing the time spent on each iteration.

Before beginning my drawings, I needed to determine the physical size of each mirror. Since we specified that CIRCE should have a $3.4' \times 3.4'$ FOV, (§2.1) any light from within this area of sky should fall completely on every optic. Thus, two dimensions of each mirror, the width and height, were linked to the optical design. If a mirror is undersized in either dimension, light at the edge of the field will miss the mirror, thus failing to propagate to the next optic.

To avoid any loss of photons, I ensured that the mirrors were large enough to capture and reflect light from the entire field. In ZEMAX, I launched beams from ten field angles, marking out the FOV of CIRCE. Using footprint diagrams (see §2.5) I mapped where the

beams landed on each mirror. I enlarged the width and height of the mirrors one-by-one until the footprint diagram for every surface showed that all the beams fell completely on the mirror. I then added 6mm to the height and width. This created a 3mm buffer around the edge of each mirror, where defects and tool marks are most likely to occur during machining. This prevents unplanned aberrations caused by the manufacture process. I present the footprint diagrams of the eight CIRCE mirrors with corrected apertures in Figure 3-3. Table 3-1 gives the final widths and heights of the mirrors. Recall from §2.2 that X corresponds to height, Y to length, and Z to width in optical design parlance. It is important for later discussions §3.8 to recognize that many of these optics are quite large; the largest mirror, Collimator 1, is 10 inches $\times$ 10 inches $\times$ 5 inches.

With the dimensions of the optics now well-defined, I produced sketches of the YZ and XY cross-sections of each mirror. Here, I present and discuss in detail the mechanical drawings created for the first collimating mirror; however I also completed similar drawings for the remaining seven optics.

Figure 3-4 is an XY cross-section of collimator 1. This slice shows the mirror as it would look if we viewed it from its back surface. It gives both the length and height of the mirror, as defined by the footprint analysis, and defines the bolt- and pin- hole patterns on the back surface of the optic. The two pinholes and three bolt holes will secure the mirror to its bracket.

Pins are tight fitting cylinders of metal that are used to precisely position optics. The locations of the pinholes are constrained by tight tolerances, generally in the range of 10 - 25 μm in each direction. Since the locations of the pinholes are only one possible source of error when positioning and aligning our optics, the tolerance for each hole must be less than the total 37 μm budgeted in our tolerancing analysis for each of the the X, Y, and Z decenters.

The pinholes are also referenced very accurately to the aspheric surface of the mirror. Two pinholes per optic are necessary: one to fix the lateral motion and the other to

prevent rotation. Three bolt holes per optic lie at 120 degree intervals on a circle centered on the central pinhole. The bolts support the bulk of the mirror's weight and secure it to its bracket. However, the front of the bracket and back of the mirror do not sit flush against each other; instead three raised " contact pads" surrounding the bolt holes are the contact points between the bracket and mirror. These three points of contact provide the most stability and flatness when mounting the mirror. This is a geometric argument - since three points define a plane, any object with three contact points will stabilize itself on a flat surface.

In Figure 3-4, I indicate several dimensions, including the size of the contact pads, bolt holes, pinholes, and bolt circle. I used mirror drawings from a previous UF instrument, T-ReCS (Telesco et al. 1998), as a general reference for screw and pin sizes. As the CIRCE design progressed, recommendations from the IAG led me to alter many of these specifications. I discuss this process in more detail.

The next two dimensional drawing, Figure 3-5, is a YZ cross-section, sliced at the X = 0 plane. To make the YZ cross-section I considered two surfaces, the back and front of the mirror. Both surfaces had the same Y dimension, or width, set by the footprint diagram analysis outlined above. The front surface of the mirror was modeled using Equation 2–1. Since this aspheric equation defines Z is a function of Y, we chose critical values for Y at the top, bottom, and mechanical center of the mirrors; computed the corresponding values of Z; marked them in AutoCAD, and connected them with a curve. Recalling that the mirrors in the CIRCE design are segments of larger parent mirrors (see §2.2, we also marked the vertex, the center of the parent mirror where Y and Z = 0, and the aperture decenter, or distance from the mechanical center to the vertex.

I then diagrammed the back surface of the mirror, as seen in the YZ cross-section, referencing Figure 3-4 for positions and sizes. Using the locations and depths of the bolt and pin holes and contact pads specified on the XY cross-section, I modeled these objects with two-dimensional shapes available in AutoCAD.

Examining Figure 3-5, we see that the width of the mirror (Δ Z) is not constant. This is because Z is a function of Y on the front surface of the optic but constant on the back, creating a uniform back to mount to a flat bracket. To find the correct widths for the mirrors, I consulted mirror designs from the previously constructed UF instrument T-ReCS (Telesco et al. 1998). I found that the minimum width of each T-ReCS mirrors was $\sim$ 25-30% of its length, which guaranteed rigidity, preventing the optic from bending either during manufacture or once mounted in the instrument. This rule-of-thumb for sizing optics was confirmed by IAG engineers and I applied it to all the CIRCE mirrors. For example, the length of the Collimator 1, is $\sim$ 10 inches, so the minimum width, as shown in Figure 3-5, is $\sim$ 2.7 inches.

I completed two-dimensional drawings of the XY and YZ cross-section of all six powered CIRCE mirrors following the procedure described above. I created similar drawings for the two unpowered fold mirrors; with only minor differences in the YZ cross-sections. The final dimensions for all optics are listed in Table 3-1. Finally, I combined the XY and YZ cross-sections for each optic into one mechanical drawing for the manufacturer's use. I show an example of the completed diagram of Collimator 1 in Figure 3-6.

With the first two-dimensional sketch of the CIRCE optics complete, I presented my work to the IAG for review. Senior UF mechanical engineer Jeff Julian advised me to make several changes to the drawings including the addition of the aspheric equation on each aspheric mirror drawing; a list of important notes for manufacture regarding surface irregularities, coatings, and clear aperture (determined from the footprint of the beams; see §3.3); more detail regarding the locations of the pin and bolt holes; and instructions requiring specific surface flatness to make sure the contact pads were smooth.

Further, the IAG suggested important alterations to the mirrors themselves. First, they recommended that I add bolt "reliefs" to alleviate pressure from the mounting bolts. Reliefs are semi-circular cut-outs toward the back of the mirror that intersect the

bolt holes near their greatest depth. Since many of the mirrors are quite large (recall Collimator 1 is 10 inches × 10 inches × 5 inches), the weight of the optic pulling on the bolt could slightly warp the surface of the mirror opposite the hole. The reliefs would alleviate this pressure and prevent warping. I implemented this correction to the mirrors and made the suggested additions to the drawings. I show an example of a new mechanical design with a close-up of the reliefs in Figure 3-7.

The IAG also suggested a modification to the fold mirrors. As shown in Figure 3-8, the fold mirrors were initially rectangular blocks. To minimize the total weight of the instrument and reduce the area the folds occupy on the bench, I removed material from the sides of the mirror so that the sides tapered from the front to the back surface. I show an example of a new fold trapezoidal-shaped fold1 mirror in Figure 3-9.

3.4 Opto-Mechanical Layout

In §3.3, I discussed the creation of individual mechanical drawings for every mirror in the CIRCE optical design. In the remainder of this chapter, I present my work on the opto-mechanical layout, which is a mechanical design of the complete optical assembly including the mirrors, brackets, and the optical bench.

As discussed in the introduction of this chapter, optical software programs like ZEMAX only model the front surface of each CIRCE mirror in the optical layout. These surfaces are ultimately machined onto 1 - 5 inch thick blocks of aluminum (see §3.3) with heights and widths of up to 10 inches. Thus, while the ZEMAX optical layout portrays the aspheric surfaces of CIRCE with precision, it does not provide a realistic picture of what the assembled optical system will look like once it is complete.

The challenge of producing an opto-mechanical layout is to create mechanical drawings for manufacture that accurately portray how the finished assembly of mirrors and brackets will appear, while staying true to the optical prescription. The opto-mechanical layout must model the aspheric surfaces, with the correct locations, decenters, and tilts

(see §2.2), as accurately as the optical layout, while showing the precise position of pin and bolt holes on the back of mirrors and exact locations of the brackets.

Although this sounds simple in principle, the execution is quite difficult. While optical designers can use ZEMAX to theoretically"place" free-floating mirrors in the correct position on the optical layout every time, the reality requires more physical detail. In the assembled instrument, the mirrors will bolt to brackets, which in turn will bolt to the optical bench. If any of these pieces is designed or machined incorrectly, the aspheric surface will not be in the correct position with respect to the other optics, adversely affecting image quality.

In §2.7, I placed limits on the amount of error we could tolerate before the image quality degraded to an unacceptable level. For instance, the tolerances for the decenters, the X, Y, and Z position of an aspheric surface with respect to the the previous surface, are $\sim 40\mu$m in each direction (see Table 2-3). This is the total allowable error for pin and bolt holes in the bench, brackets, and mirrors for both design and manufacture. While designing to this level of precision is feasible, it still requires careful work on the part of the mechanical designer and (as I discovered) powerful CAD tools.

In the following sections, I detail attempts to construct a mechanical design of the cryo-mechanical layout using two-dimensional cross-sections and three-dimensional solid models.

3.5 Two-Dimensional Opto-Mechanical Layout

Using the YZ cross-section of the eight CIRCE optics (see §3.3), I created a two-dimensional opto-mechanical layout of CIRCE. Figure 3-10, shows the first results: a YZ cross-section of the optical assembly at X = 0.

To create this layout, I first needed the positions and rotations of the mirrors from the optical prescription. In ZEMAX, I defined a "global reference", a surface designated as the reference point by the user. I chose the entrance window, the first optic in the CIRCE optical path. ZEMAX output the X, Y, and Z location of the vertex of each mirror, as

well as the α, β, and γ rotations around the vertex, with respect to the entrance window. In AutoCAD, I defined the location of the entrance window as X = Y = Z = 0, so that all positions and rotations would be with respect to the origin.

Since the CIRCE mirrors are off-axis segments of larger parent mirrors (§2.2), their vertices are not located within the defined aperture. However, the two-dimensional YZ cross-sections of each mirror, like that shown in Figure 3-5, include the vertex. I imported all eight YZ cross-sections with their vertices into a single file. Then using a various tools in AutoCad, I positioned and tilted each mirror by the prescribed amounts.

Once I produced the layout shown in Figure 3-10, I checked to ensure that none of the mirrors blocked or intersected any other optic. We noted that the GTC re-design necessitated by the envelope specifications (see §2.3) left very tight spaces between the first collimator (C1) and fourth imager (Im4) and the first fold mirror (F1) and the second collimator (C2). Throughout the opto-mechanical design it was critical to be conscious of potential space issues when placing mechanical elements, like brackets, into the system.

However, as I described in §3.4, the true test of the opto-mechanical layout is whether the mirror surfaces are in the same location (within the tolerances) as the aspheric surfaces in the optical design. This is counterintuitive at first; one would expect a powerful program like AutoCAD to very precisely position any shape. However, given the complexity of the aspheric surface and its rotation about a distant point (the vertex), accuracy is not ensured. In fact, when I compared the X. Y, and Z global position of the mechanical center derived from ZEMAX, I found that the AutoCAD layout was off by over 100 μm in Y and 1000 μm in Z for collimator 2. Further, two of the imaging mirrors, two and four, had errors > 20 μm in more than one direction. While these errors were below our ~ 40 μm tolerances, if we accepted the AutoCAD layout as-is, this level of error would be incorporated into the design, leaving little room for manufacturing or placement errors for these mirrors later on.

After several attempts to track down possible sources of error in the software with no improvement of the AutoCAD positions, the CIRCE team decided to move on to a more robust method: solid modeling. However, this work ultimately proved useful; I determined that the CIRCE optics would fit into the space provided and developed a technique for comparing the global location of any point on a mirrors in AutoCAD and Zemax.

3.6 Design and Analysis of Three-Dimensional Mechanical Layout

Seeking a solution to the layout problem, I explored solid modeling in AutoCAD. Solid modeling is the creation of three-dimensional models using spheres, boxes, cylinders, cones, and other solid shapes. Using AutoCAD, a designer can slice models to create cross-sections, rotate models for views of any face, and add and subtract solids to build more complex objects. Solid modeling is often more intuitive then two-dimensional modeling; one creates an object exactly as one would see it in reality, as opposed to imagining cross-sectional views or slices in perfect detail.

Since AutoCAD provides no method to produce aspheric surfaces from scratch, I made simplistic solid models of the CIRCE optics using spherical surfaces (see Figure 3-11 for an example). Using a similar technique to the one developed for the two-dimensional layout, I placed the solid models on an optical bench with the correct decenters and tilts. Although this layout had the same basic problems as the previous design, exacerbated by the fact that the shape of CIRCE's powered optics are not spherical, I could, for the first time, probe the CIRCE optical mechanical design from every angle, checking that mirrors did not intersect each other off the X = 0 axis; this was not possible to do before because of the limited viewpoint offered by the two-dimensional design.

I then sought to improve this design and complete the three-dimensional opto-mechanical layout by modeling the mirrors with the correct aspheric surface. While ZEMAX can export surfaces and beams to files readable by AutoCAD, the resulting three-dimensional design was so complex, with thousands of objects and intersecting surfaces, editing the file was too difficult and time-consuming to be practical.

Instead, working in collaboration with Senior Mechanical Engineer Jeff Julian, we iterated several times with various ZEMAX outputs and two dimensional designs until he produced an accurate three-dimensional optical layout of CIRCE in SolidWorks, another powerful mechanical design program. This resulting design, presented in Figure 3-12, is also readable by AutoCAD.

Applying the technique described in §3.5, I analyzed this design, using the four corners of the mirrors' front surfaces to compare positions in AutoCAD against positions in ZEMAX. The results were excellent; I found an average difference of < 1 μm in X, ~ 5 μm in Y, and ~ 3 μm in Z. The largest difference along any axis was ~ 15 μm.

Using my two-dimensional drawings as a reference, I checked the locations of bolt holes, pinholes, contact pads, and bolt reliefs making additions and changes where necessary. Then, using this solid model, I completed two-dimensional cuts of all the optics, creating XY and YZ cross-sections of each optics for mechanical drawings.

3.7 Development in the Manufacture of the CIRCE Optics

During the opto-mechanical design of the CIRCE mirrors, the CIRCE team contacted several vendors to find a manufacturer for the optics. After consulting with several companies, we noted that the price for the basic machining of the blanks and subsequent testing of each optic was approximately half the total cost of the optics.

To drastically reduce costs, Janos Technology, one of the potential vendors, and the CIRCE PI developed an alternate plan. Rather than having Janos manufacture the blanks, the Astronomy and Physics Machine Shop at UF would machine them. The UF shop would also produce the brackets and the optical bench. These pieces would be shipped en masse to engineers at Janos, who would diamond-turn the mirrors, set-up the entire bench, and test the optics in concert, rather than individually testing each optic. Any aberrations caused by errors in the decenter, tilt, or mirror curvature would be found using inteferometry and corrected by slightly altering the shape of the mirrors. Then

Janos would gold coat the mirrors, re-mount the optics, and send the entire optical bench back to UF, where we could test and install it directly into the cryogenic dewar.

The tolerances that I calculated would still be useful guidelines for the mechanical design of the optical bench and the precision machining of the pin and bolt holes on each mirror. However, with this process we would avoid the majority of decenter and tilt errors, which generally surface during the alignment process.

The CIRCE PI consulted with the CIRCE team and we decided that this was an elegant and frugal plan. The only potential downside was the extended wait; while the design of the optics was nearing completion, design of the brackets and bench had not yet begun. Janos could not start work on the optics until we delivered the mirror blanks, brackets, and bench.

In the meantime, using the mechanical drawings produced in §3.6, the Physics and Astronomy Machine Shop at UF produced tests of all eight CIRCE optics. Two of these optics, the second and third imager are shown in Figure 3-13. After examining these test mirrors, we noted that the weight of the larger optics was problematic. For instance, Collimator 1, the largest mirror, weighed > 23 kgs. Considering weight constraints set by the GTC (~ 800 kgs total for the whole instrument) and concerns that the mirror would be difficult to support with a bracket, we decided to lightweight the larger CIRCE optics.

3.8 Lightweighting the CIRCE Optics

The first step in lightweighting the CIRCE optics was to decide which mirrors needed modification. After carefully considering our optics, we chose both flat mirrors, the first collimator, and the first and fourth imager. These optics are twice the size of the smaller optics and estimated to weigh over 14 kgs each.

Generally when lightweighting optics, two options are available. The first is to manufacture the mirror blank from a light material. For instance, the secondary mirror of the GTC is made of beryllium (Devaney et al. 2004), a low density material that is also very strong. However this solution is unsuitable here because these materials [1]

are prohibitively expensive for the CIRCE budget and [2] have coefficients of thermal expansion different than 6061-T6, nullifying one of the major benefits of the all-reflective design,namely homologous contraction.

The second choice was to remove large blocks of material from each mirror blank without compromising the rigidity of the optics. A common technique that meets this criterion is to create a "honeycomb" pattern on the back surface of the optic. Honeycomb patterns are both very strong and capable of greatly reducing the weight of an optic; one honeycombed 8.4-meter mirror on the Large Binocular Telescope is an order of magnitude stiffer and 40% lighter than a similar sized solid blank (Hill et al. 1998). Honeycomb patterns are also used to lightweight other opto-mechanical elements, such as optical benches.

We decided to employ a slightly modified version of this method, removing triangular pieces of material of varying sizes and depths to create honeycomb-like hexagonal structures on the back of the mirrors. This was easier, and thus less expensive, than machining many small intersecting hexagons.

I first created a two-dimensional sketch of a honeycomb pattern for each of the five larger mirrors, avoiding pin and bolt holes while maximizing the number of triangles on the back surface of the optic. I show a cross-section of one of these patterns in Figure 3-14. Next I used this pattern to construct the three-dimensional honeycomb structure. I calculated the depth of each triangular pockets, taking into consideration the IAG recommendation of leaving at least 1 inch from the front surface of the mirrors intact. This precaution would prevent any bulging or pressure on the mirror surface from the tools used to create the pockets. Since the mirror depth varied across the Y axis, the depth of the pockets also varied; the ones at the thicker part of the mirror were deeper than those at the slimmer end.

I then removed the bolt reliefs added in an earlier phase of the mirror design. This decision was based on two considerations. First, lightweighting the mirrors decreased the

need for reliefs; the pressure on the bolts that the reliefs alleviated was much smaller due to the mirror's lighter weight. Secondly, the reliefs inteferred with the new lightweighting, unavoidably driving through the now honeycombed pockets, which threatened to weaken the entire structure. Since the lightweighting was crucial and lessened the need for the relief holes anyway, we chose to remove the latter.

An example of a finished three-dimensional lightweighted mirror is shown in Figure 3-15. Analysis of the mirror designs using AutoCAD estimation tools showed that we reduced the weight of the mirrors by 20 - 25% with our lightweighting technique.

3.9 Finalized Mechanical Drawings of the CIRCE Mirrors

With our three-dimensional designs of lightweight mirrors complete, we moved on to produce finalized two-dimensional mechanical drawings. We completed two sets of these drawings, one for the machine shop at UF and one for Janos. The set of drawings for the mirror blanks were slightly modified; we removed the aspheric surface in the YZ cross-section and replaced it with a flat surface with slightly larger dimensions than the final mirrors. This ensured that Janos would have enough material to diamond-turn the correct aspheric surface. I present an example of the blank drawings in Figure 3-16. I show an example of the accurate two-dimensional mechanical drawings prepared for Janos from the lightweighted solid models described in §3.8 in Figure 3-17.

3.10 Mechanical Design of the Mirror Brackets

Upon completing the two- and three- dimensional design of the CIRCE mirrors, I began to design the mirror brackets. Brackets are machined pieces of 6061-T6 aluminum that attach to both the back of the mirror and top of the optical bench. They serve to suspend the mirror above the bench so that the optical axis of the system intersects the mirror at the correct height. They also firmly attach the mirror to the liquid nitrogen cooled optical bench.

While a variety of bracket and brace types exist, the CIRCE team took the advice of the IAG and chose the strong and simple to manufacture "L" and "T" shaped brackets.

Figure 3-18 shows an example of both a simple L- and T- bracket. For CIRCE, we also added gussets; these are triangular shaped wedges that add rigidity to the vertical member. I discuss this in greater detail later in this section.

Before I could begin to manufacture the brackets, I determined how high off the bench the mirrors would sit. CIRCE is designed so that the mechanical center of every optic is aligned with the X = 0 axis, or "optical axis". The optical bench will therefore rest at a negative X value in the final three-dimensional design. The exact distance between the optical axis and the bench depended on the largest optic: the first collimator . The height of the Collimator 1 is 10.037 inches; thus, the bench needs to be at least 5.0185 inches below the X = 0 axis. We added extra space for clearance, so that the mirror would not rest directly on the bench. In the end the optical bench was inserted into the optical design at X = -5.375 inches.

With this information, I could design the brackets. First I determined the size of the upright part of the bracket, the piece that attaches to the mirror. The width of this support, the Y-dimension, was the same as the Y-dimension of its mirror. The X-dimension or height of the upright was equal to the X-dimension of its mirror added to the mirror's height off the bench. For instance, a mirror with a height of 6.000 inches, centered on X = 0 would extend down to X = -3.000. Since the bench rests at X = -5.375, the distance between the bottom of the mirror and the bench is 2.375. The upright would therefore be 8.875 inches: 6.000 inches added to 2.375 inches. Finally, the length or Z-dimension of the bracket was 0.5 inches, rigid enough to resist flexure due to the weight of the optic without adding significant extra weight to each bracket.

We then designed the horizontal base of the L and T brackets. In both cases, the Y-dimension of the bracket was set by the Y-dimension of the mirror. The X-dimension, or height, was set as 0.5 inches, as discussed above. The Z-dimension was set by the height of the upright. For L brackets, the IAG recommended that the base be approximately 50% of the height of the upright. T brackets were less constrained; I

chose to make the horizontal base the same size as the upright, so that either side of the T base met the same 50% rule-of-thumb.

With this information, I completed three-dimensional solid models of the CIRCE brackets. After drawing the basic shapes that composed a bracket, I added pinholes to the base. The pinholes served the same purpose as the pinholes for the mirror; they secured the bracket in a precise location. Again, the tolerances on these pinholes were very tight; $\sim 20\ \mu$m in each axis. The size of the hole was specified to 0.0005 inch or $\sim 10\ \mu$m. I then added bolt holes that we will use to tightly secure the bracket to the optical bench.

I then designed the gussets (wedges that support and strengthen the upright). In the preliminary designs, the wedge-shaped gussets for the larger mirrors bisected the bracket, starting at the middle of the upright, as shown in Figure 3-18. However, the CIRCE team decided that instead of one thick gusset, two thinner gussets at the edges of brackets would distribute the weight more effectively and provide a stiffer support (see Figure 3-19) Meanwhile, we designed smaller brackets with three gussets, two in the front at the edges and one in the back bisecting the bracket. I present an example of this type of bracket in Figure 3-20.

After completing the basic solid models of the brackets, I imported them into our three-dimensional layout of the CIRCE optics. Using a variety of tools in AutoCAD, I aligned each bracket precisely to its mirror. This required making sure that only the contact pads on the mirrors touched the bracket. I then copied the bolt- and pin- hole patterns directly from the back of the optics onto the brackets, ensuring that that they matched.

Next, I checked for any places in the layout where a bracket intersected another bracket or mirror. I noted that the back gusset on the bracket for the second collimator mirror blocked the optical path of light traveling from the first fold mirror to the second fold mirror. I reduced the size of the gusset, solving the problem. The first collimator and fourth imager presented a more serious problem. Both mirrors are very large and

require equally large brackets. However, examining Figure 3-11 we see that there is little space between the two optics. The solution was to make a compound bracket, a large base with two uprights. Instead of a gusset, a removable wedge supported both vertical pieces. This allowed room to tighten bolt holes with the necessary tools while providing adequate rigidity. Figure 3-21 shows the final solid model of the compound bracket.

I then created two-dimensional drawings of the brackets for manufacture. These drawings featured three cross-sections (XY, YZ, XZ) and a solid model. I present an example of these drawings in Figure 3-22. In Figure 3-23, I show a picture of two of the finished brackets, manufactured by the UF Physics and Astronomy Machine shop. The brackets are bolted to their respective "practice" mirrors, which were discussed in §3.7

3.11 Preliminary Designs of the Optical Bench

The optical bench that supports the optical components of CIRCE is located directly above a tank of cryogen, in this case liquid nitrogen, the temperature of the bench is ~ 77 K. All components must have excellent thermal contact with the bench to remain cold.

The size of the bench determines the overall size of the dewar, as the heat shields and the vacuum jacket are generally positioned at known distances from each other in relation to the bench. In turn, the bench size is set by the optics. As indicated in §2.3 the CIRCE optics are centered at Y = 0. The farthest optical element from this central position is the first collimator at Y $\sim$ 17 inches. Allowing another 1 inch from the edge for clearance, yields a bench width of 36 inches. We then found the furthest optical element in the Z-dimension, the detector focal plane at Z $\sim$ 57.5 inches. Adding another 3 inches to account for the electronics necessary to run the detector and the detector stage, we calculated a Z-dimension for the bench of 60.5 inches.

The thickness of the bench is of critical importance. If the bench is too thin, it will warp under the weight of the optics and cryogen. This warping or bending is called flexure. If the flexure is too great, the instrument will bend and the positions of individual mirrors will change as the telescope and attached instrument moves. Thus, light from

the telescope will not propagate correctly, striking optics in the wrong position on their surface, creating aberrations in the system.

Miguel Charcos, a CIRCE team member, created a program in IDL to measure flexure in the bench. Considering a cantilever beam (a horizonal member suspended on one side from a vertical upright) he calculated the flexure of the bench given its thickness and the total weight of the mirrors, bench, and liquid nitrogen. He found that for a bench with a thickness of 2 inches, the flexure was less than 20 μm, the same order of magnitude as the tolerances on our X, Y, and Z, decenters. Further, this was the "worst-case" scenario, calculated with all the optics at the very edge of the bench.

Using this bench thickness, I constructed a preliminary CIRCE optical bench. To add rigidity and reduce the weight, I applied the same honeycomb pattern as used on the CIRCE mirrors to the underside of the bench. I then positioned this bench at X = -5.375, as discussed in §3.10. Using tools in AutoCAD, I mirrored the pin and bolt hole patterns from the brackets onto the bench to ensure that they matched. I present a solid model of the bench in Figure 3-24 and the completed three-dimensional opto-mechanical design of CIRCE in Figure 3-25.

Table 3-1. Dimensions of the CIRCE mirrors. ΔX corresponds to height, ΔY to length, ΔZ min to the thinnest width, and ΔZ max to the thickest width.

Mirror	ΔX (in)	ΔY (in)	ΔZ min (in)	ΔZ max (in)
Fold 1	7.480	9.370	1.980	1.980
Fold 2	8.189	10.394	1.980	1.980
Collimator 1	10.079	10.079	2.020	3.965
Collimator 2	4.488	4.567	1.200	1.367
Imager 1	7.244	6.772	1.820	5.413
Imager 2	3.071	3.780	1.000	1.352
Imager 3	2.913	3.386	0.900	1.123
Imager 4	7.402	8.189	1.720	5.055

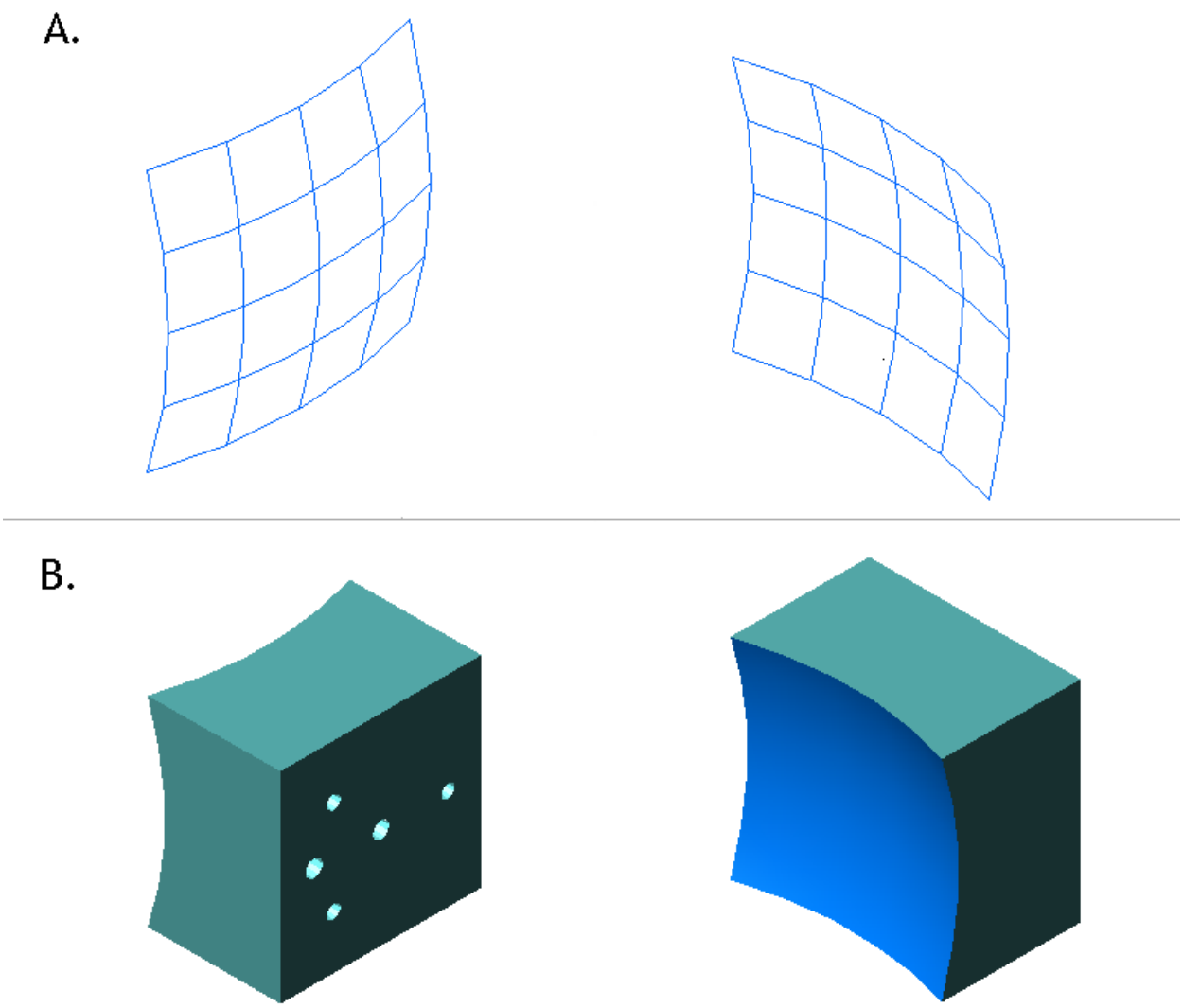

Figure 3-1. The difference between optical and opto-mechanical representations of a hypothetical spherical mirror. A) Optical programs like ZEMAX only model the front surface of the mirror B) Using mechanical drawings I can create a more detailed image of the entire mirror, with hole patterns and a realistic thickness.

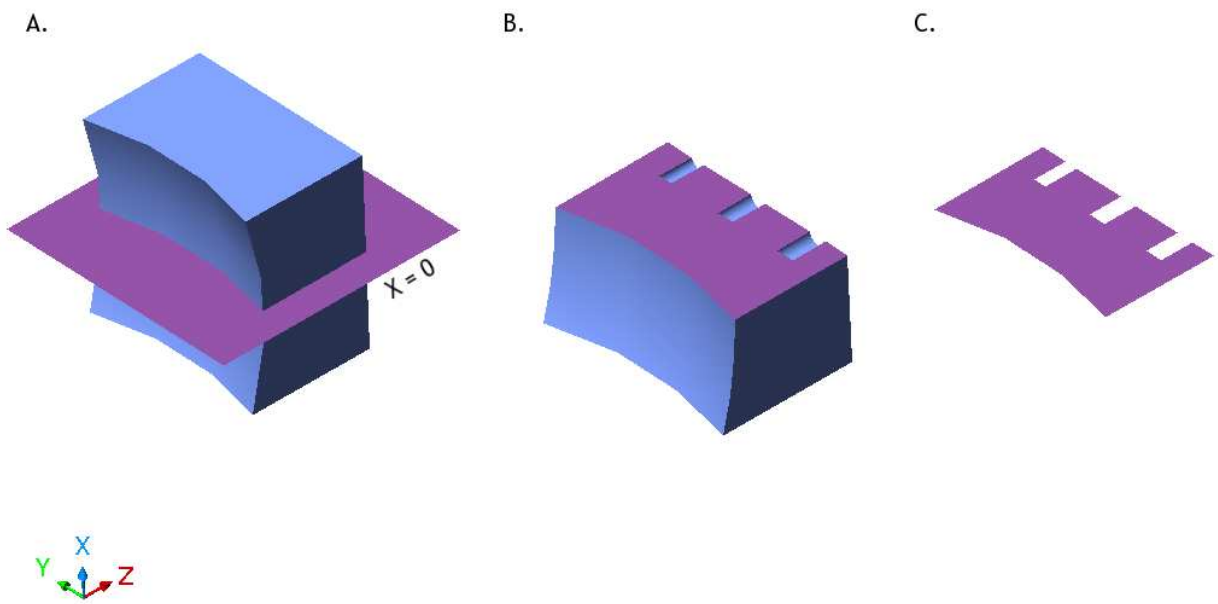

Figure 3-2. The relationship between a mechanical cross-section and a three-dimensional solid model. A) The solid model of an optic bisected by a plane at X = 0. B) Removing the top half of the mirror – the purple surface represents the intersection of the plane with the optic. C) Removing the entire three-dimensional optic, we are now left with only the intersection of the mirror with the cutting plane, in this case, a YZ cross-section.

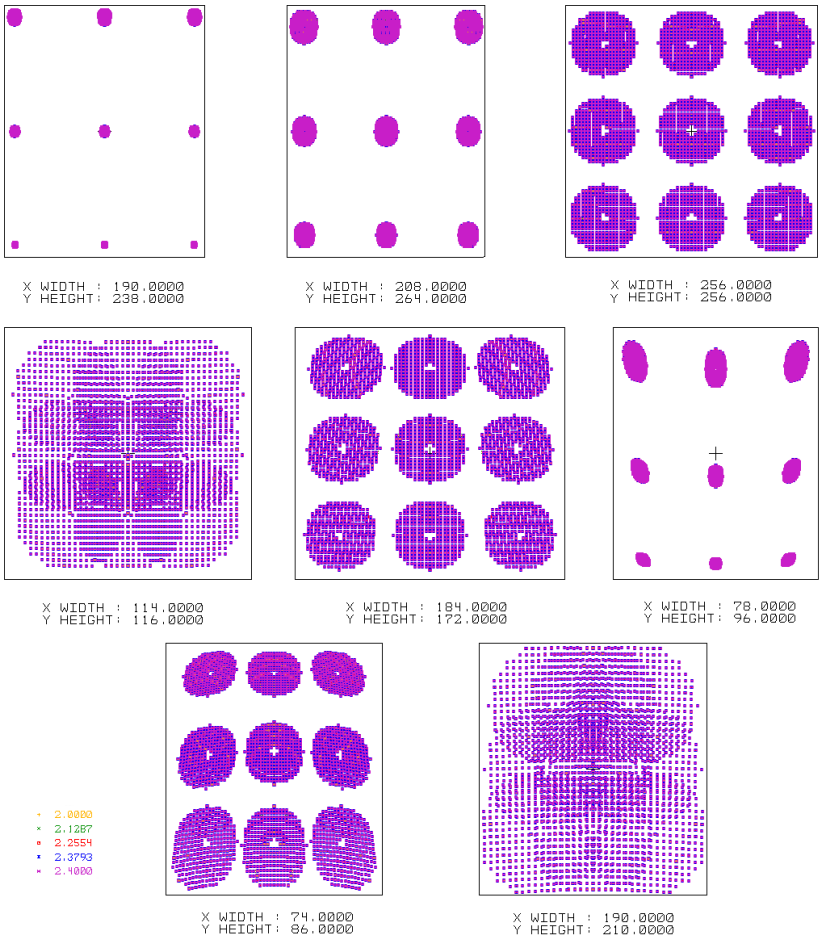

Figure 3-3. K-band footprint diagrams of the CIRCE Mirrors. Note that the beams were launched from nine field positions outlining a $3.4' \times 3.4'$ area of sky. All mirrors were sized to capture all beams from these positions and then oversized by 6 mm in each dimensions to allow for machining defects, which are most common around the edges of optics.

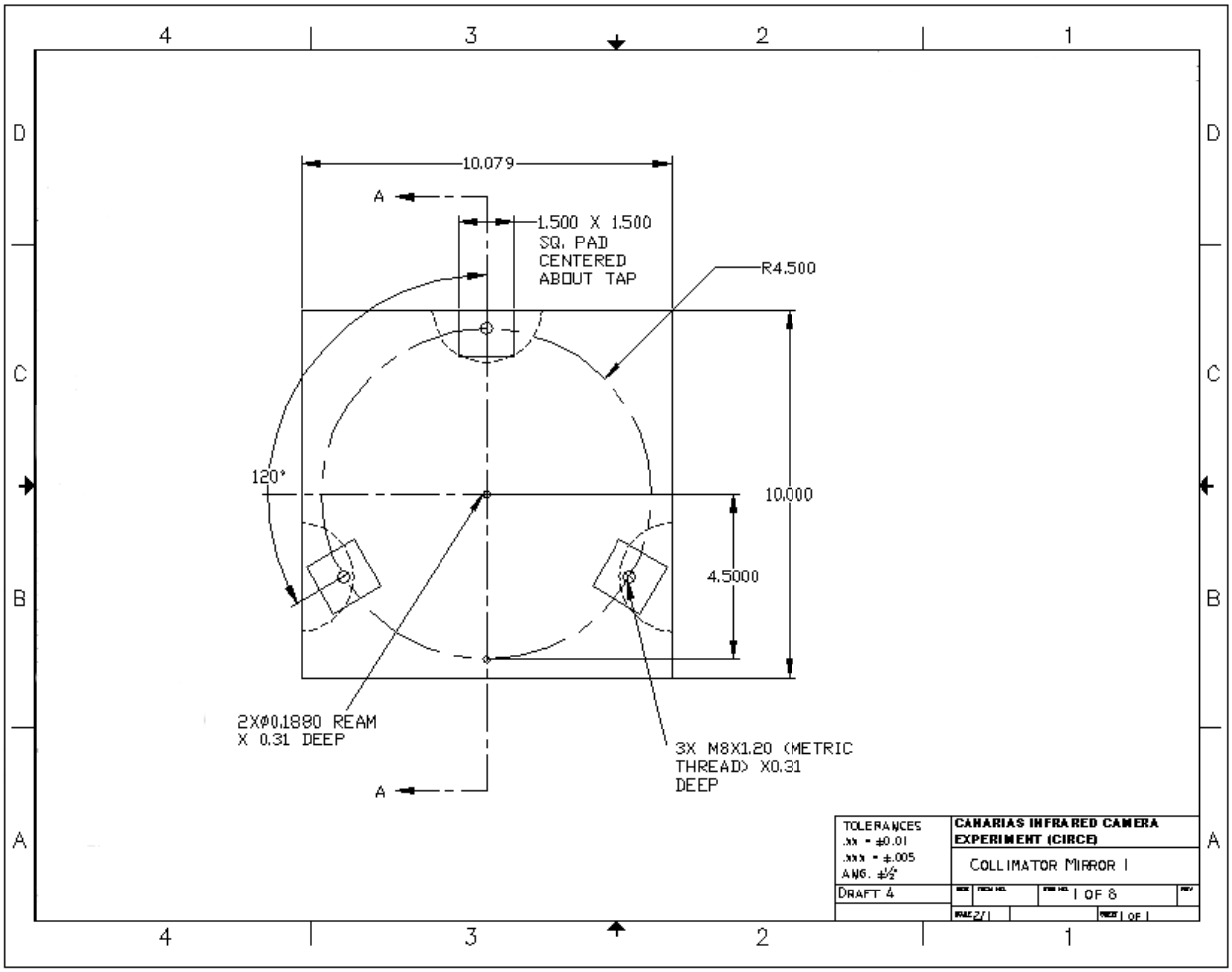

Figure 3-4. Preliminary XY Cross-section of collimator 1. The dimensions of the mirror, locations of the pin and bolt holes, radius of the bolt hole circle and position of the contact pads are included on the diagram.

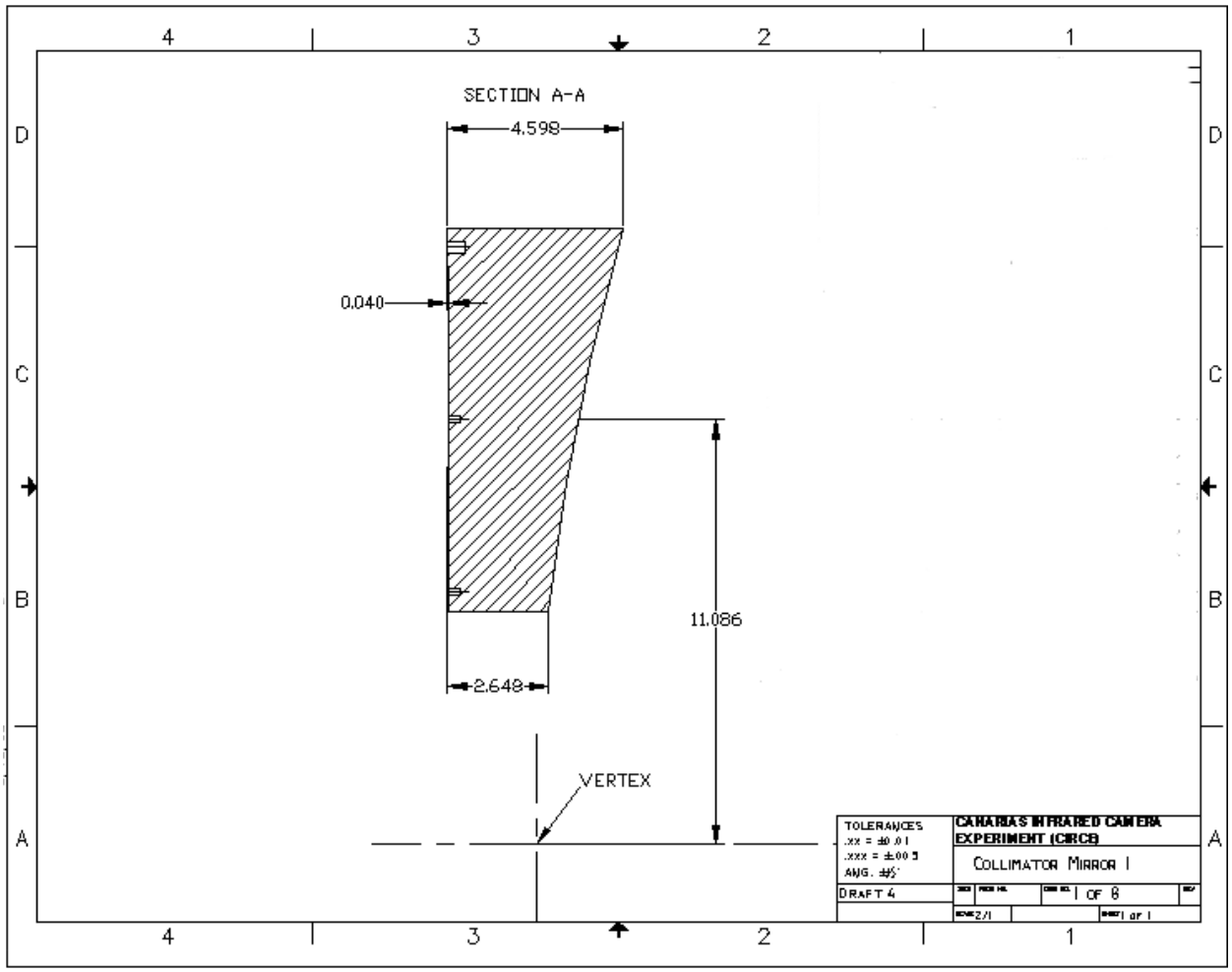

Figure 3-5. Preliminary YZ Cross-section of Collimator 1. The drawing shows the aspheric surface, the distance to the vertex, and the thickness of the mirror at the edges.

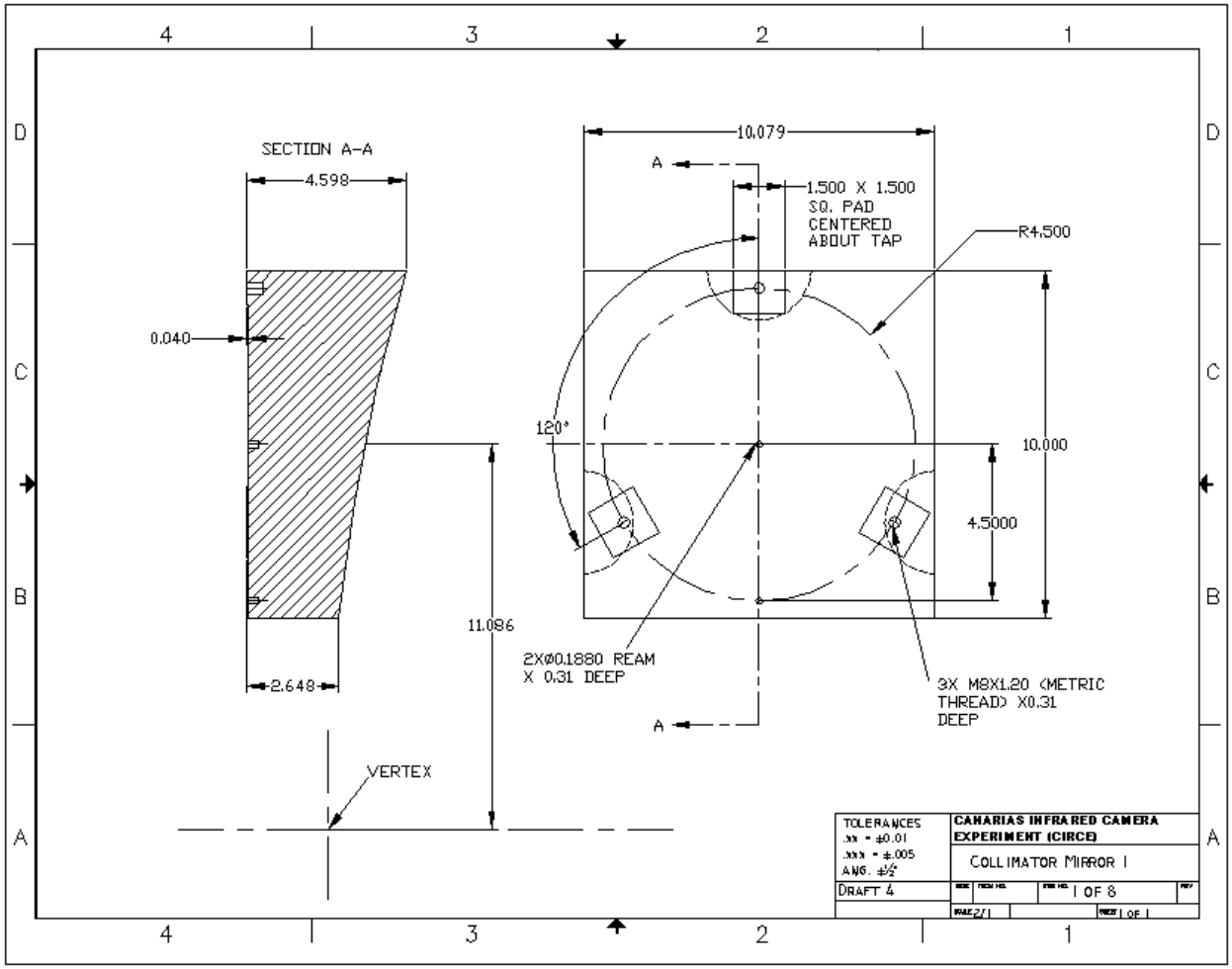

Figure 3-6. Preliminary two-dimensional mechanical drawing for Collimator 1 showing both XY and YZ cross-sections. Note that the section labeled A-A shows the YZ cross-section for a cut taken across the line labeled A-A in the XY drawing. This line represents the X = 0 plane, which bisects all the CIRCE optics.

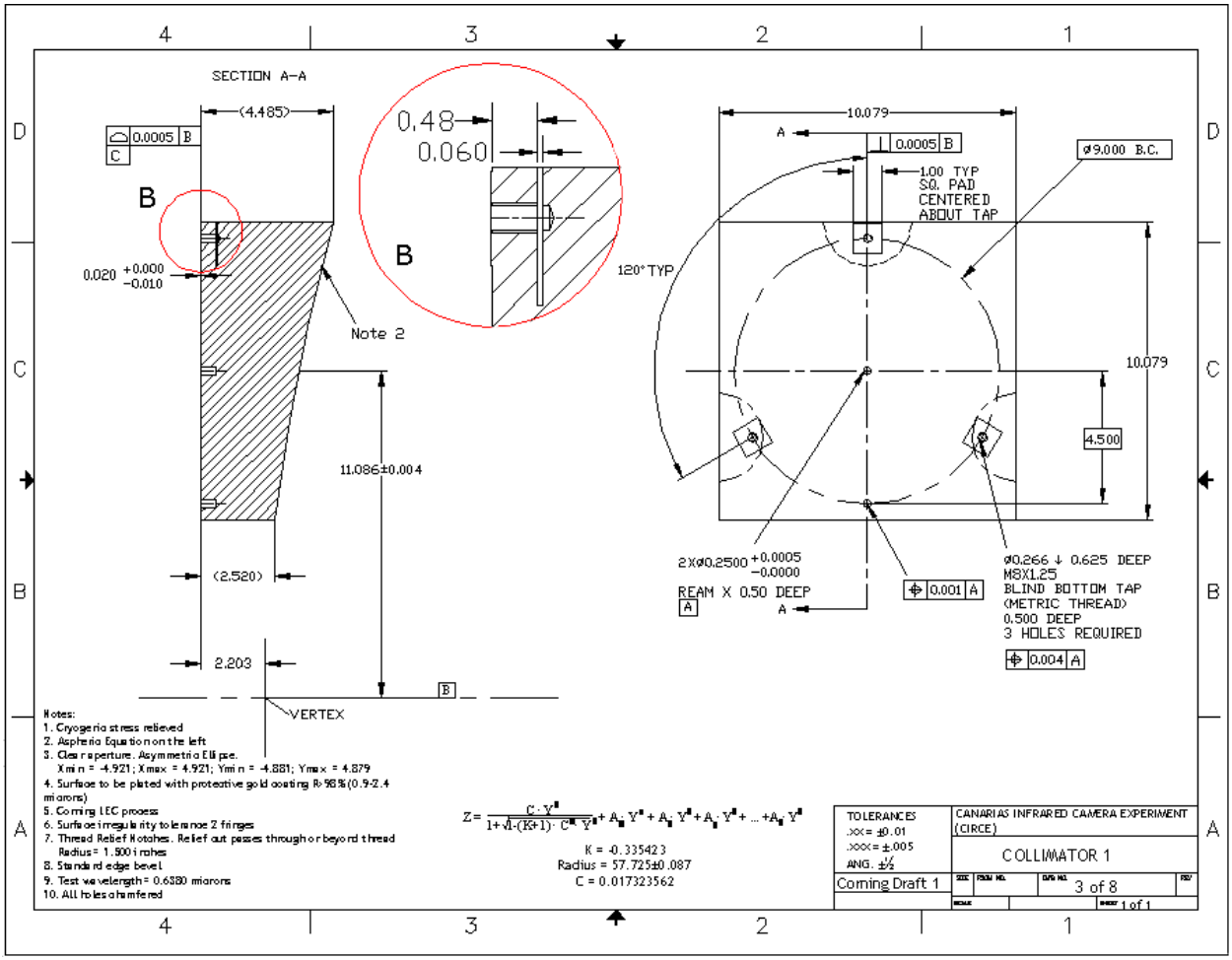

Figure 3-7. Revised two-dimensional cross-sections of Collimator 1 following a design review. Note the addition of bolt reliefs. A detail of this feature is shown the circle labeled B.

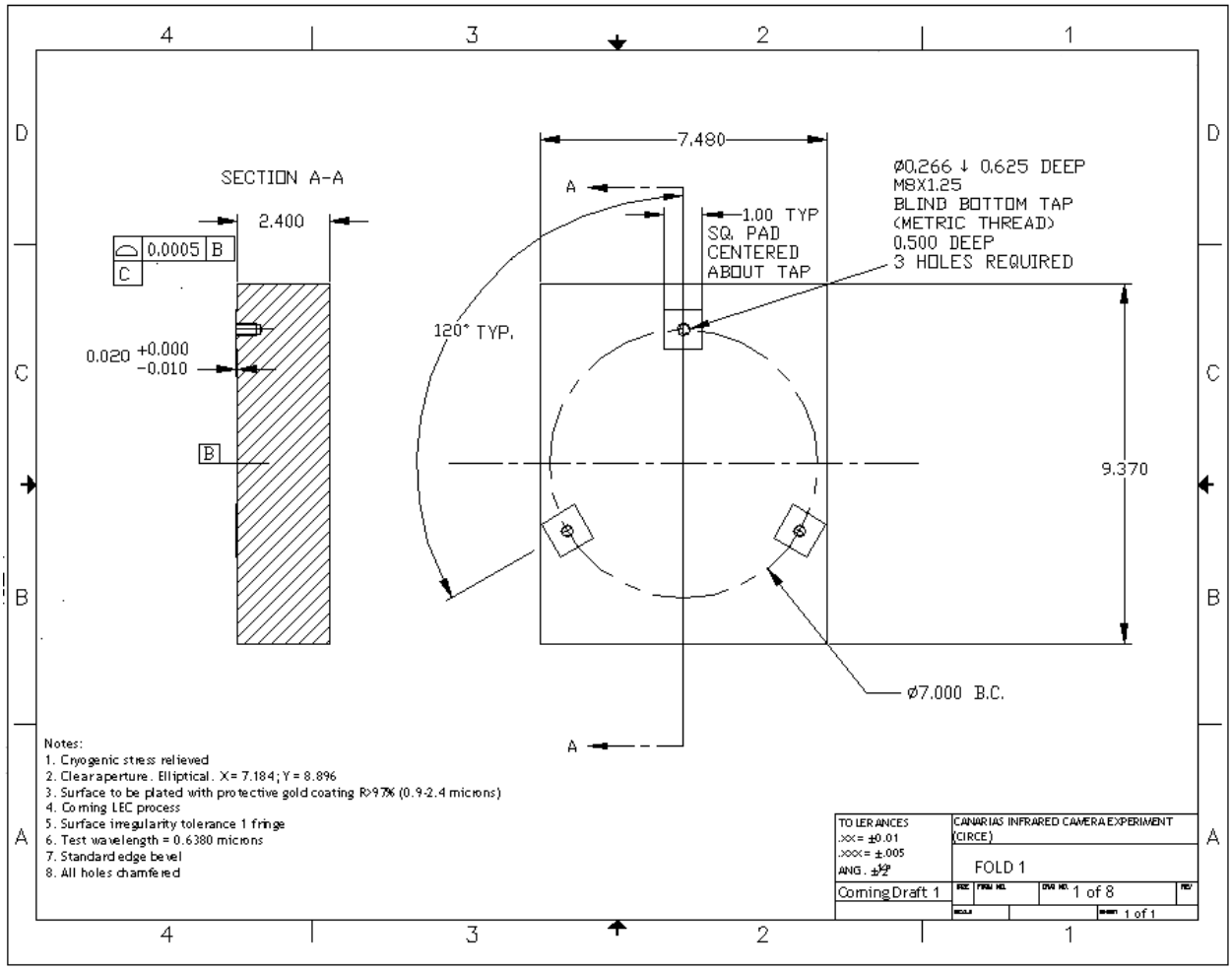

Figure 3-8. The original 2-D mechanical drawing of Fold 1. The block shape of the mirror was revised to reduce weight. See Figure 3-9 for the new design of Fold Mirror 1.

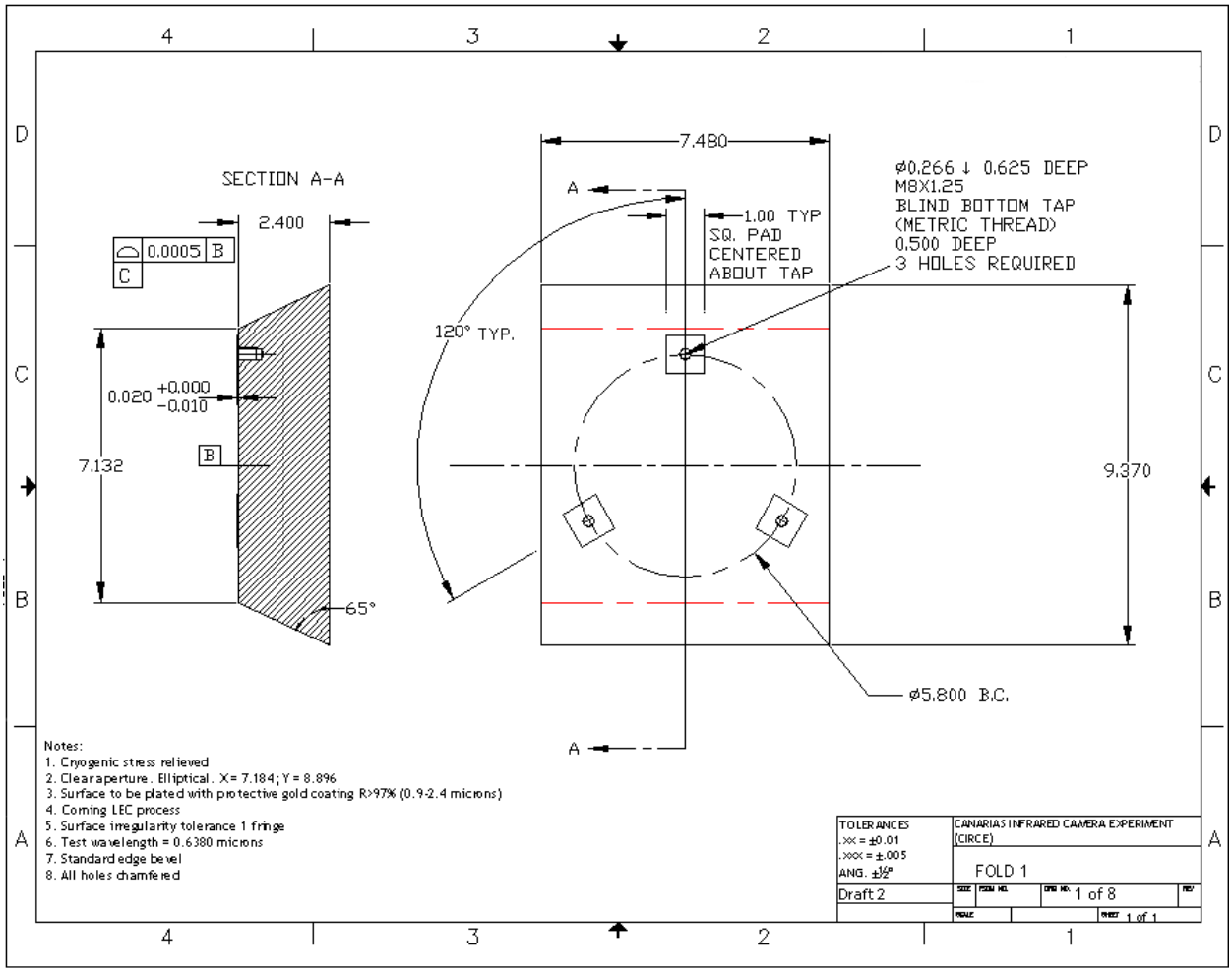

Figure 3-9. Fold Mirror 1 after a design review and redesign. The sides now slope inward, which reduces both the mirror's weight and the space they occupy on the bench.

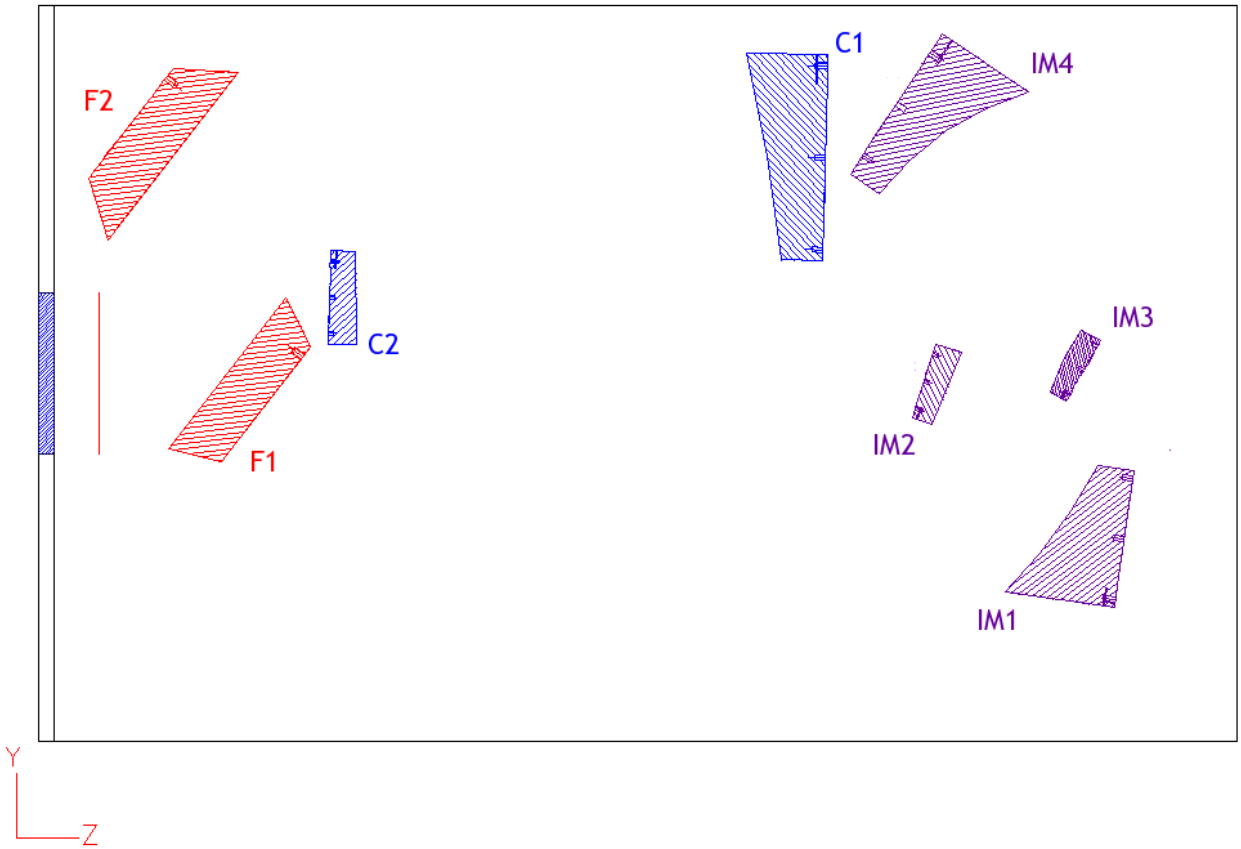

Figure 3-10. The 2-D opto-mechanical layout of CIRCE. This shows the first attempt to place the physical mirrors in the correct location with respect to each other.

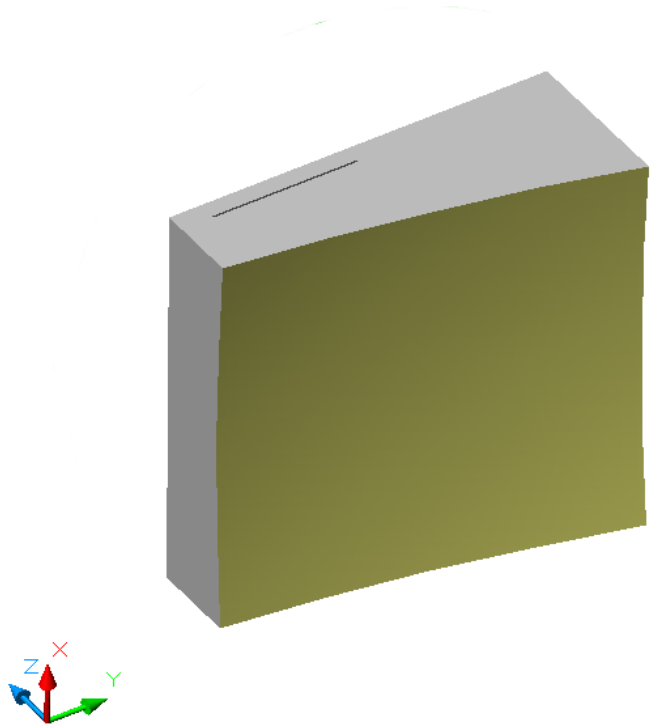

Figure 3-11. Preliminary solid model of a Imager 4. The mirror has a spherical surface with a radius of curvature that best approximates its true aspheric shape.

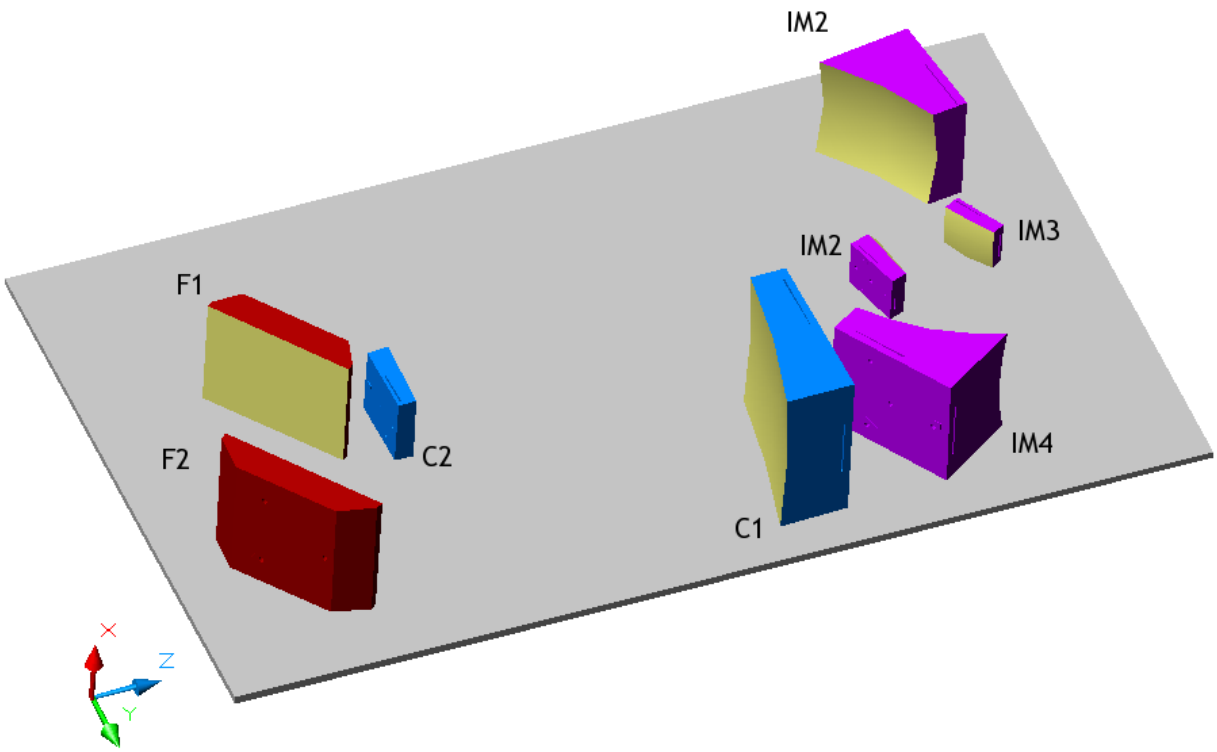

Figure 3-12. A 3-D solid model of the opto-mechanical layout of CIRCE with the correct optical surfaces, locations, and rotations.

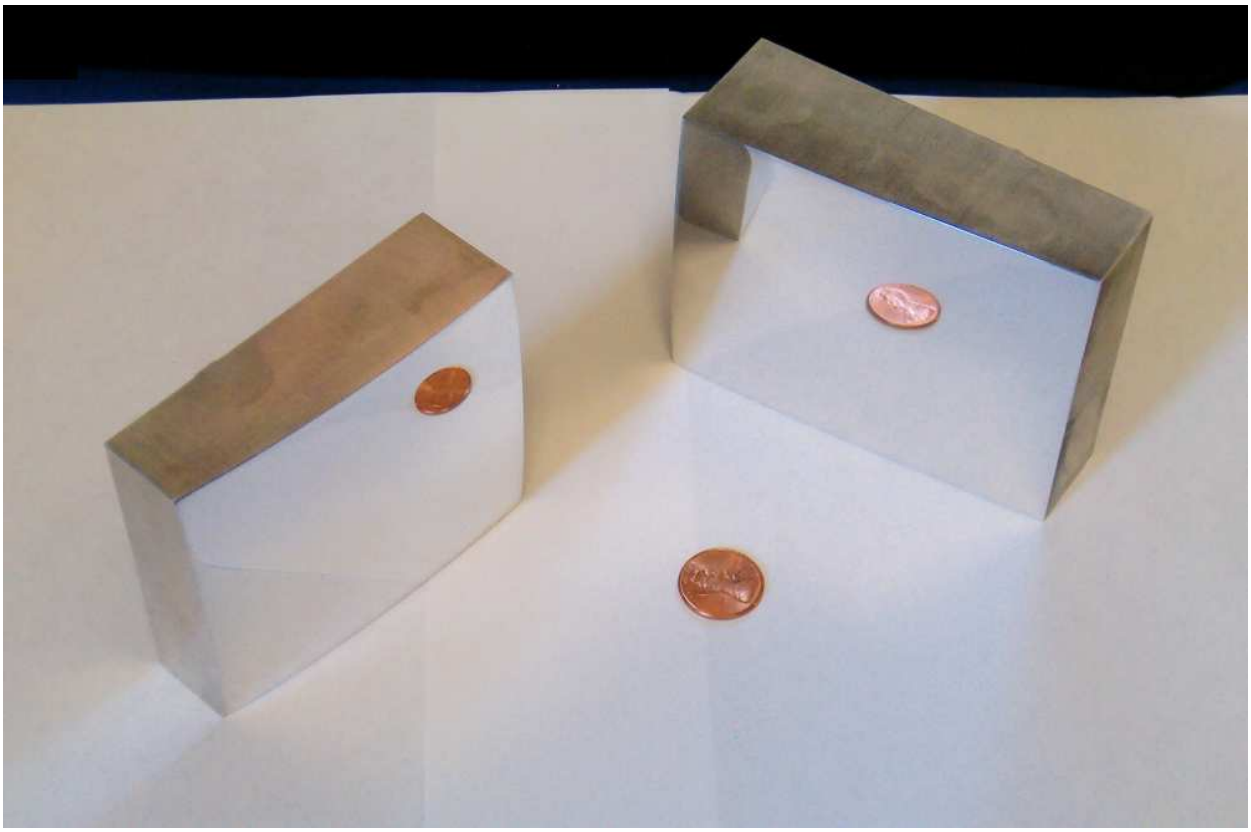

Figure 3-13. Two practice mirrors, Imagers 2 and 3, produced by the UF Physics and Astronomy Machine Shop.

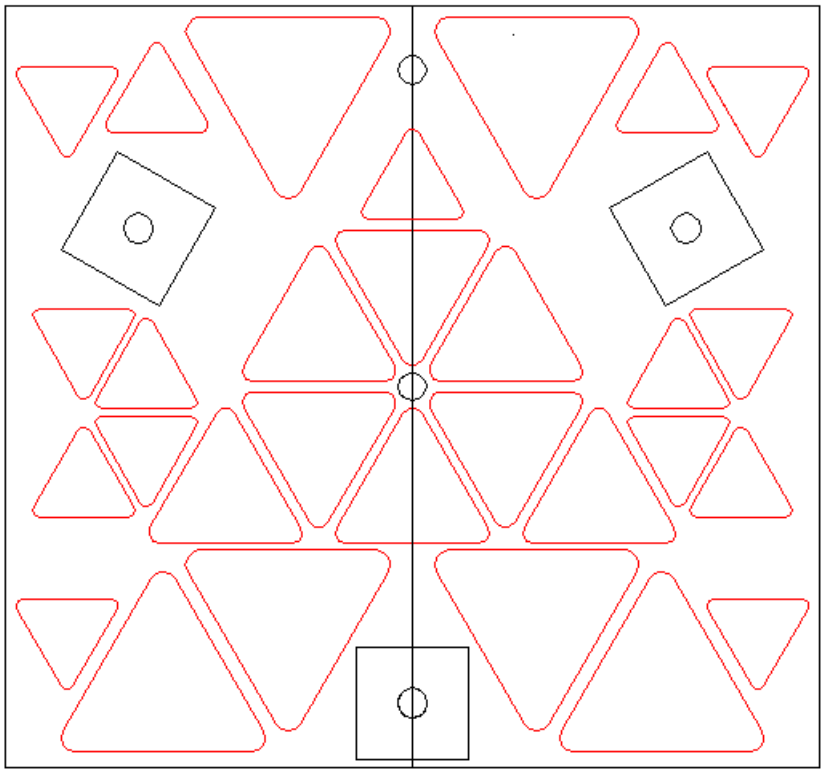

Figure 3-14. A typical pattern used to lightweight Fold 1, Fold 2, Collimator 1, Imager 1, and Imager 4.

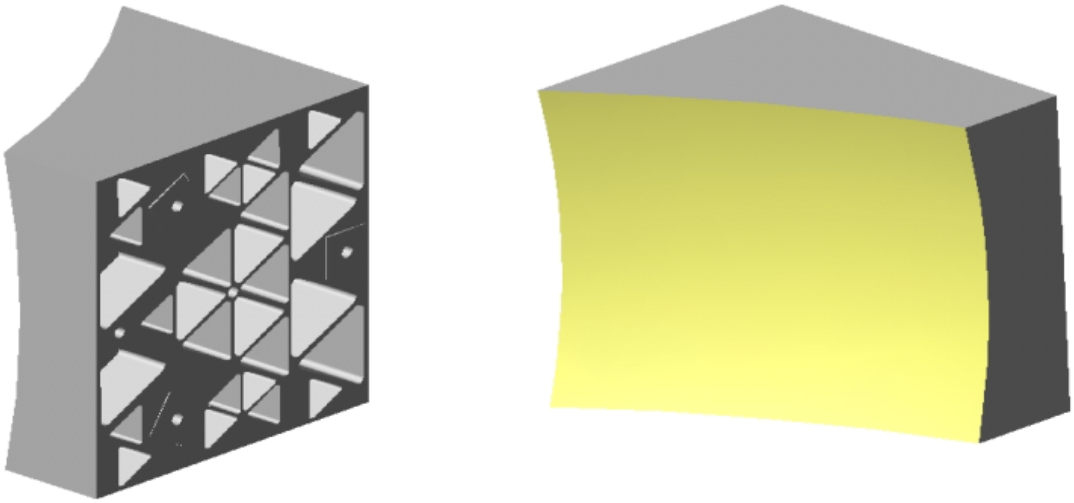

Figure 3-15. Two different views of a lightweight solid model of Imager 4. The image to the left shows the back surface and the image on the right shows the front.

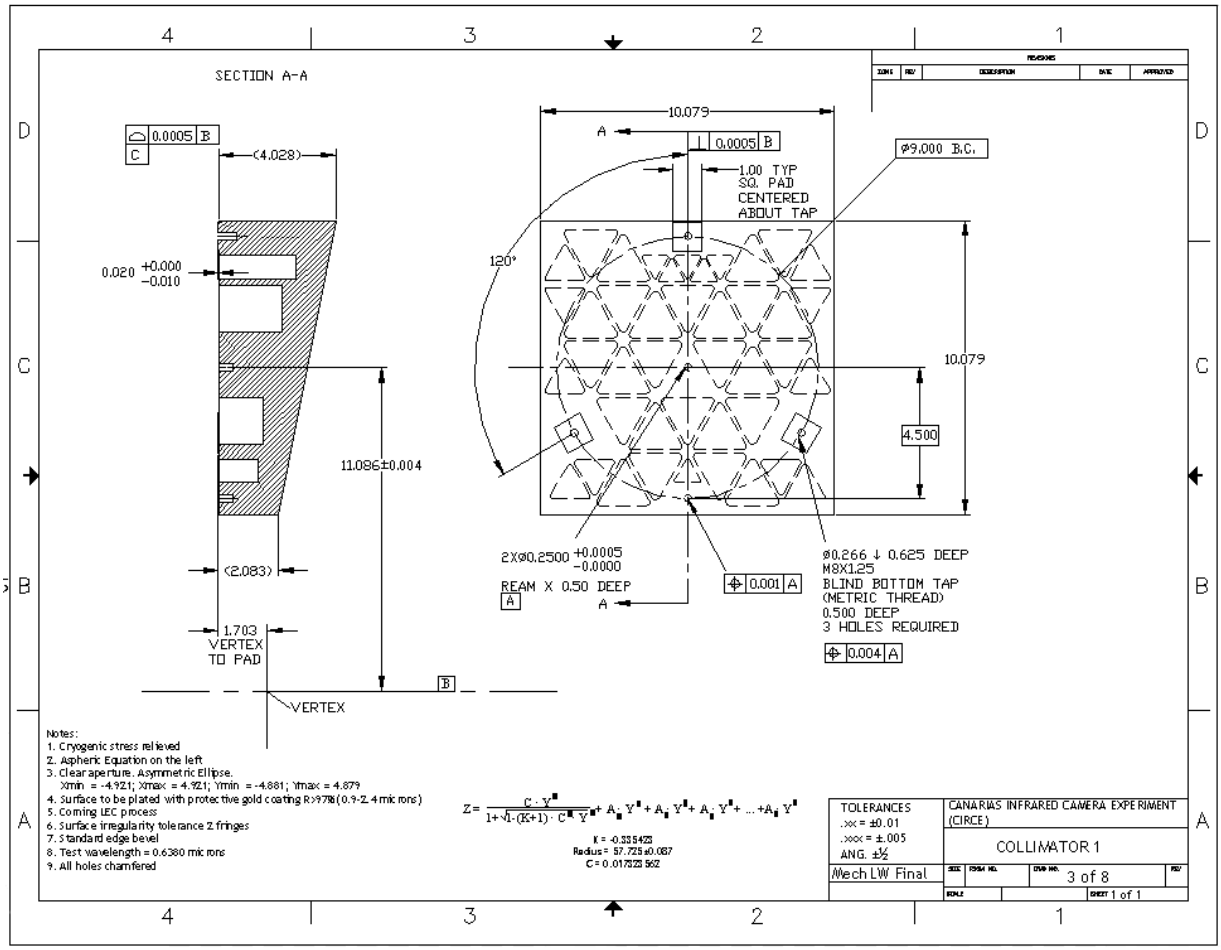

Figure 3-16. The final mechanical drawing of the blank for Collimator 1. The mechanical drawings for all eight CIRCE mirrors are currently at the UF Physics and Astronomy Machine Shop awaiting manufacture.

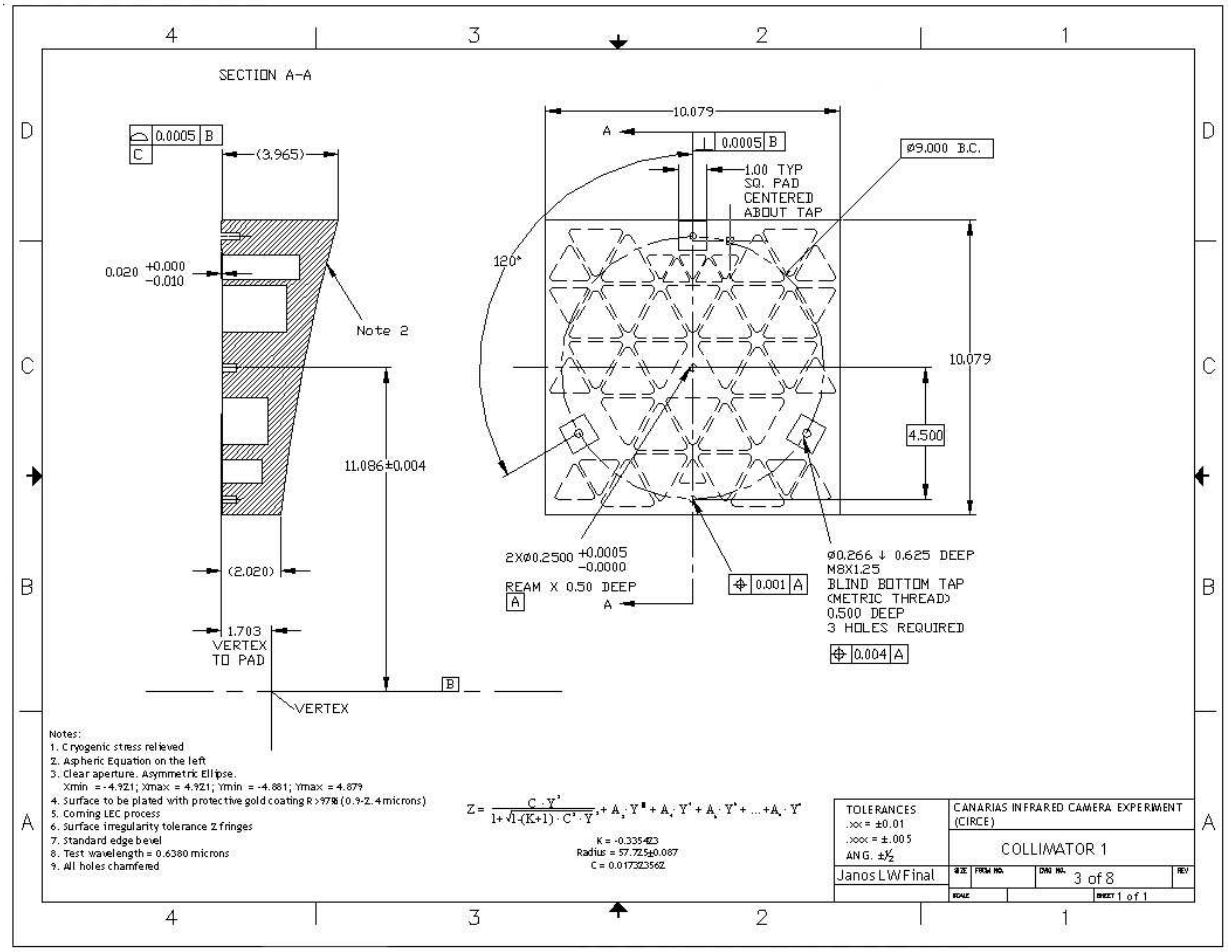

Figure 3-17. The final mechanical drawing of Collimator 1 sent to Janos Technology. I completed similar drawings for all eight CIRCE mirrors

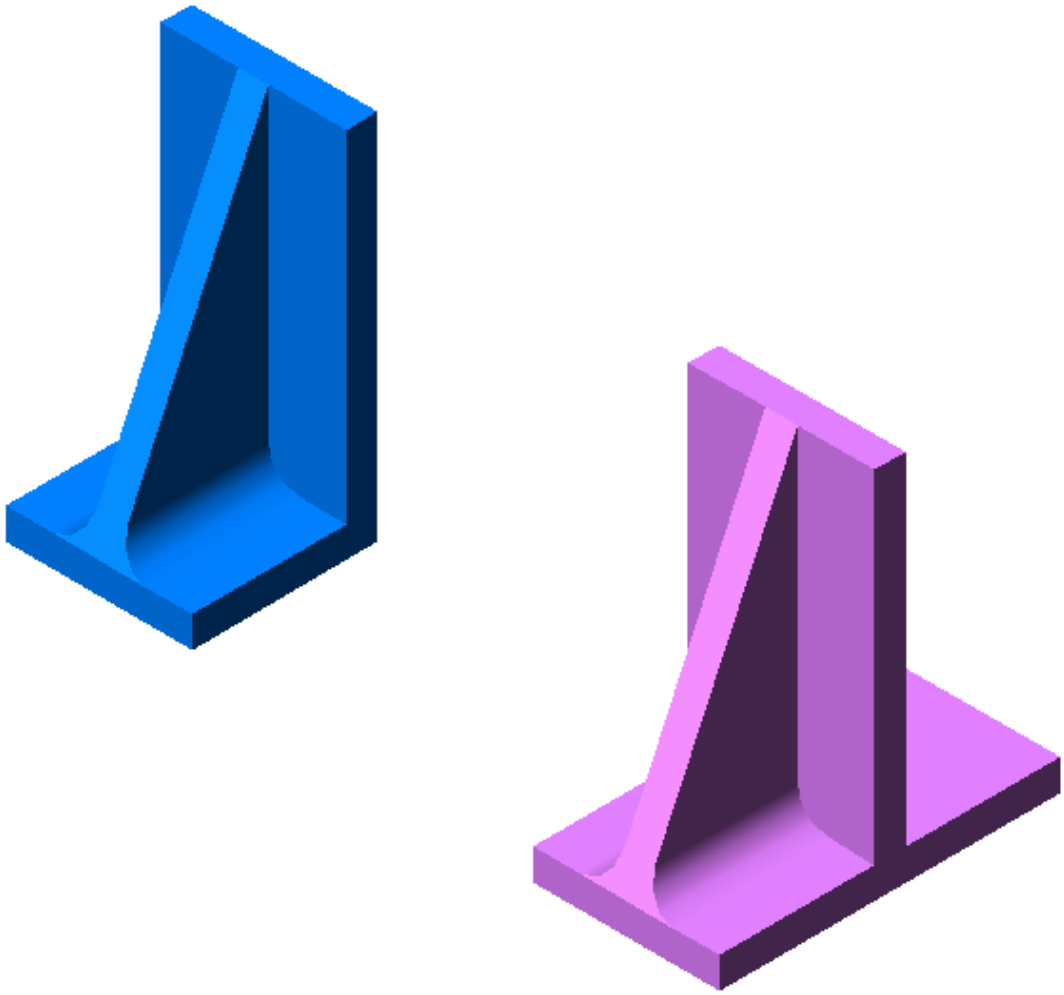

Figure 3-18. Examples of an L and T bracket. These were used for the smaller CIRCE optics

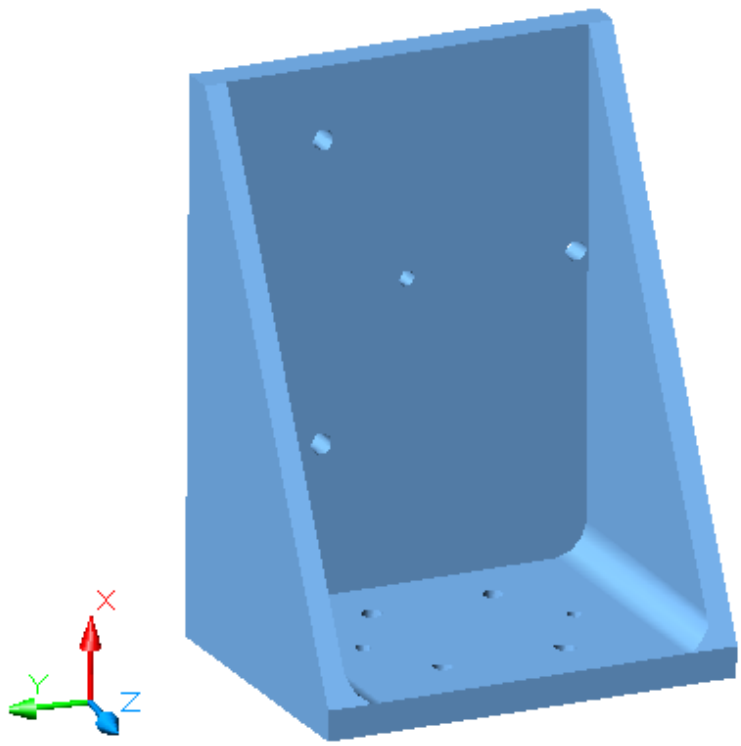

Figure 3-19. This figure shows a redesigned bracket for Imager 4. We removed the central back gusset and inserted two thinner gussets at the side. This added stability while decreasing weight.

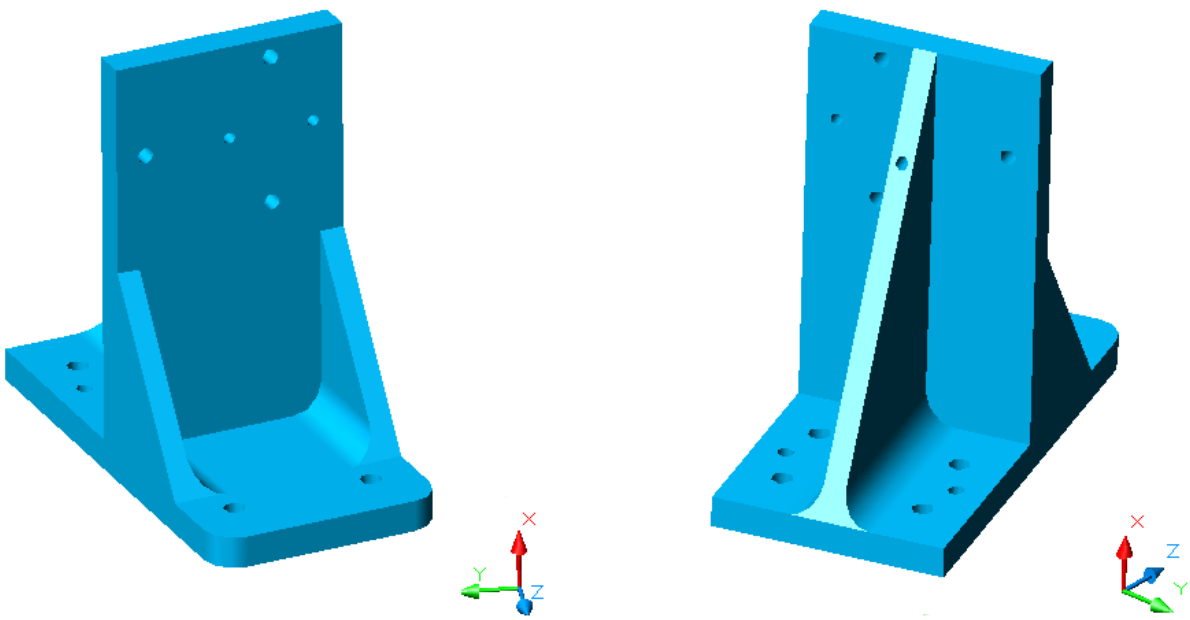

Figure 3-20. A front and back view of the bracket for Imager 2

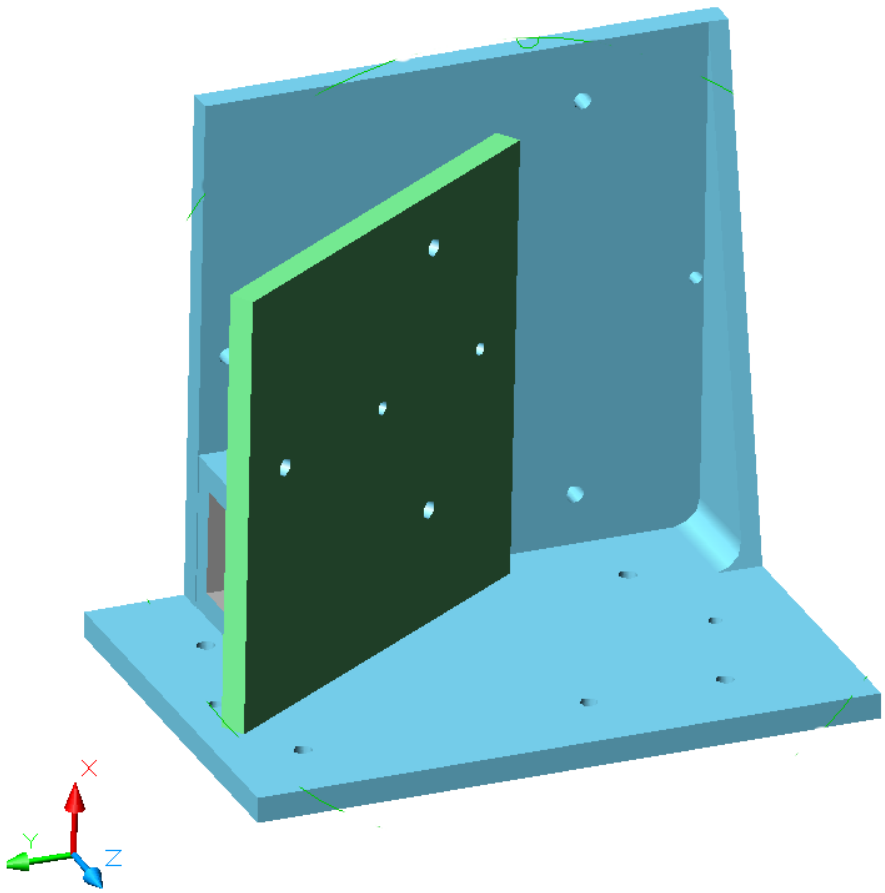

Figure 3-21. The compound bracket that supports Imager 4 and Collimator 1

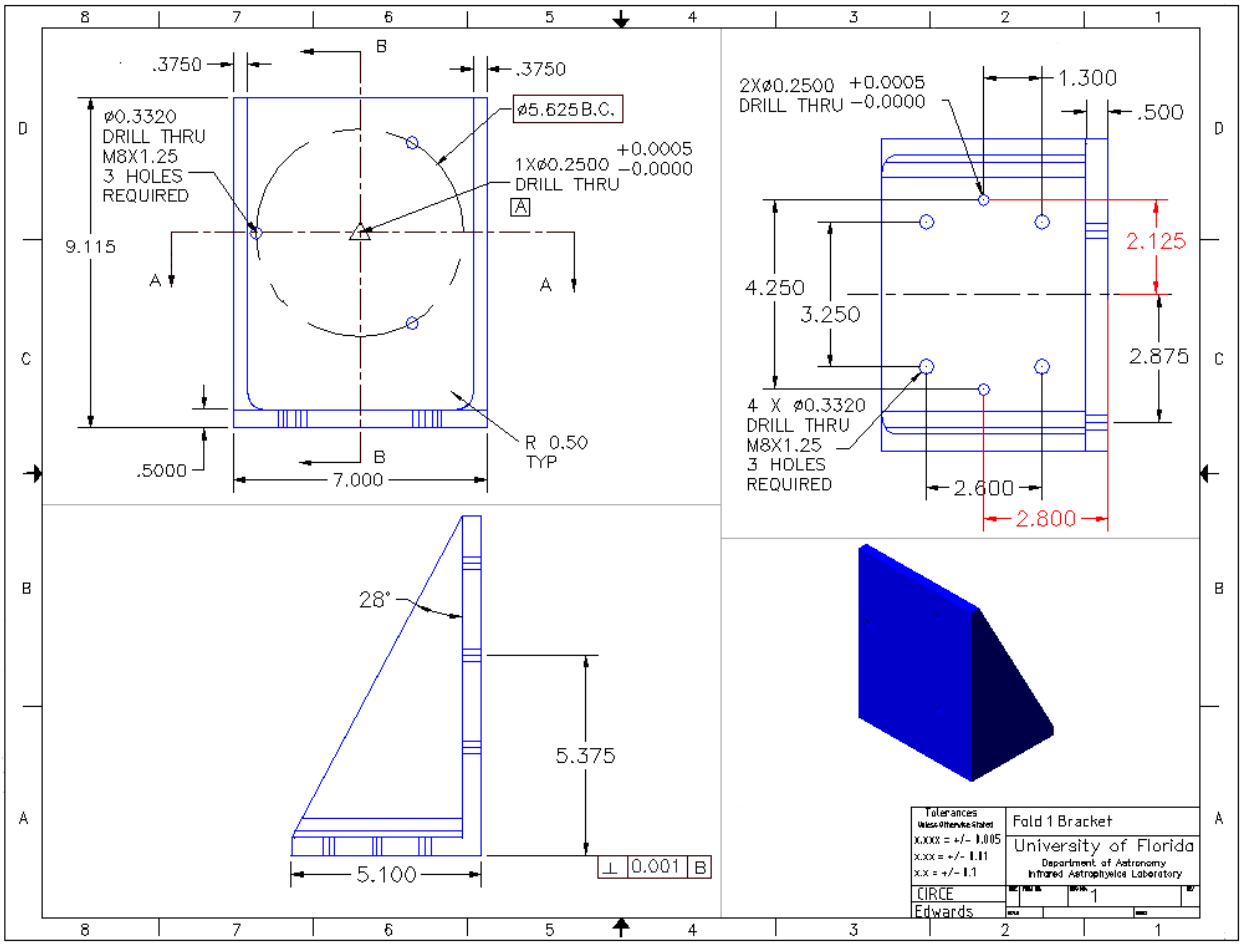

Figure 3-22. The final mechanical drawings for the bracket for Fold Mirror 1.

Figure 3-23. Two of CIRCE's brackets with their "practice" mirrors.

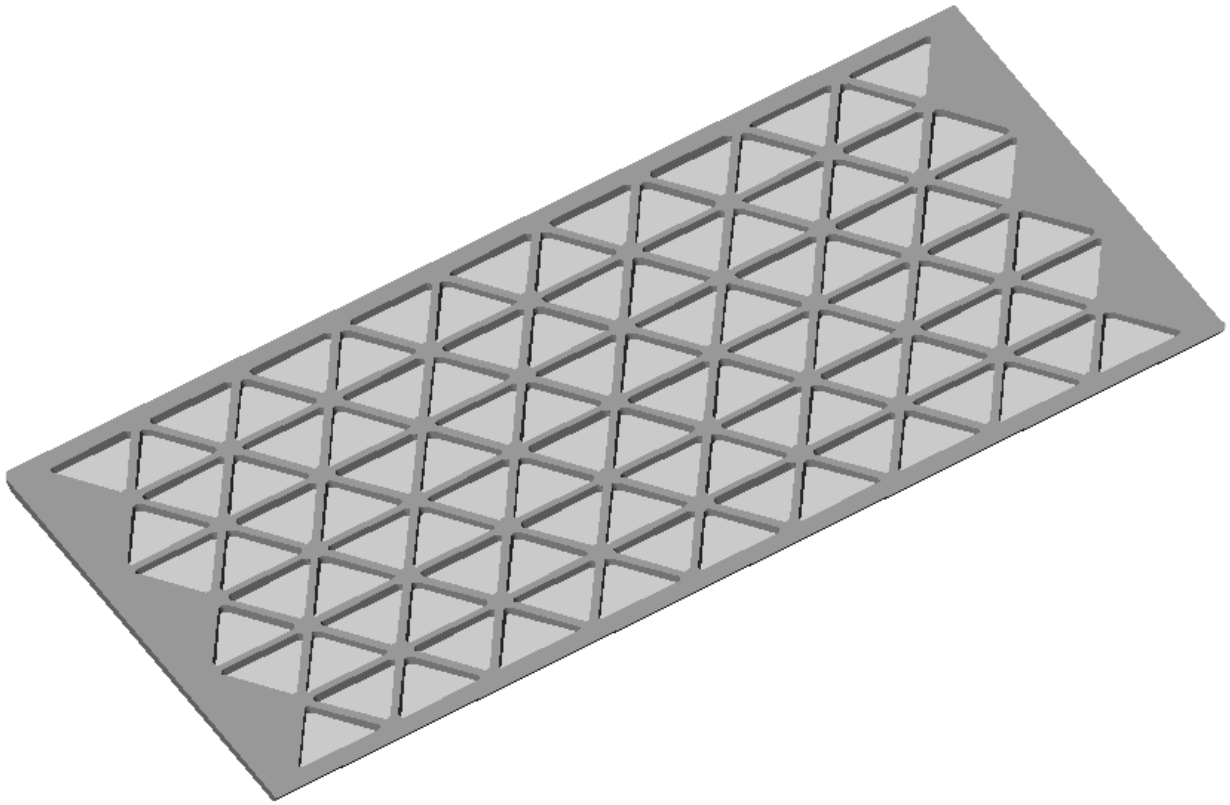

Figure 3-24. A preliminary design of the CIRCE lightweight bench. The concept for the CIRCE bench was later modified by Miguel Charcos to allow the UF Physics and Astronomy Machine Shop to manufacture it in-house (see Chapter 8)

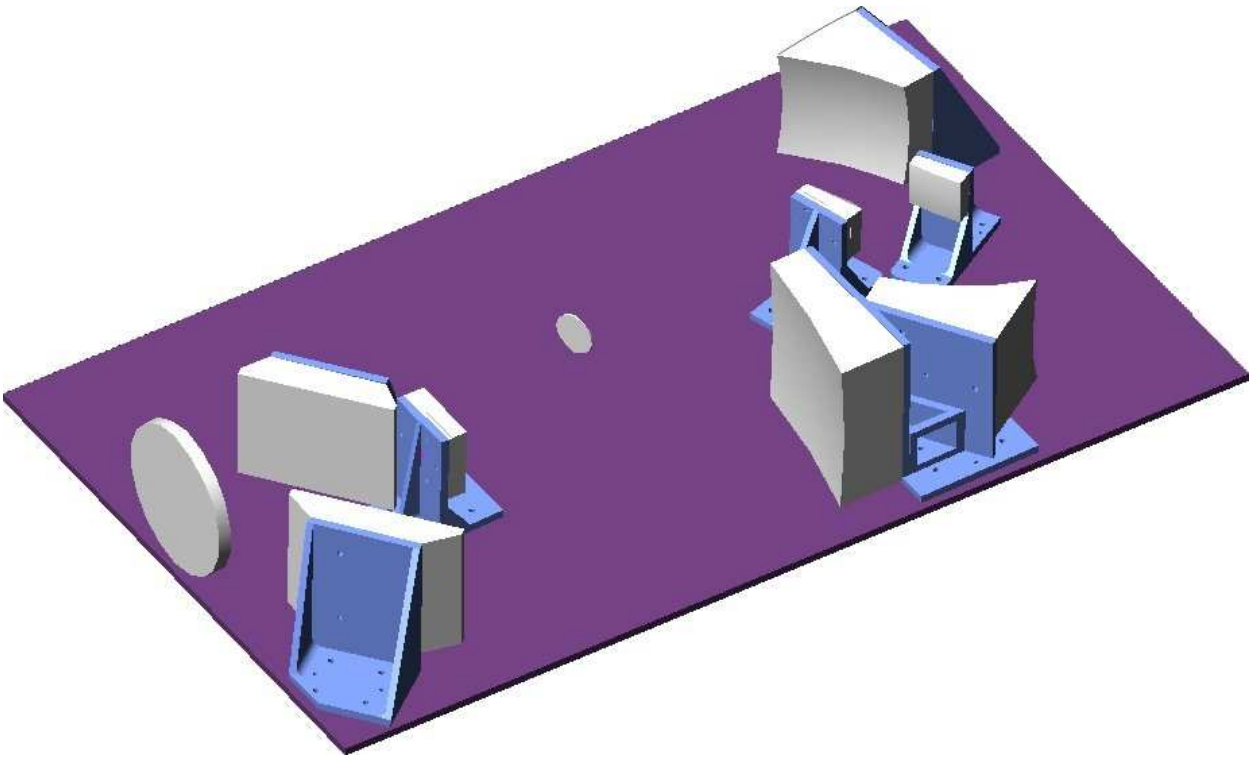

Figure 3-25. A solid model of CIRCE's optical bench, brackets, and mirrors.

CHAPTER 4
CRYO-MECHANICAL DESIGN OF THE PUPIL BOX MECHANISM

4.1 Introduction to Cryo-Mechanisms

In Chapter 3, I discussed the mechanical design of CIRCE's mirrors and brackets. Once manufactured, bolted into place, and sealed inside the CIRCE dewar, these components become static; they do not move with respect to the optical bench. In this chapter, I describe the design of CIRCE's cryo-mechanisms – moving parts and machines that operate in a cryogenic environment. In particular, I focus on my design of the pupil box assembly. Positioned directly aft of the collimators (see §2.1) at the location of the exit pupil, the "pupil" box contains rotating Lyot, filter, and grism wheels. These wheels hold a variety of optical elements including [1] grisms for spectroscopy, [2] a Wollaston prism for polarimetry, [3] narrow- and broad- band filters for imaging, and [4] masks for engineering tests. Ultimately the goal of the pupil box assembly is to allow observers to switch seamlessly between CIRCE modes without warming up the instrument and manually changing elements.

The pupil box itself, sometimes called a "filter" or "filter wheel" box is a enclosure made of 6061-T6 aluminum that houses the rotating Lyot, grism, and filter wheels, as well as the switches and motors used to control them (see Figure 4-1 for an example of a pupil box). The back of the box is covered by a lid, which protects the filters and grisms inside from stray and scattered light. To allow collimated light into and out of the box, the front and back faces have "pass-through" holes that are aligned with the optical axis. Another larger hole on the front of the box allows access to the interior mechanisms without removing the back cover.

Each filter, grism, or lyot wheel in the pupil box is a gear. Every gear has multiple circular holes for grisms, filters, and masks at evenly-spaced angles and a single central hole for an axle (see Figure 4-2). This axle runs through all of the wheels and is attached to the front and back of the pupil box. Motors, modified to operate in the extreme

cold, advance the filter, lyot, and grism wheels. The wheels turn to the locations for the specified filter, grism, or prism required, aligning with the "pass-through" holes in the front and back of the CIRCE pupil box. This allows light from Collimator 2 to propagate into the box, through the optical element, and out of the box, where it will continue on to Imager 1, as shown in Figure 4-3.

One of the key ideas for CIRCE was to design and manufacture the cryo-mechanisms, dewar, and electronics using drawings and/or parts from previous UF instruments. The obvious advantage of this plan was that we could save time by modifying already existing designs or assemblies instead of starting from scratch. The CIRCE pupil box benefited from this philosophy; the final design of the assembly is a hybrid of the Flamingos 1 and 2 (Elston et al. 2003; Eikenberry et al. 2006b) pupil boxes. While the size of the wheels, number of teeth on the gears, and other crucial dimensions changed to accommodate the differences between the optical designs, the basic structure of the CIRCE box and internal mechanisms is very similar to its predecessors.

4.2 Optical Elements in the Pupil Box

The first step in designing the pupil box is to determine the number and type of optics that it will hold. To meet the needs of the GTC community, we will include the following nine filters in CIRCE: J, H, and K_s broad-band filters, JH and HK filters for use with the grisms, 2.16 μm Brγ and 2.06 μm HeI narrow-band filters, and 2.14 μm and 2.03 μm narrow-band K_{cont} filters. We will also place a Wollaston prism for polarimetry in one of the filter wheels. While the Wollaston prisms are traditionally housed in the grism wheel, CIRCE is also equipped for spectropolarimetry. Since this requires that light pass first through the prism and then a grism, the Wollaston prism must be fore of the grism wheel.

The CIRCE grism wheel will have two grisms, both of which share the grating ruling masters custom-built for Flamingos-2. The Lyot wheel will contain several masks, which are stiff pieces of material machined with hole patterns, which we will use to test for

distortion, focus, and image quality during integration and engineering runs. The Lyot wheel will also house the pupil stop: a 55 mm diameter hole cut into a mask. This will act as CIRCE's cold stop (see §2.1).

4.3 Design of the Pupil Box Components

4.3.1 The Filter, Grism, and Lyot Cartridges

The first step towards completing our pupil mechanism was determining the size of the filters, masks, and grisms in our wheels. ORA designed CIRCE with a 55 mm diameter collimated beam at the exit pupil (see §2.1). Accounting for the extra space necessary to mount the optics into the wheels and still have a 55 mm clear aperture, we planned to purchase $\sim$ 60 mm diameter filters. However, NIR filters are not off-the-shelf items; specially ordered these optics can cost $>$ \$10,000 each and take months to deliver. Fortunately, Research Electro-Optics (REO), an optics manufacturer, had just completed producing filters for a large order and had an extra set of J, H, and K_s filters with a 70 mm diameter. Since these cost less than half the price of specially ordered filters, were immediately available, and would not negatively impact the CIRCE image quality, we purchased them. I show a picture of one of the three broadband filters currently in-hand at UF in Figure 4-4. Since the grism and Lyot masks must be custom designed with no option for a serendipitous purchase, the 70 mm filters set the scale for the remaining optical elements.

Once we the knew the size of the CIRCE filters, grisms, etc., I designed a method to mount and secure each element into its respective wheel. I chose the solution utilized by Flamingos-1: filter cartridges. Using the 70 mm filter diameter as a guide, I scaled up existing Flamingos-1 designs and, using AutoCAD, created a solid model of a cartridge. I show an example of both my preliminary and final design in Figure 4-5. The bottom of the cartridge has a large clear aperture that allows light to pass through to the optical element. The filter rests on a small lip that surrounds the hole. The lid of the cartridge is similarly designed. Tightly fitting, the rim of the lid presses the filter into the cartridge.

A soft compressible material is positioned between the metal rims of the cartridge and the glass optic; this prevents scratching and also helps to insure that the element does not shift inside the cartridge.

Each optic will have its own cartridge, which will slide into large holes machined directly into the Lyot, filter, or grism wheels. My preliminary designs of the cartridge included a wide rim that bolted to the wheel (see Figure 4-5A). After consulting with the IAG, I opted for the the semi-circular tabs shown in Figure 4-5B. These took up less space but were as functional as the bulkier rims.

4.3.2 The Filter, Grism, and Lyot Wheels

Before I began the design of the filter, grism, and Lyot gears, I assessed the space available on the optical bench for the pupil box assembly. In Figure 4-3, I show the approximate location of the pupil box in the CIRCE optical layout. The box is very close to light rays passing between the first and second collimators. To avoid blocking the rays, I needed to carefully limit the size of the box and therefore the size of the wheels. With the size of the filters, grisms, and prisms set, our only available option was to decrease the number of holes in each wheel.

This solution is not without issues; fewer elements per wheel result in more wheels, driving up the cost and complexity of the pupil box. Using the optical layout and the size of the filters as a guide, I found that the best compromise is a $\sim$ 9.5 inch diameter wheel with five holes. Four of the spaces hold optical elements while one hole remains empty to allow light to pass through to other wheels. After considering the number of filters, grisms, prisms, and masks discussed in §4.2, I decided that CIRCE would contain five wheels: 3 "filter" wheels, 1 Lyot wheel, and 1 Grism wheel. More information about these five wheels and the filters they will house appears in §4.4.

Using a wheel diameter of 9.375 inches, large enough for five of the cartridges designed in §4.3.1 and less than the 9.5 inch limit calculated from the optical design, I made a solid model of a filter wheel. I included a large central hole to accommodate a

filter gear hub and bearing race. I present the solid model of the filter wheel in Figure 4-6 and the 2-D drawings for manufacturing purposes in Figure 4-7.

4.3.3 Wheel Hubs and Bearing Races

In both Flamingos-1 and Flamingos-2, the filter and grism wheels slide onto a central axle inside the pupil box. "Belleville" washers at the back of the box act like a spring to compress all five wheels until they are almost touching (see Figure 4-8) ensuring that they do not wobble or slide up and down the axle as they rotate. However, this close contact presents a problem. As a motor turns one of the wheels, friction causes the neighboring wheels to turn as well. To prevent this, small sapphire balls are placed between the wheels as spacers. Mounted in a bearing race, circular grooves machined into the aluminum surface of the wheels, the low friction balls are free to rotate and revolve. When a cryogenic motor turns one wheel, the rotational energy that would normally be imparted to the neighboring wheels is instead dissipated by the motion of the balls in the bearing race.

I used these same concepts for the CIRCE pupil box assembly. I designed a filter wheel hub, shown in Figure 4-9, with a bearing race machined into its front and back surfaces. This hub bolts directly into the center of the filter wheel, as shown in Figure 4-10. The hole in the center of the hub will accommodate the 0.25 inch steel axle.

4.3.4 Filter, Grism, and Lyot Gears

Each of the five wheels in the CIRCE pupil box is a spur gear with hundreds of teeth at its edge. These teeth mesh with teeth on one of five smaller "drive" gears attached via an axle to a cryogenic stepper motor (see Figure 4-11). These electric motors are capable of very fine motions called "steps", each of which advance the axle and drive gear 3.6 degrees. Thus a full revolution of the drive wheel requires 100 steps. As the teeth of each drive gear are meshed with the teeth of a Lyot, grism, or filter wheel, "stepping" a motor advances one of the larger geared wheels, moving filters, grisms, and prisms into and out of the instrument's optical path.

The first step in designing the Lyot, filter, and grism wheels was to determine the number of teeth necessary for each gear. On the advice of senior engineer Jeff Julian, we used a gear pitch of 48. A gear pitch is the number of teeth per diameter of the gear. Using this specification, I calculated that the 9.375 inch wheels in our pupil box would each have 450 teeth. I then chose a 0.50 inch diameter stock precision gear with the same pitch and 24 teeth. This produced a gear ratio of 18.75.

Using AutoCAD, I created a solid model of a filter gear which I show in Figure 4-12. Since manufacturers often produce a hole in the wheel "blank" to hold it steady as they create the precision teeth, I included a central bore hole in the exact location of the filter wheel hub. I sent my solid model and completed 2-D drawings to Ascent Gears. They manufactured the blanks and sent them back to UF. I checked the finished product, measuring the diameter and number of teeth. I show a picture of a finished gear in Figure 4-13.

4.3.5 Pupil Box and Motor Mounts

After designing the interior components of the pupil box mechanism, I began my work on the pupil box itself– the enclosure that would house the wheels, drive gears, motors, and axles. In Figure 4-14 and Figure 4-15, I show my final two- and three-dimensional design of the pupil box. The box has an arch-shaped main body with a 9.75 inch diameter, large enough to accommodate the 9.375 inch CIRCE filter wheels with a 0.1875 inch gap on either side. The walls of the box are also 0.1875. This was thick enough to provide stiffness for the box and thin enough to avoid adding unneccesary weight. The arch contains three holes: one in the center of the arch for a pupil box hub (similar in design to the wheel hubs), one left of center for light from the collimator to pass through to the filters, grisms, and prisms, and one at the top of the box for quick access to interior without removing the lid.

Connected to the arch-shaped main body is a rectangular protrusion designed especially for the motor mounts. I utilized dimensions from existing Flamingos-1

two-dimensional drawings of the motor mounts to create solid models in AutoCAD; I show these models in Figure 4-16. CIRCE will use modified Portescap stepper motors, the same motors used for Flamingos-1. The position of the motors and motor mounts is entirely dependent on the size of the gears; each 0.50 drive gear must be near enough to its corresponding filter, grism, or Lyot wheels to ensure the teeth of the gears mesh. I carefully positioned the holes in the body of the pupil box for the motor mounts to ensure the drive gears were 0.25 inches from the filter, grism, and lyot gears.

Since the rectangular protrusion on the pupil box was not large enough for all the motor mounts to bolt to the front of the box without overlapping each other, I planned to place two of the mounts on the back lid. I mirrored the motor mounting holes from the front surface onto the lid to ensure the two attached drive gears would also be in the correct location with respect to the larger gears. Figure 4-17 shows the filter box with the front three motor mounts attached.

Finally, I created a 0.25 inch thick rectangular base for the pupil box that will bolt onto a mounting plate on the optical bench. The base contained holes for 13 bolts and 2 pins. The bolts ensured that the box would not move with respect to the optical bench once it was mounted in place. The pins, as with the optics, guaranteed precision alignment. This was important, as incorrect placement of optical elements inside the box could result in obscuration of the beam, reflections from the filters, and poor image quality.

4.4 Integration of the Pupil Box Mechanism Designs

After completing the filter, grism, and Lyot wheels, I identified which filters, grisms, prisms, and masks would occupy which wheels. I also determined the order of the wheels within the box. I included several blank spaces for four additional narrow-band filters requested by scientists within the GTC community.

The first wheel contains the narrow-band filters, 2.16 μm Brγ and 2.06 μm HeI narrow-band filters, and 2.14 μm and 2.03 μm narrow-band K_{cont} filters. This wheel is

mounted "backwards" so that filter cartridges are easily accessible through the large hole in the front of the pupil box. I placed narrow-band filters, the most likely to be exchanged over CIRCE's lifetime, in this wheel since it is the most accessible.

The second wheel contains the J, H, and K_s broad-band filters. It also contains the "dark" filter, which observers can use for taking dark exposures. It can also be placed in position at the end of the night to "home" the instrument. Since this wheel is also inaccessible without opening the pupil box, I filled it with filters that should not need replacing or switching.

The third wheel is the Lyot wheel. It is inaccessible without opening the pupil box. This wheel contains a cold stop, a Hartmann mask used for testing the instruments focus, the Wollaston prism for polarimetry, and a blank space for a narrow-band filter. The fourth wheel contains the JH and HK filters for spectroscopy. It has two free spaces to accept two of the additional narrow-band filters proposed by GTC collaborators.

The fifth and last wheel in the box is the grism wheel; grisms are thick (3 - 5 inches) and are traditionally placed at the back of the pupil box where they will not interfere with the other optics as the wheels turn. Since I wanted the ability to replace filter cartridges in the wheel in front of the grisms, for example to add a narrow-band filter, without taking apart the pupil box assembly, for example to add a narrow-band filter, I modified the wheel; I removed the space reserved for the "blank" and replaced it with a hole large enough to pass a filter cartridge through. I show the new grism wheel in Figure 4-18.

In Figure 4-19, I present the completed CIRCE pupil box assembly with motor mounts, filter, grism, and Lyot wheels, cartridges, and the pupil box.

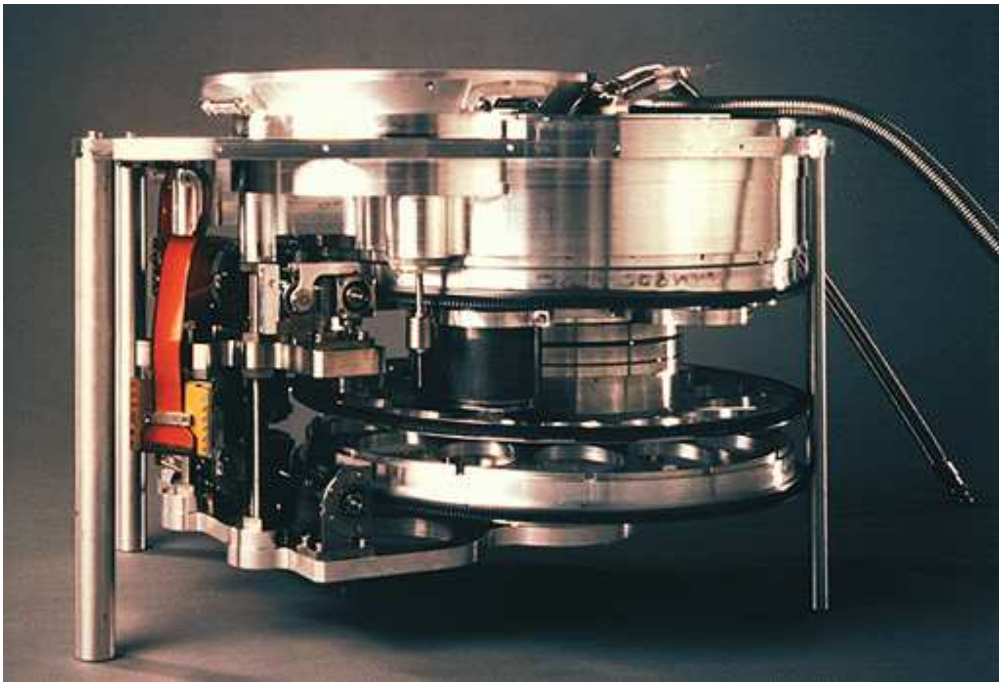

Figure 4-1. Example of a filter wheel assembly

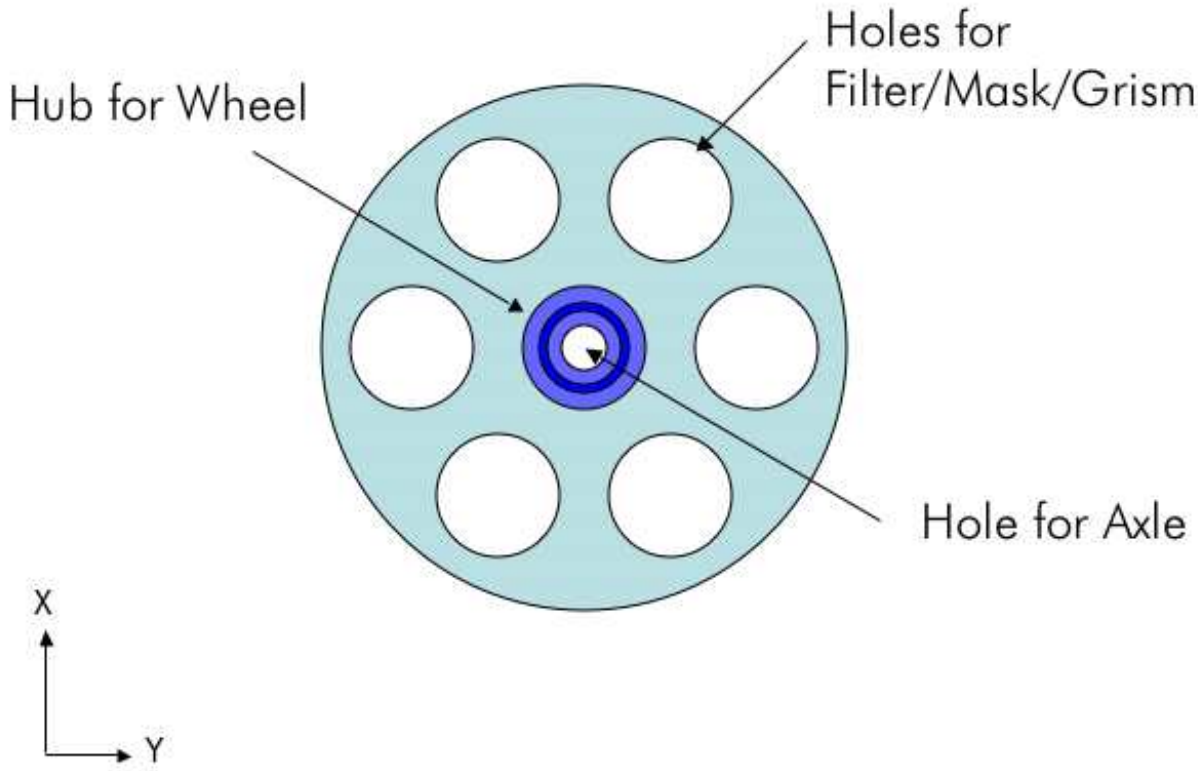

Figure 4-2. A rough sketch of a filter wheel with 5 holes for filters, grisms, prisms, or masks, a filter wheel hub, and a hole for an axle.

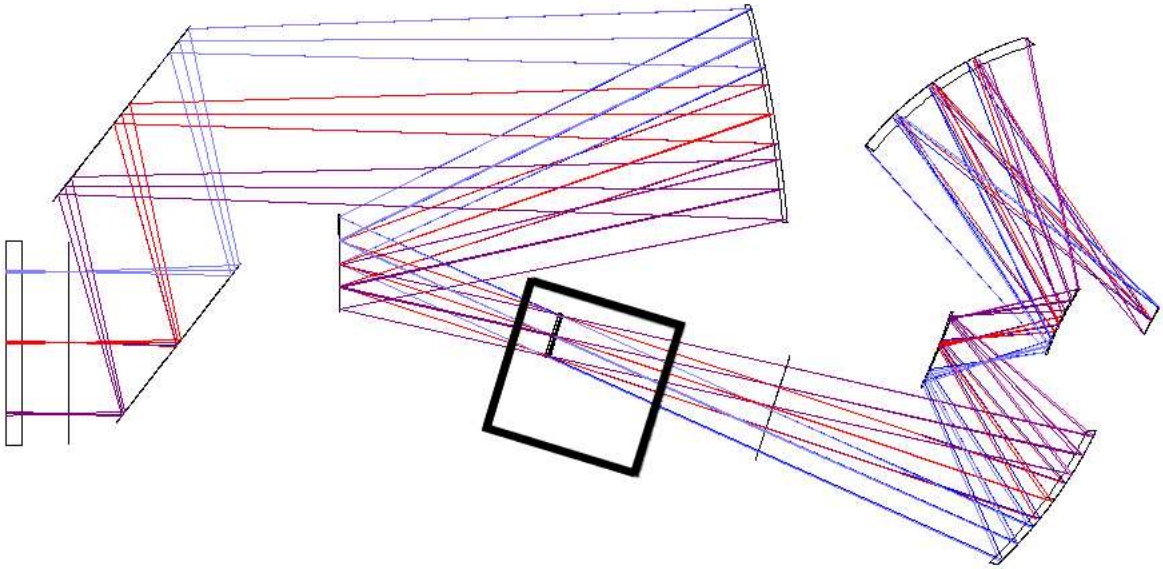

Figure 4-3. The CIRCE optical layout with the sketch of a pupil box included. The top of the pupil box is very close to rays traveling between the first and second collimator. This space constraints were an important consideration when designing the wheels and box.

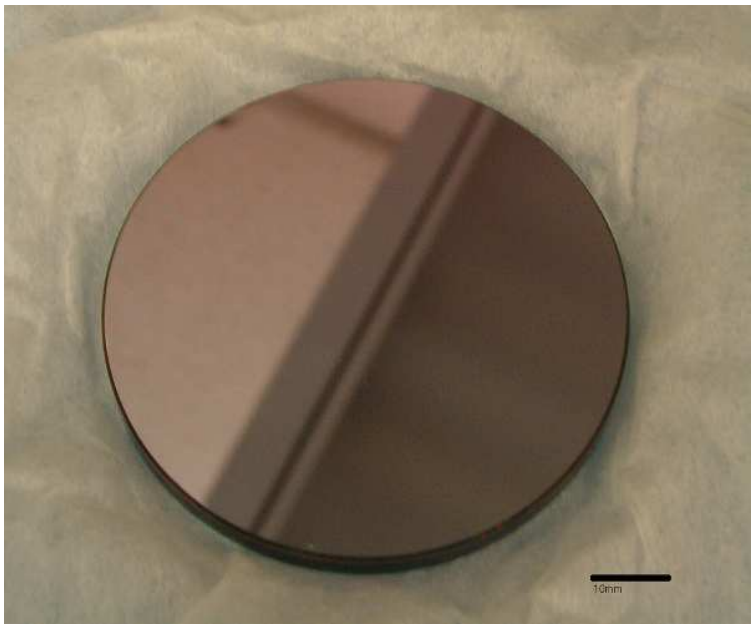

Figure 4-4. The CIRCE H-band filter as delivered from REO.

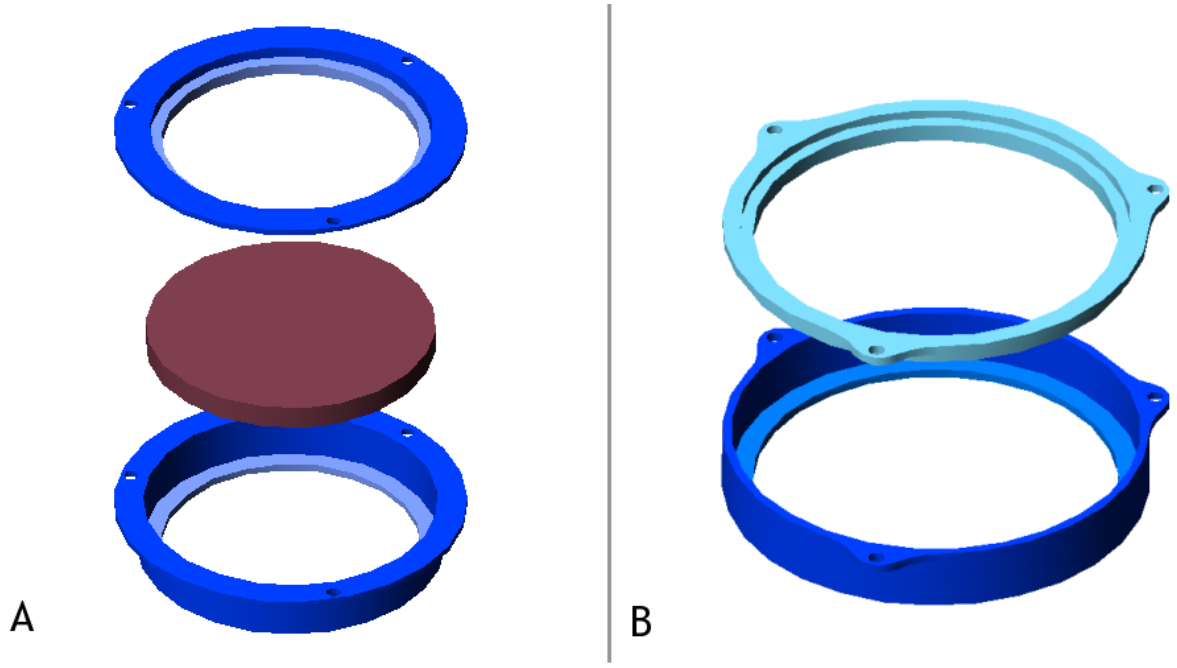

Figure 4-5. These are our preliminary and final designs of a filter cartridge. A) is slightly heavier with a bulky rim at the top of the cartridge B) is streamlined and lighter with tabs for bolts.

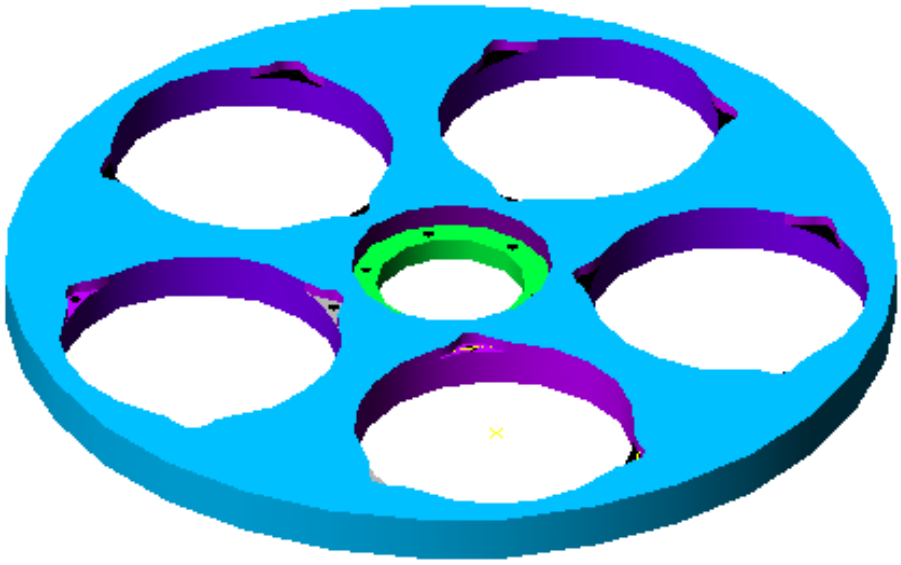

Figure 4-6. This is a solid model of a CIRCE pupil wheel. Note the five large spaces for an optical element and a central space for a filter wheel hub.

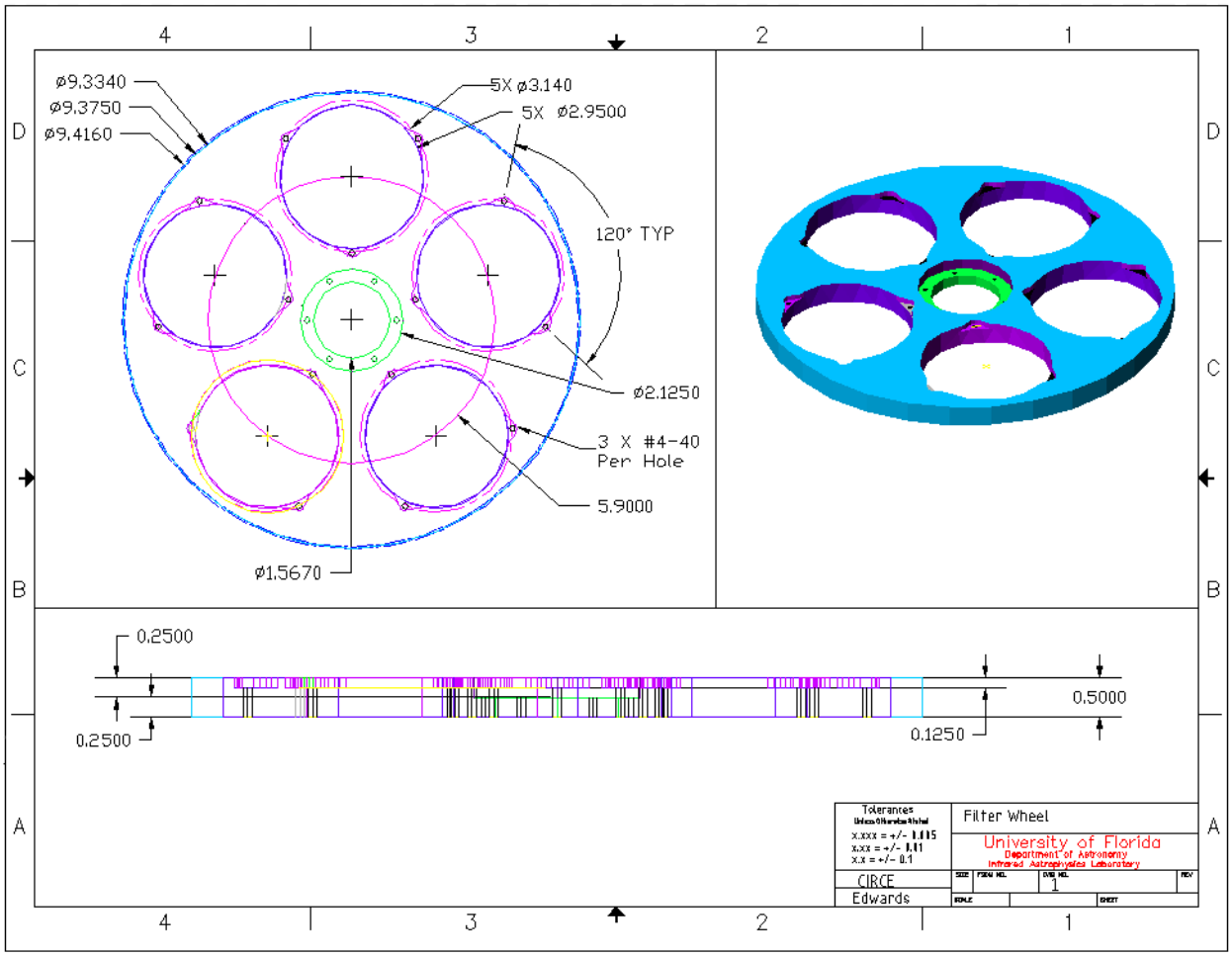

Figure 4-7. This is an example of a mechanical drawing for a CIRCE pupil wheel. The details in the pupil wheel will be manufactured in the Physics and Astronomy Machine Shop at UF.

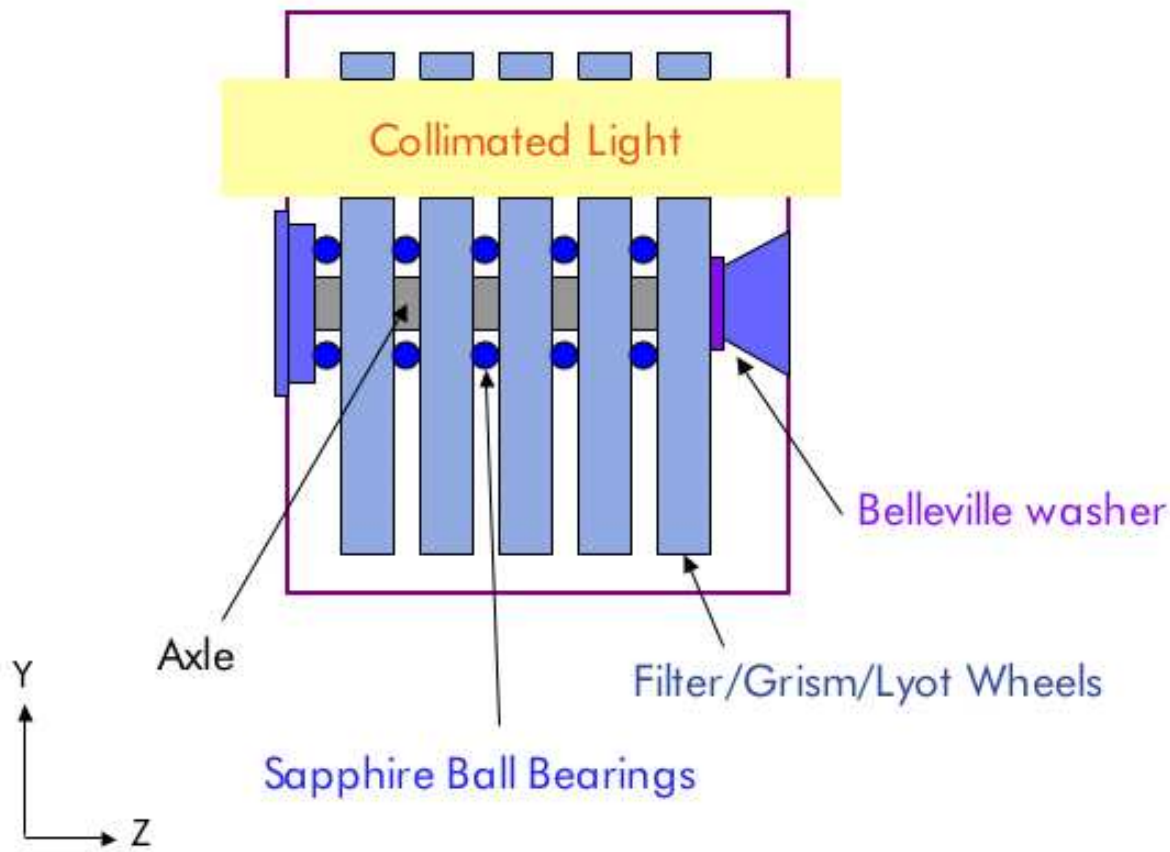

Figure 4-8. This drawing shows inside of a hypothetical pupil wheel box. The pupil wheels are mounted on an axle and separated by sapphire ball bearings. A Belleville washer, a compression washer that acts like a spring, holds the wheels in tension.

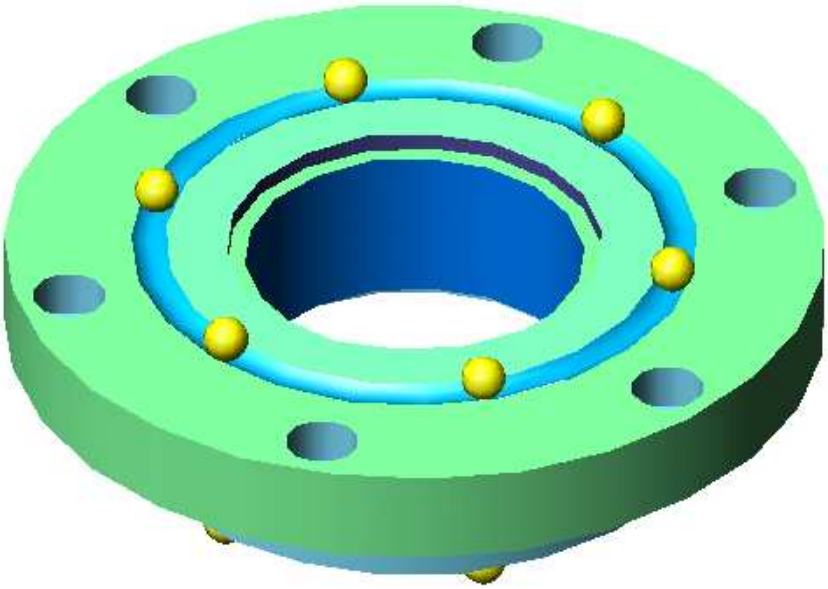

Figure 4-9. A solid model of a pupil wheel hub. This hub fits into the central hole of a pupil wheel. It has two main features - a tightly toleranced hole for the pupil box axle and a bearing race. Also pictured are the sapphire ball bearings.

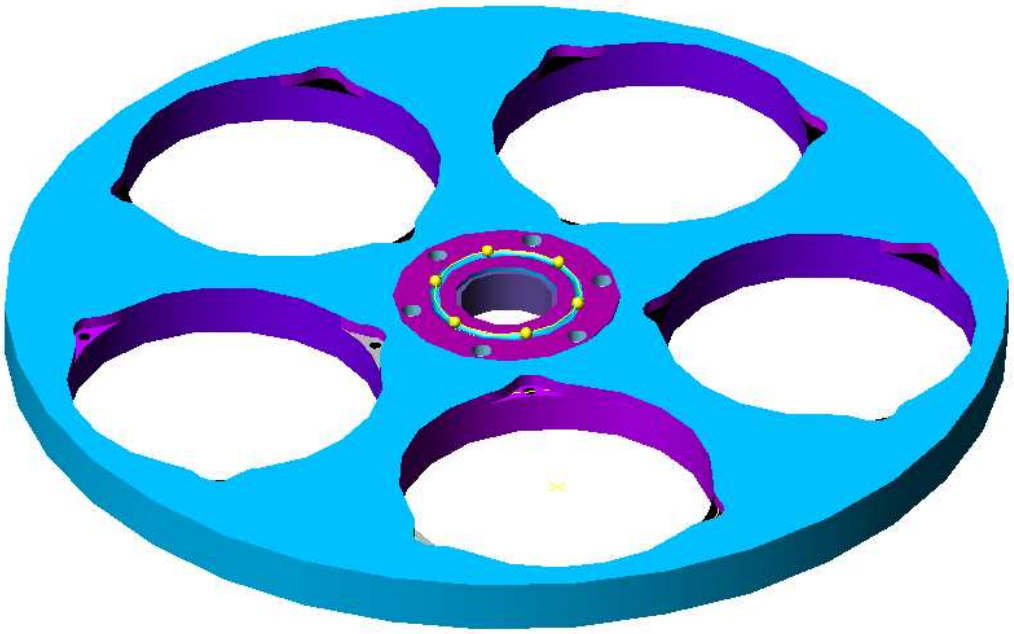

Figure 4-10. Solid model of a filter wheel with its wheel hub.

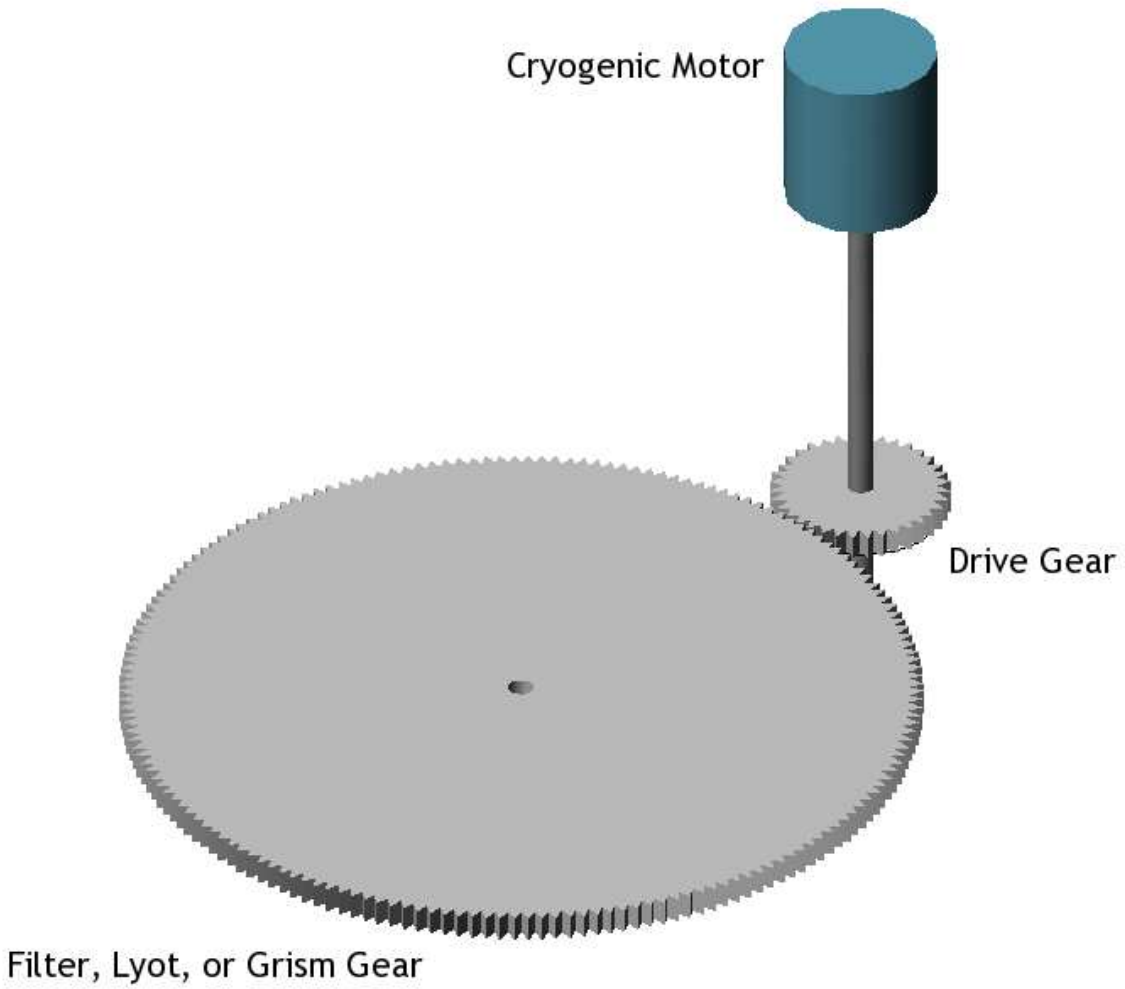

Figure 4-11. A simplistic model of the gears inside a pupil box. The smaller "drive" gear is affixed to an axle protruding from a cryogenic stepper motor. As the motor "steps", the drive gear revolves, turning the larger filter, grism, or Lyot gear.

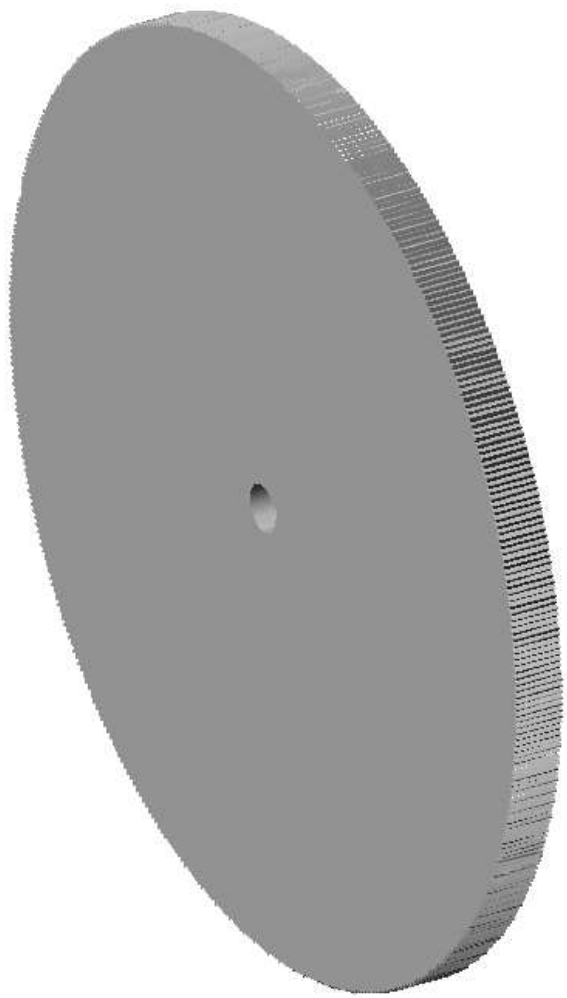

Figure 4-12. A solid model of a filter, grism or Lyot gear blank. Note the central bore hole created for gear manufacturing purposes

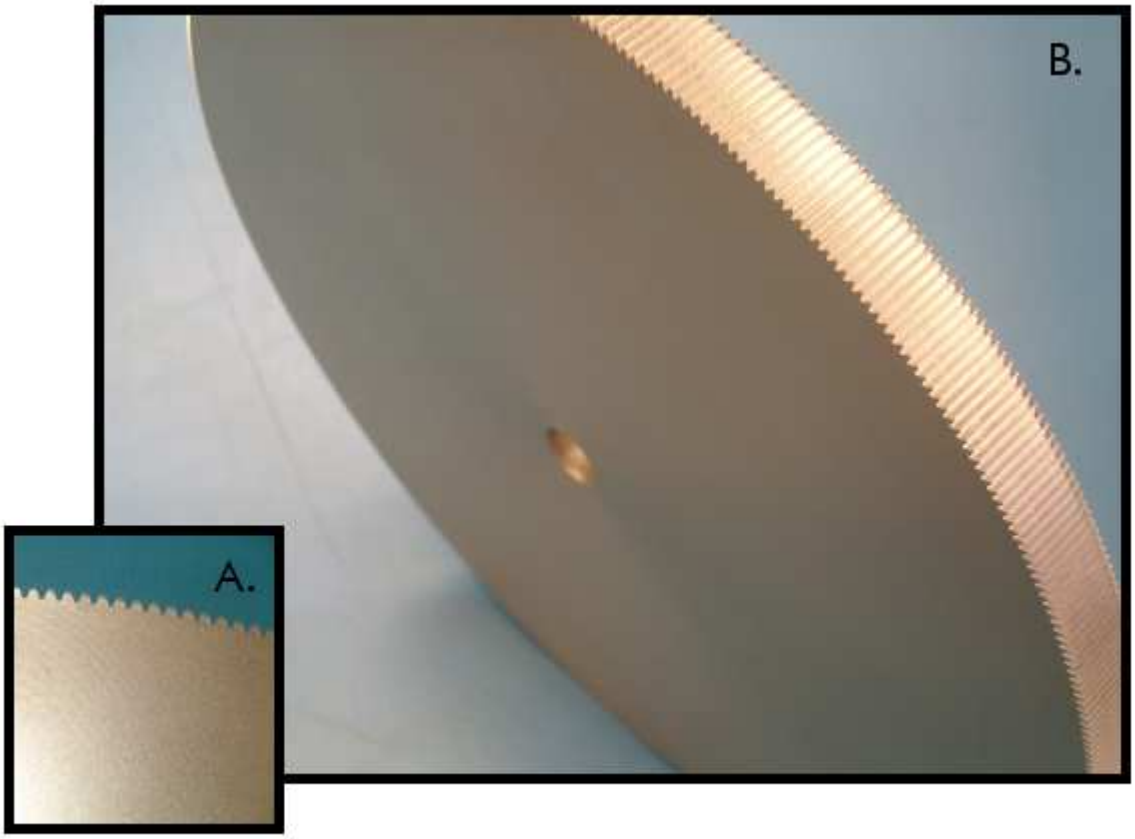

Figure 4-13. A finished gear blank created by Ascent Gears. A.) is a zoomed image of the precision teet while B.) shown the image of an entire wheel All five blanks are currently in-hand at the University of Florida.

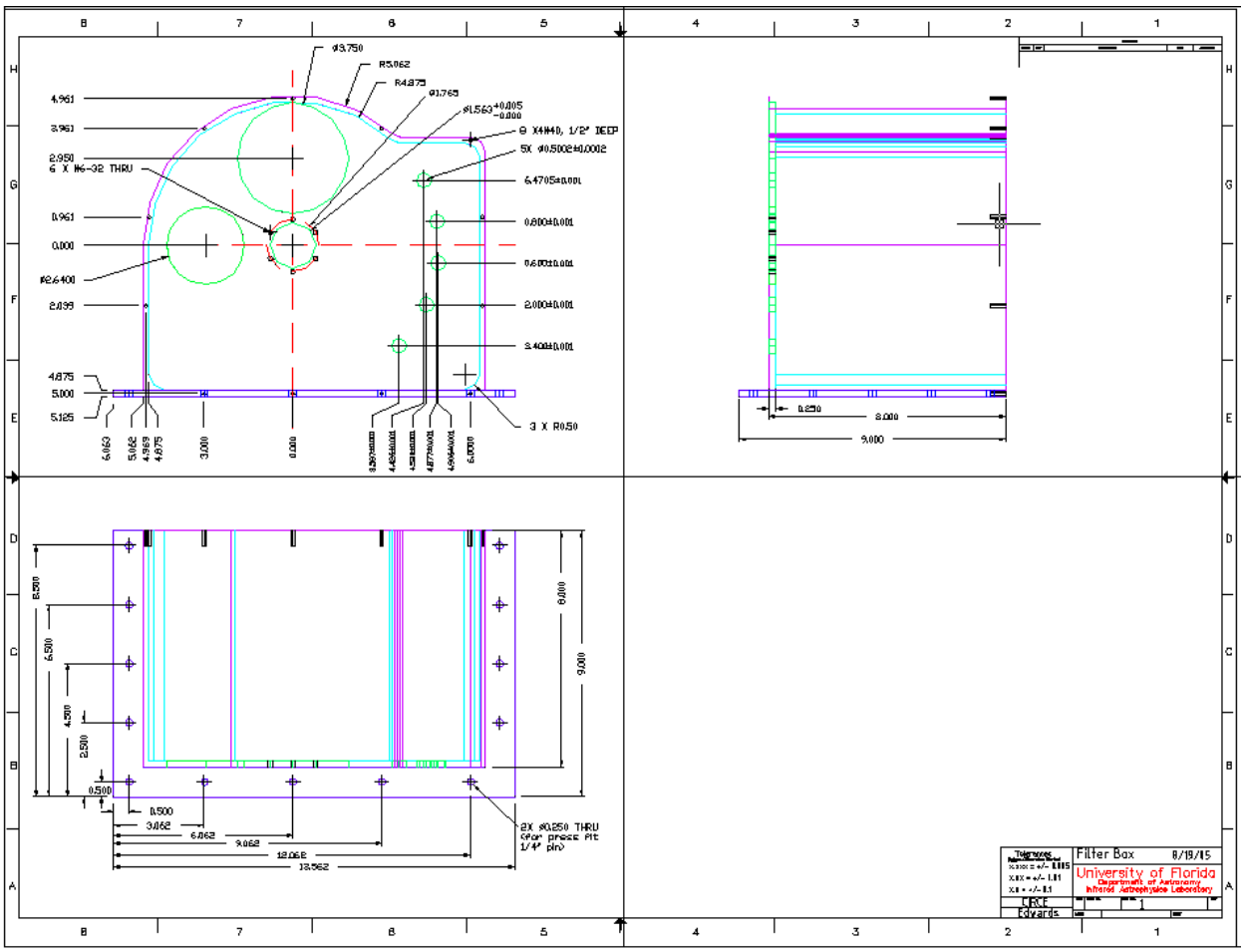

Figure 4-14. Two-dimensional design of the CIRCE pupil box. Notice the three large holes, one for the pupil box hub, another for light from the collimator to enter the enclosure, and a third for access into the interior of the box. The five smaller holes on the right side of the box are for the motor mounts.

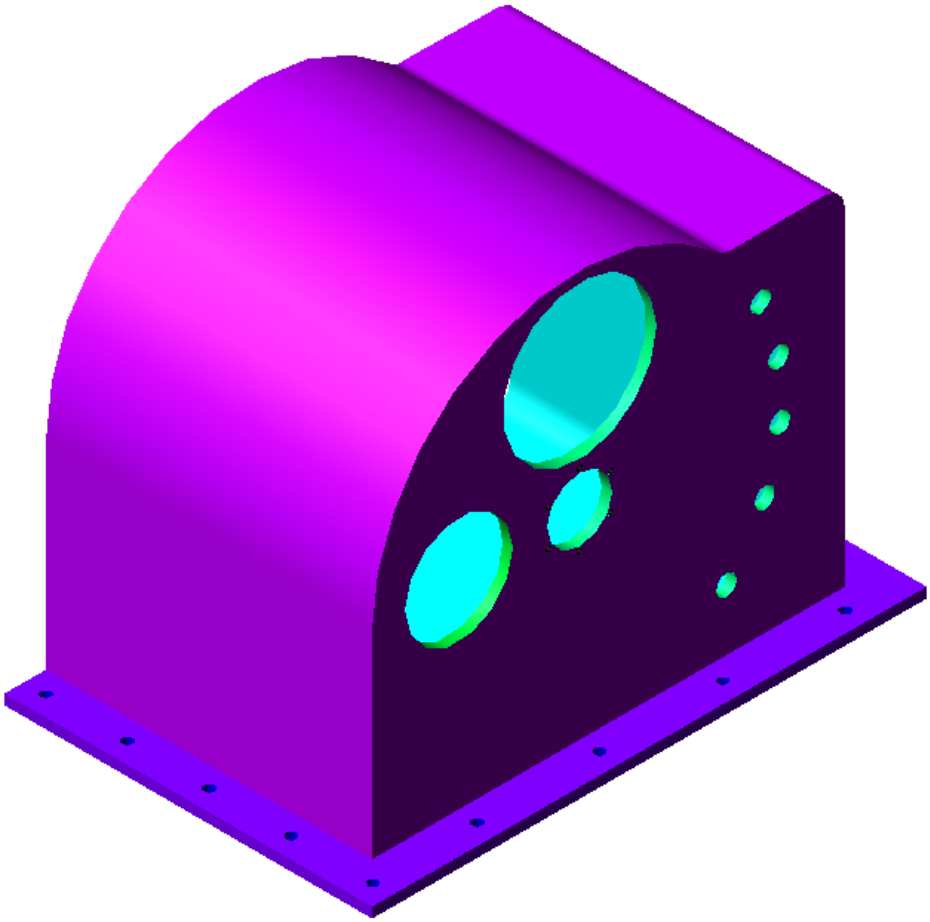

Figure 4-15. Solid model of the CIRCE pupil box.

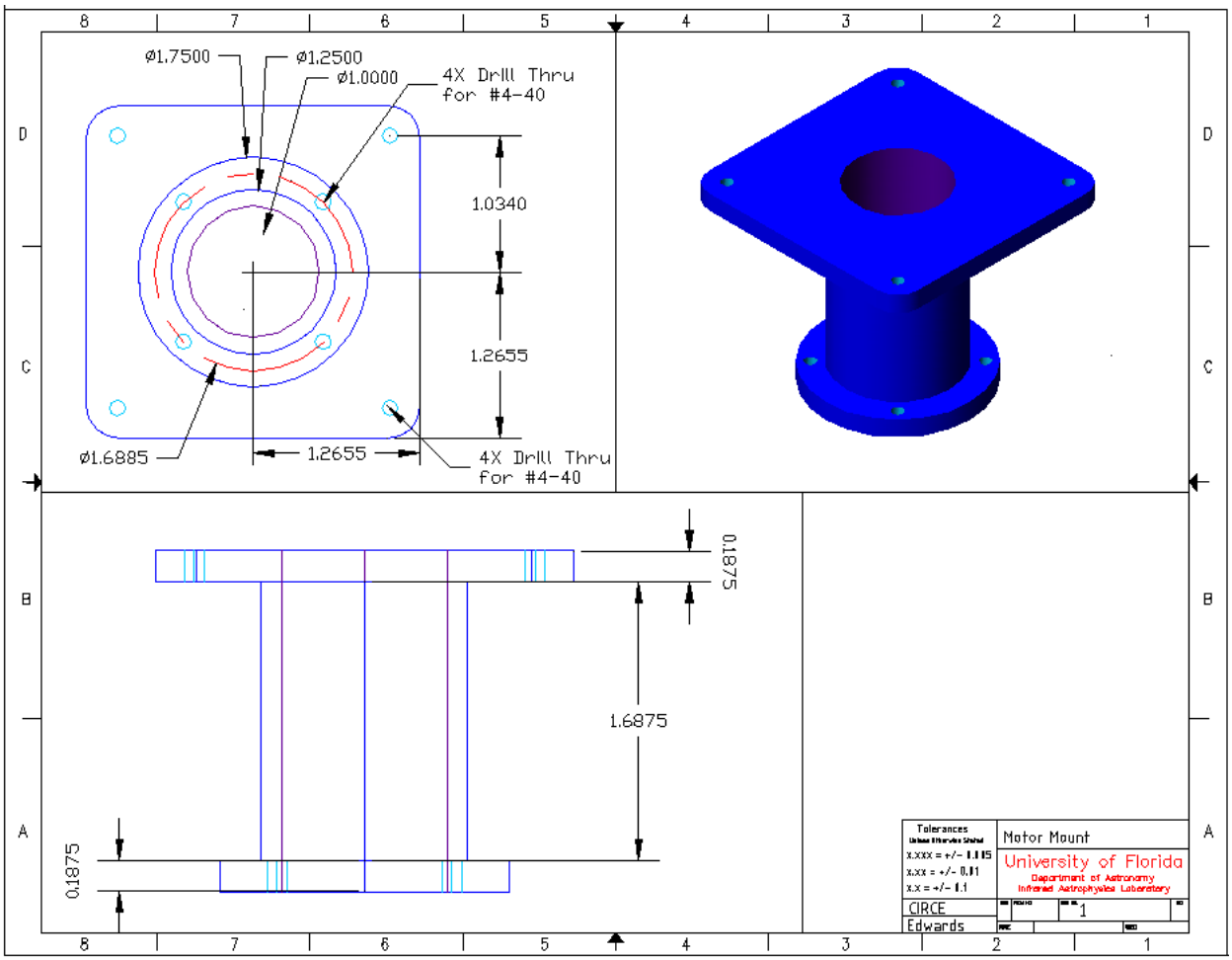

Figure 4-16. Solid model of a motor mount. The platform supports a Portescap motor. The bottom pedestal bolts onto the face of the pupil box. An axle attached to the motor runs through the hollow pedestal and into the hole in the pupil box.

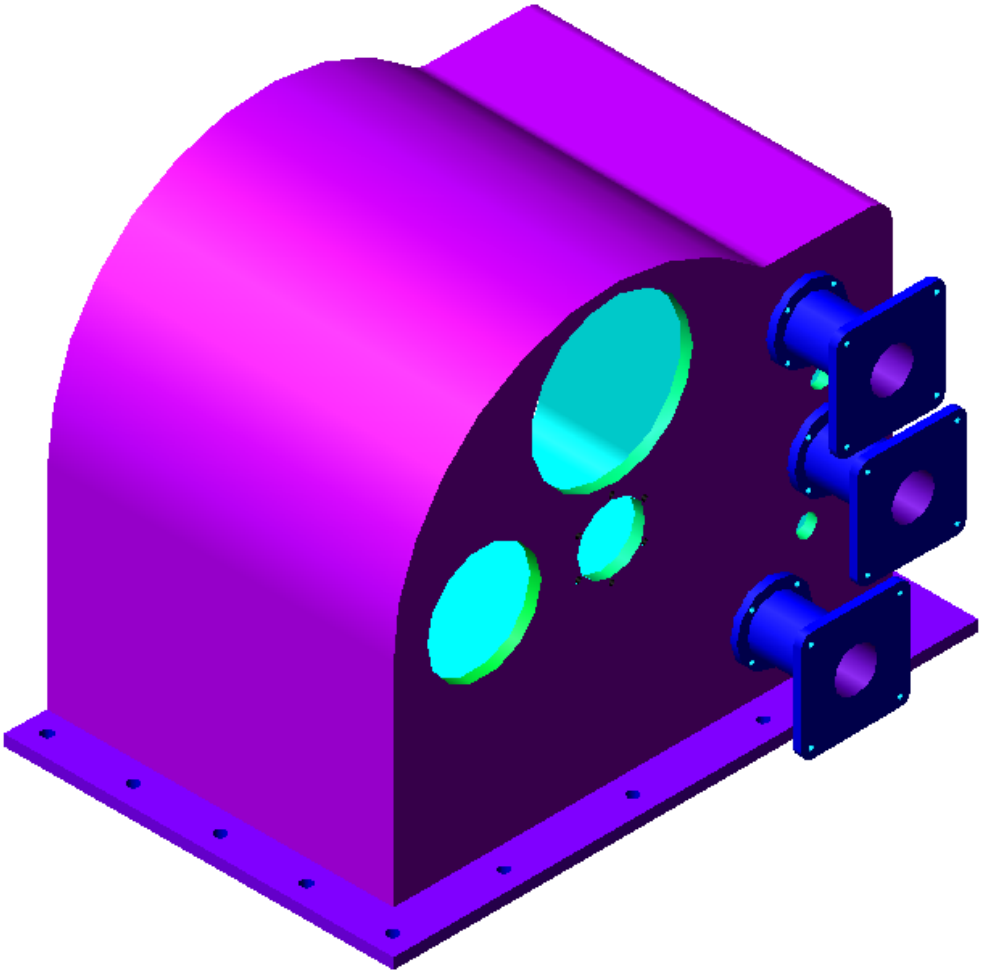

Figure 4-17. A solid model of the pupil box with the motor mounts in place. Three of the mounts attach to the front side and two attach to the lid. This was necessary to ensure the mounts did not overlap or touch each other.

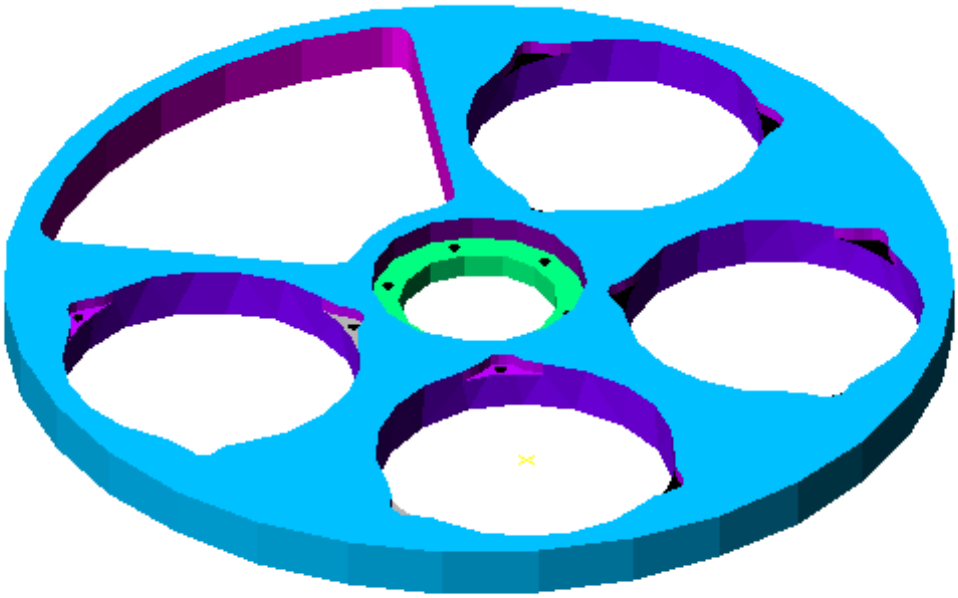

Figure 4-18. Solid model of the revised grism wheel. I enlarged the "blank" hole in the grism wheel to accommodate a large cartridge. This will allow the CIRCE team to change filters in wheel four, the wheel immediately in front of the grism wheel, without disassembling the entire pupil box.

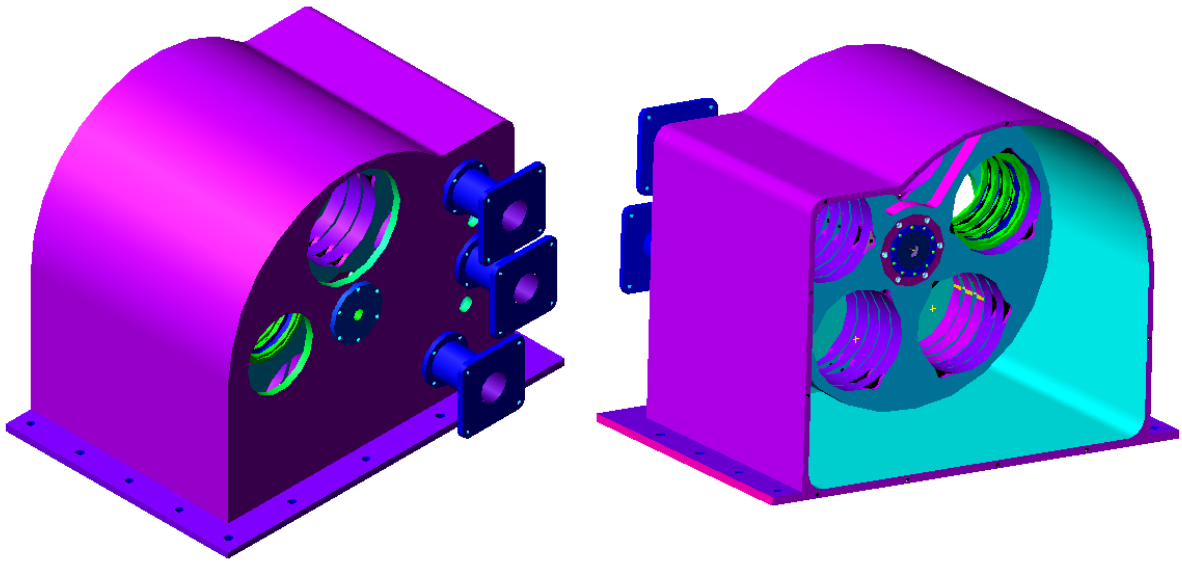

Figure 4-19. A solid model of the integrated pupil mechanism, with filter, lyot, and grism wheels, wheel hubs, axles, ball bearings, motor mounts, and pupil box

CHAPTER 5
THE SEARCH FOR MASSIVE STARS AROUND 1806-20

5.1 Introduction

In the previous three chapters, I discussed my role in the design of the Canarias InfraRed Camera Experiment (CIRCE), a NIR camera for the Gran Telecopio Canarias. While, the development of cutting-edge astronomical instrumentation is a crucial step in the scientific process, cameras like CIRCE are fundamentally driven by research. The ultimate question astronomers ask when presented with a new tool like CIRCE is: what science can I pursue with this instrument?

In Chapter 1, I outlined several projects possible with NIR instruments like CIRCE. In particular, I focused on a survey to search for massive stars around the environments of Soft Gamma Repeaters (SGRs). In this chapter, I discuss the observations, analysis, and photometric techniques used in this study, particularly as they apply to Cl 1806-20. In Chapter 6, I present results on my imaging of the remaining SGR environments. This study will lead to a better understanding of SGRs and the techniques necessary to probe their environments.

Until the recent discovery of magnetar CXO J164710.2-455216 in Westerlund 1 (Muno et al. 2006), SGR 1806-20 was the sole magnetar clearly linked to the surrounding cluster of massive stars, namely Cl 1806-20 (Corbel & Eikenberry 2004; McClure-Griffiths & Gaensler 2005; Bibby et al. 2008). Discovered by Fuchs et al. (1999) and further characterized by numerous authors (LaVine et al. 2003; Eikenberry et al. 2004a; Figer et al. 2005; Bibby et al. 2008), Cl 1806-20 is home to a variety of interesting and rare objects, including a Luminous Blue Variable (LBV), multiple Wolf Rayets (WRs), and several OB supergiants. However, while previous studies have explored individual stars in the region surrounding SGR 1806-20, no concerted effort to fully characterize the cluster's massive stellar population has materialized. Without these data it is difficult to place

absolute limits on the mass and age of the cluster, both necessary to constrain the nature of the SGR progenitor and star formation history of the cluster.

Utilizing near-infrared (near-IR) narrow-band imaging, I search for emission lines indicative of stellar winds in massive stars (Figer et al. 1997; Hanson et al. 1996) in an $\sim 9' \times 9'$ region surrounding SGR 1806-20. Specifically, I will use a Brγ 2.16μm narrow-band filter. In rare, evolved massive stars like WRs and LBVs, Brγ 2.16μm emission lines produced by large stellar winds can exceed $\sim$ - 40Å (LaVine et al. 2003; Figer et al. 2005). Furthermore, since the Brγ emission is located in the NIR as opposed to the optical, it is able to penetrate the dusty, extinguished regions surrounding SGR 1806-20 better than Hα emission typically used to search for massive clusters. Finally, this near-IR narrow-band study also uncover OBI cluster stars with Brγ absorption, with more moderate Brγ absorption $\sim$ EW = 5Å (Hanson et al. 1996).

5.2 Detecting Emission and Absorption Lines with Narrow-band Photometry

While SGRs offer a small, discrete, and well-defined source sample, seemingly ideal to test theories regarding their formation and evolution, the environments surrounding these objects present a number of challenges. All four SGRs are found in areas with high stellar densities and large or patchy extinction. In particular, SGR 1806-20 is located in a heavily crowded region of the Galactic Plane with $A_V \sim 29$ mag (Corbel & Eikenberry 2004). In an effort to circumvent these issues, I undertook a near-IR narrow-band imaging survey. I concentrated my efforts in the near-infrared to counter the effects of extinction. Since $A_K \simeq 0.112 A_V$ (Rieke et al. 1985), observations in this bandpass reduce the impact of reddening inherent in optical studies, greatly increasing the number of observable sources.

Using narrow-band photometry to probe for Brγ emission or absorption indicative of massive stars has several advantages. First, detection of emission lines would be less ambiguous than spectral typing based on J, H, K photometry alone. Often, when using the later method, it is difficult to tell a WR star with $A_V \sim 30$ mag from an M star with $A_V \sim 15$ mag; narrow-band imaging has the potential to break this degeneracy, since only

the WR star will have emission lines. Furthermore, as mentioned in §5.1, the Brγ lines associated with massive stellar winds have large EWs, offering an improved chance to detect emission line flux above the continuum. However, some questions remain about the efficacy of this method. What level of effect are we looking for? How might the effects of reddening confuse the data?

Using two 1% filters, which transmit 1% of the total flux of a broad-band filter, my observations sample two discrete portions of a stellar spectrum. One filter, centered at 2.16μm, detects both the star's continuum flux and any flux associated with a Brγ emission line. The second, (hereafter, K_{cont}) centered at 2.27μm detects only stellar continuum. Once reduction and photometry is complete, the fluxes are subtracted. If there is an excess in the 2.16μm filter, I have detected an emission line in the selected target. Further, the scale of the excess is proportional to the EW of the proposed line.

In an idealized case, where the continuum flux detected by the two narrow-band filters is equal, the EW of a line is defined as:

$$W = \frac{F_{cont} - F_{line}}{F_{cont}} d\lambda \tag{5–1}$$

where W is the equivalent width of the line, F_{cont} is the flux from the continuum, F_{line} is the flux in the line, and $d\lambda$ is the band-pass. I define a value:

$$\alpha = \frac{F_{line}}{F_{cont}} \tag{5–2}$$

and rewrite the EW as:

$$W = (1 - \alpha) d\lambda \tag{5–3}$$

Then, considering $m_{2.16}$, the magnitude in the Brγ filter and $m_{2.27}$, the magnitude in the K_{cont} filter, and assuming an idealized situation where the zeropoint fluxes and magnitudes are equal in the two narrow-bands:

$$m_{excess} = m_{2.16} - m_{2.27} = -2.5 \log \frac{F_{line}}{F_{cont}} \tag{5–4}$$

A positive m_{excess} indicates an absorption in the Brγ or excess in the K_{cont} flux, while a negative m_{excess} indicates an excess in the Brγ flux. Then, substituting Equation 5–2 into Equation 5–4 and solving for α yields:

$$\alpha = 10^{-\frac{m_{excess}}{2.5}} \tag{5–5}$$

Noting that a 1% filter will cover $\sim$ 220Å in the K_s-band, I estimate that $d\lambda = 220$ Å. To place an upper limit on the value of m_{excess}, I set W equal to the largest Brγ equivalent width measured in the cluster to date, thus W = - 40Å (Eikenberry et al. 2004a), and solve Equation 5–3 for α. Then using this value of α in Equation 5–5, I find $m_{excess} = -0.18$ mag. This immediately sets the limit of my maximum acceptable photometric error. To successfully identify an excess caused by an emission line with an EW = - 40Å at a 3σ level, we must perform <4% photometry. Identifying lower EW lines (10 - 20Å) requires 2% photometry.

I note that the location of my K_{cont} band at 2.27μm is problematic. As wavelength increases, the ability to penetrate dust also increases. Unfortunately, at the reddening of the cluster, the level of Brγ excess expected from massive stars is the same order of magnitude, but in the opposite direction, as the excess caused by increased penetration of dust between the 2.16μm and 2.27μm bands. Thus plotting my $Br\gamma - K_{cont}$ values versus K_s magnitude would yield confusing results; interesting emission line cluster stars would display an excess close to zero, as the increased flux in the 2.27μm band would cancel the emission in the 2.16μm Brγ band. However, foreground stars with a bright K_s-band magnitude and no Brγ emission would also show no excess.

To solve this problem, I also measured the $J - K_s$ color of each source in my study. Since most massive stars have intrinsic $J - K_s \sim 0$, their apparent $J - K_s$ colors are indicative of the reddening along the line-of-sight. Thus massive stars in Cl 1806-20 will

cluster around a particular value of $J - K_s$ (see §5.4.4), while foreground stars would have a significantly bluer color. Further, cluster stars without emission lines will also have a characteristic value of $Br\gamma - K_{cont}$ solely indicative of the increased dust penetration of the K_{cont} band. Stars with large emission or absorption lines should appear grouped at the same $J - K_s$ value, but at an offset $Br\gamma - K_{cont}$.

This technique attacks a large, crowded field globally; however I am interested in pinpointing particular stars for follow-up spectroscopy. Therefore, the results should not be statistical – I must show that this global method can pick out distinct objects. Cl 1806-20 provides us with the ideal opportunity to test this approach. Of all the SGR environments, only Cl 1806-20 has extensive spectra, photometry, distance, and reddening measurements available. By comparing my results to the known emission-line star population, I can evaluate whether a narrow-band survey to search for Brγ absorption and emission would indeed select these objects as follow-up candidates.

5.3 Observations and Data Reduction

On 2005 August 26-27, I used the Wide Field Infrared Camera (Wilson et al. 2003, WIRC) on the Palomar 200" telescope to obtain J, K_s, 2.16μm Brγ, and 2.27μm K_{cont} images of an $8.7' \times 8.7'$ region around SGR 1806-20. Applying standard techniques for near-infrared (NIR) observing, I used a random 9-point dither pattern with $< 30''$ separation between each image to obtain the K_s, K_{cont}, and Brγ data. I took 3 images at each position, resulting in 27 images. The total exposure times were 13.5 minutes in Brγ and K_{cont} and $\sim$ 90 seconds in K_s. Similarly, I obtained 3 exposures at 5 random dither positions with $< 30''$ separation between images, resulting in a 48 second exposure in the J-band.

I reduced the data using FATBOY, a PYTHON based data pipeline developed at the University of Florida (Warner et al.*in preparation*). FATBOY performed standard data reduction tasks, including dark and sky subtracting, flat fielding, and dithered image combining, to produce final reduced science frames. I then performed astrometry on these

images using KOORDS in the KARMA software package. Using 25 stars, I tied each of the four frames to corresponding K-band 2MASS image of the region. This produced an astrometric match between my four science frames. The errors in the astrometry between the 2MASS frame and each of the four bands were relatively similar, yielding error circles with radii $\sim 0.3 \pm 0.2''$. However, the astrometric match between my science frames was better; between the K_s-band and each of the two narrow-band frames, the radius of the error circle was reduced to $0.13 \pm 0.06''$; between the broad-band J and K_s images the error circle had a radius $\sim 0.10 \pm 0.07''$.

5.4 Analysis

5.4.1 Photometry

Once I completed my data reduction, I performed PSF photometry with DAOPHOT II and ALLSTAR (Stetson 1987, 1992). In summary, I created a model PSF using a sample of stars isotropically distributed across each science frame. This model PSF was assigned a magnitude, which acted as an instrumental zeropoint. Each star in the frame was then fit with a model PSF scaled to the star's brightest pixel. DAOPHOT then iteratively adjusted this model to minimize error between the stellar PSF and the model PSF and assigned a magnitude proportional to the scaling factor. Finally DAOPHOT (and ALLSTAR) output the magnitude and error for each source.

Given the complexity of this technique and my moderate departures from the normal procedure, I now describe my method in more detail. First, I identified stars in each of my science images using the DAOPHOT FIND routine. I found 15000, 14000, 24392, and 22679 stars in the Brγ, K_{cont}, K_s-band, and J-band, respectively, using similar detection thresholds for all frames. Upon identifying the majority of stars in each image, I proceeded to create a model PSF.

Ideally, the user would specify the number and limiting magnitude of stars that DAOPHOT should use for the model PSF. DAOPHOT would then choose objects that fit this criteria and use these "PSF stars" to create the model. During this process, the user

would monitor the rudimentary shape and isolation of the individual stars and discard those that appeared problematic. These would not be used in further analyses.

However, I noted two complications that necessitated a more careful approach for constructing a model PSF. First, the density of my fields required a concerted effort to choose truly isolated PSF stars. In my crowded frames the potential for blending was much higher than in less-populated fields. Furthermore, these blended objects were difficult to detect with the limited visual inspection tools offered by DAOPHOT. Secondly, as described in §5.2, the scale of the effect I am searching for is small, ≤ 0.2 mag, placing strict upper limits on the acceptable photometric error. Since the quality of my PSF photometry is heavily dependent on how well the model PSF fit the stars in the frame, minimizing errors in the model will minimize the overall error. Therefore, I wanted to build a PSF model using a large number of stars distributed throughout the field to provide the best results.

With this in mind, I used DAOPHOT to identify 200 potential PSF stars in each band. I then checked the FWHM, isolation, and roundness of each source by eye using the standard IRAF procedure IMEXAMINE. I discarded any object that appeared distorted or had a bright neighboring star that might confuse the DAOPHOT PSF fitting procedure. This process generally reduced my PSF star count by 25-50%, leaving us with 100+ stars per frame, which I ensured were more or less evenly distributed across the field.

I then created model PSFs using the DAOPHOT technique described by Stetson (1992). First, I constructed a prototypical PSF with the aforementioned pre-selected PSF stars and the DAOPHOT routine, "PSF". Since stars in close proximity to the PSF stars distorted DAOPHOT's calculation of the model PSF, I needed to temporarily remove or "clean" these "neighbor" stars from the frame. Using the SUBSTAR routine in DAOPHOT, I shifted and scaled the working model of the PSF to match the position and

magnitude of each "neighbor" star. I then subtracted the appropriately scaled PSF from each neighbor star.

At first, the neighboring stars did not disappear completely. This was due to the discrepancy between the model PSF and the true PSF. Therefore, I created a new model PSF using DAOPHOT and the more-isolated PSF stars and repeated the subtraction process. I iterated this procedure until visual inspection showed that DAOPHOT had removed any substantial stray signal near the PSF stars. With isolated stars in-hand, I could then experiment to find the class of PSF (Gaussian, Moffet, Lorenz, etc.) that best described my data.

Given my careful selection process, the class of model that best fit the PSF stars would most likely be the optimal solution for the entire frame. The ideal model, when scaled and subtracted from each PSF star, would leave minimal amounts of flux. However, while a qualitative evaluation of this flux residual is possible by visually examining the PSF subtracted images, I desired a more quantitative analysis to discriminate between the PSF models.

To this end, I performed basic aperture photometry on each PSF star across two frames. In both frames, the neighboring stars were "cleaned" using the process described above. However, in one frame, the PSF star was also subtracted leaving only a residual. I divided the residual flux by the total flux for each star and multiplied this number by 100. If the PSF model was a poor representation of the actual star, the subtraction was minimal and most of the stellar flux would be left, resulting in a large residual. The remaining flux would be $\sim 100\%$ of the total flux. If the model fit well, the subtraction would be excellent, leaving few counts behind. The residual would be small and the resulting percentage would be approximately zero. I calculated the value for each PSF star and found the median. This gave us an excellent measure of how well my PSF model fit all the PSF stars in the frame. I repeated this entire procedure on all four bands. Overall, the percentage of flux remaining after the PSF subtraction of the best model is $\leq 1\%$.

Using the best fit PSF models for each frame, constructed using a quadratically varying Gaussian model, we ran ALLSTAR to complete PSF photometry on all stars in the J-band, K_s-band, K_{cont}, and Brγ images. Then, using the standard error Ioutput by ALLSTAR for each star, I calculated the median error in each band. I found errors of 0.028, 0.044, 0.027, and 0.024 mag in the J-, K_s-, K_{cont}-, and Brγ- bands respectively. I discuss the errors associated with this technique in greater detail in §5.4.5.

Finally, I calibrated the J and K_s magnitudes for my sources using 2-MASS photometry. I chose 10 isolated stars with a range of magnitudes from the 2-MASS image of my field and matched them with their counterparts in my science frames. Starting with the K_s-band, I calculated the difference between my ALLSTAR magnitude and the 2-MASS magnitude for each star, found the median value of the offset, and applied it to the remainder of my K_s-band data. I repeated this process for my J-band photometry.

5.4.2 Star Matching

The next step was to match the stars in the field across all four bands in order to derive the colors and search for Brγ excess or absorption. To accomplish this I used TOPCAT, the Tool for OPeration on Catalogues and Tables. TOPCAT is a powerful software tool that completes a variety of tasks on tabular data; most notably it is capable of matching several tables using user supplied criteria.

Using TOPCAT and a $0.3''$ radius, I matched K_{cont} (RA, Dec) to Brγ (RA, Dec) and J-band (RA, Dec) to K_s-band (RA, Dec) for all detected stars. I calculated the $0.3''$ radius from my astrometric errors, using the error radius plus 3σ. I then matched the two tables to each other, using Brγ and K_s-band coordinates and the same $0.3''$ radius. Optimally, I would have matched all four bands simultaneously, however TOPCAT was unable to perform this match directly given the size of the data sets.

I found ~ 9000 J-band counterparts to K_s-band sources, ~ 12500 K_{cont} counterparts to Brγ sources and ~ 7000 sources with matches across all four bands. I discuss these statistics further in §5.4.3.

To test the validity of my source matching, I examined my Brγ and K_{cont} table. I found 100 sources in my Brγ science image and visually identified their counterparts in the K_{cont} image. I then removed the correct K_{cont} counterpart from the K_{cont} photometry, loading this new data set, and ran my TOPCAT match algorithm. I examined the output for false matches – instances where TOPCAT assigned a false counterpart to one of the test Brγ sources that purposefully lacked a true counterpart. I found no incidents of false matches. Further, I identified 100 sources in the center of my survey area, located them by eye in each of the four frames, recorded the matches and compared my results to TOPCAT. I found 100% agreement between the four-band match created by TOPCAT and my visual match.

5.4.3 Limiting Magnitudes and Match Drop-Outs

Using my 2MASS calibrated J and K_s photometric catalogs and the four-band match catalog created by TOPCAT, I determined the limiting magnitudes of my survey. Utilizing the single band J and K_s catalogs, I plotted Figure 5-1, histograms of both K_s-band magnitude and J-band magnitude versus number of stars at each magnitude. I found that my plots peaked at $K_s \sim 16$ mag and $J \sim 18$ mag. As the previously identified OB and WR stars in the cluster fall between $\sim$ 9 - 13 mag in K_s-band and $\sim$ 16 - 18 mag in J-band (Eikenberry et al. 2004a; Figer et al. 2005), I confirmed that my photometric limits were deep enough to observe the known massive cluster stars. Furthermore, given the broad range of spectral types in the established population of massive stars and my clear ability to detect them, I expect that my data would also include previously undiscovered massive cluster stars at the distance of Cl 1806-20, should they exist.

I then addressed the issue of "drop-outs" between my matches. Drop-outs are defined as sources that appear in one band, but are absent from one or more of the remaining bands. I found a significant number of drop-outs each time I matched catalogs. Extensive analyses (detailed below) show that the majority of drop-outs fall into one of two main catagories: stars at the field edges missing from one or more images due to small

variations in the field-of-view between frames or very faint stars at my detection limits. A smaller percentage of drop-outs were objects in the most crowded regions of the field.

I first examined the Brγ and K_{cont} match and noted a significant number of drop-outs; the 2-band catalog contained 12689 objects, 1300 less than the 13989 sources in the K_{cont}, and $\sim$ 2500 less than the 15233 sources in the Brγ. Discounting the sources lost due to non-overlapping regions at the edge of my frames, I was left with 300 sources in K_{cont} with no Brγ counterpart. I plotted a histogram of the number of sources versus instrumental K_{cont} magnitude; first for the complete K_{cont} catalog and then for the 300 K_{cont} drop-outs. The plots showed that the K_{cont} drop-outs were systematically fainter than the limiting magnitude, $K_{cont} \sim 20.3$ mag. If these sources, on the threshold of my detection limit in K_{cont}, were a few counts fainter in Brγ this would account for their detection in one band and not the other. This is plausible; recall that a 2.27μm filter will detect more flux than a 2.16μm filter in stars with no absorption given the increased dust penetration by longer wavelengths (§5.2).

I then examined the remaining $\sim$ 1500 Brγ sources with no K_{cont} counterpart. I created a histogram of the number of sources versus Brγ magnitude for both the entire Brγ catalog and the Brγ drop-outs. I found a limiting magnitude of Br$\gamma \sim 20.3$ mag and noted that the drop-outs were on the faint end of the distribution. Again, if these sources were only marginally brighter in Brγ than in K_{cont}, I would detect them in one filter and not the other.

Using TOPCAT I matched my Brγ drop-outs to my J and K_s broad-band match. I repeated this for my complete Brγ catalog and plotted histograms of number of stars versus $J-K_s$ color for both catalogs. I found that my Brγ drop-outs were bluer ($J-K_s \sim$ 1 - 2 mag) than the bulk of my $J-K_s$ distribution. Thus, faint, slightly blue foreground stars most likely account for the population of dim Brγ sources lacking K_{cont} counterparts.

None of the narrow-band drop-outs affect the goal of this survey. Luminous early-type stars in Cl 1806-20 have apparent K_s-band magnitudes between 9 - 13 mag. Later in this

section, I show that this K_s magnitude corresponds to $Br\gamma$ and K_{cont} between 14 - 18 mag; my drop-outs are much fainter than this. Further, as discussed in the paragraph above, the $J - K_s$ color of the Brγ drop-outs $\sim$ 1 - 2 mag; much bluer than the $J - K_s \sim$ 5 mag attributed to the cluster (§5.4.4).

I also observed a large number of drop-outs between the J- and K_s-bands. Out of 24392 sources in K_s and 11812 sources in J, 9300 sources were included in the matched K_s and J catalog. The large number ($>$ 10000) of K_s-band sources with no J-band counterpart was unsurprising; since longer wavelengths are more efficient at penetrating dust I expected many of the K_s stars to be highly obscured and thus undetected in the J-band. This is visually noticeable in the final images themselves. However, once source of concern was the large number of J-band sources with no K_s- band matches. While I expect most sources detected in J-band to have a counterpart in K_s-band I found that $>$2000 J-band sources dropped-out of the K_s-band match. Discounting the 800 sources lost due to non-overlapping frames, I am left with 1200 dropouts.

Two factors account for the loss of J-band sources in the J to K_s match: a blue foreground population and confusion and crowding in the K_S-band image. After exploring each of these issues, I concluded that these drop-outs in my catalog caused by these factors would not affect my ability to detect massive cluster stars. I detail my drop-out analysis below.

To account for the 1200 drop-outs, I chose 100 random sources from this population, found their positions on the K_s-band image, and searched for their missing counterparts. In $\sim$ 80% of the cases, a very faint object, undetected by the DAOPHOT FIND routine, did exist in the K_s-band image. I observed that the peak counts attributed to these sources were of the same order of magnitude as the calculated noise in the background. Therefore, given my inputs, the DAOPHOT FIND routine did not recognize these faint objects as sources and excluded them from the K_S catalog. Extrapolating from the results

of my random selection of 100 stars, I estimate that 80% of my 1200 J-band drop-outs, or $\sim$ 1000 stars are members of this population.

I then examined the same 100 random stars in the J-band image. The stars, while faint in the J-band, were significantly brighter than their "undetected" K_s counterparts described above and therefore easily identified by DAOPHOT. I plotted a histogram of the 1200 J-band dropouts missing from the K_s-band catalog. I found that 1000 sources were at the faintest end of the histogram with J $>$ 17.5 mag.

While I could alter my input into DAOPHOT in an attempt to detect the faint K_s-band counterparts to these dim J-band stars, this would also result in a larger number of spurious detections. Furthermore, given that the massive cluster stars I was interested in finding are luminous in the K_s-band (between 9 - 13 mag), while these stars are very dim in the K_s band, the likelihood of this tactic yielding useful results was minimal. Thus I did not attempt to include these sources in my catalog.

The remaining $\sim$ 20% of my J-band drop-outs are most likely due to crowding in the K_s-band. Of the 100 random sources I inspected, $\sim$ 20 stars were obviously visible in both images. However in the K_s-band image, source confusion and crowding was evident; often a brighter star or a large grouping of stars that did not appear on the J-band image overlapping its K_s-band counterpart. In cases where one star almost completely overlapped another, it was unlikely that the FIND routine would recognize each star as a separate object. Correcting this problem is not trivial; even upon visual inspection, it was challenging to find the correct counterpart. Thus, in some cases, in some of the most crowded areas of my K_s-band image my observations reach the confusion limit.

Finally I examined my 4-band match. As mentioned in §5.4.2, I created this catalog by matching the Brγ to K_{cont} table, with $\sim$ 12000 sources, to the J- to K_s-band table, with $\sim$ 9000 sources. A total of 7010 sources are matched across the four bands. Since one might expect all 9000 sources with both J- and K_s- band counterparts to appear in the narrow-band catalog I again note a significant drop-out rate ($\sim$ 2000 stars).

To investigate this dropout rate, I examined the sensitivity limits of the broad-band K_s versus the narrow-band data. Using TOPCAT, I performed an astrometric match between the Brγ, K_{cont}, and K_s-band catalogs using a procedure similar to that described in §5.4.2 . I then created a histogram showing the number of sources per K_s-band magnitude bin versus K_s-band magnitude for the new 3-band match. I overplotted this histogram with the one created for the K_s-band catalog. Figure 5-2 shows that a large number of K_s-band sources with K_s magnitudes fainter than > 16 mag had no narrow-band counterparts in my data and thus were not included in the 3-band (and therefore 4-band) match. Thus, the lack of narrow-band counterparts to faint K_s stars is due to the sensitivity of my narrow-band observations; the narrow-band images have a brighter limiting magnitude for my integration times.

As mentioned in §5.4.1, I was unable to directly calibrate the Brγ and K_{cont} magnitudes from published catalogs. Instead I created a histogram of the instrumental magnitudes versus the total number of stars in each magnitude bin for both narrow-band catalogs. I then overplotted this histogram on top of the histograms presented in Figure 5-2; the result is Figure 5-3.

The shapes of the narrow-band histograms resemble the shape of the histogram of K_s-band sources with narrow-band counterparts. By matching narrow-band stars to their K_s counterparts, I have effectively photometrically calibrated each source. This is reflected in the histograms; when comparing the shape and peak of the narrow-band histograms to the 3-band match histogram, it is evident that the Brγ and K_{cont} data are offset roughly $\sim$ five magnitudes from the K_s-band data. Further, I note a significant drop in the narrow-band histogram at instrumental magnitudes of ~ 21 mag. In the K_s calibrated scale this corresponds to $K_s \sim 16$ mag.

Using this information, I conclude that the remaining source drop-outs from the J- to K_s- band catalog to the final 4-band catalog are caused by a drop in the sensitivity of my narrow-band data due to insufficient integration time; my narrow-band observations

were too short to reach the same limiting magnitude as my broad-band imaging. However, given the expected brightness of potential massive cluster stars, ($K_s < 16$) as discussed in the beginning of this section, this magnitude limit for my narrow-band imaging should not adversely affect my results.

5.4.4 Field Selection

While my data provide information about stars across the entire field, I am primarily interested in potential members of Cl 1806-20. Thus, from this point on, I only consider a subset of my field – in particular a $6\,' \times 6'$ subregion centered on the SGR. I chose the size of this region after reviewing the published radii for Galactic massive star clusters whose stellar contents, ages, and (potentially) masses are similar to Cl 1806-20 (Figer et al. 1999, see Table 5). In particular, I sought an estimate that would not exclude less compact clusters or ejected massive stars. Such a cluster is represented by Westerlund 1, a potential Galactic Super Star Cluster (SSC). While the bulk of Westerlund 1 lies within a 1.2 pc core, the cluster is elongated, with several cluster members located well outside this radius (Clark et al. 2005); in fact potential WR cluster members are located as far as ~ 8 pc away (Crowther et al. 2006).

While I recognize that Westerlund 1 is not a direct analog to Cl 1806-20, I use its size to place an upper limit on the search area necessary to locate members of a massive stellar cluster. At 15 kpc, the distance to Cl 1806-20 reported by Corbel & Eikenberry (2004) and supported by McClure-Griffiths & Gaensler (2005), a 16 pc $\times$ 16pc search area corresponds to a subfield $\sim 4' \times 4'$. However, if the cluster is at the $\sim$ 9kpc distance suggested by Bibby et al. (2008), my field would correspond to a 10 pc $\times$ 10 pc search area. To ensure that despite the disputed distance of Cl 1806-20 we still cover an approximately 16pc $\times$ 16pc area, we use a larger $6' \times 6'$ field.

We computed the $J - K_s$ versus $Br\gamma - K_{cont}$ values for all stars in my 4-band catalog within the $6' \times 6'$ area. The result is Figure 5-4. Then using the RA and Dec in my 4-band table for my stars and an RA = $18^h\ 08^m\ 39.32^s$ and Dec = -20° 24′ 39.5″ (Kaplan

et al. 2002) for the SGR, I calculated the 2-D projected distance between each field star and SGR 1806-20 . These 2-D projected distances are represented by a color gradient, with objects close to the SGR colored purple and objects further away in red.

Figure 5-4 offers a wealth of information about the stars in my field and the populations to which they belong. In particular, the $J - K_s$ color is a distance and reddening indicator; objects on the left of the graph are bluer and therefore most likely located in the foreground, while objects to the far right are heavily reddened. Since $A_K = 0.112A_V$ and $A_J = 0.282A_V$ (Rieke et al. 1985), using an $A_V = 29 \pm 2$ for Cl 1806-20, (Corbel & Eikenberry 2004; Eikenberry et al. 2004a) I calculate $A_K = 3.25 \pm 0.56$ and $A_J = 8.18 \pm 0.22$ yielding a $J - K_s = 4.93 \pm 0.34$ mag for massive stars with an intrinsic $J - K_s = 0$.

5.4.5 Errors

Quantifying and characterizing the error in my photometry is crucial for the success of this technique. In §5.2, I found that a 4σ detection of a Brγ emission or absorption line with an equivalent width $\sim$ 20 - 40Å required 2-5% photometry. As mentioned in §5.4.1, ALLSTAR outputs both a magnitude and standard error for each source in the frame. Using these data, I calculated the median photometric error in each band and found that it ranged from 0.024 - 0.044 mag. However, while these values establish that I achieved better than 5% photometry in each frame, they do not necessarily confirm that I met the criterion set in §5.2. In actuality, I require the photometric error in the Brγ excess or absorption, and thus the error in $Br\gamma - K_{cont}$, to meet the 4% limit.

To check if my photometry satisfies this standard, I initially used the Brγ and K_{cont} 2-band match described in §5.4.2. First, I calculated the median error in $Br\gamma - K_{cont}$ to be 0.032 mag. This corresponded to $\sim$ 3% photometry, confirming that, on a global level, my errors were small enough to allow for 3σ detections of modest Brγ emission and absorption lines.

I then repeated this calculation using my $6' \times 6'$ 4-band catalog and found that the median $Br\gamma - K_{cont}$ error dropped to 0.020 mag. Two factors account for this decrease. As noted in §5.4.3, dimmer sources in my field often lacked matches across all four bands and were therefore not included in the 4-band catalog. Since dimmer sources have systematically larger Poisson errors, their absence from the catalog improved my overall data quality in the area of interest. Further, by limiting the catalog to the central region of the frame, where minor distortion effects inherent in the detector were at a minimum, I effectively eliminated errors associated with poor model PSF fits. Thus, the photometry over the most interesting part of the field exceeds my 5% criterion.

Having met the necessary photometric limits on a comprehensive level, I then assessed my error on a more source specific scale. I computed the errors in the $J - K_s$ and $Br\gamma - K_{cont}$ colors for every star in my 4-band catalog using the errors output by DAOPHOT. If a particular source displays emission or absorption but a large error in either color, I can use these errors to evaluate whether it is still a good candidate for follow-up spectroscopy. I discuss this in more detail in the sections below.

5.4.6 Calculating Equivalent Widths

In Figure 5-4 I noticed a linear correlation between the $J - K_s$ color and $Br\gamma - K_{cont}$ color of sources in the field. This was expected because, as mentioned in §5.2, longer wavelengths penetrate dust more efficiently. Since my K_{cont} filter was centered at a longer wavelength than my Brγ filter, it systematically detected more flux, even if no intrinsic excess or absorption existed. However, the size of this effect depends on the reddening; if the extinction towards a particular star in the field was small, the effect was small. If the extinction was large, the effect was large – on the order of 0.1 - 0.3 mag. The slope of the line is therefore an indicator of the varying reddenings and distances of objects in the field-of-view.

Using TOPCAT, I fit a line with slope (m) = 0.028 and y intercept (b) = -0.137 to the data points. For any given $J - K_s$ color, this line defines the expected value

of $Br\gamma - K_{cont}$ for a star with neither Brγ absorption nor emission, thus acting as a narrow-band "zeropoint". This zeropoint is a combination of the dust-penetrating effect described above and differences in transmission between the narrow-band filters. To find the calibrated $Br\gamma - K_{cont}$ value of an individual star in my data set, I first solved the equation of the line using the star's $J-K_s$ value. This gave us the $Br\gamma - K_{cont}$ "zeropoint" for that particular object. I then subtracted this value from the photometrically derived $Br\gamma - K_{cont}$ color. The resulting magnitude difference was used with Equation 5–5 and Equation 5–3 to estimate the EW of the Brγ excess or absorption. Finally, using the errors in the $Br\gamma - K_{cont}$ and $J - K_s$ colors calculated for each source (§5.4.5) and the linear equation described above, I computed the errors in the EW for every star in my 4-band catalog.

5.5 Comparison to Previous Results

By comparing prior spectral and photometric information (Table 5-1) to my observed Brγ excess or absorption and $J - K_s$ colors (Table 5-2), I am able to evaluate how well this global narrow-band photometric technique estimates the properties of individual stars.

While Figure 5-4 contains substantial information about a number of stellar populations in the field (§5.6), I sought a more useful visual tool to highlight the previously known bright cluster members and identify new candidates. In Figure 5-5 I plot stars with $K_s \leq 16$, the completeness limit of my K_s catalog. As mentioned previously, cluster stars should have apparent K_s magnitudes between 9 - 13 mag; by removing the dimmer foreground stars, I limit contamination by foreground stars with large broad-band photometric errors. Further, since faint K_s stars also have faint narrow-band counterparts, I exclude sources with large narrow-band photometric error. This reduces the scatter around the "zeropoint" $Br\gamma - K_{cont}$ and makes it easier to distinguish stars with real emission or absorption features from those sources with large narrow-band photometric errors. Stars with $Br\gamma$ excess or absorption, discussed in detail below and in §5.6.1, are

clearly labeled in Figure 5-7, a $1.3' \times 1.6'$ region of my K_s-band image encompassing Cl 1806-20.

5.5.1 Wolf Rayet Stars

LaVine et al. (2003, *in preparation)*, Eikenberry et al. (2004a), Figer et al. (2005), and Bibby et al. (2008) present spectra for Wolf Rayet stars in Cl 1806-20. I summarize these results in Table 1. For the remainder of the discussion, I adopt the LaVine et al. (2003, *in preparation)* and Eikenberry et al. (2004a) nomenclature when an object has more than one designation.

Using the finder charts and coordinates provided by these authors, I visually identified each of the known WR cluster stars on my Brγ image. I then found the location of these objects on Figure 5-5 (denoted as squares) and determined their Brγ EWs from my narrow-band imaging.

Three of the four WR stars, B, 10, and 22 appear in my catalog. Star 3 is the exception. The location of Star 3 in the densest, most confused region of the cluster, prevented an accurate measure of its position or magnitude in one or more bands in my data.

Star 22 and Star B show the potential of the technique described in this paper. Star 22 has an Brγ excess of - 0.20 $\pm$ 0.01 with a $J - K_s$ error = 0.02. Using Equation 5–5 to solve for α, Equation 5–3 to solve for W (see §5.2), and incorporating the errors described in §5.4.5, I find an EW $\sim$ - 45 $\pm$ 1Å, in agreement with the EW = - 42 $\pm$ 3Å previously reported (see Table 1). Also, I measure a $J - K_s \sim 5$ mag for Star 22, consistent with earlier measurements of this source (LaVine et al. *in preparation*).

I repeated the above calculations for Star B. Surprisingly, I found that Star B does not have a Brγ excess; instead my data show a Brγ absorption of 21 $\pm$ 1Å. While at first this appears to be inconsistent with the previously reported Brγ emission, inspection of the spectra provided by Eikenberry et al. (2004a) and LaVine et al. (*in preparation*) show that this result is consistent with the earlier data. Star B is classified as a WCLd, a dust

emission WR star. Redward of 2.2μm, Star B exhibits a large IR excess. Since the K_{cont} band used in my observations is located at 2.27μm, I expect the flux in this narrow-band to be greater than the flux in the Brγ band. Thus, my apparent Brγ "absorption" is in fact a documented K_{cont} excess. Further, my J and K_s- band magnitudes (Table 5-2) are consistent with the J- and K_s- band magnitude of 17.78 and 10.5 respectively reported by LaVine et al. (*private communication*).

Star 10 is an interesting enigma. LaVine et al. (2003, *in preparation)* report a Brγ emission line $\sim$ - 25 $\pm$ 1 Å. However, I find a small Brγ absorption (1 - 3Å), which is inconsistent with previous results. To rule out a spurious match, I visually identified the object in each of the four images and verified that TOPCAT selected the correct counterpart.

Noting that Star 10 was relatively isolated, I completed an independent check of the DAOPHOT photometry by performing aperture photometry on the star in the K_{cont} and Brγ bands. The value of $Br\gamma - K_{cont}$ found with this method matched the $Br\gamma - K_{cont}$ color calculated from my PSF photometry, confirming the observed lack of excess.

One possible explanation for the absence of Brγ emission is that Star 10 is a dust emission WR. Recent spectroscopy from Bibby et al. (2008) suggests that like Star B, Star 10 is a WC9d, with warm dust masking the strength of the emission lines. Also, with a $J \sim 17.38 \pm 0.02$ mag and $K_s \sim 11.55 \pm 0.01$ mag, I calculate a $J - K_s$ color ~ 5.83 mag. This value is slightly redder than most stars in the cluster and may be indicative (as with Star B) of intrinsic reddening by circumstellar dust, consistent with the Bibby et al. (2008) result.

Another possible reason for the absence of Brγ excess in Star 10 is variability in the emission line. However, follow-up spectroscopy over multiple epochs would be necessary to test this hypothesis.

5.5.2 Luminous Blue Variable (LBV) 1806-20

First discovered by Kulkarni et al. (1995), the candidate Luminous Blue Variable (LBV) 1806-20 was originally believed to be the infrared counterpart to SGR 1806-20. Subsequent studies showed that it was not the magnetar's counterpart (Hurley et al. 1999), but a member of Cl 1806-20 (Fuchs et al. 1999; Eikenberry et al. 2001; Corbel & Eikenberry 2004).

While the mass range and potential binary nature (Eikenberry et al. 2004a; Figer et al. 2004) of LBV 1806-20 are topics of contention in the literature, the intensity of the star's massive stellar winds is well established. Eikenberry et al. (2004a) report several strong emission lines, particularly Paβ ($\sim$ - 82Å) and Brγ ($\sim$ - 44Å). Spectra in Figer et al. (2004, see their Figure 3) show similarly large emission lines.

Given the reported level of Brγ emission, I expect to find a large Brγ EW for LBV 1806-20 within my data. However, using the calculations described in §5.4.6 and my $Br\gamma - K_{cont}$ excess, I find an EW $\sim$ -4 $\pm$ 2Å. I investigate two potential reasons for this discrepancy: 1) errors in my photometry or 2) intrinsic variability of the emission line.

5.5.2.1 Evaluation of PSF photometry

While global errors in my data met the 2 - 5% photometric limit necessary to detect 20 - 40Å Brγ emission lines (see §5.2), the nature of this technique also allowed us to evaluate whether this criterion was met on a source by source basis (§5.4.5). I found that the standard error in each band for LBV 1806-20 was small ($<$ 0.01 mag); my photometric errors could not account for an inconsistency of $\sim$ 40Å between my measurements of the Brγ emission and that of Eikenberry et al. (2004a).

As a check on the DAOPHOT photometry, I performed aperture photometry on LBV 1806-20 in my Brγ and K_{cont} science frames using the procedure described in §5.5.1. I also completed aperture photometry on three other, isolated spectroscopically identified sources: Star 5 (a red giant), Star 22 (a WR), and Star C (an OBI). I then computed the value of $Br\gamma - K_{cont}$ for each source and compared it to the values from my PSF

photometry. I found that the $Br\gamma - K_{cont}$ colors derived from aperture photometry for Stars 2, C, 5, and LBV 1806-20 were consistent with the PSF photometry to within the PSF derived photometric errors. Thus my PSF photometry is consistent with simple aperture photometry. I conclude that the absence of the expected Brγ excess is not due to errors in my data or analysis.

5.5.2.2 Spectroscopy of LBV 1806-20

Variability of wind-driven lines in massive stars is not uncommon; LBVs, in particular, often show substantial spectroscopic variation in many emission lines including H, HI, and FeII (Humphreys & Davidson 1994). I explore the possibility that intrinsic variability accounts for the significantly lower than expected Brγ emission in my narrow-band image.

J. LaVine and V. Mikles obtained spectra of LBV 1806-20 on 17 May 2004 and 2 July 2005 using the near-infrared spectrograph SpeX (Rayner et al. 2003) on the InfraRed Telescope Facility (IRTF). For the data taken in 2004, they acquired twelve 60s images of LBV 1806-20, for a total exposure time of 720 second. For the 2005 run, they took six 90s images, for a total exposure of 540 seconds.

I reduced these data using standard SpeXTool procedure and produced flat-fielded, sky-subtracted, wavelength calibrated spectra for LBV 1806-20 for each of the two nights. Then, using Xcombspec (Cushing et al. 2004) I combined the individual images of the LBV to produce two weighted-mean LBV spectra, one for 2004 and one for 2005. Finally, I divided the corresponding atmospheric standard from the program star, multiplied the LBV spectra by a 5600 K blackbody spectra (the temperature of the standard), dereddened them using $A_v = 29$ mag and calculated the EW of all emission lines.

My resulting K-band spectra appear in Figure 5-7. A list of identified emission lines appear in Table 5-3. The EW of the spectral lines are consistent between the two epochs of observation. The only exception is Brγ; however the difference in the EWs between the two epochs is less than 3σ. More interesting are the differences between my 2004/2005

data and the 2001 spectrum of Eikenberry et al. (2004a) and 2003 spectrum of Figer et al. (2004). Both of the earlier spectra show large Brγ emission lines; Eikenberry et al. (2004a) reports an EW = $\sim$ - 40Å. However, I find Brγ EWs of $\sim$ - 7.9 $\pm$ 0.4Å in May 2004 and - 9.13 $\pm$ 0.6Å in July 2005. Even accounting for errors, this is a $> 50\sigma$ difference. Other lines show similar variability: e.g. while I find an emission line consistent with zero for HeI (2.053μm) Eikenberry et al. (2004a) report EW = - 17.4 – again, a $> 20\sigma$ difference.

The Brγ emission detected in my 2004/2005 spectra is significantly weaker than the Brγ emission in spectra observed in 2001/2003 confirming variability in the Brγ line. Furthermore, the Brγ EW derived from my 2004/2005 spectra are of the same order of magnitude as the 4 $\pm$ 2Å Brγ EW found by my narrow-band imaging survey. Obtained $\sim$ 15 and 2 months after my spectroscopy, the similarities in the imaging derived Brγ EW indicate that my narrow-band photometry is measuring a spectroscopically confirmed intrinsic variability in the Brγ emission line of LBV 1806-20.

My broad-band photometry reinforces this finding. I find $K_s = 8.56 \pm 0.01$ and $J = 13.45 \pm 0.02$ for LBV 1806-20, compared to $K = 8.89 \pm 0.06$ and $J = 13.93 \pm 0.08$ found by Eikenberry et al. (2004). Taking into account the errors and slight difference between the K- and K_s- band, my K_s measurements is noticeably brighter. This is in agreement with reported variability in LBVs, which often show strong line emission at photometric minimum and weaker lines at higher luminosities (Humphreys & Davidson 1994).

Further, given that the EW of the Brγ line may have varied by a factor of four between 2001/2003 and 2004/2005, it does not seem unreasonable that the Brγ flux could decrease by another factor of two between my 2005 spectrum and the narrow-band imaging 2 months later. Taken together, these data present clear evidence for variability of the Brγ emission over various timescales.

5.5.3 OBI stars

Eikenberry et al. (2004a) identify two OBI stars in Cl 1806-20: Stars C and D. Figer et al. (2005) confirmed these identifications and found another OBI star, Star 4, and two

OBI candidates, Star 7 and Star 11. Recently Bibby et al. (2008) obtained spectroscopy confirming all five objects as OBI stars and assigning more accurate spectral types (see Figure 5-1). While none of these authors give exact measurements for the EW of the Brγ absorptions, Figer et al. (2005) estimates an EW = 3 - 5Å for C, D, and 4 and no noticeable Brγ absorption in the spectra of Stars 7 and 11. Bibby et al. (2008) suggest their spectroscopy is consistent with the Figer et al. (2005) results.

I identify all five OBI stars on Figure 5-5 (labeled with triangles). Then, I estimated the $Br\gamma - K_{cont}$ color of each object as described in §5.4.6. Finally, inserting the narrow-band color and errors into Equation 5–5 and the resulting value of α into Equation 5–3, I calculated the Brγ absorption. The results are presented in Table 5-2.

For Star 4, I found a Brγ absorption line with an EW = 20 ± 5Å, four times that of Figer et al. (2005) and considerably larger than the line observed by Bibby et al. (2008, see their Figure 1). Located in the densest portion of the cluster, it is clear upon inspection that I have reached the confusion limit. I count several stars within my 0.3″ radius error circle and find it difficult to visually identify individual sources. Upon examining my subtracted DAOPHOT frame, I see that the program did not accurately fit Star 4 and the stars surrounding it correctly with the model PSF. This is a limit of my data and not the technique; with adequate resolution in future observations, I anticipate that I could solve these problems. Thus due to the crowding in the field, the uncertainty associated with my reported EW for this star is larger than the formal errors.

My values for the EWs of Stars C and D, while two times larger than the range reported by Figer et al. (2005), support those of Eikenberry et al. (2004a), who suggested that these objects were hypergiants: OBI stars with abnormally strong absorption lines. Furthermore, Bibby et al. (2008, see their Figure 1) show moderate absorption in Star C, consistent with my findings. Noting the lack of specific EW measurements for Star C and D in all three previous works, further discussion of these source must wait for follow-up spectroscopy.

In addition to the absorption detected in Stars C, D, I also found EW $\sim 5 \pm 1$Å for Stars 7 and 11, despite previous reports of no Brγ absorption (Figer et al. 2005). Since both stars were isolated, I performed aperture photometry on Stars 7 and 11 similar to that performed on Star 10. I found an EW $\sim$ 6Å for Star 11 and an EW $\sim$ 2Å for Star 7. Both sources of photometry for Star 11 are consistent and confirm a small Brγ absorption. While my aperture photometry of Star 7 predicts a slightly lower EW than that found from my PSF photometry, errors in the aperture photometry ($> 5\%$) exceed this difference. Thus, the values derived from both methods are in agreement. Comparing my measured values qualitatively to the spectra of Stars 7 and 11 presented by Bibby et al. (2008) (who do not provide EW measurements) suggests that my detection of a small Brγ absorption is consistent with their spectra.

5.6 New Results on Observed Stellar Populations in My Field

5.6.1 New Candidate Cluster Members

Having carefully compared my results for all cluster members identified to date in the literature, I find that my technique can identify potentially interesting objects. Most OBI and WR stars in the cluster show evidence for Brγ absorption or emission, marking them as interesting spectroscopic targets. Further, I am able to make reasonable estimates regarding the strength of the absorption or emission in these sources.

Assuming a reddening to Cl 1806-20 of $A_V = 29 \pm 2$ (Corbel & Eikenberry 2004; Eikenberry et al. 2004a)), I calculate a color of $J - K_s \sim 4.93 \pm 0.34$ mag for massive stars with no intrinsic reddening in the cluster. To search for new candidate cluster members, I examine this region of Figure 5-5, expanding my search to $J - K_s \sim 4.5$ - 5.5 mag to account for potential patchiness in the field (Corbel et al. 1997; Corbel & Eikenberry 2004), potential variations in the reddening law within the field (see Gosling et al. *in preparation*), and photometric errors in $J - K_s$ color. Finally, this range better encompassed the $J - K_s$ color of the known OBI cluster population.

Upon careful inspection of Figure 5-5 in the $J - K_s \sim 4.5$ - 5.5 mag color region, I observed no large population of stars with a noticeable Brγ emission. If a significant number of undiscovered emission line WRs existed, I would expect them to cluster near Star 22, yet my results show Star 22 to be relatively isolated. This suggests that Cl 1806-20 may not contain many undiscovered extreme WR stars.

On the other hand, I did observe ~ 10 Brγ absorbers in the region of the color-color diagram that contained several previously known OBI cluster members. These objects, potential OBI stars, are the most interesting candidates for follow-up spectroscopy and may represent the bulk of previously undiscovered massive star population in this cluster. I present the broad-band colors, Brγ absorption, and distance from the SGR in projected distance in Table 5-4. I note that a few of these objects are far from the position of the SGR; these could be massive stars not associated with Cl 1806-20 or OBI stars ejected from the cluster.

5.6.2 Foreground Stars

Given a $J - K_s$ color of ~ 5 mag for Cl 1806-20 (see §5.4.4) I expect a significant portion of stars in Figure 5-4 and 5-5 to belong to foreground populations. Given the bluer color of objects on the far left of Figure 5-4, this description particularly applies to stars in the $J - K_s \sim 0$ - 2.5 mag color range.

The spread in narrow-band colors for this foreground population is rather large, with the bulk of the stars lying between $Br\gamma - K_{cont}$ = -0.2 - 0.0 mag. I note that the majority of my faint K_s stars, with systematically larger photometric errors in all four bands, reside in this portion of the graph; thus there is more scatter in the narrow-band colors in the foreground population.

Most stars in the $J - K_s = 2.5$ - 4.5 mag region of Figure 5-4 also fit the definition of foreground star; compared to my cluster, they are notably bluer. However, given the patchy extinction in the direction of Cl 1806-20, it is also possible the some objects on the redder end of this distribution could be cluster stars. Unfortunately with the small

number of known cluster members it is very difficult to statistically determine if (for instance) an individual star in the $J - K_s = 4.3$ mag region of the plot is a potential cluster member. In the end, stars with large Brγ emission or absorption and broad-band colors similar to that of the cluster should be examined on a case-by-base basis.

Several interesting features are apparent in Figure 5-4, most notably the segregation of foreground stars into two discrete distributions centered at $J - K_s \sim 1.5$ mag and $J - K_s \sim 3.7$ mag. I will further explore these foreground stellar population along the line of sight to the cluster in the future.

5.7 Conclusion

I have demonstrated that a narrow-band imaging survey can be a useful method of searching for massive stars in a crowded field. Applying this technique to the environment of SGR 1806-20 yielded several results:

1) I confirmed the existence of known massive stars in Cl 1806-20, the host cluster of SGR 1806-20. Several of my reported EWs are in good agreement with the literature values. Where discrepancies exist, I explored the reasons. I found that in some cases, insufficient information in the literature prevented quantitative comparison. In other cases, the source of the discrepancy may be a result of intrinsic variations. In one case crowding in the field yielded a poor result. From this I concluded that better resolution is necessary to probe the most crowded regions of the cluster.

2) My narrow-band observations of LBV 1806-20 did not match the expected Brγ emission. I presented recent spectroscopy that confirms that the Brγ line is variable in LBV 1806-20. This suggests that the discrepancy between my imaging-derived EW width and that reported by Eikenberry et al. (2004a) may be a result of intrinsic variability in the Brγ emission line. Further systematic observations are required to determine the characteristic timescales and magnitude of the spectroscopic variability.

3) I did not detect any significant previously unknown WR population in Cl 1806-20. However I have identified a population of candidate OBI stars that may represent the bulk

of the missing cluster population. I suggest that these stars should be targeted for future spectroscopic observations.

Table 5-1. Summary of previous work on massive stars in Cl 1806-20. Columns give the ID, Spectral Type, and Brγ EW of Wolf Rayet stars in Cl 1806-20. All data are taken from literature sources. Values in parenthesis indicate uncertainties in the last digit of the EWs.Numbers indicate the nomenclature and reported spectral types of each author where discrepancies occur; when no numbers are given, all authors listed below are in agreement

Massive Star	Spectral Type	Brγ EW (Å)
Star B	WC9[a,b,d] ; WC9d[e]	-11(1)[b,d]
Star 10[b,d] ; Star 1[c,e]	WC9[b,d] ; WC8[c] ; WC9d[e]	-25(1)[b,d]
Star 22[b,d] ; Star 2[c,e]	WN4[b,d] ; WN6 [c] ; WN6b[e]	-43(3) [b,d]
Star 3[c,e]	WN7[c,e]	–
LBV 1806-20[a]	LBV	-44.2(3)[a]
Star 4[c,e]	09.5I[e]	–
Star 7[c,e]	B0I - B1I[e]	–
Star 11[c,e]	B0I[e]	–
Star C	B1 - B3I[e]	–
Star D	OBI[e]	–

[a] Eikenberry et al. 2004a
[b] LaVine et al. 2003
[c] Figer et al. 2005
[d] LaVine et al. *in preparation*
[e] Bibby et al. 2008

Table 5-2. Measured magnitudes, colors, and Brγ excess or absorption for massive stars in Cl 1806-20. Columns give the Star ID, J-band magnitude, K_s-band magnitude, $J - K_S$ value, calibrated $Br\gamma - K_{cont}$ color (see §5.4.6), and equivalent width (including errors; see §5.4.5) of previously identified massive stars in Cl 1806-20. Negative values indicate emission. All values are from this study. Values in parenthesis indicate uncertainties in the final digit of the listed magnitudes and colors. Where no values is given, the error $\leq$ 0.01 mag.

Star ID	J	K_s	$J - K_s$	$(Br\gamma - K_{cont})_{cal}$ (Å)	EW
Star 10	17.38(2)	11.55	5.83	0.01	2 ± 1
Star B	17.84(2)	10.66	7.19	0.11	21 ± 1
Star 22	17.29(2)	12.25	5.04	-0.20	-46 ± 1
LBV 1806-20	13.45(2)	8.56	4.89	-0.02	-4 ± 2
Star 11	16.93	11.98	4.95	0.03	5 ± 1
Star 7	16.47	11.94	4.54	0.03	5 ± 1
Star 4	16.20	11.21(2)	4.99	0.10(3)	21 ± 5
Star C	16.48	10.89	5.60	0.05	10 ± 1
Star D	15.91	11.05	4.87	0.06(2)	12 ± 3

Table 5-3. Select spectral lines in LBV 1806-20. Columns give the Line ID, rest wavelength in μm and EWs from the May 2004 and July 2005 IRTF runs.

Line ID	Wavelength (μm)	EW (May 2004) (Å)	EW (July 2005) (Å)
HeI	2.0581	0.15 ± 0.57	1.05 ± 0.6
Fe II	2.0888	0.97 ± 0.87	1.71 ± 1.00
Mg II	2.1368	2.28 ± 0.90	2.77 ± 1.13
Mg II	2.1432	1.62 ± 0.80	1.72 ± 1.20
Brγ	2.1655	7.95 ± 0.45	9.13 ± 0.58

Table 5-4. Measured magnitudes, colors, and Brγ absorption for potential OBI Stars in Cl 1806-20. Columns give Star ID, J-band magnitude, K_s-band magnitude, $J - K_S$ color, corrected Brγ - K_{cont} (see §5.4.6) Equivalent Width, and distance from SGR 1806-20. Positive values for EW indicate absorption.Values in parenthesis after $J - K_s$ and Brγ - K_{cont} indicate uncertainties in the last digit of the magnitude.

Star ID	J	K_s	$J - K_s$	$(Br\gamma\text{-}K_{cont})_{cal}$	EW (Å)	Distance $''$
6611	18.15	13.55	4.61(3)	0.04	8 ± 2	3.2
6547	16.61	11.84	4.77(5)	0.14(3)	25 ± 5	6.2
6451	17.93	13.15	4.78(4)	0.04	7 ± 2	8.7
7268	18.40	13.07	5.33(5)	0.05	9 ± 1	24.8
6556	18.51	13.35	5.16(2)	0.02	3 ± 1	26.6
6091	18.40	13.65	4.75(4)	0.04	7 ± 2	40.7
6526	17.91	13.08	4.83(2)	0.02	5 ± 1	47.1
4752	17.63	12.95	4.68(3)	0.03	5 ± 1	99.7
3971	18.48	13.16	5.33(2)	0.02	4 ± 2	121.0

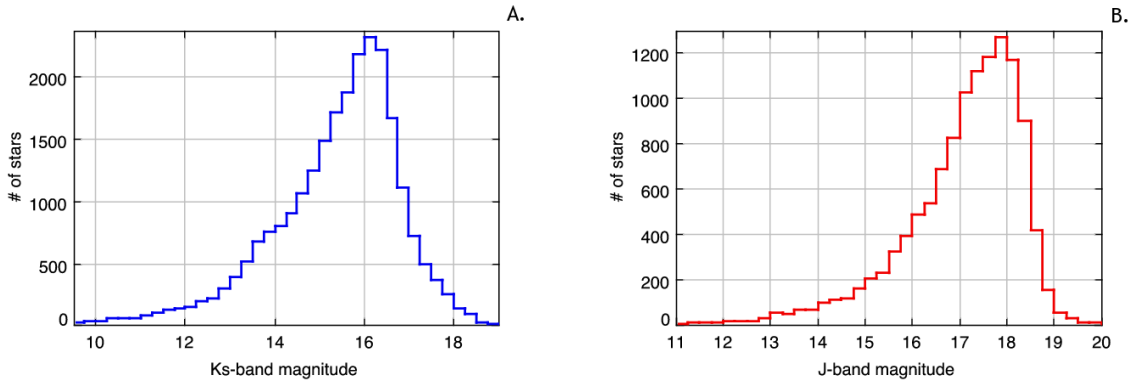

Figure 5-1. Histogram showing the number of stars at each calibrated broad-band magnitude A) K_s-band B) J-band. The bin sizes are 0.25 mag. Note the turnover at $J \sim 18$ and $K_s \sim 16$, indicating completeness (within the limits of crowding and confusion).

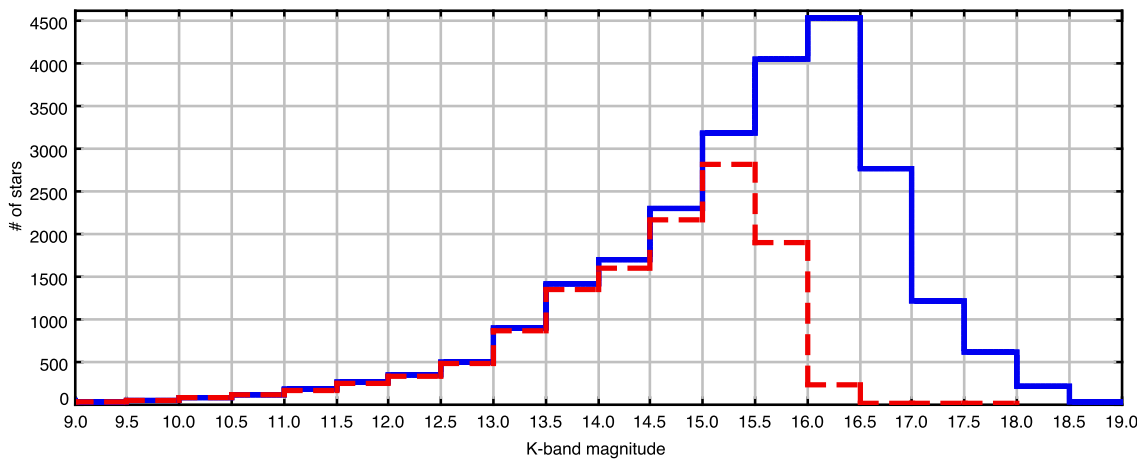

Figure 5-2. Histograms showing the number of stars at each K_s magnitude for the K_s-band catalog (solid) and the 3-band catalog (dotted). The bin sizes are 0.5 mag. Note the turnover at $K_s \sim 16$ for the K_s-band catalog and $K_s \sim 15$ for the 3-band catalog.

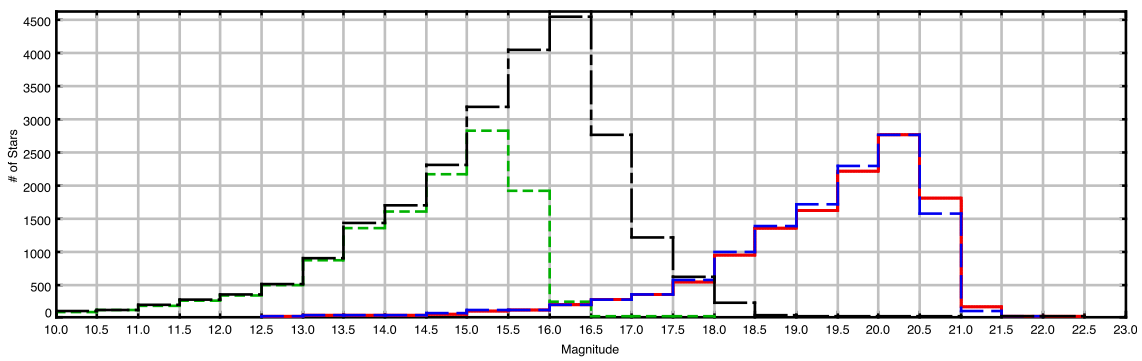

Figure 5-3. Four histograms showing number of stars in each magnitude bin vs. magnitude. The two histograms on the right show number of stars in each magnitude bin verses K_{cont} (solid) and Brγ (dashed) instrumental magnitudes. The two histograms on the left show number of stars in each magnitude bin versus K_s-band magnitude for the K_s-band catalog (dash-dot) and 3-band catalog (dotted). I note that the similar shapes for the 3-band, K_{cont}, and Brγ histograms indicates that the narrow-band data are offset from the K_s-band data by $\sim$ 5 magnitudes.

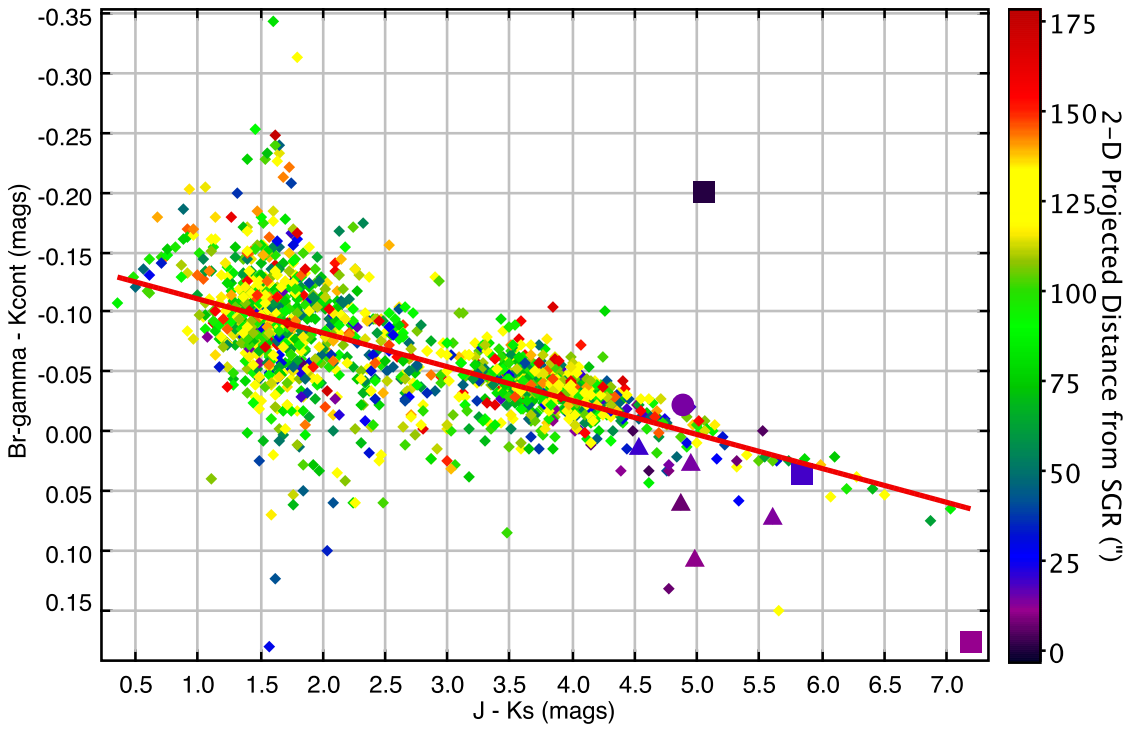

Figure 5-4. Color-color diagram of stars in my 4-band broad- and narrow- band catalog within a $6' \times 6'$ subfield centered on SGR 1806-20. The vertical axis is flipped such that negative $Br\gamma - K_{cont}$ values, which indicate Brγ absorption, appear at the top half of the graph. Objects with previously confirmed spectral types are noted; OBI stars are marked as triangles, WR stars as squares and the LBV as a circle. Color denotes projected distance (in $''$) from SGR 1806-20, with purple indicating objects closer to the SGR and yellow indicating objects further away in 2-D space. The solid black line is the narrow-band zeropoint (see §5.4.6) with m = 0.028 and b = -0.137. Bluer stars on the left of the plot with more scatter in their narrow-band colors are at the edge of my detection limits and have more Poisson noise.

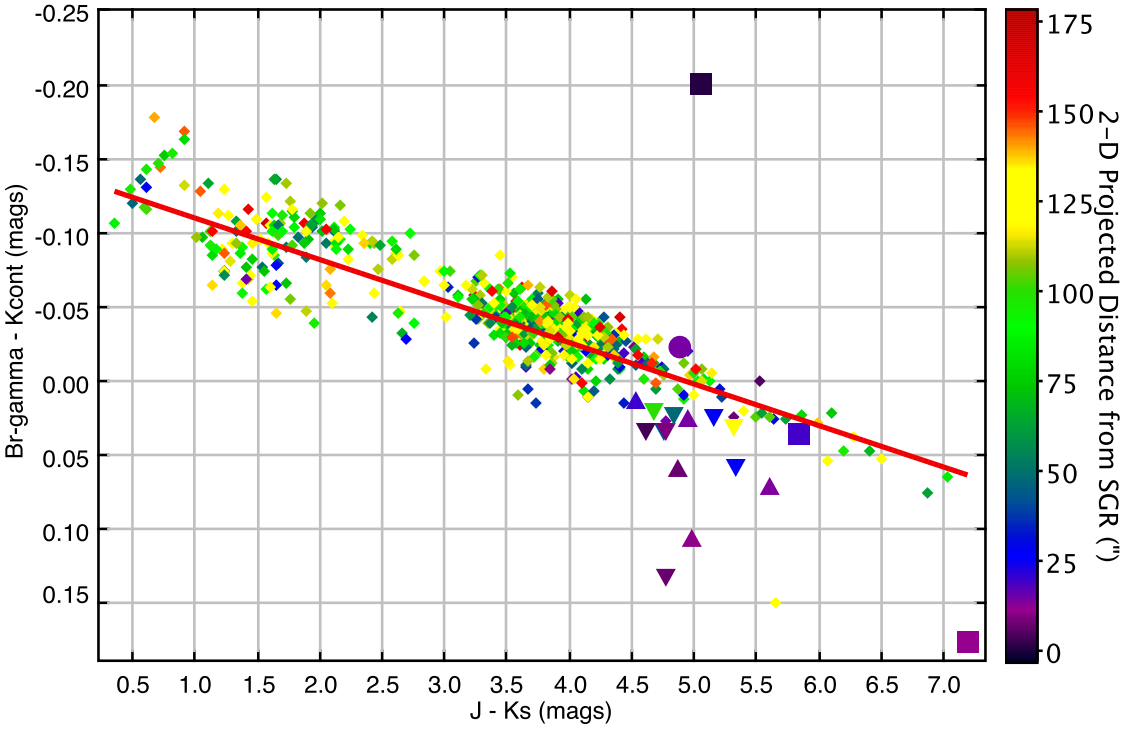

Figure 5-5. Same plot as Fig 5-6 showing all 4-band catalog objects with $K_s < 14$ magnitude. The candidate OBI stars are marked with inverted triangles (see §5.6.1).

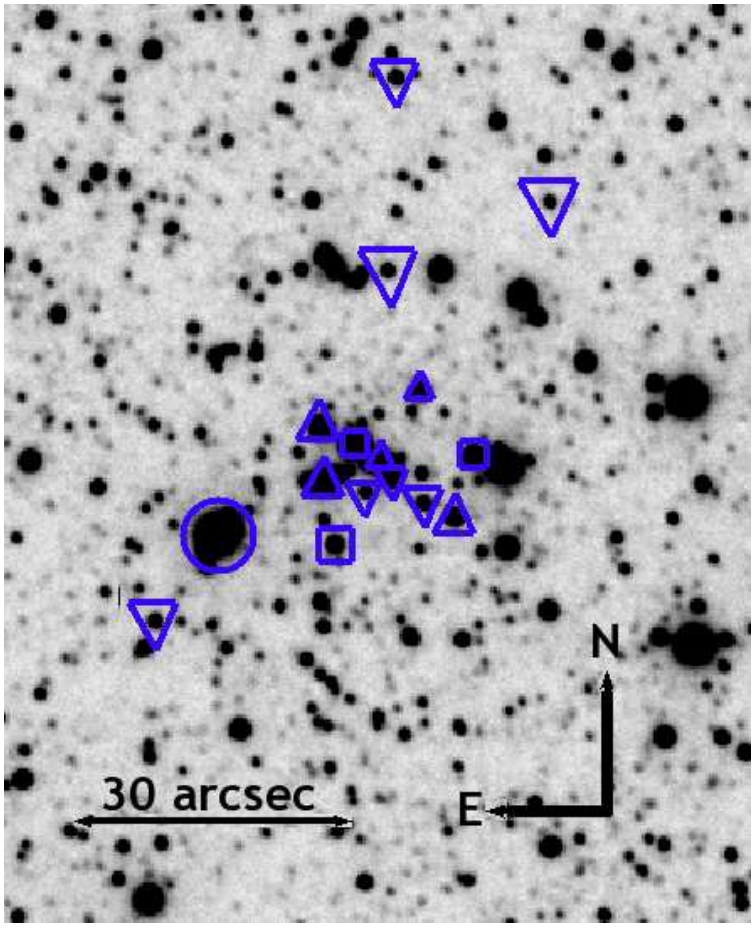

Figure 5-6. A $1.3' \times 1.5'$ region of my K_s-band image centered on Cl 1806-20. Previously discovered massive stars and newly identified OBI stars detected by this survey are indicated – OBI stars are marked as triangles, new candidate OBI stars as inverted triangles, WR stars as squares and the LBV as a circle. Two new OBI candidates (one $\sim 1.5'$ to the northwest and another $\sim 1.5'$ to the southwest of the cluster) are not shown.

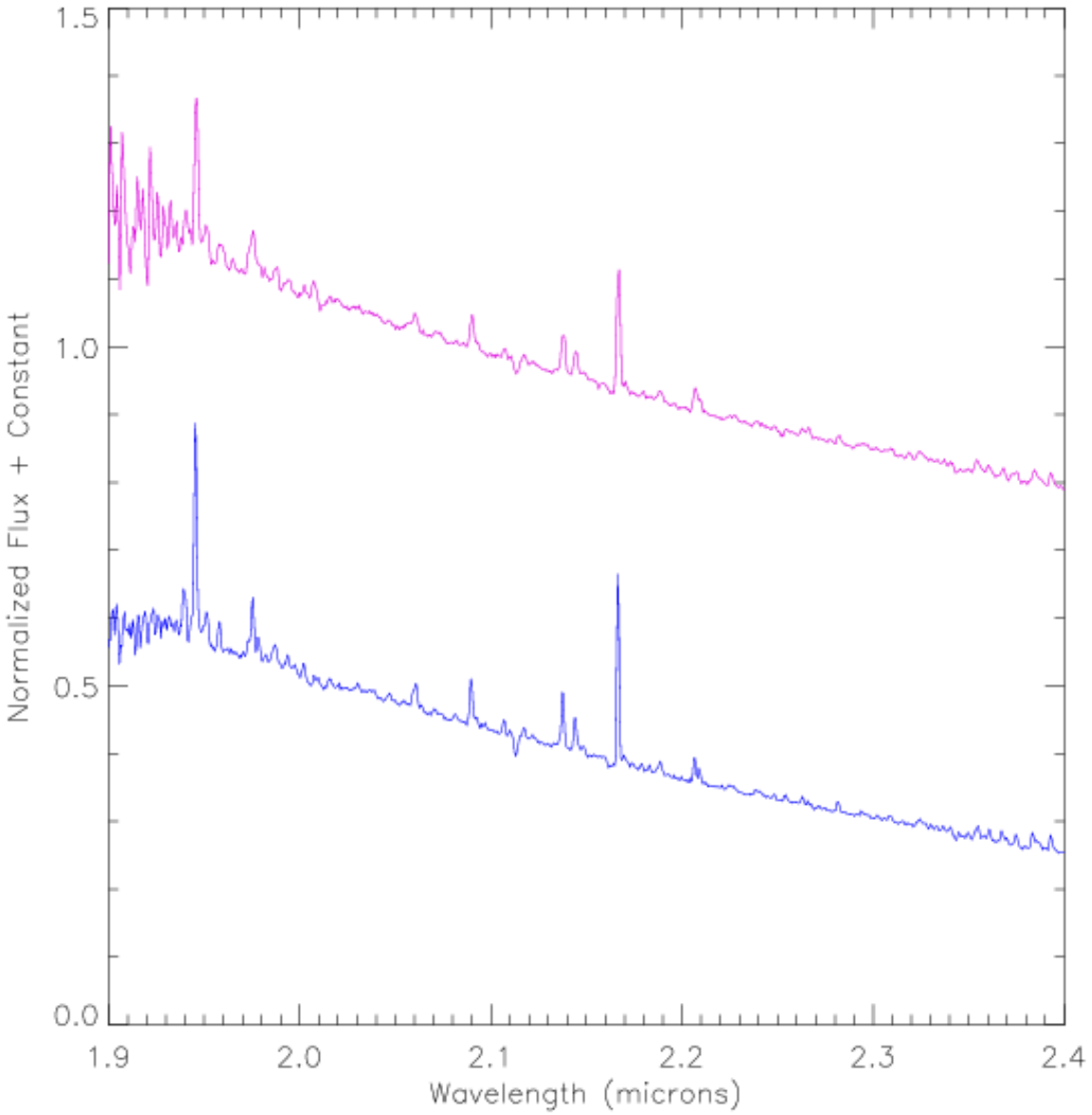

Figure 5-7. Spectra of LBV 1806-20 obtained with IRTF. The top spectrum was obtained in May 2004 and the bottom spectrum in July 2005. Each has been normalized by the last pixel and offset from each other by a constant for clarity.

CHAPTER 6
THE SEARCH FOR MASSIVE STARS AROUND SGRS 1900+14, 1627-41, AND 0526-66

6.1 Introduction

In Chapter 5, I detailed a method to search for massive stars around SGR 1806-20 using narrow-band imaging. In this chapter, I apply this technique to the three remaining Soft Gamma Repeaters: SGR 1900+14, SGR 0526-66, and SGR 1627-41. I first review previous attempts to search for clusters around each magnetar. Then, I outline my new observations, data reduction, and photometry, specifically noting where my procedure departed from that used for SGR 1806-20. Finally, I present my preliminary results and discuss potential follow-up observations.

6.1.1 SGR 1900+14

While more than 50 papers written in the the last ten years describe multi-wavelength studies of SGR 1900+14, fewer than five focus on the magnetar's environment. This relative paucity of observations has led to controversy over the membership of SGR 1900+14 in a nearby embedded cluster. First discovered by Vrba et al. (2000), the cluster consists of 11 stars hidden in the glare of two previously known M5 supergiants. Using I- and K- band photometry and assuming the same distance as that of the supergiants, they derived absolute magnitudes for the cluster stars and constructed a color-magnitude diagram. Their locations on the diagram suggests a supergiant or giant classification for many of the cluster members. Citing the small probability of finding a cluster of massive stars $12''$ from a rare compact object merely by chance, the authors concluded that the magnetar was a member of the cluster.

Problems with this picture arose when Kaplan et al. (2002) compared the reported distance and reddening of the cluster versus those of the magnetar. The hydrogen column density of the magnetar as derived from X-ray spectra yields a distance of 5 kpc and a reddening of $A_V \sim 12.8 \pm 0.8$ mag Hurley et al. (1996); Vrba et al. (1996). On the other hand, the distance to the cluster as determined by photometry of the supergiants is ~ 12

- 15 kpc and the reddening $A_V \sim 19.2 \pm 1$ mag (Vrba et al. 2000). This would suggest that the SGR is not a member of the cluster and that the superposition of the embedded cluster and magnetar is, in fact, coincidence.

This situation remained unresolved until very recently, when Wachter et al. (2008) showed that both the cluster and the SGR are embedded in a mid-IR ring or shell, most likely launched from the SGR and currently powered by the cluster stars. This is the strongest evidence to date that the magnetar is a cluster member. Furthermore, the authors calculate that reddening to the supergiants derived from 2MASS images is $A_V \sim$ 10.4 - 14.4 mag; consistent with the reddening toward the SGR. One explanation for the spread in the values of the reddening could be patchy extinction; this is particularly likely in a field with local IR emission.

Besides lingering uncertainties in the distances and reddenings, the nature and extent of the cluster has not been fully explored. To date, no one has performed spectroscopy to confirm the spectral types of the candidate massive cluster stars discovered by Vrba et al. (2000). Furthermore, the size of the MIR emission cloud enshrouding the massive stars and magnetar points to a larger cluster than that reported by Vrba et al. (2000), suggesting the existence of undiscovered massive stars Wachter et al. (2008). With the opportunity to both study previously identified OBI candidates and potentially uncover a hidden population of massive stars, 1900+14 offers an ideal opportunity to apply the method detailed in Chapter 5.

Using a narrow-band imaging survey, I will [1] probe the field surrounding SGR 1900+14 to look for undiscovered massive cluster members [2] examine the $J - K_s$ value of potential cluster stars to derive the reddening to the cluster, [3] examine the Brγ narrow-band excess of candidate massive stars identified by Vrba et al. (2000).

6.1.2 SGR 1627-41

Discovered in 1999, SGR 1627-41 is the most recent addition to the Soft Gamma Repeater class (Woods et al. 1999). Located at a distance of 11.0 ± 0.3 kpc, it is the most

heavily reddened of all the SGRs with $A_V \sim 43$ mag (Corbel et al. 1999). SGR 1627-41 is also the least studied of the SGRs; no papers concerning the environment surrounding SGR 1627-41 exist in the literature. Thus, my narrow-band observations of this field are the first effort to search for a cluster associated with the SGR.

6.1.3 SGR 0526-66

Located in the LMC, SGR 0526-66 was the first magnetar to burst onto the scene in 1979, emitting a giant flare with a peak luminosity $> 10^{44}$ ergs s^{-1} (Mazets et al. 1979). Although centrally located in supernova remnant N49, the magnetar's association with the remnant is questionable; Kaplan et al. (2001) suggest an age of 1000 yr for the SGR, while the SNR is most likely 5000 - 16000 years old (Shull 1983; Vancura et al. 1992).

While no massive cluster appears hidden by the remnant, Klose et al. (2004) report the existence of a massive cluster, SL463, $2'$ north of the SGR. Using H- and K- band photometry, the authors construct a color-magnitude diagram and find main sequence OB spectral types for ~ 30 potential cluster stars. They also derive a reddening of $A_V \sim 3.2$ mag to SL463. Although separated by a 30 pc projected distance, the authors suggest that SL463 is most likely associated with the magnetar, arguing that the ejection of either the SGR or SGR progenitor from the cluster can account for the magnetar's current location.

Currently, no follow-up observations of the findings in Klose et al. (2004) exist in the literature. My narrow-band observations of the field surrounding SGR 0526-66 are therefore the first attempt to locate OBI supergiants or emission-line stars enshrouded in the cluster or located in the field between the cluster and the magnetar. Finding these objects would make the cluster's stellar content more analogous to Cl 1806-20 and possibly strengthen the proposed association between the cluster and the magnetar.

6.2 Application of the Narrow-band Imaging Technique

In §5.2, I extensively detail a technique to search for massive members of Cl 1806-20 using narrow-band imaging. In this chapter, I apply this technique to SGR 1900+14, SGR 0526-66, and SGR 1627-41. In the case of SGR 1900+14, also observed with WIRC,

I follow the exact same procedure that I used for SGR 1806-20. However my method is slightly different for SGR 1627-41 and SGR 0526-66 , which I observed with the InfraRed Side Port Imager (ISPI) on the CTIO 4-meter telescope. ISPI has dedicated continuum filters with central wavelengths very close to the central wavelengths of the "science" bands: the K_{cont} filter for HeI 2.06μm is centered at 2.03μm while K_{cont} for Brγ 2.16μm is centered at 2.14μm. This small difference in the central wavelengths between the science band and its continuum results in a negligible difference in the dust penetration between the two narrow-band images.

Since the narrow-band color is no longer a function of reddening, it was not necessary to obtain J or K_s broad-band images of either of the fields surrounding these clusters. Instead, I will examine the $Br\gamma - K_{2.14}$ color versus the $K_{2.14}$ magnitude for each star in the field. Stars with no Brγ emission or absorption should fall on a horizontal line with a $Br\gamma - K_{2.14}$ value equal to the differences in the transmission between the two filters. Any stars with excess or absorption will fall above or below this "zerpoint" line. I will use the distance from the line to calculate the EWs of any absorption or emission detected.

I will also examine the $HeI - K_{2.03}$ versus $K_{2.03}$ color- magnitude diagram and look for stars with HeI excess or absorption. Since some types of massive stars display both $Br\gamma$ and HeI features in their spectra (Hanson et al. 1996), I can correlate my results to see which stars have emission or absorption in both lines, objects in this category will be strong candidates for follow-up spectroscopy. I discuss the advantages and disadvantages of this technique in §6.4.2

6.3 Observations and Data Reduction

On 2005 August 26-27, I used the Wide Field Infrared Camera (Wilson et al. 2003, WIRC) on the Palomar 200" telescope to obtain J, K_s, 2.16μm Brγ, and 2.27μm K_{cont} images of an $8.7' \times 8.7'$ region around SGR 1900+14. Applying standard techniques for near-infrared (NIR) observing, I used a random 9-point dither pattern with $< 30''$ separation between each image to obtain the K_s, $K_{2.27}$, and Brγ data. I took three 30

second images at each position, resulting in 27 frames. The total exposure times were $\sim$ 8 minutes in Brγ and $K_{2.27}$ and $\sim$ 90 seconds in K_s. Similarly, I obtained 3 exposures at 5 random dither positions with $< 30''$ separation between images, resulting in a 65 second exposure in the J-band.

On 2005 March 12-13, I used the Infrared Side Port Imager (ISPI) on the Cerro Tololo Inter-American Observatory (CTIO) 4 meter telescope to obtain 2.16μm Brγ, 2.14μm K_{cont}, 2.06μm HeI, and 2.03μm K_{cont} images of $10.5' \times 10.5'$ regions around SGR 1627-41 and SGR 0526-66.

For SGR 1627-20, I used a random 9-point dither pattern with $< 30''$ separation between each image. Again, I took three 30 second images at each pointing. I then moved the telescope slightly ($< 15''$) and repeated this procedure 4 - 5 times using a different random dither pattern. This resulted in a total of 135 images in the HeI and $K_{2.03}$ bands and 162 images in the Brγ and $K_{2.14}$. After examining the images and discarding any with obvious defects caused by wind-shake, etc. the total exposure times were $\sim$ 80 minutes in Brγ and $K_{2.14}$ and $\sim$ 70 minutes in $K_{2.03}$ and HeI.

For SGR 0526-66, I used a random 11-point dither and took one 100s exposure in each position for Brγ and $K_{2.14}$. After discarding images with defects, the total exposure time was $\sim$ 25 minutes in each band. For the $K_{2.03}$ and HeI observations, I returned to the 9-point dither pattern described above. The total exposure times were $\sim$ 35 minutes in $K_{2.03}$ and HeI.

As described in Chapter 5, I reduced all data using FATBOY (Warner et al.*in preparation*), which performed standard data reduction tasks, including dark and sky subtracting, flat fielding, and combining of the dithered images, to produce final reduced science frames. I performed one additional step on my SGR 1627-41 observations: distortion correction using the IRAF package MSCTPEAK. I explore the reasons for this in §6.4.2.1.

I then performed astrometry on these images using TFINDER in IRAF. For each field, I used 500 stars to tie the four science frames to the 2MASS K-band image of the region. This yielded excellent astrometric ties between the 2MASS images and each of the four science frames and between the four science frames themselves. I discuss the results of the astrometric frame-tie in §6.4.

6.4 Analysis

Here, I present a summary of the analysis of the three SGRs discussed in this chapter, offering details only when my methods deviate from those described in Chapter 5. In summary, I performed PSF photometry using DAOPHOT on the images in each filter resulting in four photometric catalogs per magnetar. I matched stars across bands using TOPCAT. Then, I identified "drop-outs"– sources that appear in one band, but are absent from one or more of the remaining bands. I carefully checked to ensure that these missing objects were not signs of mismatched tables or other major systematic errors that would affect my results. Once I was satisfied that my catalogs were correct, I narrowed my search area by applying magnitude and field size constraints. Finally, using the error output by DAOPHOT and the values of $Br\gamma - K_{cont}$ and $HeI - K_{2.03}$ computed from the catalogs, I calculated the equivalent widths of stars in the field surrounding the SGR.

6.4.1 Analysis of 1900+14

6.4.1.1 Photometry

I performed PSF photometry on 9654, 11396, 10861, and 9366 stars in the SGR 1900+14 Brγ, $K_{2.27}$, K_s-band, and J-band images using DAOPHOT and ALLSTAR. Using the standard error output by ALLSTAR, I calculated the median error in each band. I found errors of 0.07, 0.04, 0.05, and 0.05 mag in the J-, K_s-, $K_{2.27}$-, and Brγ-bands respectively. I discuss the errors associated with this technique in greater detail in §6.4.1.5. Next, I calibrated the J and K_s magnitudes for my sources using 2-MASS photometry. I chose 20 isolated stars with a range of magnitudes from the 2MASS image of my field and matched them with their counterparts in my science frames. Starting

with the K_s-band, I calculated the difference between my ALLSTAR magnitude and the 2MASS magnitude for each star, found the median value of the offset, and applied it to the remainder of my K_s-band data. I repeated this process for the J-band photometry.

6.4.1.2 Star matching

Upon completing the astrometry for SGR 1900+14 using TFINDER in IRAF, I chose 50 isotropically distributed stars in one frame, found their counterparts by eye in the other 3 frames, and recorded their coordinates on all four images. I then calculated the average offset between these positions, which is a measure of the astrometric accuracy between the frames. I found an offset $0.09 \pm 0.08''$ between the Brγ and $K_{2.27}$ frames, $0.13 \pm 0.9''$ between the J and K_s images, and $0.09 \pm 0.08''$ between Brγ and K_s. This was in good agreement with the errors reported by IRAF between each frame and the 2MASS image used to complete the astrometry.

Using TOPCAT, I matched the four photometric catalogs for SGR 1900+14. I used a $0.4''$ radius to match $K_{2.27}$ (RA, Dec) to Brγ (RA, Dec) and $0.4\ ''$ radius to match J-band (RA, Dec) to K_s-band (RA, Dec) for all detected stars. I then matched the two tables to each other, using Brγ and K_s-band coordinates and a $0.4''$ radius. I calculated these radii from the astrometric errors using the error radius plus 3σ. Optimally, I would have matched all four bands simultaneously, however TOPCAT was unable to perform this match directly given the size of the data sets.

I found 5274 J-band counterparts to K_s-band sources, 7866 $K_{2.27}$ counterparts to Brγ sources and 4574 sources with matches across all four bands. I discuss these statistics further in §6.4.1.3.

6.4.1.3 Limiting magnitudes and match drop-outs

Using the 2MASS calibrated photometric catalogs, I determined the limiting magnitudes for the J- and K_s- band images of the field surrounding SGR 1900+14. In Figure 6-1 I present histograms of both K_s-band magnitude and J-band magnitude versus number of stars at each magnitude. These distributions peak at $K_s \sim 15.5$ mag

and $J \sim 17.5$ mag. As potential OBI supergiants in the cluster will fall between $\sim$ 13 - 16 mag in the J-band (Vrba et al. 2000), I confirmed that my J-band photometric limits are deep enough to observe known cluster members in the J-band.

To confirm that my K_s-band photometric limit is adequate to detect potential massive cluster stars, I estimated K_s-band magnitudes using known J-band magnitudes of candidate OBI stars in the embedded cluster. Given that the values for the reddening toward the cluster range from $A_V \sim 10.4$ - 19.2 (Vrba et al. 2000; Wachter et al. 2008), I expect a minimum $J - K_s$ value of approximately 2 magnitudes for stars in the cluster. Assuming an intrinsic $J - K_s \sim 0$ for OBI stars (Cox 2000), I anticipate massive cluster members to be at least 2 magnitudes brighter in the K_s-band than the J-band. Therefore, the most conservative values for the reddening predict that the massive stars in the cluster will fall between $\sim$ 11 - 14 mag in the K_s-band, well within my photometric limits.

As with Cl 1806-20, I found a considerable number of drop-outs each time I matched catalogs. Drop-outs are defined as sources that appear in one band, but are absent from one or more of the remaining bands. In §5.4.3, I discuss a variety of reasons for drop-outs in the Cl 1806-20 data. I found that drop-outs are most likely [1] stars at the field edges missing from one or more images due to small variations in the central positions of the field-of-view between frames or [2] very faint stars at the detection limits of one or both bands. In both cases these are unlikely to be the bright supergiants or emission-line stars that I am searching for here. While in Cl 1806-20, a small percentage of drop-outs were potentially interesting objects in the most crowded regions of the field, it was obvious that adjusting detection thresholds in DAOPHOT to find every star in the frame would simply result in a large number of incorrect matches and spurious detections of background noise. After completing a similarly extensive review of the drop-outs between each band in the SGR 1900+14 catalogs, I come to similar conclusions, which I detail below.

The largest number of drop-outs occurred between the J- and K_S- band match. Finding K_s-band sources with no J-band counterpart was unsurprising; since longer

wavelengths are more efficient at penetrating dust I expected many of the K_s stars to be highly obscured and thus undetected in the J-band. However, I noted that a number of ($\sim$ 4000) J-band sources were missing from the J- and K_S- band match. After examining both the J- and K_s- band limiting magnitudes in each individual catalog compared to the 2-band match, I found that the majority of these drop-outs were dim J-band stars with no K-band counterparts. These stars, with a median J-band magnitude = 18.5 are > 2 magnitudes dimmer than any massive star currently known in the cluster. Thus, these drop-outs should not affect my results.

I then inspected the drop-outs in my Brγ and $K_{2.27}$ band match. Given the slightly longer central wavelength of the $K_{2.27}$ filter, I expected to find some unmatched faint $K_{2.27}$ sources. However, I also found $\sim$ 2000 Brγ dropouts. After analyzing histograms of narrow-band magnitudes versus star counts and images of the stars on each frame, I found that the majority of the unmatched sources are faint objects at the detection limits of both filters. Thus, slight difference in limiting magnitudes accounted for the majority of missing counterparts between the two narrow-bands.

Finally, I looked for drop-outs in my 4-band match. I found $\sim$ 700 drop-outs between the J- to K_s- band catalog to the final 4-band match. As with the Cl 1806-20 data, I concluded that the majority of these are caused by a drop in the sensitivity of my narrow-band data due to differing integration time; my narrow-band observations were too short to reach the same limiting magnitude as my broad-band imaging. However, given the expected brightness of potential massive cluster stars ($K_s < 14$) as discussed in the beginning of this section, this magnitude limit for my narrow-band imaging should not adversely affect my results.

6.4.1.4 Field selection

My observations of the three SGRs discussed in this chapter encompass 8 - 10′ fields centered on the magnetars. However, in the case of SGR 1900+14, where a large massive

cluster has already been detected near the magnetar, I can narrow my search for massive stars by considering a subregion of my data.

I chose the subregion around 1900+14 using the estimates of the Galactic massive star clusters whose stellar contents, ages, and (potentially) masses are similar to Cl 1806-20. These were discussed in detail in §5.4.4. At 12 kpc, the "middle" distance estimate to the cluster associated with SGR 1900+14, a search area with a 16pc diameter corresponds to a $\sim 2.5'$ radius centered on the magnetar. If the SGR is at the ~ 5 kpc distance suggested by Hurley et al. (1996), my search area would correspond to a 7 pc diameter search area; still large enough to contain all but the most extreme outliers.

I present the color-color diagram for stars within a $5'$ diameter of SGR 1900+14 in Figure 6-2. I note that the $J - K_s$ color is a distance and reddening indicator; objects on the left of the graph are bluer and therefore most likely located in the foreground, while objects to the far right are heavily reddened. Since $A_K = 0.112A_V$ and $A_J = 0.282A_V$, I can use the conflicting reddening values to help constrain potential search areas for the cluster. Using an A_V = 10.4 - 14.4 for SGR 1900+14, (Wachter et al. 2008) I find $J - K_s$ = 1.8 - 2.5 mag. For an $A_V = 19.2 \pm 1$ for SGR 1900+14 (Vrba et al. 2000) I find a $J - K_s = 3.3 \pm 0.2$ mag. I discuss my results in §6.5.1.

6.4.1.5 Calculating errors and equivalent widths

Using my newly created four-band catalog and the errors output by ALLSTAR, I calculated the error in the $Br\gamma - K_{cont}$ narrow-band color for every star in the $5'$ diameter subregion. I found an average error of 0.04 mag corresponding to $\sim 4\%$ photometry; the limit necessary to allow for 3σ detections of modest Brγ emission and absorption lines (§5.2). This error is lower than the median errors calculated using the entire field. As with Cl 1806-20, the elimination of dim stars (a by-product of the catalog matching) and slightly distorted stars (by the application of a subfield) accounted for this decrease.

Once I determined that my global photometry satisfied the 4% criterion, I assessed my error on a more source-specific scale. I computed the errors in the $J - K_s$ and

$Br\gamma - K_{cont}$ colors for every star in my 4-band catalog using the errors output by ALLSTAR. If a particular source displays emission or absorption but a large error in either color, I can use these errors to evaluate whether it is still a good candidate for follow-up spectroscopy. I discuss this in more detail in the sections below.

In Figure 6-2, I note a linear correlation between the $J - K_s$ color and $Br\gamma - K_{2.27}$ color of sources in the field. Since longer wavelengths penetrate dust more efficiently, the $K_{2.27}$ filter, centered at a longer wavelength than the Brγ filter, systematically detected more flux, even if no intrinsic excess or absorption existed. The size of this effect depends on the extinction along the line-of-sight; the slope of the line is therefore an indicator of the varying reddenings and distances of objects in the field-of-view.

Using TOPCAT, I fit a line with slope (m) = 0.021 and y intercept (b) = -0.143 to the data. This line is a "zeropoint"; it defines the expected value of $Br\gamma - K_{cont}$ for a star with neither Brγ absorption nor emission. Using this linear equation, the $Br\gamma - K_{cont}$ values of stars in my catalog, errors in the narrow-band and broad-band color, and the technique described in §5.4.6, I calculated the equivalent widths and associated error for potential massive star candidates. I present these results in §6.5.1

6.4.2 Analysis of 1627-41

6.4.2.1 Departures from the standard technique: distortion correction and field selection

In §6.2, I outlined a departure from the original method used to search for massive stars around SGR 1900+14 and SGR 1806-20. While this technique continues to use narrow-band colors to find emission or absorption indicative of massive stars, I use two narrow-band "color-magnitude" diagrams: $HeI - K_{2.03}$ versus $K_{2.03}$ and $Br\gamma - K_{2.14}$ versus $K_{2.14}$ instead of a 4-band "color-color" diagram, to search for massive stars.

One advantage of this method is the ability to correlate the results; since some massive stars exhibit both HeI and Brγ spectral features (Hanson et al. 1996), evidence of emission or absorption in both the $HeI - K_{2.03}$ and $Br\gamma - K_{2.14}$ color-magnitude

diagrams may indicate a strong candidate for follow-up spectroscopy. This is, however, not a requirement for establishing massive star candidacy; many massive stars do not exhibit features in both lines.

Unlike the other magnetars in my study, I search for massive stars across the entire $10.4' \times 10.4'$ field surrounding SGR 1627-41. Since this is the first attempt to find massive stars associated with the magnetar, I do not want to exclude any region from my analysis. This is particularly important given possible formation scenarios of magnetars; it is not unreasonable for a supernova associated with the death of a massive star to eject the resulting compact object from its natal cluster.

The decision to survey the entire ISPI frame resulted in an extra step in the reduction of the SGR 1627-41: the application of a distortion correction. Upon examining my unreduced ISPI data, I noted a significant distortion of stellar PSFs in the outer regions of my images. This distortion not only affects the location of the central pixel in each star, limiting my ability to perform accurate frame-ties, it increases errors in the PSF photometry.

I completed a distortion correction for each of my narrow-band filters using the TFINDER package in IRAF. I did not perform this correction on my final image; instead I used one of the flat-fielded, dark- and sky- subtracted frames produced by FATBOY. I then applied this correction to approximately 150 reduced frames per filter before drizzling them together to create the final science frame. This resulted in tighter stellar profiles in every dithered image, ensuring that the PSF in the final frame was not artificially inflated by the superposition of many irregularly shaped distorted stars.

6.4.2.2 Photometry and band matching

I performed PSF photometry on 23284, 25487, 17371, and 19268 stars in the SGR 1627-41 Brγ, $K_{2.14}$, HeI, and $K_{2.03}$ band images using DAOPHOT and ALLSTAR. I calculated median errors of 0.05, 0.05, 0.04, and 0.04 mag across the Brγ, $K_{2.14}$, HeI, and $K_{2.03}$ bands respectively.

Upon completing astrometry for SGR 1627-41 using TFINDER in IRAF, I calculated the astrometric error as described in §6.4.1.2. I found an average offset of 0.18 ± 0.09 between the Brγ and $K_{2.14}$ frames, 0.12 ± 0.07 between the HeI and $K_{2.03}$ images, again in good agreement with the errors reported by IRAF between each frame and the 2MASS image used to complete the astrometry.

Using TOPCAT, I matched the photometric catalogs for SGR 1627-41. I used a 0.5″ radius to match $K_{2.14}$ (RA, Dec) to Brγ (RA, Dec) and 0.4 ″ radius HeI (RA, Dec) to $K_{2.03}$-band (RA, Dec) for all detected stars. I calculated these radii from my astrometric errors using the error radius plus 3σ. Since I was not creating a color-color plot, I did not need a four-band match for my primary analysis, however, I did match the two narrow-band tables to simplify my search for stars with both HeI and Brγ features (§6.2. I used a radius of 0.4″ for this match. I found 14620 $K_{2.03}$ counterparts to HeI sources, 19043 $K_{2.14}$ counterparts to Brγ sources, and 13507 sources with matches across all four bands. I discuss these statistics further in §6.4.2.3.

I present my $HeI - K_{2.03}$ versus $K_{2.03}$ and $Br\gamma - K_{2.14}$ versus $K_{2.14}$ diagrams in Figures 6-3 and 6-4.

6.4.2.3 Limiting magnitudes and match drop-outs

One disadvantage of eschewing J- and K_s- band photometry in favor of a second set of narrow-band observations is the lack of a universally available photometric catalog to calibrate narrow-band data. For my analyses of SGR 1806-20 and SGR 1900+14, I calibrated my instrumental broad-band magnitudes using 2MASS. I then used these results to estimate the limiting magnitudes of my images and compared them to the magnitudes of potential cluster stars. Thus, I could assure that my photometry was deep enough to observe any potential massive stars. The uncalibrated instrumental magnitudes output by DAOPHOT for the stars surrounding SGR 1627-41 do not allow for such an assessment.

To address this issue, I compared my narrow-band data with 2MASS broad-band images. Using the distance to and reddening of the cluster, I calculate that a typical OBI star with an absolute magnitude $M_K \sim 6$ mag will have an apparent magnitude $m_k \sim 14$ mag. I found 25 stars in my field with a K_s-band magnitude ~ 14.5 in the 2MASS catalog. I then located these stars in my 4-band match and recorded the magnitude of each object in all four bands. I found that the mean instrumental magnitudes of ~ 14.5 magnitude 2MASS stars in my Brγ, $K_{2.14}$, HeI, and $K_{2.03}$-images are 21.0, 20.8, 21.2, and 21.0 respectively. This is brighter than the 22.0 mag limiting instrumental magnitude of all four bands. While this calibration is by no means extensive, it suggests that my observations are deep enough to observe most massive stars around SGR 1627-41, should they exist.

I then examined drop-outs within my two narrow-band catalogs. I determined that in most cases, the drop-outs resulted from a slight difference in the limiting magnitudes of the narrow-band filters. The vast majority of drop-outs are very faint, beyond the limiting instrumental magnitude in each frame. Considering the magnitude arguments established above, it is unlikely that these drop-outs will affect my results.

6.4.2.4 Photometric errors and equivalent width calculations

The median error in both the $Br\gamma - K_{2.14}$ and $HeI - K_{2.03}$ colors for SGR 1627-41 is 0.06 mag, slightly larger than the errors reported for other fields in this study. I hypothesize that my initial decision to survey the entire field surrounding SGR 1627-41 caused the elevation in my photometric errors. I noted that distortion effects, which could result in poor PSF fits and therefore larger errors, persisted at the edges of the final frame despite my distortion correction. I discuss this issue in greater detail in §6.5.2.

These errors may also reflect the different technique applied to the field surrounding SGR 1627-41. Since this method uses $Br\gamma - K_{2.14}$ versus $K_{2.14}$ and $HeI - K_{2.03}$ versus $K_{2.03}$ diagrams, I produced two 2-band catalogs as opposed to one 4-band match. The 4-band catalogs, used to create "color-color" diagrams for SGR 1900+14 and SGR

1806-20, excluded thousands of the dimmest sources in every band. The inclusion of these faint objects in the 2-band catalogs used to calculate the color error for the SGR 1627-41 data increased the total Poisson noise, potentially resulting in the 0.06 mag median errors.

Given that my global errors are larger than the 4% criterion established to yield 3 - 4 σ detections of moderate narrow-band emission and absorption lines, I placed more weight on the $Br\gamma - K_{2.14}$ and $HeI - K_{2.03}$ errors that I calculated for each source. As with the other clusters, I ultimately used these values to determine whether a star was a viable candidate for follow-up spectroscopy.

Finally, I calculated the EWs of stars in my color-magnitude diagrams. Unlike the color-color diagrams used for SGR 1806-20 and SGR 1900+14, the "zeropoint" line in Figures 6-3 and 6-4 are independent of reddening and therefore have a slope (m) ~ 0. Since the majority of sources do not have Brγ or HeI spectral features, their narrow-band colors should be zero. However, an offset, (Y) indicative of the transmission differences between the filters, is evident upon inspection of both color-magnitude diagrams. To find this offset, I calculated the median value of each of the narrow-band colors for all objects in the field. I found Y = 0.17 for $Br\gamma - K_{2.14}$ and Y = 0.24 for $HeI - K_{2.03}$. To find the calibrated color of my sources, I subtracted the corresponding value of Y from the $HeI - K_{2.03}$ or $Br\gamma - K_{2.14}$ value of each star. I then calculated the EWs and errors using the techniques described in §5.4.6. I present these results in §6.5.1

6.4.3 Analysis of 0526-66

6.4.3.1 Photometry and band matching

I performed PSF photometry on 1473, 1604, 1097, and 984 stars in the SGR 0526-66 Brγ, $K_{2.14}$, HeI, and $K_{2.03}$ band images using DAOPHOT and ALLSTAR. I calculated median errors of 0.1, 0.1, 0.15, and 0.15 mag across the Brγ, $K_{2.14}$, HeI, and $K_{2.03}$ bands respectively. I attribute these large errors to the overabundance of very faint stars in the field, which I discuss further in §6.4.3.3.

Upon completing astrometry for SGR 0526-66 using TFINDER in IRAF, I calculated the astrometric error as described in §6.4.1.2. I found an average offset of 0.20 ± 0.07 between the Brγ and $K_{2.14}$ frames, 0.07 ± 0.07 between the HeI and $K_{2.03}$ images, again in good agreement with the errors reported by IRAF between each frame and the 2MASS image used to complete the astrometry.

Using TOPCAT, I matched the photometric catalogs for SGR 1627-41. I used a 0.5″ radius to match $K_{2.14}$ (RA, Dec) to Brγ (RA, Dec) and 0.3 ″ radius HeI (RA, Dec) to $K_{2.03}$-band (RA, Dec) for all detected stars. I calculated these radii from my astrometric errors using the error radius plus 3σ. Like SGR 1627-41, I used two color-magnitude diagrams to analyze the stars surrounding SGR 0526-66. Since I was not creating a color-color plot, I did not need a four-band match for my primary analysis, however, I did match the two narrow-band tables to simplify my search for stars with both HeI and Brγ features (§6.2. I used a radius of 0.4″ for this match. I found 840 $K_{2.03}$ counterparts to HeI sources, 942 $K_{2.14}$ counterparts to Brγ sources, and 588 sources with matches across all four bands. I discuss these statistics further in §6.4.2.3.

I present my $HeI - K_{2.03}$ versus $K_{2.03}$ and $Br\gamma - K_{2.14}$ versus $K_{2.14}$ diagrams in Figures 6-5 and 6-6

6.4.3.2 Limiting magnitudes and match drop-outs

Without J- and K_s- band photometry I could not easily determine whether the narrow-band observations of SGR 0526-66 were deep enough to detect massive stars around the magnetar. However, unlike SGR 1627-41, SGR 0526-66 has a potential associated massive cluster, SL 463, with one OBI candidate. This star has a reported K-band magnitude $\sim$ 12 mag (Klose et al. 2004). Thus, if my observations reach this depth, I can be assured that I will detect other potential massive cluster stars, should they exist.

I compared my narrow-band frames to 2MASS broad-band images to find a rough offset between standard 2MASS K_s-band magnitudes and my instrumental

magnitudes. I chose 25 isolated stars in my field with a broad distribution of 2MASS K_s- band magnitudes. I then located these stars in my 2-band catalogs and recorded the instrumental magnitude of each object in all four bands. I found a ~ 6.5 magnitude offset between the 2MASS K_s- band magnitudes and my instrumental magnitudes, approximately the same offset for the SGR 1627-41 data. This yielded an expected narrow-band instrumental magnitude of 18.5 mag for a 12 mag star, well within the 22.5 mag limiting instrumental magnitude for the $K_{2.03}$ and $K_{2.14}$ bands and 23 mag limiting instrumental magnitude for the HeI and $Br\gamma$ bands.

I then examined drop-outs within my two narrow-band catalogs. Again, I determined that in most cases, the drop-outs resulted from a slight difference in the limiting magnitudes of the narrow-band filters. The vast majority of drop-outs are very faint, beyond the limiting instrumental magnitude in each frame. Considering the magnitude arguments established above, it is unlikely that these drop-outs will affect my results.

6.4.3.3 Field selection, errors, and equivalent widths

As mentioned in §6.1.3, SL463, the potential natal cluster of the SGR, is located $2'$ away from SGR 0526-66. Thus, I chose a $4'$ search radius centered around the SGR that encompassed both the cluster and the magnetar. Using the errors output by ALLSTAR for the stars in this subfield, I computed a 0.04 mag median error for both the $Br\gamma - K_{2.14}$ and $HeI - K_{2.03}$ colors. This met the 4% criterion required to detect moderate spectral features in massive stars to a 3σ level. I then computed the errors in the $J - K_s$ and $Br\gamma - K_{cont}$ colors for every star in my 4-band catalog using the errors output by ALLSTAR.

Finally, I calculated the EWs of stars in my color-magnitude diagrams, which I present in Figures 6-5 and 6-6. Like SGR 1627-41, both narrow-band colors are offset from zero, representing transmission differences between the bands. To find this offset, I calculated the median value of each of the narrow-band colors for all objects in the field. I found Y = 0.27 for $Br\gamma - K_{2.14}$ and Y = 0.22 for $HeI - K_{2.03}$. To find the calibrated

color of my sources, I subtracted the corresponding value of Y from the $HeI - K_{2.03}$ or $Br\gamma - K_{2.14}$ value of each star. I then calculated the EWs and errors using the techniques described in §5.4.6. I present these results in §6.5.3

6.5 Preliminary Results

6.5.1 SGR 1900+14

To better identify previous cluster candidates and find new potential cluster members, I further constrain my search to stars with $K_s \leq 14.2$. I show the resulting plot in Figure 6-7. Using the most conservative estimate for the reddening, I anticipate that stars in the cluster should have K_s-band magnitudes between $\sim$ 11 - 14 mag; by removing the dimmer foreground stars, I limit contamination by foreground stars with large broad-band photometric errors. I also exclude fainter narrow-band sources, limiting the error and reducing the scatter around the line. Stars with $Br\gamma$ excess or absorption, discussed in detail below, are clearly labeled in Figure 6-8, a $1.5' \times 1.5'$ region of my K_s-band image centered on SGR 1900+14 .

By comparing my observations to previous results in the literature (Table 6-1), I am better able to evaluate how well my application of this narrow-band technique worked to identify potential massive stars around SGR 1900+14. Vrba et al. (2000) found 11 OBI candidates in the embedded cluster associated with the magnetar. Unfortunately, the majority of these stars lie directly next or behind one or both of the bright M5 supergiant cluster members. While Vrba et al. (2000) is able to remove these bright objects from their I and J -band image using PSF subtraction, this was impossible in our K_s - band image, where the stars are completely saturated, even using the shortest exposure time. Given these limitations, only four of the stars are not affected by saturated pixels, namely Stars 1, 2, 3, and 4. These stars are shown by triangles in Figure 6-7.

While Star 1 shows moderate Brγ absorption (1 -4Å) suggesting that it may be an OBI star, Stars 4 and 2 are both consistent, within the error bars, with no absorption or emission. Star 3, meanwhile, exhibits a Brγ emission with EW = -(5 - 13)Å. Also, while

the other three stars are located at a $J-K_s \sim 2$, Star 3 is at a $J-K_s \sim 2.6$. One possible explanation for this discrepancy may be that Star 3 is a dust emission WR, with warm circumstellar dust intrinsically reddening the star and producing a slightly redder color than other cluster members. In this case, the strength of the emission may be masked; the line could be even stronger than predicted by the narrow-band color.

Another option is the presence of patchy extinction along the line-of-sight to the cluster, resulting in varying values of $J - K_s$ for different cluster members. This explanation might also explain the broad distribution of reddenings (A_v = 10.4 - 19.2 mag) derived for the cluster. As discussed in §6.1.1, Vrba et al. (2000) suggest a reddening $A_v = 19.2 \pm 1$ mag yielding a $J - K_s = 3.2 \pm 0.18$ color for the cluster (assuming massive stars with no intrinsic color term) while Wachter et al. (2008) find A_v = 10.4 - 14.4 mag or a $J - K_s$ = 1.8 - 2.6 mag. While I observe a few stars in the $J - K_s = 3.2 \pm 0.18$ mag regime of both Figure 6-7, the $J - K_S$ color of four of the stars identified by Vrba et al. (2000) (shown as triangles) are more consistent with A_v = 10.4 - 14.4 mag. Thus my results support those of Wachter et al. (2008) and are also consistent with the reported reddening of the SGR, $A_V \sim 12.8 \pm 0.8$ mag (Vrba et al. 1996). However, it is clear that a more thorough study of the extinction law in the vicinity of the cluster is necessary.

I then compared my J-band magnitudes for Stars 1 - 4 to other values in the literature. While similar to the J- band magnitudes reported by Vrba et al. (2000), they do not agree within the error bars; my observations are systematically dimmer by 0.06 - 0.14 mag. This is notable given the high precision of both sets of photometry. Slight differences in the zeropoint used to calibrate the instrumental magnitudes or errors in the PSF subtraction of the nearby M5 supergiants may account for these discrepancies.

Before exploring potential massive star candidates in the field surrounding SGR 1900+14, I compare my results with those from SGR 1806-20. I immediately note significant differences between the color-color diagram of SGR 1900+14 (Figure 6-7) and SGR 1806-20 (Figure 5-4). In Figure 5-4, the region surrounding $J - K_s = 5$, the color

of the cluster, is sparse, making it relatively easy to pick out potential cluster candidate using reddening constraints alone. In6-7, the scatter in the $Br\gamma - K_{2.27}$ color at the potential $J - K_s$ colors of SGR 1900+14 hinder my ability to easily identify potential massive stars.

To solve this problem, I applied an additional constraint to my search; I identified all stars with K_s-band magnitudes > 14.2 within a $45''$ radius of the SGR and examined their narrow-band colors. I chose this radius based on the size of the mid-infrared ring discovered around SGR 1900+14 by Wachter et al. (2008). While this method may exclude any massive cluster members ejected from the cluster, it offers a better chance to locate massive stars in the cluster's 1 - 2 pc core should they exist.

I show the final color-color diagram in Figure 6-9. Objects within a $45''$ radius of the SGR with K_s-band magnitudes > 14.2 that have EW consistent with either Brγ emission or absorption after taking into account the errors, are marked with inverted triangles. These results are presented in Table 6-2. These objects, potential OBI and emission line stars, are the most interesting candidates for follow-up spectroscopy and may represent the bulk of previously undiscovered massive star population in this cluster.

6.5.2 SGR 1627-41

Figures 6-3 and 6-4 show the $HeI - K_{2.03}$ versus $K_{2.03}$ and $Br\gamma - K_{2.14}$ versus $K_{2.14}$ diagrams for the stars surrounding SGR 1627-41. Since there have been no prior attempts to locate a cluster associated with this magnetar, I do not have previous data with which to compare my observations.

In both color-magnitudes diagrams, there is an obvious correlation between "magnitude" and error in the narrow-band color; the error increases with magnitude, resulting in a larger spread of the data away from the "zeropoint" line. This spread, combined with the sheer number of stars on the plot, made it impossible, to identify an obvious cluster of stars with either $HeI - K_{2.03}$ or $Br\gamma - K_{2.14}$ emission or absorption. While my initial intention was to avoid focusing on any one region of the field, I

hypothesized that, like SGR 1900+14, limiting my search to a small area surrounding the SGR might offer the best opportunity to locate massive stars associated with the SGR.

I located all stars within a 45″ radius from the SGR corresponding to a $\sim$ 2 pc search radius at the distance of the magnetar. First, I calculated the $Br\gamma - K_{2.14}$ and $HeI - K_{2.03}$ colors of all the stars in this subregion, taking into account the error bars. I found a number of objects with only Brγ emission or absorption; these stars are marked with diamonds on Figure 6-3. I also found a few candidates with only HeI emission ; these objects are denoted as squares. Objects with emission or absorption in both HeI and Brγ are denoted as triangles on both plots. I list all potential massive star candidates and their EWs in Table 3. Stars with $Br\gamma$ and/or HeI excess or absorption, are clearly labeled in Figure 6-10, a $1' \times 1'$ region of my Brγ image centered on SGR 1627-41.

While my analysis of the field surrounding SGR 1627-41 succeeded in identifying potential massive stars around the magnetar, the amount of error in the narrow-band color raises concerns. Evidence of this problem surfaced when I was evaluating the PSF photometry; the error in the narrow-band colors for the entire data set did not meet the original 5% criterion discussed in the methodology section of Chapter 5.

One potential source of photometric error is the distortion correction performed during the reduction of my observations. I noted that even after considerable correction, distorted PSFs were still evident in the final science images, especially toward the outer edges. While the distortion correction completed in IRAF on each sky-subtracted image did eliminate the errors in that frame, applying this calibration to all $\sim$ 150 images observed with the same filter may have not solved the distortion problem. Flexure in the telescope and instrument can create a different distortion pattern at each hour angle; since I took my observations over a number of hours, the distortion correction calculated from data at the beginning of the night may not fit data observed later.

One solution to this problem would be to find a distortion correction for each of the six dither runs completed per filter. I could then apply the correct distortion pattern to each set of dithered frames and combine the results into a final science image. In the future, I will attempt this correction in the hope of reducing the errors in my narrow-band color. Once I reduce the scatter on my color-magnitude diagrams, I hope to further explore the rest of the field to search for more massive star candidates.

6.5.3 SGR 0526-66

Since Klose et al. (2004) do not provide photometry or proposed spectral types for individual cluster stars in SL463, I cannot compare my results for SGR 0526-66 on a star-by-star basis with previous data in the literature. However, I do identify the single OBI star reported by Klose et al. (2004) and find Brγ absorption; I estimate a Bryγ EW = 9 - 13 Å.

Upon visual inspection of Figures 6-3 and 6-4, I note the absence of an obvious population of stars with HeI and Brγ emission or absorption. Given the $\sim$ 6.5 magnitude offset between the Brγ instrumental magnitudes and broad-band K_s magnitudes (§6.4.3.2), I expect to find potential massive cluster members with K-band magnitudes $\sim$ 12 mag (Klose et al. 2004) at a $K_{2.14} \sim 18.5$ mag and $K_{2.03} \sim 18.5$ mag. Besides an obvious paucity of stars at this magnitude on the color-magnitude diagrams, my calculations show that the few bright stars do not exhibit narrow-band spectral features.

To more throughly search for massive stars in this field and reduce the scatter in the narrow-band colors, I further limited my search area to a 45″ radius centered on the cluster, corresponding to the cluster size estimated by (Klose et al. 2004) (see Figures 6-11 and 6-12). Additionally, I searched another 45″ radius surrounding the SGR itself (see Figures 6-13 and 6-14). At 50 kpc, my search areas correspond to a 1 pc cluster radius; the typical size of a cluster core (§5.4.4).

I detected no signatures of massive stars in the search area centered on the SGR, a result in agreement with the findings of Klose et al. (2004). However, given the presence

of bright NIR nebulous emission from nearby SNR N49, I can not completely rule out the presence of massive stars. I also failed to find additionally OBI candidates in SL463. I do detect many of the candidate main sequence OB cluster members. As expected of stars of these spectral types, these objects show no signs of HeI or Brγ absorption or emission. I present an image of the two search areas in Figure 6-15. A box indicates the one OBI candidate in SL463.

Clearly, more work to establish whether SL463 is indeed the natal cluster of SGR 0526-66 is necessary. Broad-band photometry and a color-color diagram, like those created for SGR 1900+14 and SGR 1806-20, may help illuminate the stellar population in the field. Reducing the photometric error and culling foreground objects by identifying stars at the reddening of the cluster should allow for a more conclusive result regarding SGR 0526-66 and its environment.

6.6 Conclusions

In this chapter, I describe my search for massive stars associated with SGR 1900+14, SGR 0526-66, and SGR 1627-41 using a narrow-band technique successfully applied to Cl 1806-20.

1) I observed the embedded cluster associated with SGR 1900+14. While I could not analyze many of the OBI candidates discovered by Vrba et al. (2000) due to their proximity to two bright M5 supergiants, I successfully detected four previously identified OBI candidates. I confirm Star 1 as an OBI candidates and suggest that Star 3 may be an massive star with Brγ emission. My data support the reddening values suggested by Wachter et al. (2008), A_v = 10 - 14.4 mag. Furthermore, I identified a population of candidate massive stars that may represent the bulk of the missing cluster population. I suggest that these stars should be targeted for future spectroscopic observations.

2) Using color-magnitude diagrams, I probed the environment of SGR 1627-41 for massive stars. While I found a number of potential massive stars with Brγ and HeI

emission and absorption, I noted the large photometric error associated with the data. I discuss corrections to the data that may yield better results.

3) Using the same technique applied to SGR 1627-41, I probed two 45″ regions: one around cluster SL463 and another around SGR 0526-66. While I did identify the previously discovered lone OBI candidate in SL463, I found no evidence for a large OBI or emission-line star population. Further work to evaluate whether SL463 is indeed the birth cluster of the magnetar and to determine the stellar content of is clearly necessary.

4) Upon comparing the technique used for SGR 1806-20 and SGR 1900+14 to that used for SGR 1627-41 and SGR 0526-66, I find the former to be more effective. Although this method was originally contrived to sidestep an observational difficulty – the lack of a continuum filter at a wavelength close to the central wavelength of the science filter, the color-color diagram proved to be more useful. In situations where the $J - K_s$ color of potential massive stars is known, I could focus on a specific region of the diagram to search for potential cluster members.

5) The color-color method turns out the best results when the cluster is at a high reddening and sharply separated from the remaining data, as was the case with Cl 1806-20. Thus, a similar analysis for Cl 1627-41, at a very large reddening might yield better results.

Table 6-1. Measured magnitudes, colors, and Brγ excess or absorption for previously known massive stars in Cl 1900+14. Columns give the Star ID, I-band magnitude, J-band magnitude from (Vrba et al. 2000) then continue with results from this study including J-band and K_s-band magnitudes, calibrated $Br\gamma - K_{2.27}$ color (see §5.4.6), and equivalent width (including errors; see §5.4.5). Negative values indicate emission. Stars with no photometry from this study lie directly behind or next to one of two M5 supergiants in the cluster.

Star ID	I^a	J^a	J	K_s	$(Br\gamma - K_{2.27})_{cal}$	EW (Å)
Star 1	20.00 ± 0.02	13.17 ± 0.02	13.26 ± 0.01	11.22± 0.01	0.01	1 - 4
Star 2	21.10 ± 0.02	14.26 ± 0.02	14.37 ± 0.02	12.37± 0.03	0.00	0
Star 3	21.85 ± 0.02	14.51 ± 0.02	14.68 ± 0.02	12.12± 0.01	-0.04	-(5 -13)
Star 4	22.01 ± 0.02	15.06 ± 0.04	15.20 ± 0.04	12.98± 0.04	0.03	0 [a]
Star 5	22.77 ± 0.03	....	...	...	...	...
Star 6	23.18 ± 0.04	....	...	...	...	...
Star 7	23.16 ± 0.05	15.70 ± 0.09	...	...	...	...
Star 8	22.85 ± 0.04	15.62 ± 0.06	...	...	...	...
Star 9	23.01 ± 0.05	15.53 ± 0.05	...	...	...	...
Star 10	23.60 ± 0.06	16.41 ± 0.07	...	...	...	...
Star 11	23.78 ± 0.06	16.12 ± 0.04	...	...	...	...

[a] Vrba et al. 2000

[b] consistent with 0 within the error bars

Table 6-2. Measured magnitudes, colors, and Brγ emission or absorption for potential massive stars in the embedded cluster around SGR 1900+14. Columns give Star ID, J-band magnitude, K_s-band magnitude, $J - K_S$ color, corrected Brγ - $K_{2.27}$ (see §5.4.6) Equivalent Width, and distance from SGR 1900+14. Positive values for EW indicate absorption. Unless otherwise stated, errors in the J- and K_s-band magnitude are ± 0.01

Star ID	J	K_s	$J - K_s$	$(Br\gamma\text{-}K_{2.27})_{cal}$	EW (Å)	Distance $''$
3588	16.04	13.66	2.37	0.023	2 - 7	43.1
3674	15.10	13.19	1.91	0.060	10 - 13	39.9
3883	14.14	12.96	1.19	0.023	3 - 7	34.9
3970	13.75	10.88	2.87	-0.011	(-)1 - 3	23.5
4137	16.27	14.11	2.15	-0.029	(-)3 - 9	17.9
4498	14.40	11.94	2.46	-0.011	(-)1 - 4	3.4
4554	14.86	13.68	1.18	-0.018	(-)1 - 7	8.0
4586	13.95	11.59	2.36	-0.012	(-)1 - 4	22.3
4715	16.91± 0.03	14.12	2.79	0.026	1 - 9	18.6
4761	16.49± 0.03	14.04	2.46	-0.048	(-)6 - 14	45.0
4937	15.26	14.13	1.13	0.03	2 - 9	36.0
5031	14.89	12.67	2.22	0.025	4 - 6	31.4
5095	16.18± 0.02	14.04	2.14	0.022	1 - 8	38.8
5180	15.05	13.09	1.96	0.022	3 - 6	38.5
5254	14.57	12.62	1.95	0.017	2 - 5	41.6

Table 6-3. Measured magnitudes, colors, and Brγ absorption and emission of potential massive stars in the embedded cluster around SGR 1627-41. Columns give Star ID, instrumental $K_{2.14}$-band magnitude, corrected Brγ - $K_{2.14}$ (see §5.4.6), Brγ - $K_{2.14}$ error, Equivalent Width, and distance from SGR 1900+14. Positive values for EW indicate absorption. Unless otherwise stated, errors in the $K_{2.14}$-band magnitude are ± 0.01.

Star ID	$K_{2.14}$	$(Br\gamma\text{-}K_{2.27})_{cal}$	$(Br\gamma\text{-}K_{2.27})_{cal}$ error	EW (Å)	Distance $''$
12456	20.18	0.05	0.02	7 - 14	37.1
12860	19.93	0.10	0.02	17 - 23	30.0
12981	20.15	0.10	0.02	16 - 22	20.0
13013	19.77	0.07	0.02	10 - 17	21.2
13079	16.03	-0.04	0.02	- (5 - 13)	32.6
13326	19.43	0.09	0.02	15 - 21	10.0
13813	20.62	0.07	0.02	9 - 17	34.1
13826	21.03 ± 0.02	0.08	0.03	10 - 20	19.1
13860	20.76	0.07	0.02	9 - 17	41.1
13894	19.11	0.08	0.01	13 - 18	30.4
13908	17.34	-0.03	0.02	- (2 - 9)	38.2
13951	19.27	0.07	0.01	11 - 16	9.4
13959	20.82 ± 0.02	0.08	0.03	9 - 21	36.8
14516	20.28	0.06	0.02	8 - 15	33.9
14665	20.23	0.07	0.02	10 - 17	33.8
14744	19.22	0.05	0.02	8 - 14	40.2
14844	18.79	0.05	0.01	7 - 12	36.8
14925	19.72	0.06	0.02	9 - 15	40.5

Table 6-4. Measured magnitudes, colors, and HeI absorption and emission for potential OBI Stars in the embedded cluster around SGR 1627-41. Columns give Star ID, instrumental $K_{2.03}$ magnitude, corrected HeI - $K_{2.03}$ (see §5.4.6), HeI - $K_{2.03}$ error, Equivalent Width, and distance from SGR 1900+14. Positive values for EW indicate absorption. Unless otherwise stated, errors in the $K_{2.03}$- band magnitude are ± 0.01

Star ID	$K_{2.03}$	$(HeI - K_{2.03})_{cal}$	$(HeI - K_{2.03})_{cal}$ error	EW (Å)	Distance $''$
13959	21.12	-0.11	0.07	- (8 - 40)	36.8
13826	21.38	-0.09	0.05	- (8 - 32)	19.1
13813	20.97	-0.06	0.05	- (2 - 25)	34.1
13079	16.39	0.07	0.05	4 - 22	32.6
12504	17.64	0.12	0.05	14- 31	39.2
12705	16.64	0.17	0.04	23 - 39	33.0
12954	16.02	0.18	0.05	25 - 40	21.2
13801	15.96	0.17	0.05	23 - 39	44.2
14176	17.88	0.10	0.05	11 - 29	36.4

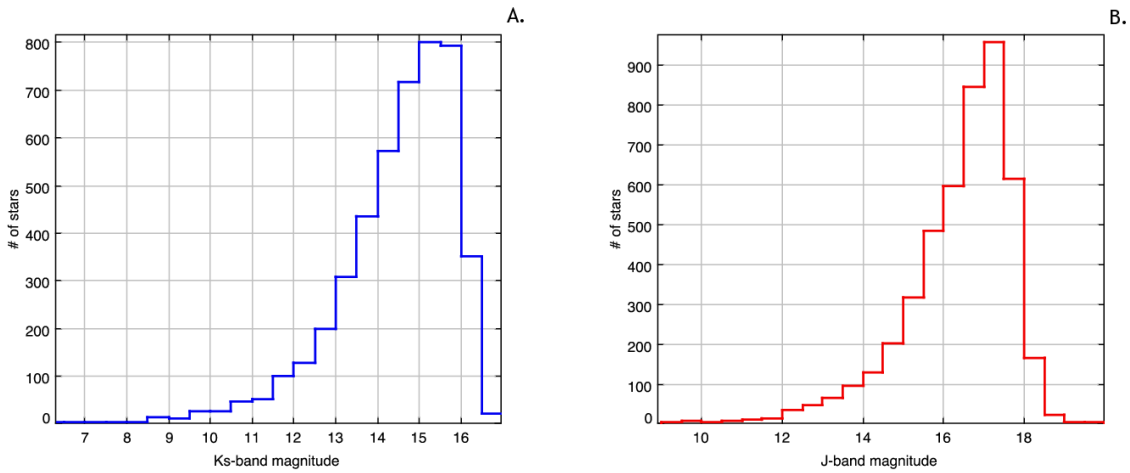

Figure 6-1. Histogram showing the number of stars at each calibrated magnitude for stars around SGR 1900+14. A) Ks-band B) J-band. The bin sizes are 0.25 mag. Note the turnover at $J \sim 17$ and $K_s \sim 14.5$, indicating completeness (within the limits of crowding and confusion).

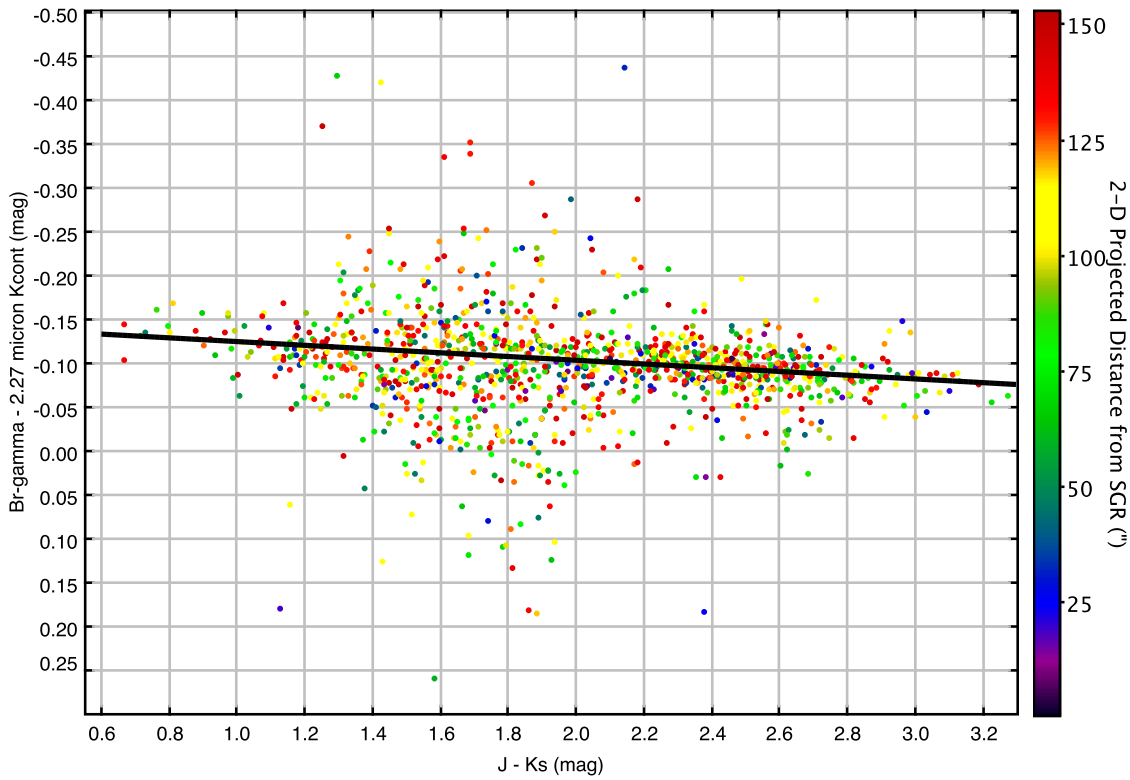

Figure 6-2. Color-color diagram of stars in the 4-band broad- and narrow- band catalog within a $5' \times 5'$ subfield centered on SGR 1900+14. The vertical axis is flipped such that negative Brγ - K_{cont} values, which indicate Brγ emission, appear at the top half of the graph. Color denotes projected distance (in $''$) from SGR 1900+14, with purple indicating objects closer to the SGR and yellow indicating objects further away in 2-D space. The solid black line is the narrow-band zeropoint (see §5.4.6) with m = 0.021 and b = -0.14. Bluer stars on the left of the plot with more scatter in their narrow-band colors are at the edge of my detection limits and have more Poisson noise.

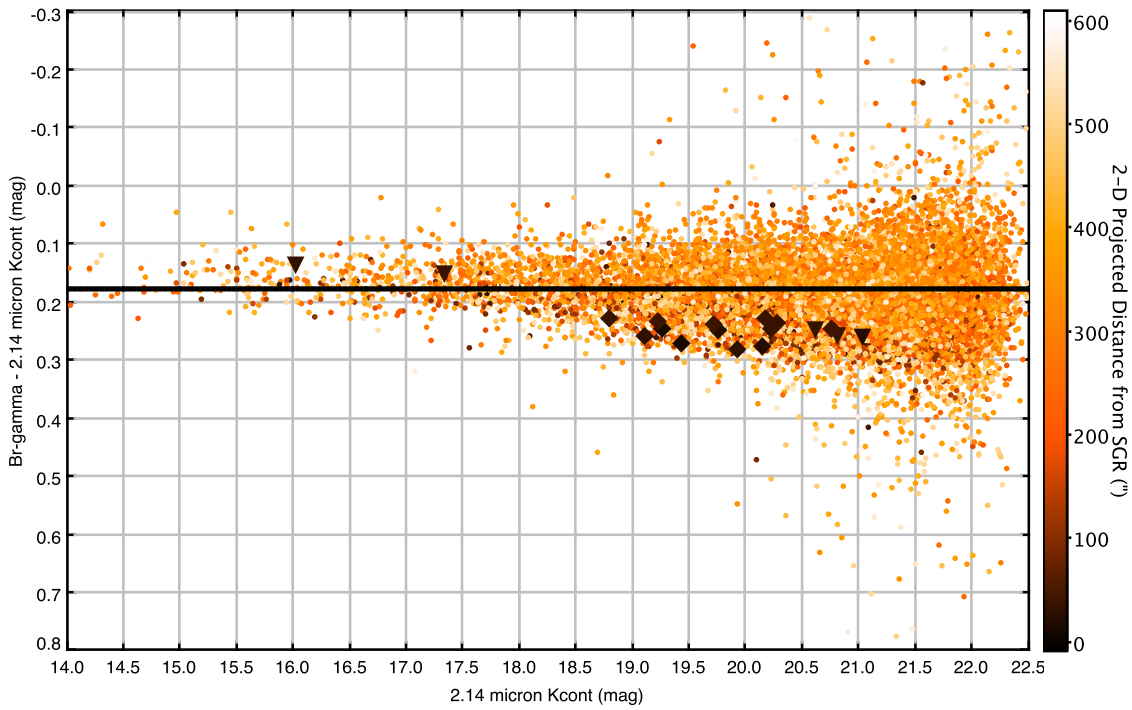

Figure 6-3. Brγ - $K_{2.14}$ versus $K_{2.14}$ color-magnitude diagram of the field surrounding SGR 1627-41 The vertical axis is flipped such that negative Brγ - $K_{2.14}$ values, which indicate Brγ emission, appear at the top half of the graph. Color denotes projected distance (in $''$) from SGR 1627-41, with darker colors indicating objects closer to the SGR and yellow indicating objects further away in 2-D space. The solid black line is the narrow-band zeropoint (see §5.4.6) with Y = 0.18. Black circles are objects within a 45$''$ radius of the SGR with Br γ absorption or emission. Triangles have both Br γ and HeI emission or absorption.

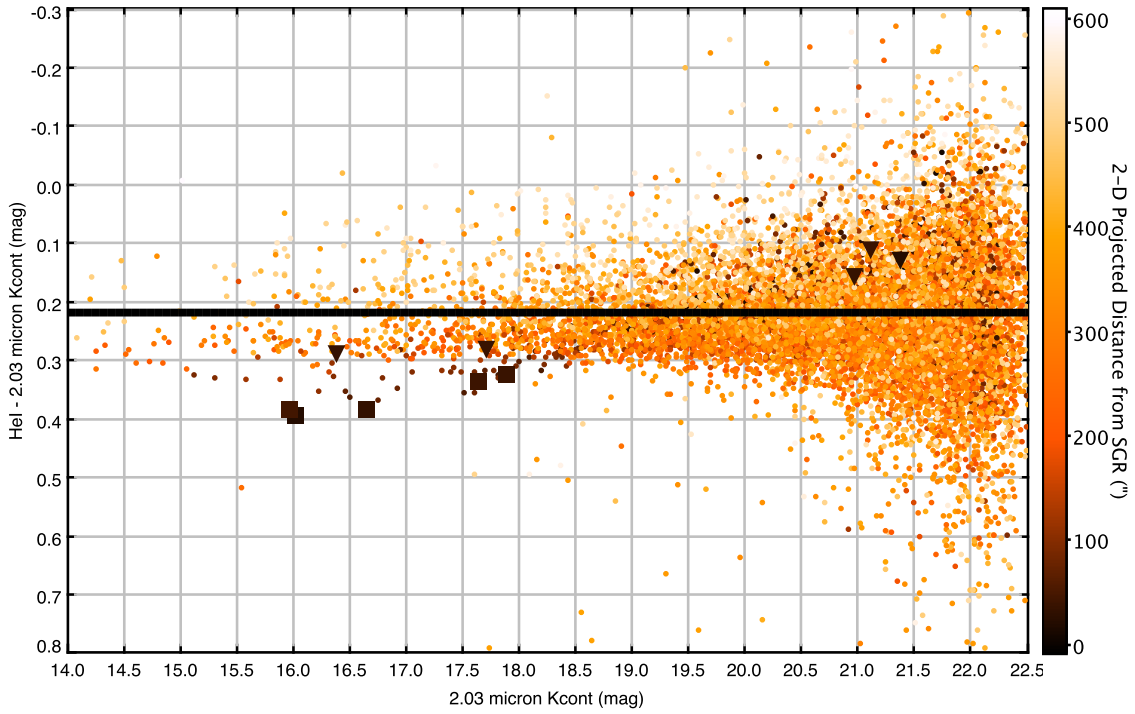

Figure 6-4. HeI - $K_{2.03}$ versus $K_{2.03}$ color-magnitude diagram of the field surrounding SGR 1627-41. The vertical axis is flipped such that negative HeI - $K_{2.03}$ values, which indicate HeI emission, appear at the top half of the graph. Color denotes projected distance (in $''$) from SGR 1627-41, with darker colors indicating objects closer to the SGR and yellow indicating objects further away in 2-D space. The solid black line is the narrow-band zeropoint (see §5.4.6) with Y = 0.21. Black triangles are objects within a 45$''$ radius of the SGR that have both have both Br γ and HeI emission or absorption.

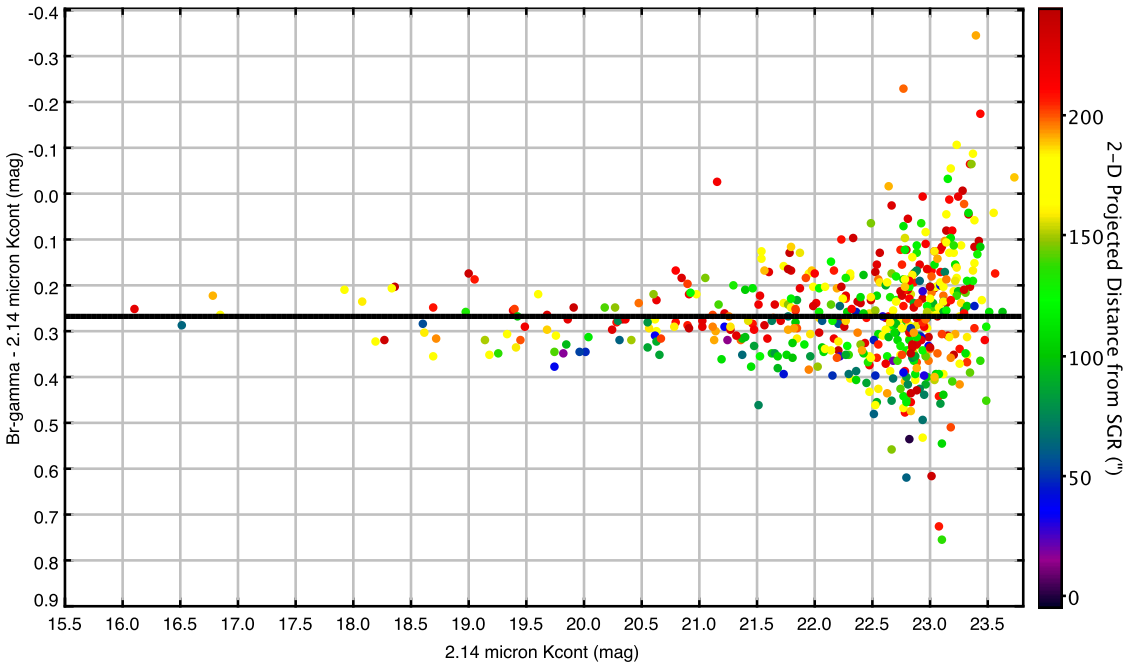

Figure 6-5. Brγ - $K_{2.14}$ versus $K_{2.14}$ color-magnitude diagram of a field surrounding SGR 0526-66 The vertical axis is flipped such that negative Brγ - $K_{2.14}$ values, which indicate Brγ emission, appear at the top half of the graph. Color denotes projected distance (in $''$) from SGR 0526-66, with darker colors indicating objects closer to the SGR and yellow indicating objects further away in 2-D space. The solid black line is the narrow-band zeropoint (see §5.4.6) with Y = 0.27. These data are within a $4'$ search radius centered on the cluster.

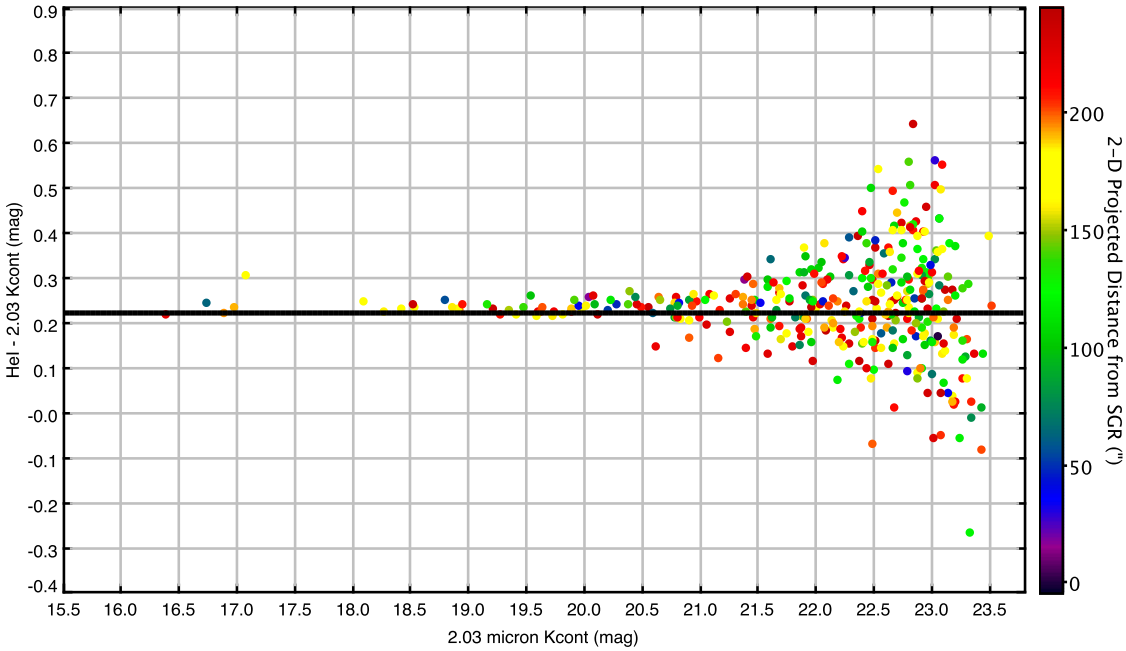

Figure 6-6. HeI - $K_{2.03}$ versus $K_{2.03}$ color-magnitude diagram for the field surrounding SGR 0526-66. On the vertical axis, positive $HeI - K_{2.03}$ values, which indicate HeI absorption, appear on the top half of the graph. Color denotes projected distance (in $''$) from SGR 0526-66, with darker colors indicating objects closer to the SGR and yellow indicating objects further away in 2-D space. The solid black line is the narrow-band zeropoint (see §§5.4.6) with Y = 0.22. These data are within a $4'$ search radius centered on the cluster.

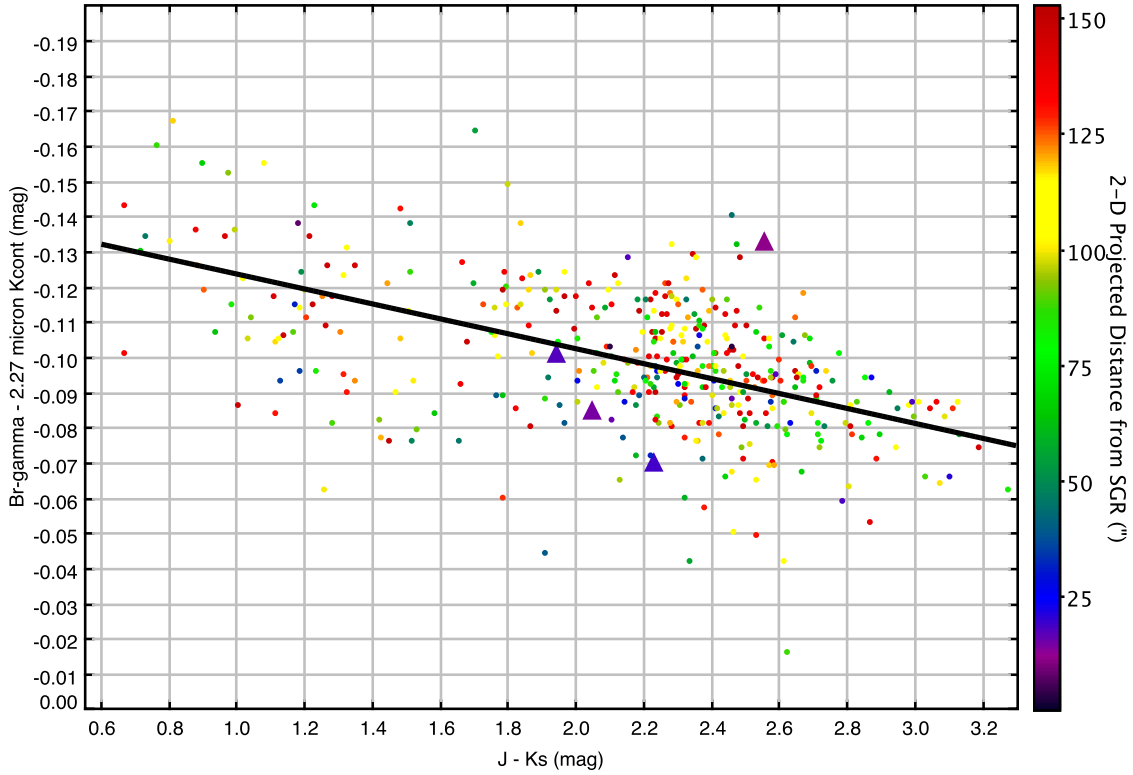

Figure 6-7. Same plot as Fig 6-2 showing all 4-band catalog objects with $K_s < 14.5$ magnitude. The candidate massive stars from Vrba et al. (2000) are marked with inverted triangles.

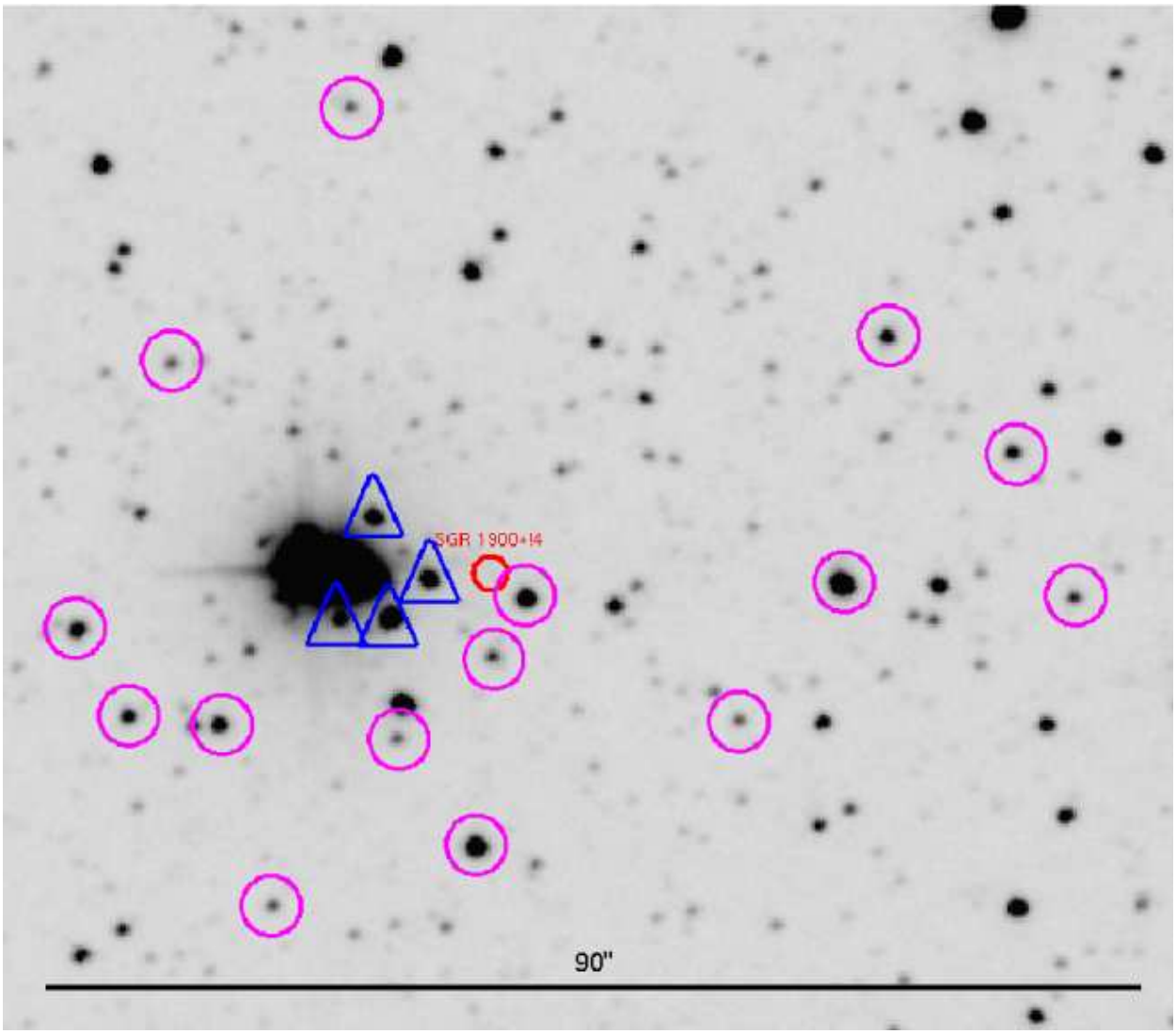

Figure 6-8. A $1.5' \times 1.5'$ region of our K_s-band image centered on Cl 1900+14. Previously discovered OBI stars and newly identified massive stars detected by this survey are indicated – OBI stars from Vrba et al. (2000)are marked as triangles, new candidate massive stars as circles. The location of the SGR is also noted.

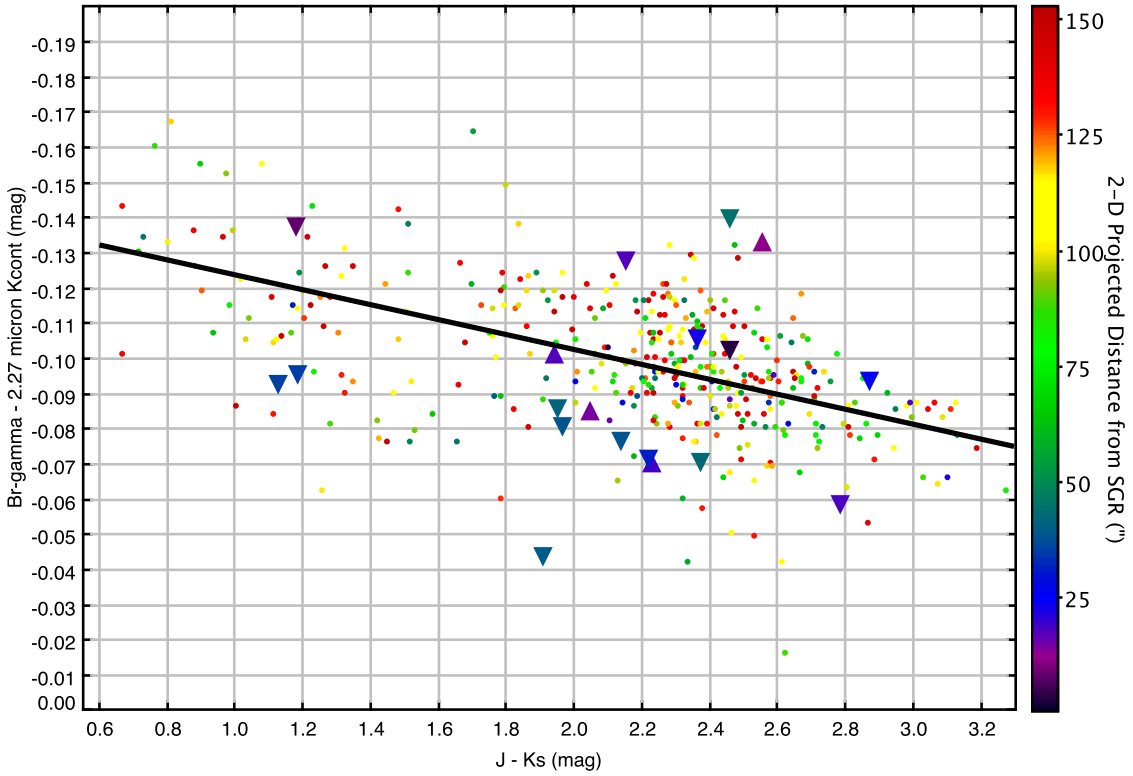

Figure 6-9. Same plot as Figure 6-2 showing all 4-band catalog objects with $K_s < 14.5$ magnitude. The candidate massive stars from Vrba et al. (2000) are marked with inverted triangles. The new candidates from this study are marked with triangles.

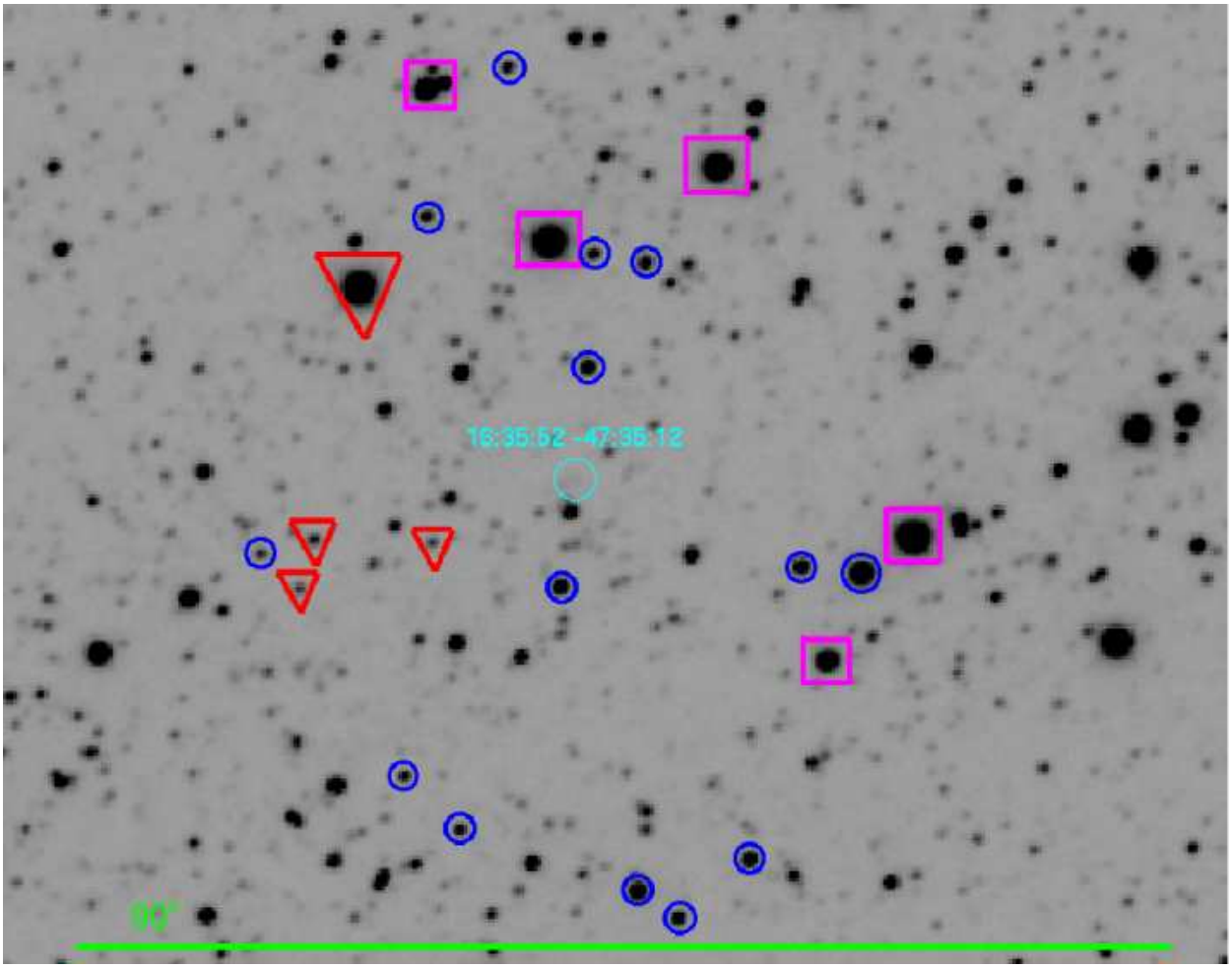

Figure 6-10. A 1.5′ × 1.5′ region of our Brγ image centered on Cl 1627-41. New candidate massive stars exhibiting only Brγ emission or absorption are marked with circles, stars exhibiting only HeI emission or absorption are marked by boxes, while sars with absoption or emission in both narrow-band filters are indicated by inverted triangles

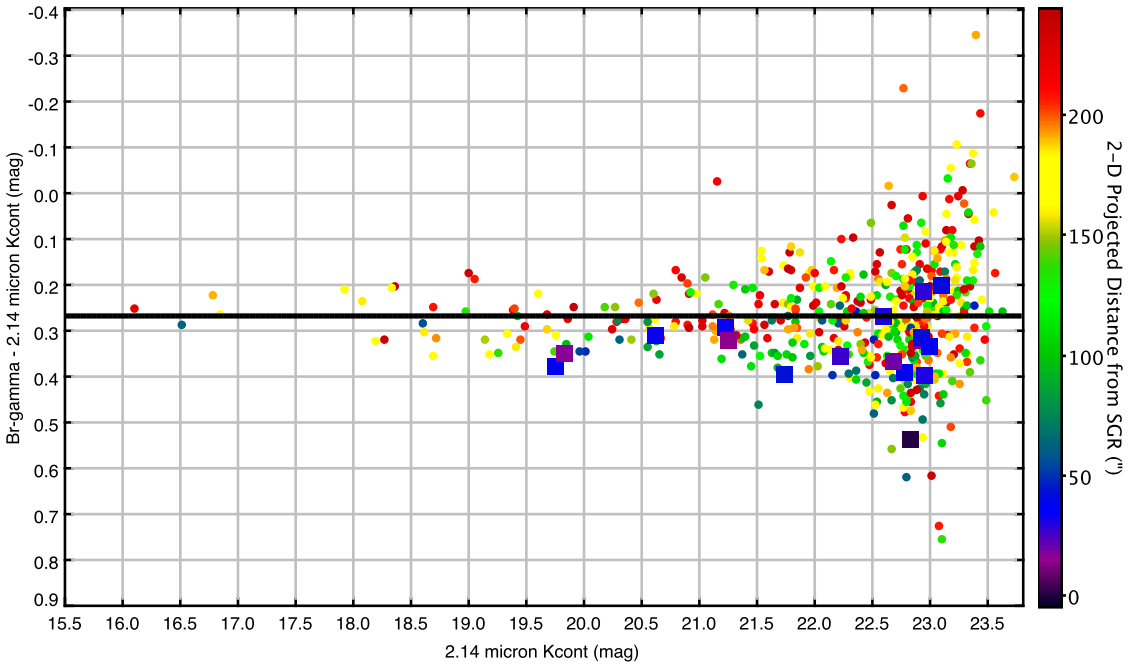

Figure 6-11. Same plot as Figure 6-5. Stars within a 45″ radius of the SGR are marked as boxes.

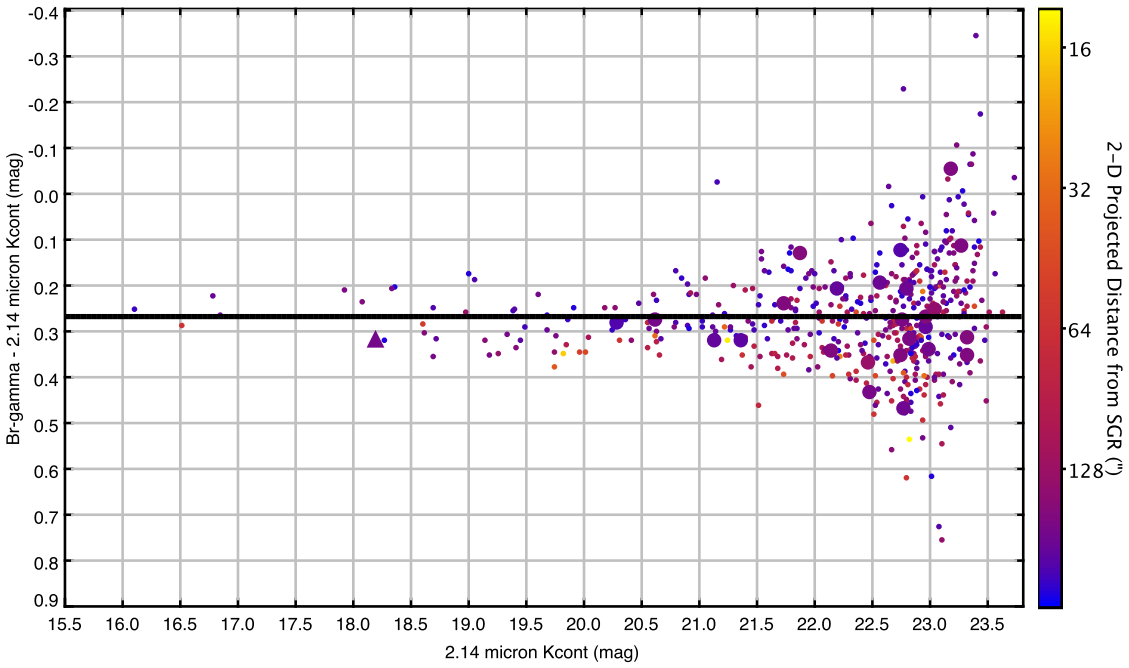

Figure 6-12. Same plot as Figure 6-4. Stars within a 45″ radius of the cluster center of SL463 are marked as circles. The lone OBI candidate is indicated with a triangle.

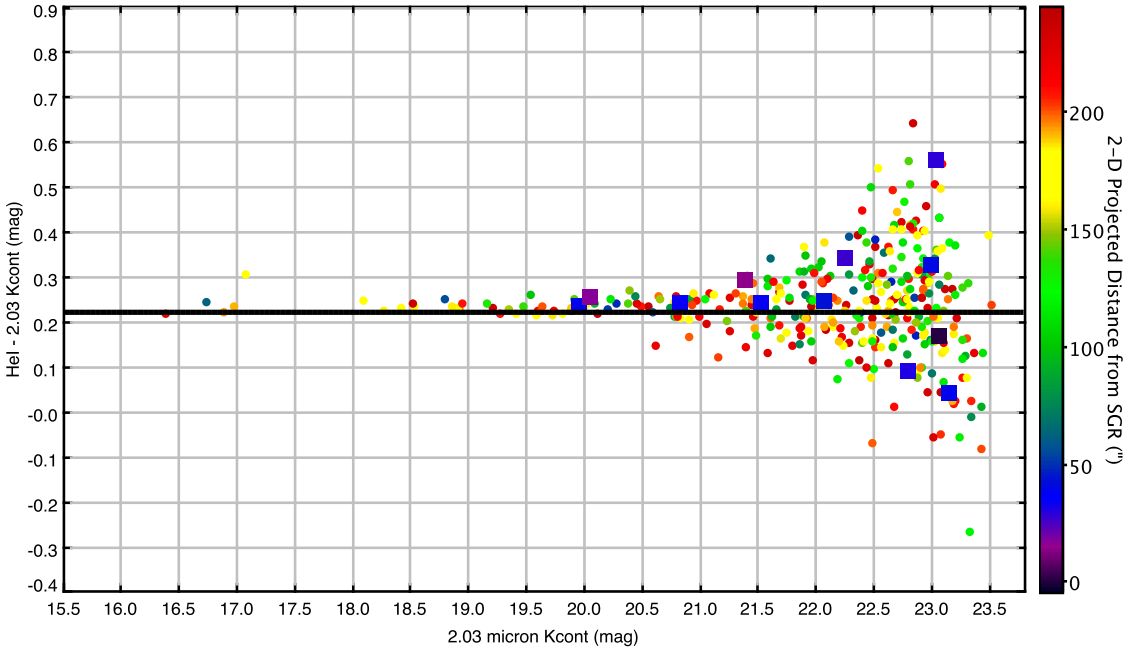

Figure 6-13. Same plot as Figure 6-5. Stars within a 45″ radius of the SGR are marked as boxes.

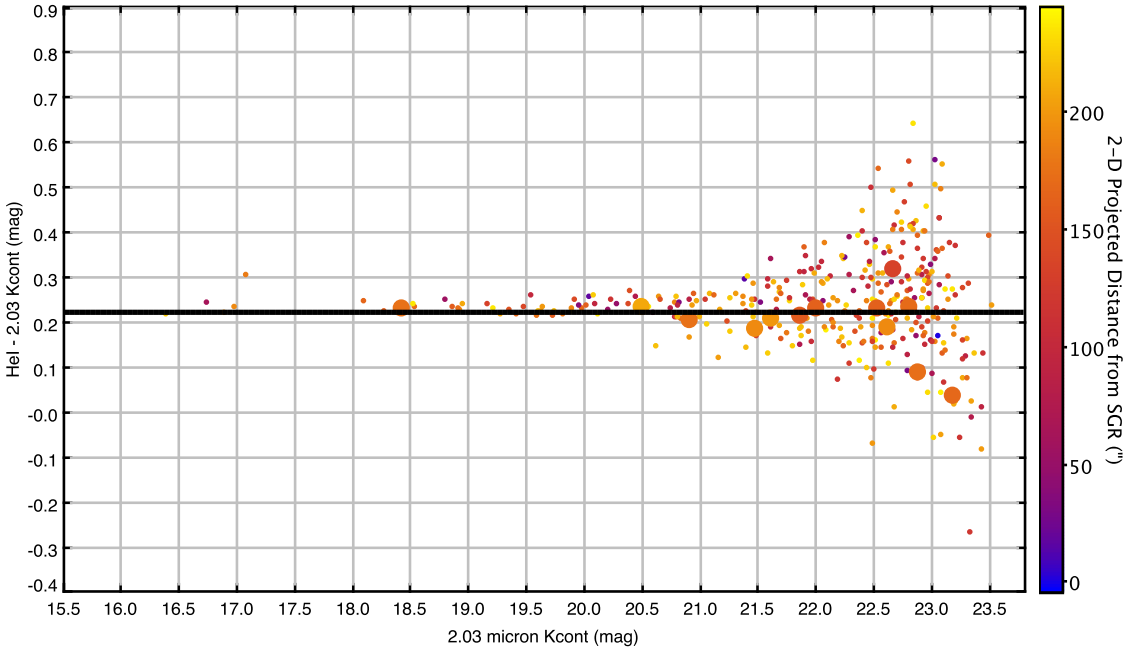

Figure 6-14. Same plot as Figure 6-5. Stars within a 45″ radius of the SL463 are marked as circles.

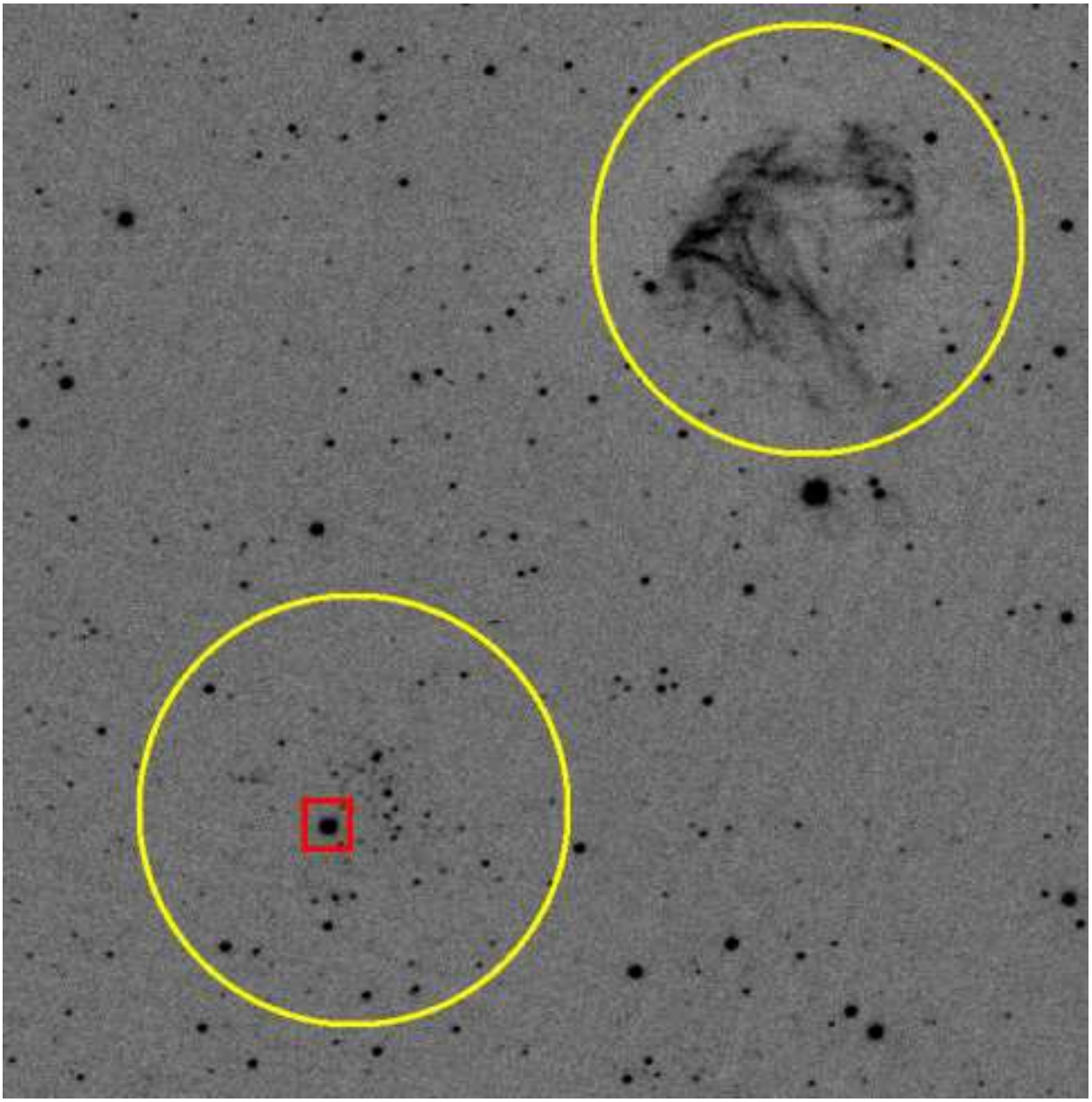

Figure 6-15. A $2.5' \times 2.5'$ region of SGR 0526-66. The two circles indicate $45''$ search radii centered on SGR 0526-66 and SL463, the potential natal cluster of the magnetar. The red box marks the location of the lone OBI star in the cluster, discovered by citetklo04.

CHAPTER 7
LOCATIONS OF LUMINOUS BLUE VARIABLES IN THEIR HOST CLUSTERS

7.1 Introduction

Characterized as luminous, windy behemoths capable of mass loss rates upwards of 10^{-4}–10^{-5} $M_{\odot}$ per year, Luminous Blue Variables (LBVs) are arguably some of the most dramatically unstable and rare stars in the stellar zoo (Humphreys & Davidson 1994). Recognized as evolved stars, LBVs are also thought to be at the extreme of the mass spectrum; in fact one bona fide LBV (Eta Carinae) and two LBV candidates (the Pistol Star and LBV 1806-20) vie for the title of most massive star in the Galaxy (Figer et al. 1998; Eikenberry et al. 2004a). As such, LBVs offer us a unique opportunity to study stars near the theoretical upper mass limit and the compact objects that form when they die (Eikenberry et al. 2004a).

Besides their distinguishing bolometric luminosities, large masses, and extreme mass loss rates, LBVs are often identified by their emission-line rich spectra, photometric and spectroscopic variability, and circumstellar ejecta (Humphreys & Davidson 1994). Of these characteristics, stars that lack large amplitude variations (1-2 mag) but display several other physical features are often identified as "candidate" LBVs, though the exact segregation of candidates and confirmed LBVs remains somewhat subjective and may vary between authors (Clark et al. 2005).

While LBVs have garnered a fair share of attention and study, the dearth of information regarding their environments is notable. This is largely due to two factors – the rarity of the stars themselves and the location of their environments. Found in the dusty, crowded Galactic Plane of the Milky Way, the majority of massive star clusters containing LBVs and other unusual massive stars have evaded detection by optical surveys (Hanson 2003; Portegies Zwart et al. 2001). Only recently have advances in infrared instrumentation enabled discoveries of elusive massive stellar environments.

The influx of new data include observations of clusters like Westerlund 1 and the Quintuplet, posited to be the analogs of Super Star Clusters (SSCs) found in other late-type galaxies, and Cl 1806-20, a smaller cousin to these objects (Clark & Negueruela 2002; Figer et al. 1999; Fuchs et al. 1999). All are notable for containing at least one LBV among numerous Wolf-Rayets, supergiants, and hypergiants. Joined by the well-studied Trumpler 16, these clusters offer us the first chance to identify characteristics of LBVs found in cluster environments.

One particularly interesting property of LBVs in the aforementioned clusters is the location of these massive stars with respect to other cluster members. During my study of Cl 1806-20, I serendipitously noticed that LBV 1806-20 was located at the periphery of the cluster. Given the mass of the LBV and the dictates of mass segregation (§7.4), one would expect to find this object in the center. I checked several other LBV environments and found upon visual inspection that four of five LBVs in young massive clusters appear to be located on the periphery of their host clusters. The exception to this observation is Eta Carina in Trumpler 16.

In this chapter, I evaluate the status of LBVs as "peripheral" cluster members, a term I define is §7.3. I calculate the probability of finding at least one star in every cluster at or outside the radius of the resident LBV and determine the robustness of my result using a Monte Carlo simulation. Finally, I compare my finding to theoretical models that predict the locations of massive stars in clusters and contrast these with scenarios that reproduce the observed positions.

7.2 Sample Selection

For my study I require a homogeneous sample of objects: namely LBVs that are established members of well-characterized clusters. While there are approximately 30 known Galactic LBVs, only five meet this criterion. The 15 known LBVs which have no known cluster association were not included in my analyses. The rest were accepted or rejected on a case-by-case basis, discussed below.

Four LBVs, Sher 25, ζ^1 Sco, W51 LS1, and Cyg OB2 #12, are associated with large star forming regions. Sher 25 is a member of the giant HII region NGC 3603, while W51 LS1 is associated with G49.5-0.4, a centrally located HII complex in W51 (Brandner et al. 1997; Okumura et al. 2000). ζ^1 Sco and Cyg OB2 #12 are members of OB associations, Sco OB1 and Cyg OB2, respectively (van Genderen et al. 1984; Hanson 2003).

Both NGC 3603 and Sco OB1 are hosts to young cluster of massive stars; the dense starburst cluster NGC 3603 YC is centrally located in NGC 3603 and the open cluster NGC 6231 resides in ScoOB1 (Stolte et al. 2004; van Genderen et al. 1984). While the membership of ζ^1 Sco in Sco OB1 and Sher 25 in NGC 3603 is well established, neither LBV's membership in the resident cluster is certain; mostly because the LBV is a notable distance from the cluster center. Without conclusive evidence to establish that the LBVs are de facto cluster members, I excluded these LBVs from my sample.

While Cyg OB2 #12 is a confirmed member of the famed Cyg OB2 (Hanson 2003), the lack of a young cluster within the OB association prevents us from including the LBV in my study of cluster members. W51 LS1 was excluded for the same reason. While home to many massive OB stars, including W51 LS1, the G49.5-0.4 complex in W51 has no known central cluster (Okumura et al. 2000). While in both instances I observe that the resident LBV is toward the edge, rather than the middle, of its host region, I recognize these locales are significantly different from the cluster environment I sought to explore.

Several LBVs and candidate LBVs are members of the Galactic Center Cluster. This extreme environment is highly unique; centered around a super-massive black hole and subject to strong tidal forces, magnetic fields, and stellar winds, the cluster's star formation history is far from understood. For instance, whether the cluster formed *in situ* or spiraled inward is still a matter of debate (Paumard et al. 2001). Clearly, the positions of the LBVs might result from any number of mechanisms unique to the Galactic Center region. Therefore the Galactic Center Cluster is not comparable to the homogenous clusters I assess here.

Four LBVs, HD 80077, P Cygni, and WRA 751, are associated with massive stars or star clusters in their vicinity. Moffat & Fitzgerald (1977) identified HD 80077 as a potential member of Pismis 11, noting that several suspected cluster members were reddened by the same amount as the LBV. However, since both the constituency of Pismis 11 and the membership of the LBV remain unclear I exclude it from my sample.

The status of P Cygni is akin to that of HD 80077. Turner et al. (2001) claim that P Cygni is a member of an unnamed grouping of stars that form a double cluster with the young open cluster IC 4996. P Cygni's membership in the small unnamed grouping is inferred from line-of-sight and reddening arguments, similar to those made in the case of HD 80077. Since little is known about the stars in the unnamed cluster and cluster membership of P Cygni is not confirmed, I did not include it in my sample.

WRA 751 appears to be a member of an unnamed cluster discovered by Pasquali et al. (2006). Again, similarities in reddenings and line-of-sight arguments are used to identify the LBV as a member of the cluster. However, this potential cluster is far from well-established. The authors point out that several stars distant from the cluster core have reddenings similar to the cluster proper, but may not be members. Furthermore, the techniques used to cull non-cluster objects also excludes fainter stars, even if they are indeed cluster members. Given the paucity of data about this newly discovered cluster and the need for further observation to establish the LBVs membership and the cluster census, WRA 751 was rejected from my sample.

AG Car is located in a particularly dense field of massive stars; between 50-100 massive stars are located within 20″ of the LBV (Hoekzema et al. 1992). Extensive studies by Hoekzema et al. (1992) found that while AG Car lies in the line-of-sight of both Car OB1 and Car OB2, it is a member of neither association. In fact, while they identified a few potential WR stars at a distance consistent with AG Car, they found no massive cluster associated with the LBV.

Thus, five Galactic LBV meet my criteria as confirmed members of well-characterized clusters. I present a summary of relevant characteristics and literature sources for each cluster below:

Located between 2-4 kpc away, Westerlund 1 spans 0.6-2.6 pc and has ~ 60 massive members. Counted in this census is W243, a candidate LBV (Clark & Negueruela 2002). I note that W243 is outside the $50''$ diameter core defined in a recent survey of the cluster (Clark et al. 2005). In this letter, I use the positions of massive cluster members from several recent studies of Westerlund 1 (Clark et al. 2005; Negueruela & Clark 2005; Crowther et al. 2006). Cluster membership is well-defined; Clark et al. (2005) establish the massive cluster population with optical photometry and spectroscopy, while Crowther et al. (2006) confirm the spectral type of cluster Wolf-Rayets with infrared narrow-band imaging and spectroscopy.

The Quintuplet, known for the five bright stars that lend the cluster its name, contains two potentially peripheral LBVs, the Pistol Star, and FMM 362 (Figer et al. 1995, 1999). At the distance of the Galactic Center, the cluster spans $50''$ and is composed of > 30 massive stars and potentially hundreds of unseen low mass stars. The Pistol Star and FMM 362 are located approximately $30''$ and $45''$ from the core. I use positions of the brightest members of the Quintuplet from Figer et al. (1995), who identified cluster members based on near-infrared photometry and K-band spectroscopy.

Another recently discovered massive cluster, Cl 1806-20, contains LBV 1806-20 (Eikenberry et al. 2004a; Figer et al. 1999). Smaller than the Quintuplet or Westerlund 1, it hosts $\sim$ ten massive stars (LaVine et al. 2003; Figer et al. 2005). Located at a distance of ~ 15 kpc, it spans less than $40''$ on the sky. A cursory view of the distribution of cluster stars reveals that the LBV is $30''$ from the densest region of Cl 1806-20. I utilize positions of massive stars from Figer et al. (2005), who confirmed the membership of objects in Cl 1806-20 using near-infrared spectroscopy.

Regarded as the center of the open cluster Trumpler 16, the well-studied LBV, Eta Carina, provides a contrast to the rest of the sample. At a distance of $3.6 - 4.0$ kpc, Trumpler 16 spans greater than $5'$ and is home to ~ 30 massive stars and hundreds of lower mass members (DeGioia-Eastwood et al. 2001; Carraro et al. 2004). Using positions of Trumpler 16 cluster members from DeGioia-Eastwood et al. (2001) I complete the analyses described in §7.3.1 and §7.3.2.

I present images of each cluster, indicating their resident LBV, in Figure 7-1.

7.3 Probability Analyses

While a cursory visual inspection indicates that Cl 1806-20, W243, FMM362, and the Pistol Star are not located in the cores of their clusters but the outskirts (see Figure 7-1), I sought to verify this qualitative impression with quantitative evidence. My first task was to define what it means to be a peripheral cluster member.

Mathematically assessing my initial visual observation on a cluster by cluster basis proved to be challenging. For example, I cannot use a 3σ deviation from the mean radius to define "peripheral", as no cluster members in the literature data meet this criterion. Any object located this far away from the cluster center would most likely not be considered a cluster member. Furthermore, small number statistics create additional problems. The clusters in my sample have few stars; assessing the statistical significant of the position of one star out of ten is difficult. Although this is the case, I recognized that it is difficult to explore the potential of LBVs as peripheral cluster members without addressing where LBVs lie in each host cluster and how their locations compare to other cluster stars. With this in mind, I sought to carefully characterize the positions of LBVs within individual clusters (§7.3.1).

While this analysis cannot confirm whether individual LBVs are peripheral cluster members to a high statistical certainly, it motivated the further exploration of LBVs as an ensemble of peripheral objects. In the context of a statistically significant sample, an ensemble of objects are peripheral cluster members if they have a broader radial

distribution about the mean than similarly massive stars in their clusters. I explore LBVs as an ensemble of peripheral objects in §7.3.2.

7.3.1 Individual Analyses of LBVs as Peripheral Cluster Members

Mass segregation theories suggest that less massive stars should move toward the cluster outskirts while massive stars sink toward the center (Spitzer 1987; Binney & Tremaine 1987). I seek to answer a specific question; are Luminous Blue Variables anomalously peripheral with respect to mass segregation theories? Judging whether or not an object is in an anomalous location requires a comparison population. In this case, I compare the resident LBV to the remaining massive stellar population in their respective host clusters. Are LBVs further from the center than the majority of the massive stars? Furthermore, does the area enclosed within the radius at which the LBV is located contain the bulk of the mass associated with the massive population?

Using the literature data described in §7.2, I found the average right ascension and declination of each cluster using the position of its members; this gave us a de facto cluster center. I then found the distance between each cluster star and this central position. Finally, I counted the total number of stars with a distance greater than or equal to that of the LBV. I divided this number by the total number of cluster stars and called the resulting value ζ_{LBV}. I list my values for ζ_{LBV} in Table 7-1. In each cluster more than 75% of the other massive stars in each cluster are enclosed within the radius of the LBV.

I then took this analysis a step further. Using a recent paper by Crowther (2007) I estimated masses for Wolf-Rayet stars in each LBV host cluster. The author reported that WC stars spanned a mass range of $9 - 16M_{\odot}$ while WN stars spanned $10 - 83M_{\odot}$. I assigned the average value of $12.5M_{\odot}$ to every WC and $46.5M_{\odot}$ to each WN. I then assigned masses to all cluster supergiants using values from Cox (2000). I recomputed the position of the cluster center of each cluster, weighting the position of every star by its stellar mass. I found the distance to the LBV from the mass-weighted cluster center and calculated the percentage of the total mass associated with massive stars which is

enclosed by the radius of the LBV. Finally, to eliminate any potential bias resulting from the assumption of Crowther (2007) masses for WC and WN masses, I repeated the above analysis using uniform values for both types of Wolf-Rayets. In the second iteration I used the average mass of WR stars, $46.5M_{\odot}$ for every Wolf-Rayet. In the final case, I used a value on the low end of the mass range, $25M_{\odot}$. In all calculations, the total cluster mass associated with massive stars excludes all LBVs in the cluster. I present the results in Table 7-2. I noticed that while for three LBVs in my sample, the percentage of mass enclosed within the LBV radius is fairly unaffected by my assumptions for WR masses, the values for one LBV, the Pistol Star, are more sensitive. However, in all iterations, the majority of the total cluster mass associated with massive stars is always enclosed by the LBV radius.

7.3.2 Ensemble Analysis of LBVs as Peripheral Cluster Members

In the previous section, I established that LBV 1806-20, the Pistol Star, FMM 362, and W243 do indeed lie outside the majority of massive cluster members and the bulk of the cluster mass associated with massive stars. I point out that if these stars were not members of a particular stellar type, my result would not be particularly interesting. Several stars must be at or near the edge of a cluster and one star must be furthest away; clearly, finding a star on the outskirts of a cluster is, in itself, unremarkable.

What makes my results intriguing is the context. It seems unlikely that four stars of the same rare class, would, by chance alone, lie in the outskirts of their cluster. However, I wish to analyze this "hunch" more methodically. Thus, I calculated the probability of consistently finding five stars, one in each cluster, outside the radius of the resident LBV. I define this value as ζ_{total}. A low probability, a small value of ζ_{total}, would imply that the positions of the LBVs was not merely random.

To determine the total probability, ζ_{total}, I first measured the likelihood of finding a star at or beyond the cluster radius of each individual LBV. This probability, ζ_{LBV}, is simply the number of stars lying outside the radius of the LBV and was calculated for

my analysis in §7.3.1. The results appear in Table 7-1. The product of the five values of ζ_{LBV} is equal to ζ_{total}. In all cases, my number counts exclude all cluster LBVs. When calculating values ζ_{LBV} for the two LBVs in the Quintuplet, I used the radius of the Pistol star for ζ_{Pistol} and the radius of FMM 362 for ζ_{362}.

Using my values of ζ_{LBV}, I gauged the likelihood of finding at least one star in each cluster outside the radius of LBV, the goal of this analysis. I multiplied the five values of ζ_{LBV} in Table 7-1 and found $\zeta_{total} = 1.9 \times 10^{-4}$. This value implies that there are only two chances in ten thousand that when randomly selecting n massive stars from n clusters, all will be at or beyond the radius of the LBV in each cluster. My value of ζ_{total} suggests that it would be difficult for random chance alone to account for the positions of the LBVs.

However, before I accept this conclusion, I must address an important detail. ζ_{total} is the product of five values of ζ_{LBV}; can drawing five numbers at random from a uniform distribution and multiplying them together yield a number less than or equal to 1.9×10^{-04}? If I find that the product of five random numbers between zero and one easily reproduce probabilities of 0.02% or 0.002%, my result would be less robust.

I evaluated this hypothesis using a Monte Carlo simulation. I choose a number at random from a uniform distribution for each cluster. This simulated value of ζ_{LBV} is defined as $\zeta_{sim-LBV}$. This number represents an object's rank, in distance, from the center. I choose a uniform distribution so that my analysis is independent of the functional form of the spatial distribution of stars in the cluster.

Multiplying five values of $\zeta_{sim-LBV}$, I computed a random value for $\zeta_{sim-total}$, my simulated value of ζ_{total}. I repeated this process for ten thousand iterations, resulting in ten thousand values of $\zeta_{sim-total}$. I then calculated the number of times I found a value less than or equal to ζ_{total} by random chance alone and divided by my number of iterations. I found that only 7% of the ten thousand simulated values of $\zeta_{sim-total}$ were less than or equal to the value of ζ_{total} derived from the observations. Thus, my Monte Carlo

simulation indicates that my observed value of ζ_{LBV} is difficult to reproduce in a random distribution.

7.4 Discussion

The techniques described in the previous section confirm my initial observations, that the majority of LBVs in well defined young clusters are located on cluster outskirts. I found that LBVs, as an ensemble, met the definition of peripheral cluster member defined in §7.3.2, even when including the control cluster Trumpler 16. I calculate a two in ten thousand chance that n randomly selected massive stars from n clusters will all be at or beyond the radius of the LBV in each cluster. I find that 7% of the time I can obtain a value less than or equal to my value for ζ_{total} by random chance, which implies that my result is at approximately a 2σ level.

Having established that random chance alone can not account for the observed position of LBVs in clusters, I must seek physical explanations. One might ask, where do I expect to observe LBVs in clusters? Mass segregation theories posit that massive stars in clusters sink into the center while less massive stars are relegated to the outskirts of the cluster (Spitzer 1987; Binney & Tremaine 1987). Furthermore, the massive stars that sink to the center are likely to suffer collisions, form binaries, and participate in runaway mergers. Thus, the most massive stars, often the product of multiple collisions, are expected to be centrally located (Portegies Zwart & McMillan 2002; Portegies Zwart et al. 1999).

I recall that the LBVs are generally regarded as the most massive stars in the Galaxy. The five LBVs in my analysis are easily amongst the most massive in their respective clusters, with reported masses $> 100 M_{\odot}$ (Figer et al. 1998; Eikenberry et al. 2004a; Clark & Negueruela 2004). Clearly, given the extreme masses of LBVs and the dictates of mass segregation theories, one would suppose that LBVs would be centrally located. To place my result in context; theory suggest that LBVs should not be on the outskirts of their cluster. Mass segregation strongly implies that for LBVs, ζ_{total} should approximate one;

almost every star should lie further than the LBV from the center. Furthermore this should be at least a 3σ result. Thus my result is strengthened; it lies in the opposite direction of what theory predicts.

One significant exception to my result is Eta Carina. which appears centrally located in its cluster. However, I note that since I cannot view the three-dimensional structure of Trumpler 16, it is possible that line-of-sight projection effects could account for Eta Carina's apparent central location. In the absence of dynamical evidence I can not further comment on this possibility, but it is important to recognize that I also cannot guarantee that Eta Carina is actually in the center of Trumpler 16.

My results pose several questions. What scenarios might lead to LBVs being located in the periphery rather than the core of the cluster? Is one particular process at work in these massive clusters or could several factors operate to produce these notable exceptions to the mass segregation rule?

While the clusters themselves have similar taxonomy, the Galactocentric distances vary widely. The Quintuplet, for instance is located 35 pc from the the Galactic Center (Portegies Zwart et al. 2001). Might tidal forces influence the location of the LBVs in this cluster? Portegies Zwart et al. (2001) noted that tidal effects have considerable effects that increase as Galactocentric distance decreases. Indeed, the Quintuplet is believed to be just barely bound against tidal disruption (Figer et al. 1999). While this is not a conclusive answer, it suggests that other forces might deter the normal infall of several of this cluster's massive star.

However, neither Westerlund 1 nor Cl 1806-20 is within a Galactocentric distance that might suffer from these tidal effects. How can I explain the positions of the LBVs in these clusters? One point of interest is that both clusters contain magnetars: highly magnetized neutron stars. Recently, several authors have suggested that the progenitors of these objects may be very massive stars (Eikenberry et al. 2004a; Fruchter et al. 2006). If future works confirm that very massive stars are the antecedents of magnetars, their

presence in Westerlund 1 and Cl 1806-20 would mean that the current LBVs in these clusters were not always the most massive cluster members.

In this scenario, the current LBV would not dominate the dynamical evolution of its cluster and therefore would not necessarily be the first star in the core. Still, even as the second or third most massive star in the cluster, one would still expect the LBV to sink to the center (Portegies Zwart & McMillan 2002). However, the presence of another, more massive, potentially violently-evolving star sinking toward the core offers the potential for interactions and ejections. This scenario has an important caveat; initial observations of the clusters indicate that that the magnetar in Westerlund 1 is greater than $1'$ from the cluster core and also, that SGR 1806-20 is not centrally located (Kaplan et al. 2002; Figer et al. 2005; Muno et al. 2006). It is still possible, though, that the presence of evolved and/or supermassive stars in Westerlund 1 and Cl 1806-20 during a previous epoch could offer some explanation for LBV positions.

Alternatively, my result might offer a glimpse into ongoing theoretical discussions regarding primordial mass segregation in clusters (Bonnell et al. 2001; Bonnell & Bate 2006). One important tenet of this theory is that massive stars are more likely to form in the cores of star forming regions, suggesting that even in very young clusters, massive stars should be centrally located. This prediction is at odds with the observed peripheral location of four of the massive LBVs in my sample. Although at this point I can draw no definite conclusions, I point out that these observations of the locations of massive stars in $10^4 - 10^5 M_\odot$ mass clusters may help refine theoretical models of cluster evolution and primordial mass segregation.

Finally, I address the LBVs rejected from my sample. Several authors suggest that many of the massive clusters in our Galaxy remain undiscovered (Hanson 2003; Portegies Zwart et al. 2001). It is certainly possible that LBVs with no current cluster associations may, in fact, be members of undetected clusters. If new clusters are discovered around these LBVs, it would be useful to extend my study to include them.

Additionally, confirming the host clusters of HD 80077, AG Car, P Cygni, and WRA 75 and characterizing the full extent of the cluster's massive star population would allow us to expand my study to include them, increasing my sample. Finally, if I establish cluster membership of Sher 25 or ζ Sco, two LBVs that may be peripherally located in young clusters, adding these LBVs to my analyses may significantly strengthen my results. Clearly a good deal more data are needed before I can say with certainty that LBVs in clusters are preferentially peripherally located or explain why those I discuss in this chapter are exceptions to the rule.

7.5 Conclusion

My analyses show that LBVs in Westerlund 1, Cl 1806-20, and the Quintuplet are located on the periphery of their host clusters. I also show that these LBVs are not likely to be located on the outskirts of their clusters by chance alone; only a two in ten thousand chance exists that that n randomly selected massive stars from n clusters will all be at or beyond the radius of the LBV in each cluster. Furthermore I argue that the locations of these LBVs is contrary to theoretical expectations, as mass segregation theories suggest that massive stars should quickly move to the cores of their natal clusters.

I offer potential explanations for the locations of the cluster LBVs, but conclude that the current lack of data currently available offers no answers or single mechanism to easily account for their positions. Increasing the sample size by exploring the environments around seemingly isolated LBVs, establishing LBV membership in potential host clusters, and expanding our knowledge of LBVs in new or poorly studied environments may offer us the best chance to determine if LBVs are indeed preferentially located on the periphery of massive clusters.

Table 7-1. Position of LBVs in clusters compared to other cluster members. Columns indicate Luminous Blue Variable name, host cluster name, total number of massive stars in host cluster excluding all cluster LBVs (N_{MS}), radius of LBVs (R_{LBV}) in arcseconds and pc, number of stars outside the LBV radius ($N_{R>LBV}$) excluding all cluster LBVs, and number of stars outside the LBV radius divided by total number of massive stars in each cluster (ζ_{LBV}). I assumed a $\zeta_{LBV} = 1$ for our control LBV, Eta Carina in Trumpler 16.

LBV	Cluster	N_{MS}	R_{LBV} ($''$)	R_{LBV} (pc)	$N_{R>LBV}$	ζ_{LBV}
1806-20	Cl 1806-20	10	17.0	1.24	1	0.100
W243	Westerlund 1	62	94.7	2.5	6	0.097
Pistol Star	Quintuplet	35	31.1	1.2	8	0.229
FMM362	Quintuplet	35	45.0	1.7	3	0.086

Table 7-2. Percentage of cluster mass associated with massive stars enclosed by mean-weighted LBV radius. Columns indicate Luminous Blue Variable name, host cluster, mass-weighted radius of the cluster LBV (R_{MW-LBV}), and percentage of cluster mass associated with massive stars enclosed by the LBV mass-weighted radius, % M_{enc}, for each of the three trials.

		Crowther (2006)		WR = $46.5M_\odot$		WR = $25M_\odot$	
LBV	Cluster	R_{LBV-MW}	% M_{enc}	R_{LBV-MW}	% M_{enc}	R_{LBV-MW}	% M_{enc}
1806-20	Cl1806-20	17.2	91	18.4	93	18.7	90
W243	Westerlund 1	98.2	91	94.8	88	96.9	91
Pistol Star	Quintuplet	33.5	86	30.3	72	31.4	77
FMM 362	Quintuplet	45.9	91	47.7	94	46.9	95

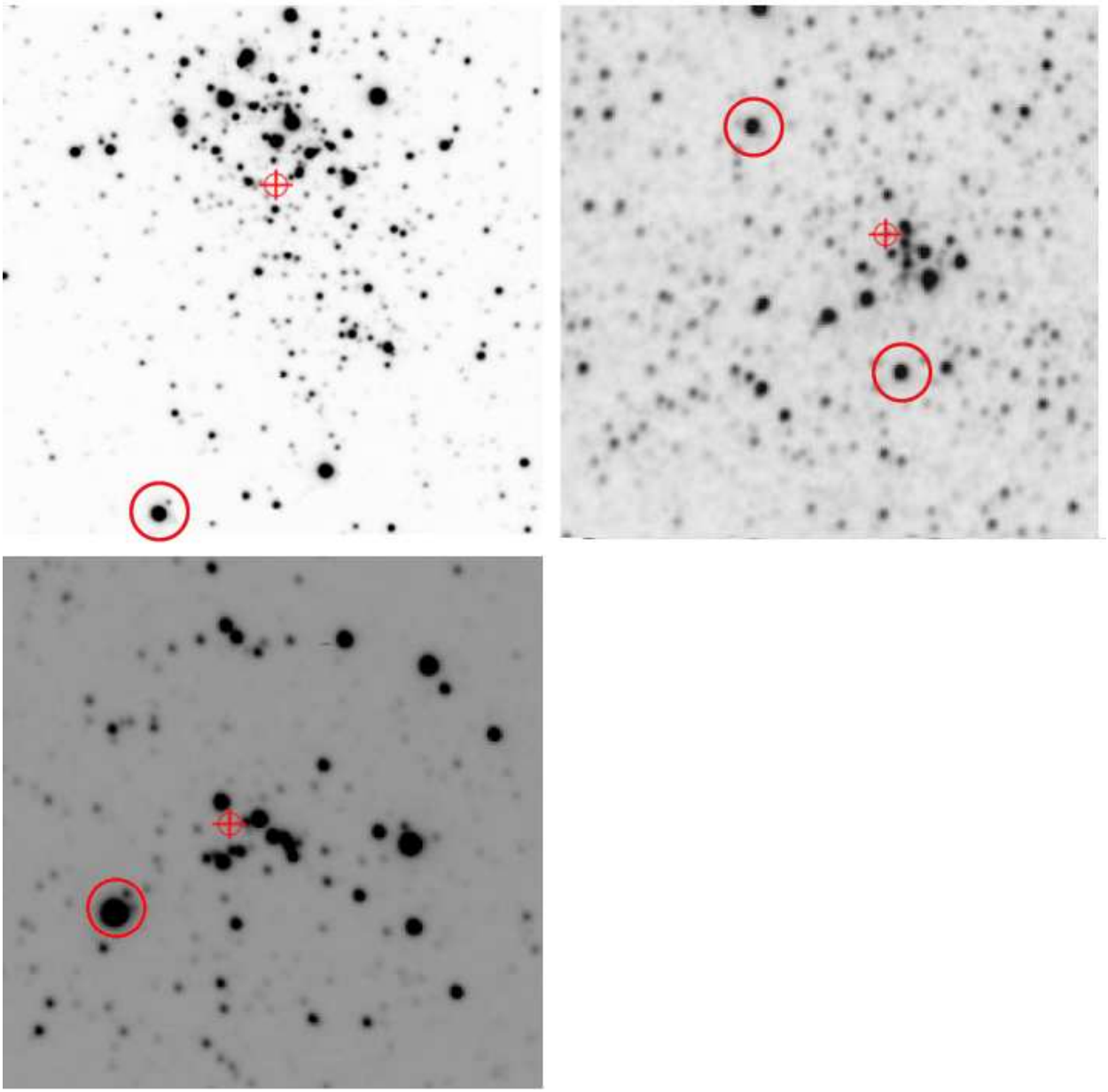

Figure 7-1. Clockwise starting from the upper left. Images of Westerlund 1 (Clark et al. 2005), the Quintuplet (Figer et al. 1999), & Cl 1806-20. In each image the LBV is circled and labeled and the cluster center is marked.

CHAPTER 8
CONCLUSION

8.1 Summary and Motivation of the CIRCE Project

Since the invention and refinement of HgCdTe detectors and infrared optimized telescopes, near-infrared instruments have become a mainstay of astronomical research. Currently, ten of the world's largest telescopes have a total of ~ 20 near-infrared instruments available for observation or in the final stages of integration. Plans for bigger and better instruments, including the next generation of NIR cameras designed for 20 and 30 meter telescopes, are already underway (Eikenberry et al. 2006a). With so many NIR instruments currently in operation and more on the horizon, what is the justification for building CIRCE?

As discussed in Chapters 1 and 2, CIRCE's first function is to fill the gap between the inception of science operations at the GTC and the commissioning of the facility NIR instrument EMIR. During that time, CIRCE will be the only NIR instrument on the world's largest optical/infrared telescope. Anticipating that it will be used for a wide-variety of science projects, we designed CIRCE as a workhorse instrument with multiple modes. Once EMIR is complete and ready for use on the GTC, CIRCE will move on to its secondary role – to complement the suite of facility instruments with spectro-polarimetric modes, high-speed photometry, and low- and mid- resolution spectroscopy.

Besides these drivers, CIRCE has a third purpose. CIRCE was conceptualized as a training instrument for students pursuing careers as instrument scientists, astronomers who guide the development of instruments to ensure they meet the scientific needs of the astronomical community. While new instruments often explore the "bleeding edge" of technology, they are fundamentally driven by the science needs of the astronomical community. While in theory any number of designs might be feasible for a given instrument, instrument scientists advocate solutions that will produce the best data. This

requires not only a working knowledge of a wide-variety of astronomical projects and the type of observations necessary to carry-out each experiment, but the ability to translate these requirements into optical, mechanical, and electronic designs and specifications.

However, at a time when the horizon of astronomical instrumentation is rapidly expanding and new instrument scientists are needed, the liability, complexity, and expense associated with facility instruments has significantly limited student participation in these projects. One of the basic tenants of CIRCE was to allow graduate students critical roles in the design and integration of an instrument destined for an 8 - 10 meter class telescope.

In Chapters 2, 3, and 4, I detailed my contributions to the optical, opto-mechanical, and cryo-mechanical design of CIRCE. In Chapter 2, I presented the development of CIRCE's all-reflective aspheric optical design, specifically my role in the redesign, analysis and tolerancing of the system (Edwards et al. 2004). In Chapter 3, I introduced the concepts behind mechanical design and discussed my creation of two- and three-dimensional drawings of mirrors, benches, and brackets (Edwards et al. 2006). Finally, I outlined my work on the solid models and two- dimensional drawings of the pupil box mechanism in Chapter 4 (Edwards et al. 2006).

CIRCE, like essentally all astronomical instrumentation, is a team effort. Two other students, Miguel Charcos-Llorens and Nestor Lasso, and a postdoctoral fellow, Dr. Antonio Marin-Franch each worked on a wide variety of other sub-systems and modes. Dr. Marin-Franch designed the software and user control interface that operate cryogenic motors, temperature sensors, and other mechanisms inside the CIRCE dewar. Nestor Lasso led the electrical layout and helped with the modification of the detector array. Miguel Charcos-Llorens developed the polarimetric mode, created a program to measure the flexure of the bench, and designed the cryostat and focal plane mechanism. He also completed the optical bench and modified the pupil box to meet new specifications required by the polarimetric design. I discuss the current status in more detail in §8.4.

8.2 Status of CIRCE

The CIRCE team has completed the design of many critical CIRCE opto- and cryo-mechanical components including the pupil box and focal plane mechanisms, brackets, mirrors, cryostat, and detector stage. Most of the manufacture will take place in the UF Physics and Astronomy Machine Shop, including the optical bench. To substantially reduce cost and lead time, M. Charcos designed the large (1 meter diameter $\times$ 1.5 meter long) optical bench in multiple pieces so that it could be manufactured on machines available in-house at UF. Flexure modeling shows that this option is viable; the large cryogen tank beneath the bench offers adequate stiffness to support the optics and cryo-mechanisms. We anticipate that completion of the bench and mirror blanks in the next three months and the remaining components approximately three months after.

Once the bench and mirror blanks are complete, we will ship them to Janos Technology, who will diamond-turn the mirrors on a CNC lathe and mount them on the brackets and bench. They will then employ a newly developed technique that emphasizes ensemble testing of the mirrors, brackets, and bench. After testing for errors, they will slightly reshape the mirrors to reduce aberrations and improve image quality. This novel solution to optical analysis allows for immediate correction of alignment problems *in situ*. Thus the completed bench, with mirrors and brackets in place and aligned, will arrive at UF ready for integration. We anticipate that the manufacture and alignment of the optics will take 3 - 6 months.

The design of the electrical layout is in the final stages of review. Cryogenic motors and the hardware to control them are currently in-hand at UF. Control software, along with a Java-based User Interface, designed by A. Marin-Franch, is complete. The interface was rigorously tested by the IAG, who used it extensively during the integration of Flamingos 2. Testing of cryo-mechanisms, creation of cables, and manufacture of the cryostat by an off-site vendor will take place in the next 6 months during the manufacture and alignment of the optics off-site.

One all of CIRCE's components return to UF, we anticipate a further 3 - 6 month integration and testing period. Thus, we expect that CIRCE will ship to the telescope sometime during the late summer or early fall of 2009.

8.3 Summary of A NIR Narrow-Band Imaging Survey

Utilizing the ability of NIR radiation to penetrate highly extinguished environments, I completed a narrow-band survey to search for the emission lines which are signatures of massive stars in the field surrounding Soft Gamma Repeaters (SGRs). By probing for clusters that host both massive stars and magnetars, I sought to link the births of these rare neutron stars with the deaths of very massive stars.

Using the current generation of NIR instruments, including the ISPI on the CTIO 4 meter and WIRC on the Palomar 200", I observed the fields around SGR 1806-20, SGR 1900+14, SGR 1627-41, and SGR 0526-66. To test whether my NIR narrow-band survey would successfully find massive star candidates, I first applied my technique to SGR 1806-20, a member of the known massive star cluster, Cl 1806-20 (Chapter 5; Edwards et al. *submitted*). My method, which utilized PSF photometry of broad- and narrow- band images to create a color-color diagram, successfully picked out a number of known WR and OBI stars. It also identified ~ 10 OBI candidates for follow-up spectroscopy.

In Chapter 6, I apply the technique developed in Chapter 5 on the remaining three SGR fields. First I studied the embedded cluster associated with SGR 1900+14. Two potential cluster members, both M5 supergiants, saturated the central region of the frame, rendering it difficult to study previously identified cluster stars or find new massive cluster members in the area. However, I identified > 10 potential OBI and rare emission-line stars within $45''$ of the SGR (Edwards et al. *in preparation*). Next, I studied the field surrounding SGR 1627-41, a virtually unexplored magnetar environment. I found a number of potential massive stars with Brγ absorption and emission. Several of these also exhibit HeI features, making them strong candidates for follow-up spectroscopy.

Finally, I studied two regions around SGR 0526-66: a 45″ search radius centered on the magnetar and a 45″ search radius centered on SL 463, a nearby massive star cluster. While I did detect one bright candidate OBI star in the center of SL 463, confirming the observations of Klose et al. (2004), I did not find a population of stars with narrow-band emission or absorption in either region. However, obscurration by local dust, especially given the existence of SNR N49 near the magnetar, could easily skew my photometry. Deeper narrow-band observations and the addition of broad-band data is clearly necessary before drawing conclusions about the stellar populations near SGR 0526-66.

While narrow-band imaging is sometimes suggested as potentiall simpler and faster way to search for massive stars without performing spectroscopy, my work shows that this technique requires extensive calibration, excellent quality narrow- and broad-bandphotometry, and careful analysis to yield reliable and unambigious results. However, once these requirements are met, the technique is viable and potentially powerful, especially in very crowded environments where color-color and color-magnitude diagrams can reduce the number of massive cluster candidate from thousands to tens.

8.4 Future Work

8.4.1 Extinction and Stellar Populations in the SGR Fields

One bi-product of my search for massive stars around SGRs is excellent broad-band photometry of thousands of stars in the regions surrounding SGR 1900+14 and SGR 1806-20. I plan to use these data to study variations in the extinction law along the line-of-sites to the clusters. This might be especially enlightening in the case of SGR 1900+14, where controversy concerning the reddening to the cluster exists. Further, I will examine populations of stars at different reddenings to construct more complete pictures of the stellar populations of the fields. Finally, I will search for unrelated serrendipitous clusters by looking for overdensities in the field.

8.4.2 Massive Stars with CIRCE

While I completed the bulk of my narrow-band imaging survey of SGR environments using the previous generation of NIR instruments, I anticipate that observations with CIRCE on the GTC will provide the keystone for this project. Using CIRCE's spectroscopic mode, I will perform long-slit grism spectroscopy to follow-up all massive star candidates. Comparing this spectroscopy to NIR atlases of massive stars (Hanson et al. 1996; Figer et al. 1998), I will determine the spectral type of each identified massive stars and estimate its distance and reddening, confirming each candidate's cluster membership.

I will also use CIRCE to further investigate the fields surrounding LBVs. In Chapter 7, I showed that LBVs in Westerlund 1, Cl 1806-20, and the Quintuplet are located on the periphery of their host clusters. I presented statistical evidence to demonstrate that these massive stars are not likely to be located on the outskirts of their clusters by chance alone. However, given the lack of LBVs with firmly established cluster membership, the need for more observations is clear. Using CIRCE narrow-band imaging and the techniques demonstrated in this dissertation, I will probe for massive stars around seemingly isolated LBVs or those in poorly studied regions. I hope to increase the population of LBVs associated with massive clusters and then reassess the locations of these objects within their host clusters using a more statistically significant sample.

8.4.3 Magnetar Environments

There are two types of magnetars; Soft Gamma Repeaters and Anomalous X-ray Pulsars. In this dissertation, I focused on SGRs, which have the most evidence for potential associations with massive clusters. Located in regions of heavy extinction, their environments offered the best opportunity to use NIR observations to find large massive clusters previously missed by optical surveys.

Similarly, many AXPs are also in the Galactic Plane where extinction is patchy and crowding problematic. Thus next logical step is to expand my probe of mangetar

environment to include AXPs. If I find massive stars around AXPs, it will strengthen the argument that magnetars form from very massive stars that lost most of their mass during their LBV and WR phases. If I confirm that all SGRs are members of massive clusters, but fail to find massive stars around most AXPs, this may suggest different formation mechanisms for the two "flavors" of magnetars. Thus, investigating AXP environments should provide substantial information about the formation channels of magnetars and the differences between SGRs and AXPs.

I have started an observing campaign to survey AXP environments with narrow-band imaging using currently available NIR instruments. To date, I have observed four AXP fields with WIRC using Brγ and 2.27 μm K_{cont} filters. In summary, I plan to continue this survey, expand it to include data from CIRCE on the GTC, perform follow-up single slit and multi-object spectroscopy of both SGR and AXP massive cluster candidates, and begin a new narrow-band survey to survey the environments of LBV. I believe that these projects will provide significant results on a variety of enigmatic objects.

APPENDIX: ZEMAX OUTPUT OF CIRCE PRESCRIPTION

The CIRCE optical prescription consists of several tables that describe the locations, rotations, and general properties of each surface. The most important of these is the Surface Data Summary, which I show in Table A-1. This table gives a very detailed description of every mirror in the prescription; listing values of the radius, thickness, glass, diameter and conic constant. Conic and flat mirrors are listed as "standard" surfaces while the higher order asphere is listed as "evenasph".

Coordinate breaks ("coodbrk") are also listed as a type of surface in the Surface Data Summary. In the Lens Data Editor, shown in Figure 2-4, columns for the X, Y, Z decenters and α and β tilts are listed for all coordinate breaks that appear in Table A-1. However, in the optical prescriptions these values are output into a different table, the Coordinate Break Summary, which I show in Table A-2.

Three surfaces always appear in the Lens Data Editor and Surface Data Summary: OBJECT, STOP, and IMAGE. The OBJECT is the surface from which ZEMAX launchs the rays that will propogate into the system. The OBJECT is always surface 0. The STOP is the aperture stop of the system. In most IR telescopes, the secondary mirror acts is defined as the aperture stop. Examining Table A-1, one can see that the Surface labeled STOP is listed as the secondary. The IMAGE is where the image of the object is formed; this is where ZEMAX performs most of the image quality diagnostics

The prescription can also include other tables, like the field angles and wavelengths used to perform optical analysis. While these are important in determining the quality of the instrument, they do not impact that layout of the camera.

Table A-1. ZEMAX Surface Data Summary

Surface	Type	Comment	Radius	Thickness	Glass	Diameter	Conic
OBJ	STANDARD		Infinity	Infinity		0	0
1	STANDARD		Infinity	0		10159.09	0
2	STANDARD		Infinity	14740		1090	0
3	STANDARD	PRIMARY	-33000	-14739.41	MIRROR	10144.61	-1.00225
STO	STANDARD	SECONDARY	-3899.678	18070.61	MIRROR	1070	-1.504835
5	STANDARD		Infinity	20	FSILICA	241.2386	0
6	STANDARD		Infinity	55		240.6069	0
7	STANDARD	FOCAL PLANE	Infinity	130		238.6015	0
8	COORDBRK	D1 (A)	-	0		-	-
9	STANDARD	F1	Infinity	0	MIRROR	289.4733	0
10	COORDBRK	D1 BEND (A)	-	-279		-	-
11	COORDBRK	D2 (A)	-	0		-	-
12	STANDARD	F2	Infinity	0	MIRROR	313.5647	0
13	COORDBRK	D2 BEND (A)	-	790.9824		-	-
14	COORDBRK	D3 (Y)	-	0		-	-
15	COORDBRK	D3 (A)	-	0		-	-
16	STANDARD	C3	-1466.211	-534.2299	MIRROR	831.7695	-0.335423
17	STANDARD	C4	-2771.235	251.5313	MIRROR	300.0933	-47.75465
18	COORDBRK	D4 (Y)	-	0		-	-
19	COORDBRK	D4 (A)	-	0		-	-
20	COORDBRK	D5 (Y)	-	0		-	-
21	STANDARD	D5 (Z)	Infinity	5		54.55716	0
22	COORDBRK	D5 (A)	-	0		-	-
23	STANDARD	LYOT	Infinity	0		53.35195	0
24	COORDBRK	D5 RET (-A)	-	0		-	-
25	STANDARD	D5 RET (-Z)	Infinity	-5		53.37644	0
26	COORDBRK	D5 RET (-Y)	-	0		-	-
27	STANDARD	FILTER	Infinity	3	FSILICA	54.94246	0
28	STANDARD		Infinity	272		54.39428	0
29	COORDBRK	D6 (G)	-	0		-	-
30	STANDARD		Infinity	368		128.4977	0
31	COORDBRK	D7 (Y)	-	0		-	-
32	COORDBRK	D7 (A)	-	0		-	-
33	STANDARD	IM5	-453.7226	-208.8597	MIRROR	625.5029	-0.581079
34	COORDBRK	D8 (Y)	-	0		-	-
35	COORDBRK	D8 (A)	-	0		-	-
36	STANDARD	IM6	-322.2179	128.3022	MIRROR	201.0975	-65.10662
37	COORDBRK	D9 (Y)	-	0		-	-
38	COORDBRK	D9 (A)	-	0		-	-
39	STANDARD	IM7	423.5224	-305.8381	MIRROR	133.2641	13.70991
40	COORDBRK	D10 (Y)	-	0		-	-
41	COORDBRK	D10 (A)	-	0		-	-
42	EVENASPH	IM8	387.7968	397.9117	MIRROR	505.0304	0.052712
43	COORDBRK	D11 (Y)	-	0		-	-
44	COORDBRK	D11 (A)	-	0.01073916		-	-
IMA	STANDARD		Infinity			52.63152	0

Table A-2. ZEMAX Coordinate Break Summary

Surface (mm)	X decenter (mm)	Y decenter (mm)	α (°)	β (°)	γ (°)
8	0	0	38	0	0
10	0	0	38	0	0
11	0	0	-38	0	0
13	0	0	-38	0	0
14	0	283.0357	0	0	0
15	0	0	1.4805	0	0
18	0	14.5212	0	0	0
19	0	0	16.906	0	0
20	0	-0.5	0	0	0
22	0	0	-4	0	0
24	0	0	4	0	0
26	0	0.5	0	0	0
29	0	0	0	0	180
31	0	-237.0789	0	0	0
32	0	0	10.0149	0	0
34	0	21.9164	0	0	0
35	0	0	-9.2779	0	0
37	0	-47.5662	0	0	0
38	0	0	-12.5764	0	0
40	0	-5.4163	0	0	0
41	0	0	-3.4666	0	0
43	0	-49.4212	0	0	0
44	0	0	3.8796	0	0

REFERENCES

Alvarez, P., Rodriguez-Espinosa, J. M., & Kabana, F. R. 2000, in Proc. SPIE, Vol. 4004, Telescope Structures, Enclosures, Controls, Assembly/Integration/Validation, and Commissioning, ed. T. A. Sebring & T. Andersen (Bellingham: SPIE), 26

Assousa, G. E., Herbst, W., & Turner, K. C. 1977, ApJ, 218, L13

Bethune, J. D. 1997, Engineering Graphics with AutoCAD Release 13 (2nd ed.; Upper Saddle River: Prentice-Hall, Inc.)

Bibby, J. L., Crowther, P. A., Furness, J. P., & Clark, J. S. 2008, MNRAS, 386, L23

Binney, J., & Tremaine, S. 1987, Galactic Dynamics (Princeton: Princeton University Press)

Bonnell, I. A., & Bate, M. R. 2006, MNRAS, 370, 488

Bonnell, I. A., Clarke, C. J., Bate, M. R., & Pringle, J. E. 2001, MNRAS, 324, 573

Brandner, W., Grebel, E. K., Chu, Y.-H., & Weis, K. 1997, ApJ, 475, L45

Carraro, G., Romaniello, M., Ventura, P., & Patat, F. 2004, A&A, 418, 525

Cepa, J., Aguiar, M., Bland-Hawthorn, J., Castañeda, H. O., Cobos, F., Correa, S., Espejo, C., Fragoso, A. B., Fuentes, J., Gigante, J. V., González, J. J., González-Escalera, V., González-Serrano, I., Joven, E., López, J. C., Militello, C., Peraza, L., Pérez, A., Pérez, J., Rasilla, J. L., Sánchez, B., & Tejada, C. 2003, in Revista Mexicana de Astronomia y Astrofisica Conference Series, Vol. 16, Science with the GTC, ed. J. M. Rodriguez Espinoza, F. Garzon Lopez, & V. Melo Martin (Mexico City: UNAM), 13

Chaisson, E., & McMillan, S. 1996, Astronomy Today (2nd ed.; Upper Saddle River : Prentice Hall, 1996)

Clark, J. S., & Negueruela, I. 2002, A&A, 396, L25

Clark, J. S., & Negueruela, I. 2004, A&A, 413, L15

Clark, J. S., Negueruela, I., Crowther, P. A., & Goodwin, S. P. 2005, A&A, 434, 949

Corbel, S., Chapuis, C., Dame, T. M., & Durouchoux, P. 1999, ApJ, 526, L29

Corbel, S., & Eikenberry, S. S. 2004, A&A, 419, 191

Corbel, S., Wallyn, P., Dame, T. M., Durouchoux, P., Mahoney, W. A., Vilhu, O., & Grindlay, J. E. 1997, ApJ, 478, 624

Cox, A. N. 2000, Allen's Astrophysical Quantities (4th ed.; New York: AIP Press; Springer)

Crowther, P. A. 2007, ARA&A, 45, 177

Crowther, P. A., Hadfield, L. J., Clark, J. S., Negueruela, I., & Vacca, W. D. 2006, MNRAS, 372, 1407

Cushing, M. C., Vacca, W. D., & Rayner, J. T. 2004, PASP, 116, 362

DeGioia-Eastwood, K., Throop, H., Walker, G., & Cudworth, K. M. 2001, ApJ, 549, 578

Devaney, N., Bello, D., Femenia, B., Castro, J., Villegas Lopez, A., Reyes, M., & Fuensalida, J. J. 2004, in Proc. SPIE, Vol. 5490, Advancements in Adaptive Optics., ed. D. Bonaccini Calia, B. L. Ellerbroek, & R. Ragazzoni (Bellingham: SPIE), 913

Duncan, R. C., & Thompson, C. 1992, ApJ, 392, L9

Edwards, M. L., Eikenberry, S. S., Marin-Franch, A., Charcos-Llorens, M., Rodgers, M., Julian, J., Raines, N., & Packham, C. 2006, in Proc. SPIE, Vol. 6269, Ground-based and Airborne Instrumentation for Astronomy, ed. I. S. McLean & M. Iye (Bellingham: SPIE), 157

Edwards, M. L., Marin-Franch, A., Eikenberry, S. S., Rodgers, M., Julian, J., Hanna, K., & Packham, C. 2004, in Proc. SPIE, Vol. 5492, Ground-based Instrumentation for Astronomy, ed. A. F. M. Moorwood & M. Iye (Bellingham: SPIE), 1710

Eikenberry, S., Andersen, D., Guzman, R., Bally, J., Cuevas, S., Fletcher, M., Gardhouse, R., Gavel, D., Gonzalez, A., Gruel, N., Hamann, F., Hamner, S., Julian, R., Julian, J., Koo, D., Lada, E., Leckie, B., Lopez, J. A., Pello, R., Perez, J., Rambold, W., Roman, C., Sarajedini, A., Tan, J., Venn, K., Veran, J.-P., & Ziegert, J. 2006a, in Proc. SPIE, Vol. 6269, Ground-based and Airborne Instrumentation for Astronomy., ed. I. S. McLean & M. Iye (Bellingham: SPIE), 188

Eikenberry, S., Elston, R., Raines, S. N., J., J., Hanna, K., Hon, D., Julian, R., Bandyopadhyay, R., Bennett, J. G., Bessoff, A., Branch, M., Corley, R., Eriksen, J.-D., Frommeyer, S., Gonzalez, A., Herlevich, M., Marin-Franch, A., Marti, J., Murphey, C., Rashkin, D., Warner, C., Leckie, B., Gardhouse, W. R., Fletcher, M., Dunn, J., Wooff, R., & Hardy, T. 2006b, in Proc. SPIE, Vol. 6269, Ground-based and Airborne Instrumentation for Astronomy., ed. I. S. McLean & M. Iye (Bellingham: SPIE), 39

Eikenberry, S. S., Elston, R., Guzman, R., Julian, J., Raines, S. N., Gruel, N., Boreman, G., Glenn, P. E., Hull-Allen, C. G., Hoffman, J., Rodgers, M., Thompson, K., Flint, S., Comstock, L., & Myrick, B. 2004a, in Proc. SPIE, Vol. 5492, Ground-based Instrumentation for Astronomy, ed. A. F. M. Moorwood & M. Iye (Bellingham: SPIE), 1264

Eikenberry, S. S., Garske, M. A., Hu, D., Jackson, M. A., Patel, S. G., Barry, D. J., Colonno, M. R., & Houck, J. R. 2001, ApJ, 563, L133

Eikenberry, S. S., Matthews, K., LaVine, J. L., Garske, M. A., Hu, D., Jackson, M. A., Patel, S. G., Barry, D. J., Colonno, M. R., Houck, J. R., Wilson, J. C., Corbel, S., & Smith, J. D. 2004b, ApJ, 616, 506

Elston, R., Raines, S. N., Hanna, K. T., Hon, D. B., Julian, J., Horrobin, M., Harmer, C. F. W., & Epps, H. W. 2003, in Proc. SPIE, Vol. 4841, Instrument Design and Performance for Optical/Infrared Ground-based Telescopes., ed. M. Iye & A. F. M. Moorwood (Bellingham: SPIE), 1611

Fahlman, G. G., & Gregory, P. C. 1981, Nature, 293, 202

Figer, D. F., McLean, I. S., & Morris, M. 1995, ApJ, 447, L29

Figer, D. F., McLean, I. S., & Morris, M. 1999, ApJ, 514, 202

Figer, D. F., McLean, I. S., & Najarro, F. 1997, ApJ, 486, 420

Figer, D. F., Najarro, F., Geballe, T. R., Blum, R. D., & Kudritzki, R. P. 2005, ApJ, 622, L49

Figer, D. F., Najarro, F., & Kudritzki, R. P. 2004, ApJ, 610, L109

Figer, D. F., Najarro, F., Morris, M., McLean, I. S., Geballe, T. R., Ghez, A. M., & Langer, N. 1998, ApJ, 506, 384

Fruchter, A. S., Levan, A. J., Strolger, L., Vreeswijk, P. M., Thorsett, S. E., Bersier, D., Burud, I., Castro Cerón, J. M., Castro-Tirado, A. J., Conselice, C., Dahlen, T., Ferguson, H. C., Fynbo, J. P. U., Garnavich, P. M., Gibbons, R. A., Gorosabel, J., Gull, T. R., Hjorth, J., Holland, S. T., Kouveliotou, C., Levay, Z., Livio, M., Metzger, M. R., Nugent, P. E., Petro, L., Pian, E., Rhoads, J. E., Riess, A. G., Sahu, K. C., Smette, A., Tanvir, N. R., Wijers, R. A. M. J., & Woosley, S. E. 2006, Nature, 441, 463

Fryer, C. L. 1999, ApJ, 522, 413

Fryer, C. L., & Kalogera, V. 2001, ApJ, 554, 548

Fuchs, Y., Mirabel, F., Chaty, S., Claret, A., Cesarsky, C. J., & Cesarsky, D. A. 1999, A&A, 350, 891

Garzón, F., Fuentes, J., Manescau, A., Díaz, J. J., Patrón, J., Pelló, R., López, J. C., Pérez, J., Fragoso, A. B., Gago, F., Beigbeder, F., Sanchez, V., Correa, S., & Villegas, A. 2003, in Revista Mexicana de Astronomia y Astrofisica Conference Series, Vol. 16, Science with the GTC, ed. J. M. Rodriguez Espinoza, F. Garzon Lopez, & V. Melo Martin (Mexico City: UNAM), 23

Gavriil, F. P., Kaspi, V. M., & Woods, P. M. 2002, Nature, 419, 142

Gillespie, C. M., Jr. 1981, in Proc. SPIE, Vol. 265, Shuttle pointing of electro-optical experiments; Proceedings of the Seminar, ed. W. Jerkovsky (Bellingham: SPIE), 1

Glass, I. S. 1999, Handbook of Infrared Astronomy (Cambridge: Cambridge University Press)

Golenetskii, S. V., Ilinskii, V. N., & Mazets, E. P. 1984, Nature, 307, 41

Hanson, M. M. 2003, ApJ, 597, 957

Hanson, M. M., Conti, P. S., & Rieke, M. J. 1996, ApJS, 107, 281

Harris, T. I. 1991, in Proc. SPIE, Vol. 1354, Intl Lens Design Conf, ed. G. N. Lawrence (Bellingham: SPIE), 104

Heger, A., Fryer, C. L., Woosley, S. E., Langer, N., & Hartmann, D. H. 2003a, ApJ, 591, 288

Heger, A., Woosley, S. E., Fryer, C. L., & Langer, N. 2003b, in From Twilight to Highlight: The Physics of Supernovae, ed. W. Hillebrandt & B. Leibundgut, 3

Herschel, W. 1801, Philosophical Transactions Series I, 90, 393

Hill, J. M., Angel, J. R. P., Lutz, R. D., Olbert, B. H., & Strittmatter, P. A. 1998, in Proc. SPIE, Vol. 3352, Advanced Technology Optical/IR Telescopes VI, ed. L. M. Stepp (Bellingham: SPIE), 172

Hodapp, K. W., Jensen, J. B., Irwin, E. M., Yamada, H., Chung, R., Fletcher, K., Robertson, L., Hora, J. L., Simons, D. A., Mays, W., Nolan, R., Bec, M., Merrill, M., & Fowler, A. M. 2003, PASP, 115, 1388

Hoekzema, N. M., Lamers, H. J. G. L. M., & van Genderen, A. M. 1992, A&A, 257, 118

Humphreys, R. M., & Davidson, K. 1994, PASP, 106, 1025

Hurley, K., Cline, T., Mazets, E., Barthelmy, S., Butterworth, P., Marshall, F., Palmer, D., Aptekar, R., Golenetskii, S., Il'Inskii, V., Frederiks, D., McTiernan, J., Gold, R., & Trombka, J. 1999, Nature, 397, 41

Hurley, K., Li, P., Vrba, F., Luginbuhl, C., Hartmann, D., Kouveliotou, C., Meegan, C., Fishman, G., Kulkarni, S., Frail, D., Bowyer, S., & Lampton, M. 1996, ApJ, 463, L13

Kaplan, D. L., Kulkarni, S. R., Frail, D. A., & van Kerkwijk, M. H. 2002, ApJ, 566, 378

Kaplan, D. L., Kulkarni, S. R., van Kerkwijk, M. H., Rothschild, R. E., Lingenfelter, R. L., Marsden, D., Danner, R., & Murakami, T. 2001, ApJ, 556, 399

Kaspi, V. M., & Gavriil, F. P. 2003, ApJ, 596, L71

Kleinmann, S. G., Gillett, F. C., & Joyce, R. R. 1981, ARA&A, 19, 411

Klose, S., Henden, A. A., Geppert, U., Greiner, J., Guetter, H. H., Hartmann, D. H., Kouveliotou, C., Luginbuhl, C. B., Stecklum, B., & Vrba, F. J. 2004, ApJ, 609, L13

Koch, D. G. 1978, in Proc. SPIE, Vol. 147, Computer-Aided Optical Design, ed. R. E. Fischer (Bellingham: SPIE), 71

Kouveliotou, C., Dieters, S., Strohmayer, T., van Paradijs, J., Fishman, G. J., Meegan, C. A., Hurley, K., Kommers, J., Smith, I., Frail, D., & Murakami, T. 1998a, Nature, 393, 235

Kouveliotou, C., Kippen, M., Woods, P., Richardson, G., & Connaughton, V. 1998b, GRB Coordinates Network, 107, 1

Kulkarni, S. R., Matthews, K., Neugebauer, G., Reid, I. N., van Kerkwijk, M. H., & Vasisht, G. 1995, ApJ, 440, L61

Lagage, P. O., & Pantin, E. 1994, Nature, 369, 628

Laros, J. G., Fenimore, E. E., Klebesadel, R. W., Atteia, J.-L., Boer, M., Hurley, K., Niel, M., Vedrenne, G., Kane, S. R., Kouveliotou, C., Cline, T. L., Dennis, B. R., Desai, U. D., Orwig, L. E., Kuznetsov, A. V., Sunyaev, R. A., & Terekhov, O. V. 1987, ApJ, 320, L111

LaVine, J. L., Eikenberry, S., & Davis, J. D. 2003, in Bulletin of the American Astronomical Society, Vol. 35, Bulletin of the American Astronomical Society, 1229

Low, F. J., Rieke, G. H., & Gehrz, R. D. 2007, ARA&A, 45, 43

Matthews, K., & Soifer, B. T. 1994, Experimental Astronomy, 3, 77

Mazets, E. P., Golentskii, S. V., Ilinskii, V. N., Aptekar, R. L., & Guryan, I. A. 1979, Nature, 282, 587

McClure-Griffiths, N. M., & Gaensler, B. M. 2005, ApJ, 630, L161

Mezger, P. G. 1986, Ap&SS, 128, 111

Moffat, A. F. J., & Fitzgerald, M. P. 1977, A&A, 54, 263

Morris, M., & Serabyn, E. 1996, ARA&A, 34, 645

Mountain, M., Gillett, F. C., & Kurz, R. 1997, in Proc. SPIE, Vol. 2871, Optical Telescopes of Today and Tomorrow., ed. A. L. Ardeberg (Bellingham: SPIE), 15

Muno, M. P., Clark, J. S., Crowther, P. A., Dougherty, S. M., de Grijs, R., Law, C., McMillan, S. L. W., Morris, M. R., Negueruela, I., Pooley, D., Portegies Zwart, S., & Yusef-Zadeh, F. 2006, ApJ, 636, L41

Munoz-Tunon, C., Vernin, J., & Varela, A. M. 1997, A&AS, 125, 183

Murakami, T., Tanaka, Y., Kulkarni, S. R., Ogasaka, Y., Sonobe, T., Ogawara, Y., Aoki, T., & Yoshida, A. 1994, Nature, 368, 127

Negueruela, I., & Clark, J. S. 2005, A&A, 436, 541

Neugebauer, G., & Leighton, R. B. 1969, Two-micron sky survey. A preliminary catalogue (NASA SP, Washington: NASA,)

Okumura, S.-i., Mori, A., Nishihara, E., Watanabe, E., & Yamashita, T. 2000, ApJ, 543, 799

Pasquali, A., Comerón, F., & Nota, A. 2006, A&A, 448, 589

Paumard, T., Maillard, J. P., Morris, M., & Rigaut, F. 2001, A&A, 366, 466

Phillips, A. C. 1999, The Physics of Stars, 2nd Edition (New York: Wiley)

Pilbratt, G. L. 2004, in Proc. SPIE, Vol. 5487, Optical, Infrared, and Millimeter Space Telescopes, ed. J. C. Mather (Bellingham: SPIE), 401

Portegies Zwart, S. F., Makino, J., McMillan, S. L. W., & Hut, P. 1999, A&A, 348, 117

Portegies Zwart, S. F., Makino, J., McMillan, S. L. W., & Hut, P. 2001, ApJ, 546, L101

Portegies Zwart, S. F., & McMillan, S. L. W. 2002, ApJ, 576, 899

Pozzo, M., Naylor, T., Jeffries, R. D., & Drew, J. E. 2003, MNRAS, 341, 805

Preibisch, T., & Zinnecker, H. 2001, in Astronomical Society of the Pacific Conference Series, Vol. 243, From Darkness to Light: Origin and Evolution of Young Stellar Clusters, ed. T. Montmerle & P. André (San Francisco: ASP), 791

Rayner, J. T., Toomey, D. W., Onaka, P. M., Denault, A. J., Stahlberger, W. E., Vacca, W. D., Cushing, M. C., & Wang, S. 2003, PASP, 115, 362

Rieke, G. H. 2007, ARA&A, 45, 77

Rieke, G. H., Lebofsky, M. J., & Low, F. J. 1985, AJ, 90, 900

Roche, P. F. 2004, Advances in Space Research, 34, 583

Rodríguez Espinosa, J. M., & Alvarez, P. 2003, in Revista Mexicana de Astronomia y Astrofisica Conference Series, Vol. 16, Science with the GTC, ed. J. M. Rodriguez Espinoza, F. Garzon Lopez, & V. Melo Martin (Mexico City: UNAM), 1

Rodriguez Espinosa, J. M., & Alvarez Martin, P. 2006, Astronomical Facilities of the Next Decade, 26th meeting of the IAU, Special Session 1, 1

Rothschild, R. E., Kulkarni, S. R., & Lingenfelter, R. E. 1994, Nature, 368, 432

Sabelhaus, P. A., Campbell, D., Clampin, M., Decker, J., Greenhouse, M., Johns, A., Menzel, M., Smith, R., & Sullivan, P. 2005, in Proc. SPIE, Vol. 5899, UV/Optical/IR Space Telescopes: Innovative Technologies and Concepts II., ed. H. A. MacEwen (Bellingham: SPIE), 241

Schroeder, D. J. 2000, Astronomical Optics (New York: Academic Press)

Shull, P., Jr. 1983, ApJ, 275, 611

Skrutskie, M. F., Cutri, R. M., Stiening, R., Weinberg, M. D., Schneider, S., Carpenter, J. M., Beichman, C., Capps, R., Chester, T., Elias, J., Huchra, J., Liebert, J., Lonsdale, C., Monet, D. G., Price, S., Seitzer, P., Jarrett, T., Kirkpatrick, J. D., Gizis, J. E., Howard, E., Evans, T., Fowler, J., Fullmer, L., Hurt, R., Light, R., Kopan, E. L., Marsh, K. A., McCallon, H. L., Tam, R., Van Dyk, S., & Wheelock, S. 2006, AJ, 131, 1163

Smith, W. J. 2005, Modern Lens Design (2nd Ed.; New York: The McGraw Hill Companies, Inc.)

Spitzer, L. 1987, Dynamical evolution of globular clusters (Princeton: Princeton University Press)

Stetson, P. B. 1987, PASP, 99, 191

Stetson, P. B. 1992, in Astronomical Society of the Pacific Conference Series, Vol. 25, Astronomical Data Analysis Software and Systems I, ed. D. M. Worrall, C. Biemesderfer, & J. Barnes (San Francisco: ASP), 297

Stolte, A., Brandner, W., Brandl, B., Zinnecker, H., & Grebel, E. K. 2004, AJ, 128, 765

Telesco, C. M. 2000, in Astronomical Society of the Pacific Conference Series, Vol. 219, Disks, Planetesimals, and Planets, ed. G. Garzón, C. Eiroa, D. de Winter, & T. J. Mahoney (San Francisco: ASP), 268

Telesco, C. M., Ciardi, D., French, J., Ftaclas, C., Hanna, K. T., Hon, D. B., Hough, J. H., Julian, J., Julian, R., Kidger, M., Packham, C. C., Pina, R. K., Varosi, F., & Sellar, R. G. 2003, in Proc. SPIE, Vol. 4841, Instrument Design and Performance for Optical/Infrared Ground-based Telescope, ed. M. Iye & A. F. M. Moorwood (Bellingham: SPIE), 913

Telesco, C. M., Pina, R. K., Hanna, K. T., Julian, J. A., Hon, D. B., & Kisko, T. M. 1998, in Proc. SPIE, Vol. 3354, Infrared Astronomical Instrumentation, ed. A. M. Fowler (Bellingham: SPIE), 534

Thompson, C., & Duncan, R. C. 1996, ApJ, 473, 322

Turner, D. G., Welch, G., Graham, M., Fairweather, D., Horsford, A., Seymour, M., & Feibelman, W. 2001, Journal of the American Association of Variable Star Observers (JAAVSO), 29, 73

van Genderen, A. M., Bijleveld, W., & van Groningen, E. 1984, A&AS, 58, 537

Vancura, O., Blair, W. P., Long, K. S., & Raymond, J. C. 1992, ApJ, 394, 158

Vasisht, G., Kulkarni, S. R., Frail, D. A., & Greiner, J. 1994, ApJ, 431, L35

Vrba, F. J., Henden, A. A., Luginbuhl, C. B., Guetter, H. H., Hartmann, D. H., & Klose, S. 2000, ApJ, 533, L17

Vrba, F. J., Luginbuhl, C. B., Hurley, K. C., Li, P., Kulkarni, S. R., van Kerkwijk, M. H., Hartmann, D. H., Campusano, L. E., Graham, M. J., Clowes, R. G., Kouveliotou, C., Probst, R., Gatley, I., Merrill, M., Joyce, R., Mendez, R., Smith, I., & Schultz, A. 1996, ApJ, 468, 225

Wachter, S., Ramirez-Ruiz, E., Dwarkadas, V. V., Kouveliotou, C., Granot, J., Patel, S. K., & Figer, D. 2008, Nature, 453, 626

Werner, M., Roellig, T. L., Low, F. J., Rieke, G., Rieke, M., Hoffmann, W. F., Young, E., Houck, J., Fazio, G., Hora, J., Gehrz, R., Soifer, T., Helou, G., Keene, J., Eisenhardt, P., Gallagher, D., Gautier, T. N., Irace, W., Lawrence, C., Simmons, L., Wright, E. L., Jura, M., Cruikshank, D., & Brandl, B. 2004, in Bulletin of the American Astronomical Society, Vol. 36, Bulletin of the American Astronomical Society, 699

Wilson, J. C., Eikenberry, S. S., Henderson, C. P., Hayward, T. L., Carson, J. C., Pirger, B., Barry, D. J., Brandl, B. R., Houck, J. R., Fitzgerald, G. J., & Stolberg, T. M. 2003, in Proc. SPIE, Vol. 4841, Instrument Design and Performance for Optical/Infrared Ground-based Telescopes, ed. M. Iye & A. F. M. Moorwood (Bellingham: SPIE), 451

Woods, P. M., Kouveliotou, C., van Paradijs, J., Hurley, K., Kippen, R. M., Finger, M. H., Briggs, M. S., Dieters, S., & Fishman, G. J. 1999, ApJ, 519, L139

Woods, P. M., & Thompson, C. 2006, Compact Stellar X-ray Sources, ed. W. Lewin & M. van der Klis (Cambridge: Cambridge University Press), 547

Wszolek, B., Rudnicki, K., Masi, S., de Bernardis, P., & Salvi, A. 1989, Ap&SS, 152, 29

BIOGRAPHICAL SKETCH

Michelle Lynn Edwards was born on December 17, 1979 in Trenton, NJ to Walter and Linda Edwards. A voracious reader from an early age, Michelle attended Little Friends Day School, Mercerville Elementary School, and Crockett Middle School, where she had an excellent childhood education. When not reading, she was often studying geography or visiting historical sites in Trenton and Philadelphia with her dad, an avid history buff. She also loved to sing and was in choirs from a very early age.

Michelle and her younger brother Matthew Scott, always got along well. Matt grew to be a talented musician and is now married to Jacquelyn Edwards nee O'Rourke, and working as both a UPS driver and self-employed music engineer.

At the end of her 6th grade year, the Edwards moved to North Hanover Township, NJ, where Michelle would spend the next six years attending Northern Burlington County Regional Junior/Senior High School (NBC). While in high school, Michelle was interested in law, history, and political science. She was a top debater and one of the founding members of the NBC Debate Team directed by Mr. Joe Coleman. She also participated in musical and theatrical productions, mock elections, and the National Honor Society. She was a library aid and captain of the Color Guard in the NBC Greyhound marching band. On weekends, she worked at the local farm market and bakery, Mr. McGregor's Garden, making pies and baked goods.

After high school, Michelle attended Dickinson College in Carlisle, PA where she was introduced by Drs. Priscilla Laws, Robert Boyle, and Windsor (Tony) Morgan to Workshop Physics, an activity-based course that replaced introductory physics lectures. After excelling in the class and showing interest in astronomy, she was invited by her adviser Tony Morgan, to travel to Flagstaff, AZ and observe with the 31" Lowell Telescope on Anderson Mesa. The beautiful skies, excitement of observing, and especially the instrumentation, drew Michelle further into the field of astronomy. She declared her physics major and astronomy minor soon after returning from the observing run. The

next summer she completed an REU with Drs. Stephen Levine and David Monet at the Naval Observatory in Flagstaff, AZ.

With hard work and encouragement from the faculty in the Physics and Astronomy Department at Dickinson, Michelle earned a position as a graduate school at the University of Florida in Gainesville, Florida. During her senior year at Dickinson, she was inducted into Sigma Pi Sigma and Phi Beta Kappa. She graduated from Dickinson College, Summa Cum Laude with Departmental Honors. She was the first member of her mother's extended family and her father's immediate family to earn a four year degree and the first person since her mother to attend college.

During her tenure at Dickinson, Michelle met her husband David Edmeades, only child of Marie and Paul Edmeades. David moved to Florida with Michelle after they both graduated from Dickinson. Avid gourmets, the couple enjoys entertaining and cooking for their friends in the townhouse they share with their cat, Puck. After seven years together the couple were married on October 9th, 2006.

While in graduate school, Michelle was fortunate to TA for three years for Dr. John Oliver, an excellent teacher, good friend and confidant. She worked on her second year project with Dr. Ata Sarajedini, who later graciously agreed to join her thesis committee, along with Drs. Rafael Guzman, Guido Mueller, and Charlie Telesco. Then in March 2003, she began working for Dr. Stephen Eikenberry on a summer instrumentation project. After a few months of successful work, including passing her qualifying exam and earning her Master's Degree, Steve took Michelle on as a thesis student to work on the CIRCE project. In 2006, Dr. Reba Bandyopadhyay agreed to join Steve as Michelle's co-adviser.

Throughout her graduate career, Michelle served as president, secretary, and admission committee liaison for the UF Graduate Astronomy Organization (GAO). She also organized and co-organized a variety of successful public outreach programs throughout Alachua County. During her final two years at Florida, she earned a P.E.O.

Scholar Award, a monetary award given to outstanding female graduate students throughout Canada and the US, and a University of Florida McLaughlin Dissertation Scholarship.

In August 2008, Michelle and David will move from Florida to La Serena, Chile where Michelle will start her new position as a Gemini Science Fellow with Gemini South Observatory.